Nano-Electro-Mechanical Systems at Ultra Low Temperatures as Probes for Quantum Fluids

With Superconducting Quantum Interference Device Transduction

Rupert James Edward Mellor

Thesis presented in partial fulfilment of the requirements
for the degree of
Doctor of Philosophy

Department of Physics
Royal Holloway and Bedford New College
University of London

Declaration of Authorship

I, Rupert James Edward Mellor, hereby declare that this thesis and the work presented in it is entirely my own. Where I have consulted the work of others, this is always clearly stated.

Sign: .....

Date: .....

For Alan, Lutha, Norris, and Barbara

Acknowledgements

The completion of this degree is for me the fulfilment of an ambition I set myself almost a decade ago, and so first and foremost I must thank my parents, Marlane and Simon, and my sisters Imogen and Hermione, for encouraging me to achieve my goals even when they seemed unattainable. Next longest suffering is Stacey, who has been both my emotional support and conceptual sounding board for the whole of my PhD (and more) without whom I can't imagine having completed. My supervisor, Andrew Casey, I owe an enormous debt of gratitude to for guidance and knowledge imparted alike. Throughout the course of my PhD Chris Lusher, Brian Cowan, and John Saunders have been of exceptional help in all matters theoretical and have steered the project and my work clear of many a treacherous obstacle, and so a warm thanks to them. Thanks go also to my NPL Supervisor, Olga Kazakova, and to Vishal Panchal and Vladimir Antonov for thier excellent work wire bonding my samples. Kunal Lulla and Aya Shibahara were instrumental in teaching me about NEMS and running a cryostat respectively and to this day their notes and charts make work in the laboratory possible. My thanks also go out to the Parpia group led by Jeevak Parpia, and the UBT group at the NEEL Institute led by Eddy Collin for the fabrication of the devices I studied. For ongoing cryostat complaints and tricks of the trade I needed to look no further than Lev or Jan, to whom I am immensely grateful.

My project would not have been possible without the fastidious attention to detail and precise craftsmanship of Richard, Ian, Paul and Mass who made my designs a reality. Of course I owe my sanity to those outside of my group, most importantly my fellow PhD students (although some now Doctors themselves): Alex, James, Katie, Dave B, Dave V, Toby, Tom, Jacob, George, Will, Tim, Sayeed, Steph, Harriet, Sercan, Giri, and Chris B. Without the teatime conversations and office discussions my work would have been much harder. Life in the Physics department would grind to a halt if it weren't for the work put in by Andy, Gill, Tracy, and Carmella and so thanks to them for making sure the necessities of department life were taken care of. Lastly for people within Physics I'd like to thank Flossie who worked so diligently with me on assembling the experiment for a summer, without whom I could not have completed the build in time for conference.

Outside of the department I was incredibly lucky to have a support network of friends who I met through medical pursuits, and so I'd like to thank Harry (without whom I wouldn't be at Royal Holloway) in particular for being the best of friends in school and beyond. I'd like to thank some of the first members of my dutiful management team; Dan, Arianwen, Ellie, Helen, and Simon, fellow PhD or undergraduate students who's support and company have been and continue to be invaluable to me.

Abstract

This thesis describes experiments developing the use of Nanoelectromechanical systems as low temperature sensors, and for use as nanoscale probes in quantum fluids. The investigations revolve around the characterisation of these devices at low temperatures and their interaction with a DC Superconducting Quantum Interference Device (SQUID). The report begins with the background of NEMS research in the field of low temperature research and proceeds to discuss the important theoretical concepts around a doubly clamped beam resonator. The equivalent electrical circuit for a NEMS in the relevant transduction scheme is developed before a discussion of the experimental techniques used throughout the project. The first set of experiments involving vacuum measurements are described and the interaction between the NEMS and SQUID characterised with a qualitative model, demonstrating the ability to cool the first mode of the resonator with specific SQUID settings, and the ability to induce self-sustained oscillations. The process of designing and fabricating a new type of experimental cell for NEMS that is capable of better thermalisation is described, which enables further experiments in liquid helium. The important properties of helium with respect to immersed objects subject to excitations is discussed to enable examination of the preliminary results obtained from the new cell, before conclusions are drawn and further work discussed.

Contents

List of Figures

List of Tables

Chapter 1

Introduction

Nano Electro Mechanical Systems (NEMS) are a broad class of devices, ranging from nanoscale motors to passive mechanical sensors. They are preceded by MEMS (Micro...), which have been at the forefront of technological innovation since the first patented device developed by H.C. Nathanson in 1965 [1, 2]. The key common feature of these devices is that they are fabricated using modern lithographic processes onto a single chip. MEMS have become a prolific feature of modern consumer electronics, from car accelerometers [3] to household printers [4], and as fabrication technology has improved, the scale of these devices has reduced to length scales at which macroscopic quantum mechanical phenomena can occur [5].

Not only are the devices themselves capable of displaying quantum mechanical behaviour, but they can serve as mechanical probes of materials governed by quantum mechanics. Liquid helium, when sufficiently cooled, becomes one such material at different temperatures depending on the atomic species: 2.17 K for ^{4}He and 2.7 mK for ^{3}He [6]. ^{4}He is a spin zero boson, and as such the formation of a condensate is

expected and understood. ^{3}He however is a spin 1/2 fermion and so the emergence of superfluidity is unconventional. In addition, the coherence length of superfluid ^{3}He ranges from 13 nm to 65 nm between the melting pressure and zero pressure [7], which is on the same order as the dimensions of a NEMS.

In development of NEMS devices as both passive and active probes in helium, we used a high-sensitivity transduction scheme, implementing a two-stage Superconducting Quantum Interference Device (SQUID) with high coupled energy resolution [8]. This setup resulted in some feedback interactions between NEMS devices and the SQUID chip, which could be used to actively drive or damp the resonator motion, as well as allowing observation of the purely thermomechanical motion of the device. This scheme connected the NEMS with the SQUID via conventional twisted pair, rather than on-chip [9], allowing change of samples with high control of measurement parameters.

Achieving the temperatures required for the superfluid transitions in helium is difficult with small thermally isolated structures such as NEMS, and we developed a cell capable of cooling the devices both in vacuum and immersed in liquid helium, with the aim of achieving sub-milliKelvin temperatures, compatible with both standard nuclear demagnetisation techniques and cryogen free cryostats [10].

1.1 Background

Nanomechanics is a relatively recent feature in the ultra low temperature physics landscape, when compared with optics or quantum technologies. The range of publications in the literature reduces further still when SQUID transduction is considered, though measurement schemes exist that have parallels with our own. In order to illustrate the similarities in techniques, it is logical to review the literature by measurement scheme rather than by phenomenology.

1.1.1 High Quality-Factor NEMS

A key concept when studying MEMS and NEMS is the 'Quality factor' of the devices. The Quality, or 'Q'-factor of a device is a measure of the energy lost per period of its vibration. In the context of these devices, it is a measure of the sensitivity of the device, with higher Q-factors indicating a higher sensitivity. A high Q-factor resonator will have a narrow linewidth compared to its amplitude in the frequency domain, making it sensitive to a narrow frequency range. A high Q-factor also means that the time taken for the device to relax from excitation is long compared to its frequency. This would mean that at temperatures where the NEMS behaves quantum mechanically, a quantum state could be stored on a NEMS with a high enough Q-factor. There has been extensive research into developing resonators with high Q-factors, from using carbon nanotubes [11], silicon nitride beams such as used in this thesis [12], through to use of exotic materials such as superfluids [13]. The sources of dissipation that govern the Q-factors of these materials are typically caused by thermoelastic damping [14], or additional vibrational modes at the edges of materials [15]. Silicon nitride beams are used because of their low intrinsic damping, attributed

to high crystal uniformity reducing the phononic reflections within the material, and the high tension. In these beams, damping mechanisms are dominated by losses at the clamping sites [14]. It has been shown that by increasing the stress in the resonator, the beam can become acoustically decoupled from the substrate [16]. For these reasons, the NEMS devices studied here are silicon nitride beams. There has also been work in controlling the Q-factor of the devices post-fabrication by using feedback mechanisms or sideband excitation [17, 18], which can be seen as analogues to some of the work discussed in this thesis.

1.1.2 Classical Electronics

Electronic transduction and drive of NEMS devices is typically achieved in one of two ways: capacitively or inductively. In either of these cases the structure must have an electrically conductive component, commonly achieved by depositing a thin film of metal on top of the structure via standard lithographic means [19] or constructing the resonator out of a conducting material entirely [20].

Using classical electronics allows access to a much larger parameter space, and the measurement is likely unaffected by small resistances incurred by large temperature and field variations. Typically, however, it is important to note that superconductivity is generally required to take full advantage of these techniques.

One such experiment is well described by Collin *et al.* [5], whereby an alternating current is driven through the structure, such that it experiences a force perpendicular to an applied magnetic field. On resonance, the amplitude of motion of the NEMS will

increase significantly and a voltage will be induced, which is measured using a lock-in amplifier. This technique is limited to detection only when driving the resonator as the small displacements generated by Brownian motion generate insufficient voltage to be detected. Recently, new techniques have sought to achieve Brownian motion detection using a lock-in amplifier by injecting calibrated noise [21].

One of the most common methods for transducing and driving NEMS is using lasers and interferometry, using a laser tuned to the resonant frequency of the NEMS to drive motion. The same beam can be used to then transduce the motion using interferometry as shown in fig. 1.1 [22, 23].

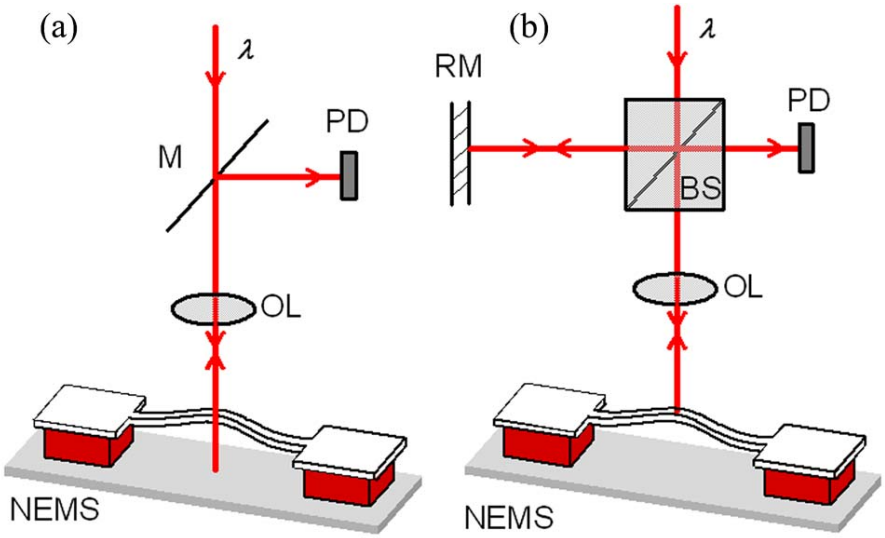

Figure 1.1: A diagram of two laser transduction setups for NEMS, both using a photodetector (PD) and objective lens (OL). (a) Shows Fabry-Perot interferometry, and (b) shows Michelson interferometry using a beamsplitter (BL) and reference mirror (RM) to create a reference beam with which to interfere the reflected light from the NEMS [22].

Whilst this method has high sensitivity it relies on driving the resonator, but can still be used to detect thermomechanical motion and to artificially cool the mode of a resonator using Doppler-cooling similar to atomic trap experiments [24]. However this cools the mode and not the electrons within the material [25, 26].

1.1.3 Quantum Technologies

Moving to higher sensitivities, and thus the ability to resolve small deflections associated with Brownian motion, requires quantum limited technologies. There are multiple ways of achieving this but all use some element of quantum technology, such as a Superconducting Quantum Interference Device (SQUID) [27] or a Superconducting Single Electron Transistor (SSET)[28]. In this thesis, the experiments performed use SQUIDs for detection.

Whilst the study of NEMS is a broad field, the use of flux-based position detectors is relatively rare. Flux-dependent sensing means that the NEMS must generate a current inductively with magnetic fields, which brings with it the key issue of damping from the magnetic field. To increase the signal amplitude requires a higher magnetic field which increases the damping [29].

SQUIDs and NEMS have previously been coupled by fabricating the SQUID such that there is a NEMS inside the superconducting loop [27, 30] as seen in fig. 1.2. This means that the motion of the NEMS in a magnetic field directly couples into the SQUID and produces an amplified voltage change. This approach has lead to femtometer precision at milliKelvin temperatures [27] and is presently limited by the

cryogenic preamplifier rather than the SQUID itself. In this configuration the SQUID is damped by application of magnetic field and then biased above the critical current. Because the SQUID is underdamped below fields of 100 mT, the fields explored are limited, which is not the case in the experiments described in this thesis due to the separation of the SQUID and NEMS. Our setup allows us to reduce the magnetic field to microTesla and still be able to detect the motion of the resonator. The experiments described in this thesis utilise an on-chip preamplifier array of SQUIDs [8]. As has been mentioned, the main advantage of using SQUIDs is their high sensitivity [8], but this sensitivity comes at the cost of the difficulty in providing a flux noise free environment.

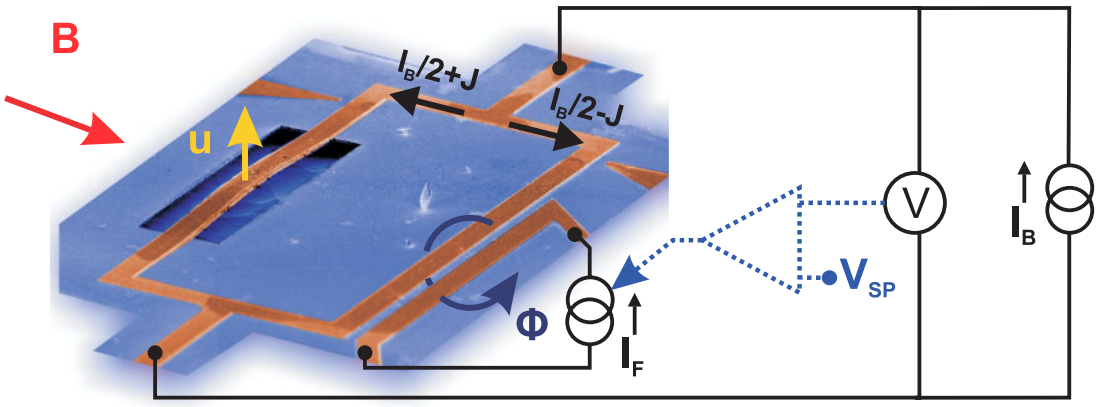

Figure 1.2: A NEMS incorporated into a SQUID loop for transduction fabricated by the Poot group at the Technical University of Munich [17].

The coupling of SQUIDs to NEMS can result in inadvertent driving of the NEMS through interactions between the two, referred to as backaction [31], generated by the SQUID's feedback electronics. In experiments by Etaki *et al.* the backaction has been tuned, and has resulted in self-sustained oscillations [17, 32]. Tuning of

the backaction results in altering the Q-factor of the resonator: this was achieved by altering the bias current and magnetic flux. By doing this they were able to vary the coupling between the SQUID and the resonator, and noticed deviations between the bath temperature and effective temperature of the resonator when the coupling was weak. The self-sustained oscillations observed were a consequence of the back-action, and allowed the Q to be driven up or down. They were able to distinguish two distinct patterns of behaviour from hodographs of the signal, showing a regime in which the resonator was driven by thermal motion, and a regime where it was driven by the backaction. It has been shown that this backaction can be used for heating or cooling of the resonator [29, 28, 33], analogous to laser cooling of ions. The motion of the resonator is opposed by forces in the opposite direction from the feedback, thus slowing the motion and effectively reducing the power in the resonator.

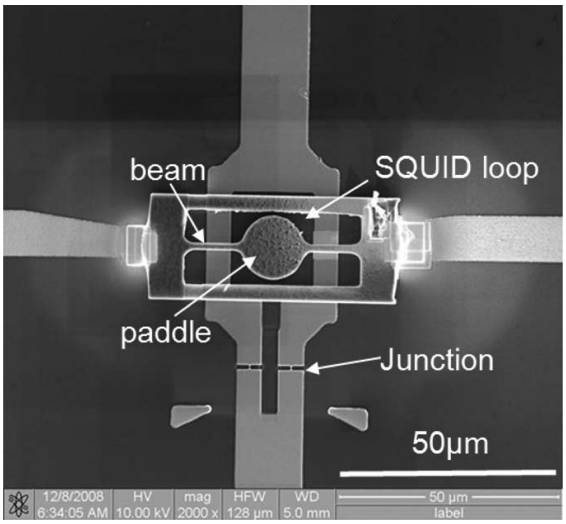

Figure 1.3: A 'paddle' NEMS placed over a nano SQUID, a second example of the SQUID and NEMS being placed in the same environment [34].

When not incorporating the NEMS into the SQUID loop, they have been mounted over the top of the SQUID such that the motion of the resonator induces voltage fluctuations in the detector. This has been done by creating resonators that slot into SQUID loops [35, 9], although in these examples the SQUIDs are nanoSQUIDs fabricated using Ion Beam Milling seen in fig. 1.3. These SQUIDs are far smaller than the SQUIDs used in this thesis, and again depend on separate off-chip amplifiers.

By mounting a magnetic nanoparticle on the end of a singly clamped resonator, it is possible to measure the motion of the beam using a flux transformer and a SQUID [36]. The system using a magnetic particle on the end of the beam [36] is particularly effective, achieving sub-attoNewton resolution at low temperatures. From a SQUID perspective, this experiment is closest to our set up, as the SQUID is separated from the resonator by a flux transformer. This arrangement, however, does not include a

magnet.

A combination of the aforementioned laser transduction mechanism and quantum limited technologies exists, broady refered to as cavity optomechanics [29]. This method of transduction involves coupling an optical cavity that is designed to resonate close to a NEMS frequency to a NEMS device. This technique is capable of measuring the thermomechanical noise of a NEMS at room temperature [37], and of influencing the behaviour of the NEMS by both 'cooling' [24] and driving [18] a NEMS mode. It will become apparent that there are analogues to these behaviours in the work presented in this thesis.

1.1.4 NEMS at Low Temperatures

A consistent problem with the cooling of NEMS devices is cooling the resonator itself down to low temperatures. Issues arise when it is considered that in the experiments in this thesis the beam has its main thermal link through a deposited metal surface layer, which at milliKelvin temperatures is superconducting giving it extremely poor thermal conductivity. On top of this, the beam is a long thin suspended element, so thermal conductivity would be reduced regardless. In our system, the limit to cooling the resonator would appear to be the minimum bond wire temperature which (from noise thermometry) we find to be around 14 mK using standard thermalisation techniques.

The objective of cooling in vacuum is to enter the quantum regime of a resonator, such that the quantum behaviour of a macroscopic object can be observed. This limit

is described by:

$$k_{\mathrm{B}}T \approx \frac{1}{2}\hbar\omega \tag{1.1}$$

where T is the temperature, and ω the fundamental angular frequency of the NEMS. This will allow us to understand the extent to which macroscopic objects are affected by the laws of quantum mechanics, which could lead to use of NEMS in quantum computing owing to their high coherence times [38].

Previous experiments by other groups at low temperatures have also experienced a decoupling of the resonator temperature from the bath temperature [17, 36], with the temperature of the resonator hanging above the temperature of the bath. We would hope to solve this problem by the use of liquid helium as a thermal ground, as discussed later in the thesis.

SQUID detection is considered a promising technology for observing the quantum motion of resonators, partially motivating the project. Although ultimately this objective was not achieved, it has been proposed that observation of quantum motion could be performed by taking spectroscopic measurements, indicating a splitting of the degenerate doublet state near to the degeneracy point [38].

1.1.5 Helium 4

This section of the introduction begins with a description of the more massive of the two helium isotopes, helium 4 (^{4}He). ^{4}He consists of two protons and two neutrons and is a highly stable element due to its complete electronic shell. Of the two isotopes this was the first to be used in testing the cell described in chapter 5 due to its cost. Helium is a unique element in that it never solidifies at saturated vapour pressure due to its low mass and weak Lennard-Jones potential. The shallow Lennard-Jones potential of helium requires two helium atoms to get very close to be able to bind and form a solid lattice. Atoms bound in a solid lattice have an uncertainty in position within which the atom vibrates with a frequency ω_0 thus defining the zero-point energy E_0 given by Annett [6]:

$$E_0 = \frac{3}{2}\hbar\omega_0 \tag{1.2}$$

The amplitude of this vibration is dependent on the energy of the atom, and on the mass. Lower mass atoms have a higher vibrational amplitude than heavier atoms of similar energy. This zero-point motion is larger than the maximum interatomic spacing required for lattice formation in helium, and as such both isotopes will not form a solid until subjected to pressures exceeding 25 Bar [39].

It is because of this lack of a solid phase at saturated vapour pressure that the behaviour of liquid helium is governed by quantum statistics. ^{4}He liquefies at 4.21 K and behaves as a normal fluid until it is cooled below 2.17 K whereupon it goes though a transition to superfluidity, which is known as He II. The transition from normal fluid to superfluidity is marked by a dramatic increase in the specific heat of the

fluid, called the lambda point. This transition is well within the temperature ranges accessible on a cryogen free cryostat and as such was a convenient choice for testing.

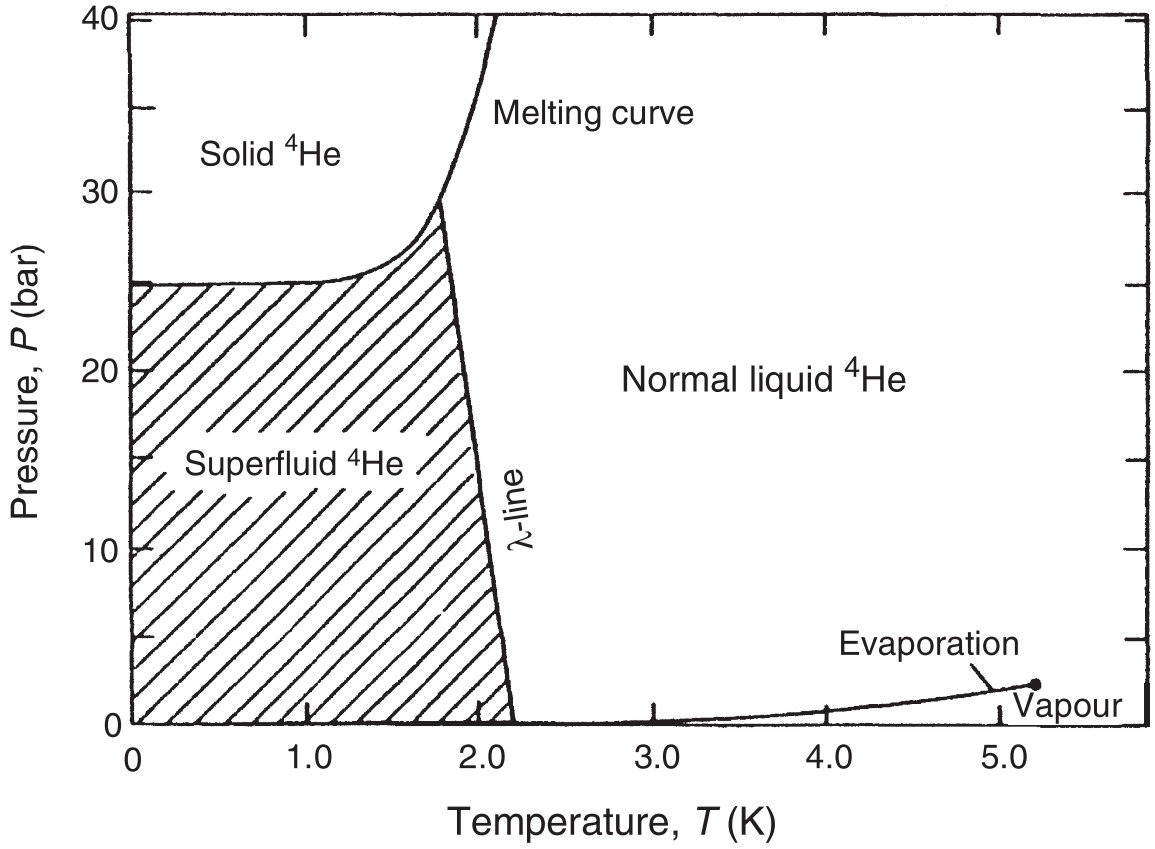

Figure 1.4: The phase diagram for ^{4}He, illustrating the superfluid transition on the left of the plot [40].

^{4}He has an even number of nucleons meaning it has integer spin, making it a boson. The occurrence of superfluidity in ^{4}He is due to reduction of the chemical potential to zero and the collapse of the momentum distribution into a single shared momentum state, which is only possible for bosons. This is evident when the exchange of identical

particles is considered for symmetric and antisymmetric wavefunctions:

$$\Psi_S = \frac{1}{\sqrt{2}}[\psi_{\alpha,1}\psi_{\beta,2} + \psi_{\alpha,2}\psi_{\beta,1}] \tag{1.3}$$

$$\Psi_A = \frac{1}{\sqrt{2}}[\psi_{\alpha,1}\psi_{\beta,2} - \psi_{\alpha,2}\psi_{\beta,1}] \tag{1.4}$$

Under particle exchange any two particles with the same spin and position will result in a non-zero probability density $|\Psi^2|$ for a symmetric total wavefunction, but zero for an antisymmetric wavefunction. Bosonic particles like ^{4}He have a symmetric wavefunction, and thus are capable of occupying the same state unlike fermionic particles such as ^{3}He. This collapse into the same momentum state is known as Bose Einstein condensation; all atoms in the fluid share the same state and thus a single-valued macroscopic wave function describes the entire fluid, defined as:

$$\psi_0(\boldsymbol{r}) = \sqrt{n_0(\boldsymbol{r})}e^{i\theta(\boldsymbol{r})} \tag{1.5}$$

Where $n_0(\boldsymbol{r})$ is the density of particles in the condensate, and $\theta(\boldsymbol{r})$ is the phase. $\psi_0(\boldsymbol{r})$ is also referred to as the order parameter as it describes the order of the system, with high order corresponding to the superfluid state.

Superfluidity is a complex phenomenon with many facets that are actively researched. Here we shall focus on those properties that affect the motion of submerged bodies such as the viscosity and the propagation of sound.

Motion in Superfluid

The resistance to motion of a superfluid within a superfluid is theoretically zero, and indeed the resistance to superfluid flow has been measured to be effectively zero in ^{4}He [41]. However, there is resistance to motion for an object through the fluid measured for rotating cylinders and for rotating disk experiments [42], and importantly recreated with vibrating wire experiments [43] close to the superfluid transition temperature. This is an effect of the two-fluid model which asserts that He II consists two fluids, one normal and one superfluid. The fraction of He II that is normal decays rapidly with reduction of temperature with a T^4 dependence.

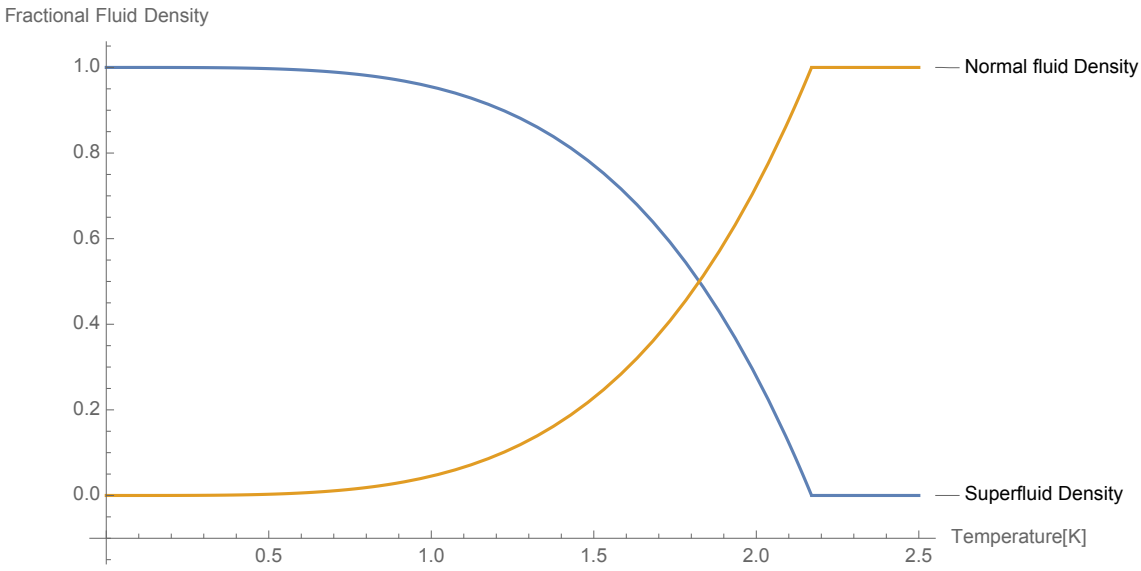

Figure 1.5: The components of the total fluid density with reducing temperature with T^4 dependence of superfluid fraction below $T_c = 2.17$ K.

The superfluid fraction flows with zero viscosity and as such does not contribute to the inertial mass of moving objects. The normal fraction of the fluid however 'clamps' to the surface of a moving body, as was seen in the rotating plate experiments described

in Hollis-Hallett [42]. The two-fluid model states that the normal and superfluid components are inseparable and non-interacting, such that it is not possible to identify any single atom that is participating in either component individually.

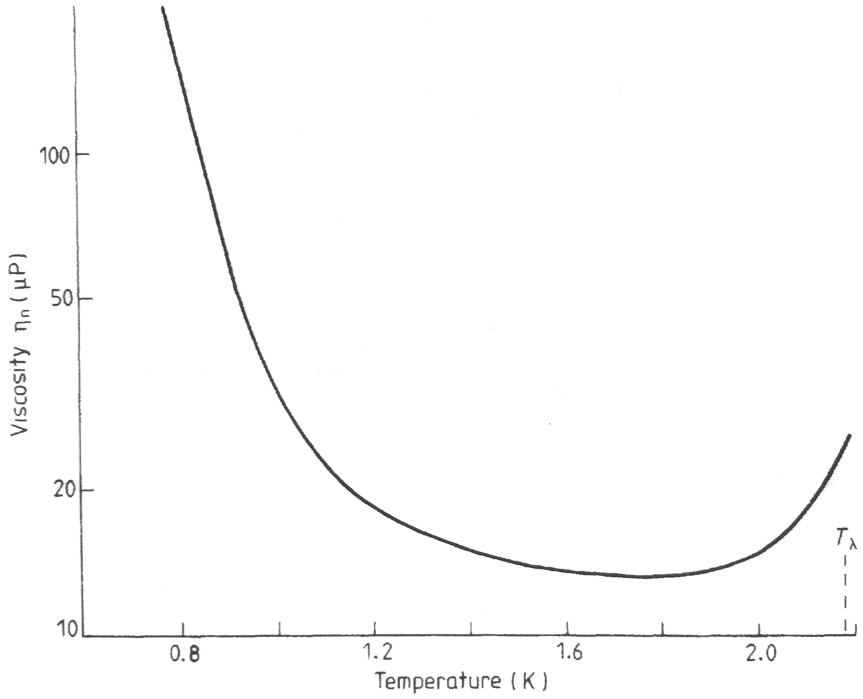

Figure 1.6: Viscosity with temperature for an object moving in the fluid [39, 42] where the behaviour near T_λ, the critical temperature, is due to the two-fluid model and the behaviour far below this is due to excitations in the fluid [44].

Because of the two-fluid model is it understood that heat transfer in He II is via the normal component of the fluid, and that this component flows from the source of heat to the coldest point. The superfluid fraction flows in the opposing direction to maintain local density of the superfluid, and this leads to the oft demonstrated '*fountain effect*' by which a superleak is used along with a heat source to generate a bulk flow of He II. This pattern of thermally induced mass flow is referred to as 'second

sound', where 'first sound' is the conventional pressure wave colloquially referred to as sound in everyday life.

Excitations

^{4}He is described as a condensate for the purposes of this project, and in the context of motion within the fluid it is now appropriate to consider the depletion of the condensate due to thermal excitations. There are two excitations that we consider for interaction with the NEMS, those of phonons and rotons. Phonons are the elementary quasiparticle of sound, constituting a longitudinal vibration. Transverse vibrations are not considered because a fluid is not capable of transmitting such a force. The phonon and roton populations are regarded as non-interacting. Phonons are responsible for

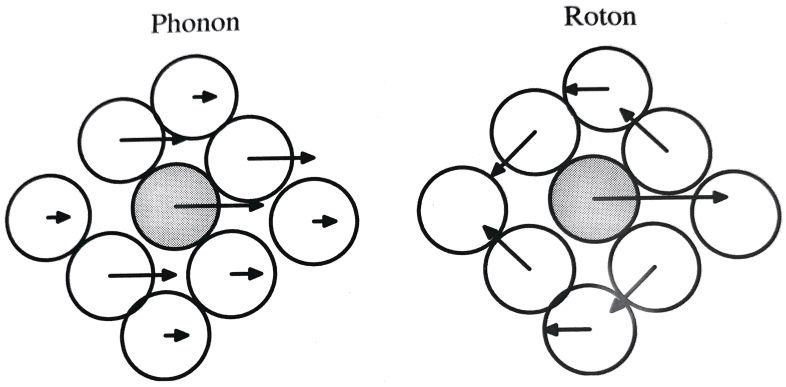

Figure 1.7: A visual representation of the mechanical behaviour of a phonon and roton which aids understanding of their interaction with the NEMS [6].

heat transport at low energies far below the superfluid transition temperature, when the normal fluid fraction is much less than the superfluid fraction as seen in fig. 1.5. This low energy region is seen in fig. 1.8 as the dashed straight line through the origin describing low energy phonon behaviour with the gradient of the speed for first sound.

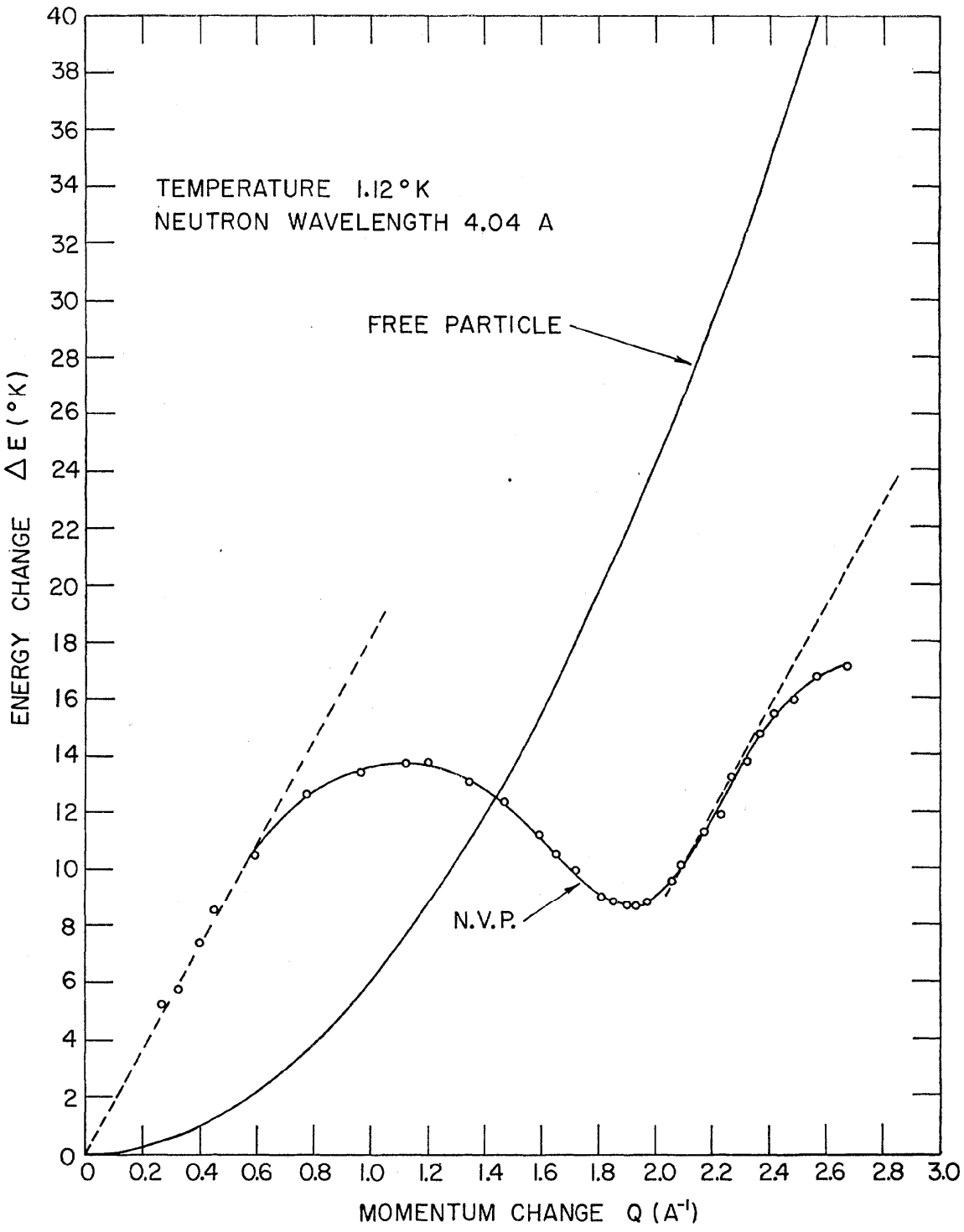

Figure 1.8: The dispersion plot for superfluid ^{4}He under normal vapour pressure (N.V.P.). The behaviour indicative of phonons is described by the dashed line passing through the origin, magnons by the first maxima of the curve, and rotons by the second minima, thus illustrating the diversity of quasiparticle excitations present in a superfluid [45].

At higher energies the dispersion deviates from the straight line and curves into a local maxima, which is the magnon peak. Magnons are another excitation that can be described as the quanta of spin-waves through a material, but shall not be discussed further within this thesis. The dispersion then dips into a minima that indicates the presence of rotons. Notably rotons share the transmission of thermal excitations at this energy with phonons, and as such contribute to the viscosity for objects with energy of this order moving through the fluid, which was described by Landau and Khalatinkov [44]. Figure 1.9 shows a more detailed, extended version of fig. 1.6 with

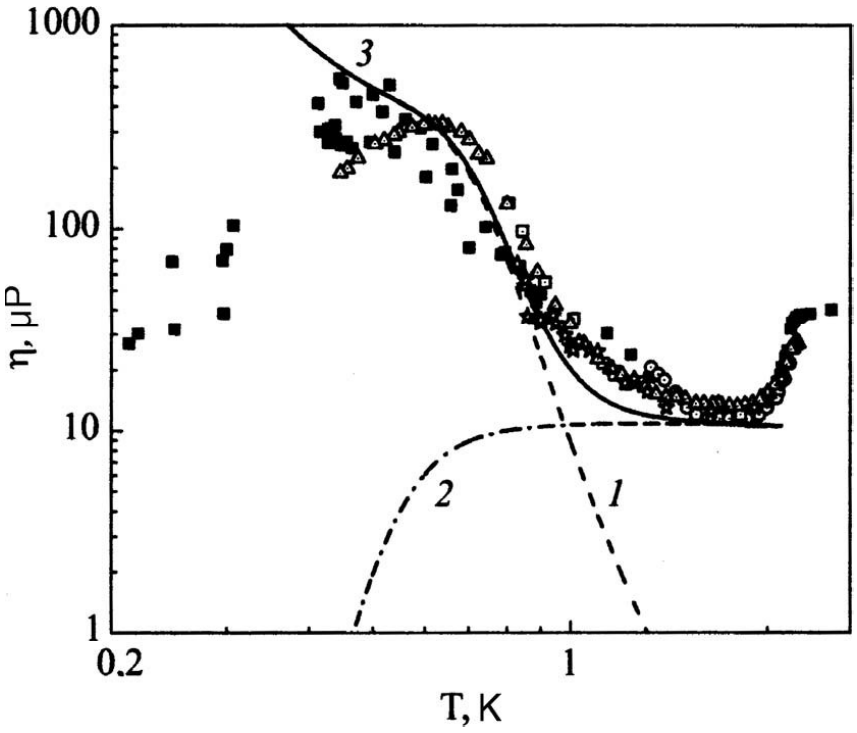

Figure 1.9: He II viscosity measured using quartz tuning forks where 1 is the phonon viscosity, 2 is the roton viscosity and 3 is the total viscosity [46].

the contributions from rotons and phonons illustrated by the dashed lines (1) and (2) respectively, where there is a sharp increase in viscosity as the mean free path

of the phonons means phonon-phonon scattering becomes more important. There is a deviation from the predicted solid curve (3) which is due to the effective viscosity seen by an object moving through the fluid of a given size, where the mean free path of the phonons is close to this size. This effect occurs because the mean free path of the phonons in the fluid grows with decreasing temperature until the phonons in the fluid no longer behave like a fluid, but like a rarefied gas.

Oscillating devices have been used to measure viscosity in ^{4}He extensively, involving rotating cylinders, disks, vibrating wires and quartz tuning forks [47, 48]. Viscosity is perhaps the most obvious property of the fluid to measure using these devices, however it has been used to measure a wide range of phenomena such as quantum turbulence [49] and even in generation of vortices [50]. This is sufficient motivation to immerse a resonator in He II and gives key features that should be observed in later experiments.

1.1.6 Helium 3

Unlike ^{4}He, ^{3}He is a fermionic system due to the odd number of nucleons compared with the full electron shell. It is lighter than ^{4}He and as such does not liquefy until a lower temperature of 3.19 K and does not become superfluid until 2.7 mK (which was discovered much later than superfluidity in ^{4}He) [51]. However the occurrence of superfluidity is not expected for a fermionic system unless BCS theory is considered, and indeed the formation of Cooper pairs is responsible. To explain this pairing intuitively it is best to consider a gas of electrons in a crystalline lattice (thus modelling a superconductor). The passage of an electron through the lattice will cause a minute contraction of the lattice spacing as the positively charged nuclei are attracted to the electron. This in turn creates a weak localised positive charge that accompanies an electron as it travels through the lattice, which attracts other electrons. At sufficiently low energies the electrons find it energetically favourable to exist within these small regions of positive charge and thus the electrons form pairs. However, this description can only account for a resulting spin singlet due to the antisymmetric spin wavefunction of fermions:

$$\frac{1}{\sqrt{2}}(|\uparrow\downarrow\rangle - |\downarrow\uparrow\rangle) \tag{1.6}$$

In addition ^{3}He has a spin triplet wavefunction [52], and as such this mechanism does not describe the interaction between helium atoms well, although this should be evident from the lack of an external lattice in which the helium atoms move to provide a phonon coupling. In fact the pairing mechanism in ^{3}He is due to spin pairing where the alignment of spins tends to be ferromagnetic, and as such the quasiparticles surrounding a helium atom will anti-align and form an attractive potential. It has

been shown that the most attractive potential is formed when the helium has a total angular momentum of $l = 1$, or 'p-wave' pairing [6] .

Phases of Superfluid ^{3}He

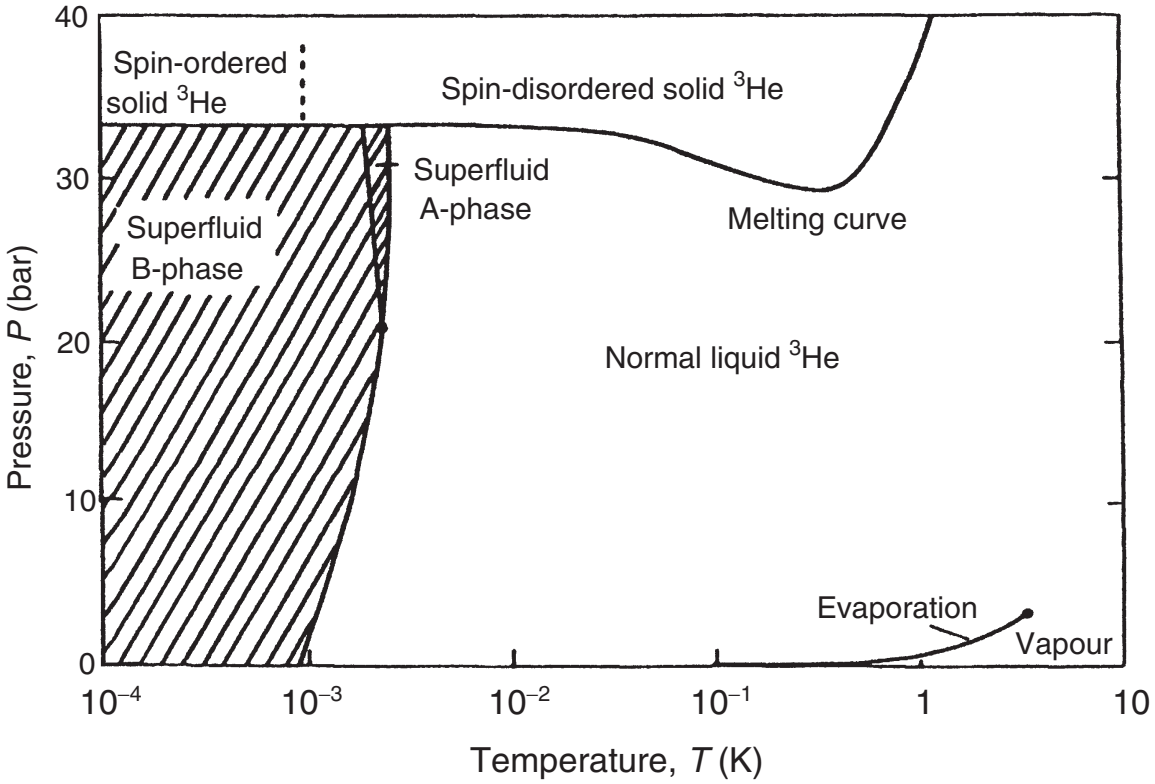

Figure 1.10: The phase diagram for ^{3}He, detailing two of the three superfluid phases. the A-phase boundary extends the length of the B-phase interface such that all transitions to B-phase must go through A-phase [40].

^{3}He has three superfluid phases denoted A1, A and B phase. These phases are all magnetic, a property not reflected in superfluid ^{4}He. Generally the B-phase dominates as shown in fig. 1.10. The A1 phase shall not be discussed in this thesis, as the conditions required for its presence are not met in these experiments, but it is discussed thoroughly by Leggett [52].

The separate phases of superfluid arise from the spin triplet:

$$\begin{pmatrix} |\uparrow\uparrow\rangle \\ |\downarrow\downarrow\rangle \\ \frac{1}{\sqrt{2}}(|\uparrow\downarrow\rangle + |\downarrow\uparrow\rangle) \end{pmatrix} \tag{1.7}$$

Indicating the three possible combinations of spin for the pair of helium atoms. To describe the phases, first recall that the pairing of the atoms to form the condensate leaves an energy gap above the Fermi surface equivalent to the pairing strength. Phase A, or the 'Anderson-Brinkman-Morrel state', consists only of the unidirectional spin pairings i.e. the first two kets in eq. (1.7). This means that the spin vector as seen in projects along the x-y but not z axis of momentum space.

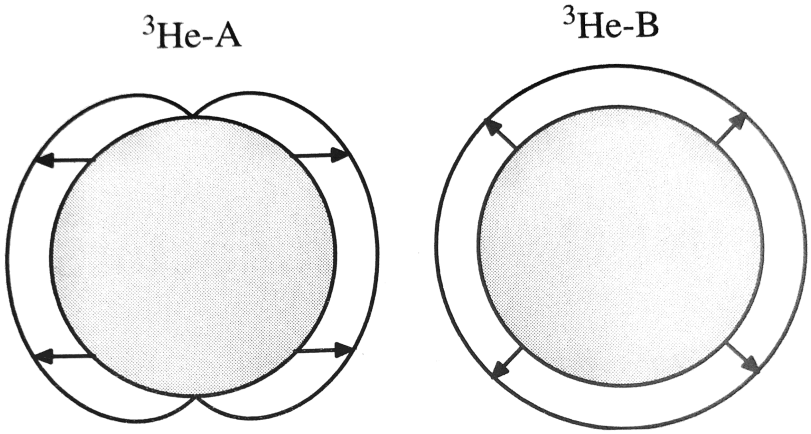

Figure 1.11: A graphical representation of the energy gap over the Fermi surface for the two phases of superfluid helium, where the arrows indicate the spin orientation of the phase [6].

The B phase, or 'Balain-Werthamer' state comprises the entire spin triplet, eq. (1.7), which allows the spin vector to rotate freely. Thus the energy gap for the B-phase is spherically symmetric. The differences between these two phases lead to some in-

teresting effects, such as magnetic suppression of B-phase compared with A-phase. The application of magnetic field to the superfluid favours A-phase, as it can align parallel or anti-parallel with the applied magnetic field. B-phase however cannot, and once the magnetic field is strong enough to make opposite-spin pairing energetically unfavourable the state is destroyed.

The surfaces of materials immersed in ^{3}He are preferentially wetted by the A-Phase [53]. This behaviour is due to the suppression of the order parameter near surfaces alien to the superfluid. The two phases can be described with order parameter matrices:

$$A_A = \Delta \begin{pmatrix} 1 & i & 0 \\ 0 & 0 & 0 \\ 0 & 0 & 0 \end{pmatrix}, \qquad A_B = \Delta \begin{pmatrix} 1 & 0 & 0 \\ 0 & 1 & 0 \\ 0 & 0 & 1 \end{pmatrix} \tag{1.8}$$

Where A_A is the order parameter for A phase, and A_B is the order parameter for B phase. At the diffuse surface of an object the order parameter of both phases is suppressed over the order of a coherence length as both the transverse and longitudinal elements of the order parameter are heavily modified. For specular boundaries however, only the longitudinal elements are reduced whilst the transverse elements are unaffected, meaning the order parameter for the A phase is unmodified. In fact the A phase spin vector can become anchored to a specular surface [54]. The B phase is suppressed at specular boundaries, again healing over a coherence length.

It is quite unlikely that the surface of the resonator is smooth and specular due to the

etching process used to create it, which would mean the resonator will be coated in normal fluid if immersed in ^{3}He. To solve this issue it is planned to use a thin layer of ^{4}He to 'pre-plate' the surfaces within the cell, which has been shown to render diffuse surfaces specular [55]. The resonator used for these experiments has dimensions close to those of the coherence length of ^{3}He, 13 nm to 65 nm between the melting pressure and zero pressure [7]. This would indicate that at low displacements the resonator will move less than a coherence length, over which the B phase will not have healed, so in future experiments immersing NEMS in superfluid, it may only be possible to observe the A-phase environment due to the dimensions of the resonator. However this proximity to the coherence length could allow direct probing of Cooper pairs in the superfluid by driving the beam capacitively, and should allow better coupling to phonons.

1.2 Thesis Structure

In chapter 2 the underlying theoretical concepts for modelling NEMS as tensioned strings is described, followed by the derivation of the equivalent electrical circuit for the NEMS as commonly used in the field.

Chapter 3 focusses on the range of experimental techniques used in this project. Starting with a description of the various NEMS devices studied in the project and their fabrication process performed at Cornell and the NEEL Institut, the chapter then introduces SQUIDs and their basic underlying theory of operation before specifying the two-stage SQUIDs from Physikalisch-Technische Bundesanstalt (PTB), Berlin, used in this project. The specifics of the measurement scheme used are described, detailing the features that set it apart from other SQUID transduced NEMS experiments described earlier. This leads on to a discussion of the thermometry techniques used in the measurement scheme which allows measurement of both the electron temperature and the mode temperature. The details of the initial calibrations and tests used to characterise the experiment behaviour are then described.

In chapter 4 the main experiment is described, starting with the process used to acquire and analyse the data, confirming that the observed behaviour is consistent with what is expected for a NEMS. The deviations from theory are described, namely the apparent mode cooling and self-sustained oscillation behaviours. Both behaviours are then analysed in detail and a qualitative model to justify the observations is presented.

Chapter 5 marks the beginning of a new generation of experiments involving liquid

helium. This chapter describes the requirements of an enclosure inside of which to perform experiments in liquid helium, and in which to cool in a vacuum using liquid helium without the need to open the cryostat. The design and fabrication of the new cell is described including details of new techniques for small device thermalisation in vacuum.

Chapter 6 reports the preliminary results from the first sets of experiments in superfluid ^{4}He. Findings include surprisingly high Q-factors, apparent damping due to immersion, and thermalisation of the NEMS to the experiment stage.

The conclusions of this thesis are presented in chapter 7, containing a brief summary of the two results chapters, describing feedback effects between the SQUID and NEMS, and preliminary results from helium immersion.

Chapter 2

Theory

2.1 Equations of Motion & Mode Shapes

In this section, the mathematical modelling for the doubly clamped beam is explored, covering the standard displacement of the beam and the modelling of the resonator as a parallel resonant circuit. These derivations can be found in *"The Physics of Nanoelectronics"* from the Oxford Master Series in Condensed Matter [56].

2.1.1 Doubly Clamped Beams

The beam is modelled as a lattice structure under high stress along the length of the beam - this is the case with the SiN resonators studied in this thesis. This thesis uses the Euler-Bernoulli theory of beams, which is accurate for long thin beams with a low total displacement. This theory is based on the principle that force incident upon a beam generates a torque transverse to both the beam axis and the force. It does however, ignore shear forces for small displacements [57].

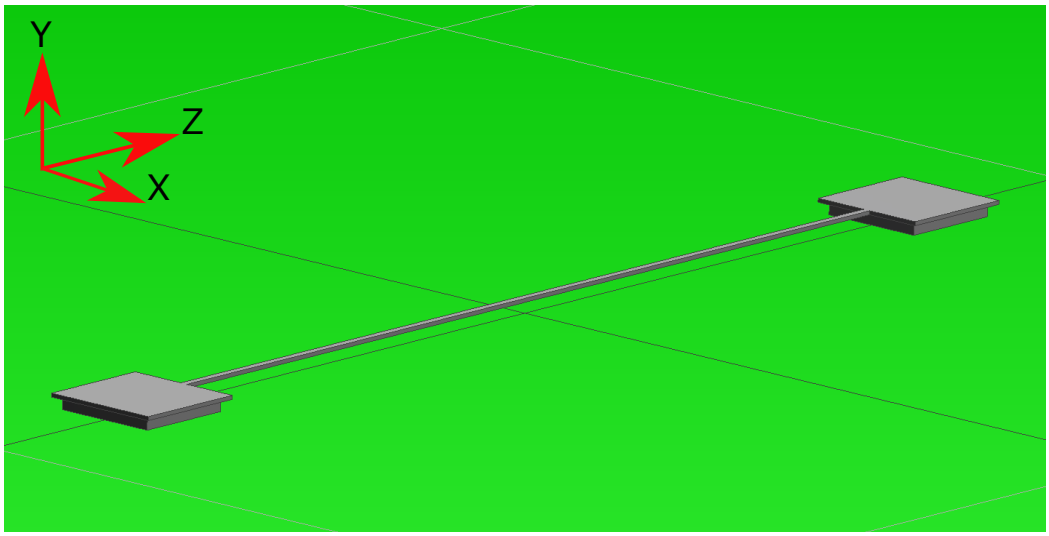

Figure 2.1: A scale drawing of a 300 µm resonator supported between two electrical contact pads, here Z is defined to reflect the orientation of z in the theoretical discussion.

The beam's motion can be decomposed into two types of deformation: a displacement in the x or y direction (this coordinate system is shown in fig. 2.1). We consider this deformation to be a function of z and disregard (for the moment) the direction that the beam is deformed in, thereby assuming the beam to have equal x and y dimensions. The beam undergoes deformation $u(z)$ in response to a force F which induces strain, leading to a stress in the beam opposing the strain relating to Young's modulus E using bulk elastic theory.

Assuming that the force F is time dependent, the resulting vibrations can be described by the Euler-Bernoulli equation:

$$\rho A \frac{\delta^2 u(z)}{\delta t^2} + \frac{\delta^2}{\delta z^2}[EI_y \frac{\delta^2 u(z)}{\delta z^2}] = F(z,t) \tag{2.1}$$

Where ρ is the mass density of the beam, A is the cross-sectional area, and E is

Young's modulus. The term I_y is the beam-dependent geometry modulus, which describes the deformation in the x direction. This accounts for the earlier assumption that the beam has equal geometry in x and y. For a rectangular beam (as is the case with our resonator) this takes the form of:

$$I_y^{Rectangle} = \frac{wh^3}{12} \tag{2.2}$$

Where w is the beam width, and h the beam height.

This would describe the movement of a rectangular beam under no external forces other than $F(z,t)$; however our resonator is under constant tension T whilst at rest. During motion, the beam will generate additional tension by being stretched by the displacement $u(z)$. As a result the tension term must be calculated by integrating the local strain over length dl over the beam length. T is then modified to become the average stress over the beam:

$$T = \frac{EA}{2L}\int_0^L u'(z)^2 dz \tag{2.3}$$

Equation (2.1) is modified to include the tension term:

$$\rho A\frac{\delta^2 u(z)}{\delta t^2} - T\frac{\delta^2}{\delta z^2}[u(z)] + \frac{\delta^2}{\delta z^2}[EI_y\frac{\delta^2 u(z)}{\delta z^2}] = F(z,t) \tag{2.4}$$

We can now introduce some boundary conditions. Given that we are modelling a doubly clamped beam, we can impose that the deformation at each end is 0. We can also infer that each end of the beam is not in motion such that:

$$u(0) = u(L) = u'(0) = u'(L) = 0 \tag{2.5}$$

Using these conditions we can now start to compute the flexular eigenmodes of the resonator. We will make the following assumptions to characterise the eigenmodes for the most simple case:

1. As above, the beam is doubly clamped and of uniform composition.
2. There are no external forces on the beam.
3. The deformations are harmonic and time dependent.

From assumption 2, we assert:

$$F(z,t) = T = 0 \tag{2.6}$$

and from assumption 3,

$$u(z,t) = u(z)e^{-i\omega t} \tag{2.7}$$

Thus separating the time dependence into an exponent. Under these conditions, eq. (2.4) becomes

$$\rho A \frac{\delta^2}{\delta t^2}[u(z)e^{-i\omega t}] + EI_y e^{-i\omega t}\frac{\delta^4 u(z)}{\delta z^4} = 0 \tag{2.8}$$

which reduces to the time independent form:

$$\rho A\omega^2 u(z) = EI_y \frac{\delta^4 u(z)}{\delta z^4} \tag{2.9}$$

Using the ansatz

$$u(z) = u_0 e^{\kappa z} \tag{2.10}$$

We can show that for the constant κ

$$\kappa^4 = \frac{\rho A \omega^2}{E I_y} \tag{2.11}$$

Let

$$\beta = \Big(\frac{\rho A \omega^2}{E I_y}\Big)^{\frac{1}{4}} \tag{2.12}$$

Such that there are now solutions for

$$\kappa = \quad \pm\beta, \quad \pm i\beta \tag{2.13}$$

which can be calculated using the previously stated boundary conditions, and an ansatz:

$$u(z) = \alpha_n \chi_n(z) = \alpha_n \Big\{ a_n[\sin(\beta_n z) - \sinh(\beta_n z)] - [\cos(\beta_n z) - \cosh(\beta_n z)] \Big\} \tag{2.14}$$

Applying our first boundary condition, $\chi_n(0) = \chi_n(L) = 0$:

$$a_n = \frac{\cos(\beta_n L) - \cosh(\beta_n L)}{\sin(\beta_n L) - \sinh(\beta_n L)} \tag{2.15}$$

and then our second condition, $\chi_n'(0) = \chi_n'(L) = 0$;

$$\frac{2\beta_n(\cos(\beta_n L)\cosh(\beta_n L)-1)}{\sinh(\beta_n L)-\sin(\beta_n L)}=0 \tag{2.16}$$

Which has real solutions

$$\beta_0 = 0 \quad ; \quad \cos(\beta_n L)\cosh(\beta_n L) = 1 \tag{2.17}$$

and results in the condition

$$\beta_n = \frac{C_n}{L} \tag{2.18}$$

This can be solved numerically, as has been done in '*Physics of Nanoelectronics*' (page 207) [56] and tabulated in table 2.1:

n	1	2	3	4	5
C_n	4.73004	7.8532	10.9956	14.1372	17.2788
a_n	0.982502	1.000078	0.999966	1.000001	$a_n \approx 1$ for $n > 4$

Table 2.1: Numerically solved constraints for an un-tensioned doubly clamped beam.

Using these values and the length of the beam it is possible to calculate the eigenfrequencies of the modes by rearranging eq. (2.12):

$$\omega_n = \sqrt{\frac{EI_y}{\rho A}}\frac{c_n^2}{L^2} \tag{2.19}$$

When it is considered that the beam is rectangular, this becomes

$$\omega_n = \sqrt{\frac{E}{\rho A}\frac{wh^3}{12}}\frac{c_n^2}{L^2} \tag{2.20}$$

So we see that the frequency of a mode has an approximately inverse squared relationship with length.

The functions χ_n form an orthogonal basis for describing the mode shapes. They are normalised such that:

$$\frac{1}{L}\int_0^L \chi_n(z)\chi_m(z)dz = \delta_{n,m} \tag{2.21}$$

meaning that any deformation $u(z)$ can be described by a combination of $\chi_n(z)$.

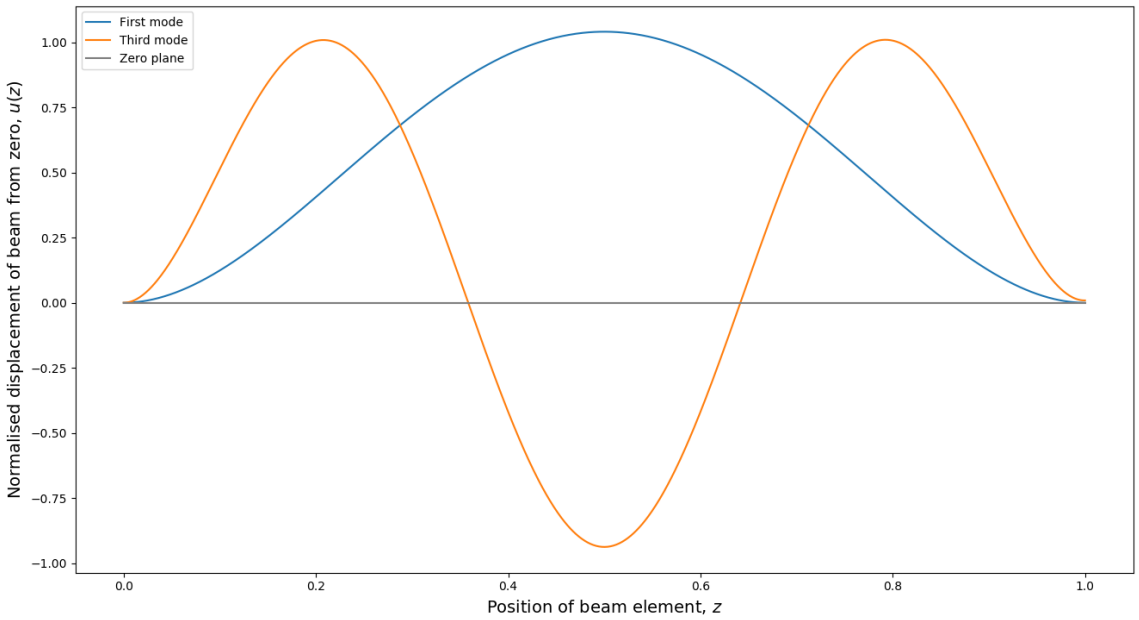

Figure 2.2: Approximate mode shapes calculated using eq. (2.14) and table 2.1 for a doubly clamped beam.

As the resonators discussed in this thesis are doubly clamped beams, it is useful to investigate the mode shape for a beam with rectangular cross-section. Figure 2.2 shows the fundamental and third mode for a doubly clamped beam. The second mode is ignored here because the transduction method we use excludes even-numbered modes from detection. The voltage developed by motion of the resonator is dependent on the net flux lines 'cut' by the beam - for even numbered modes the counter-

directional antinodes develop the same but opposite signed voltage and thus net zero voltage is developed across the beam.

2.1.2 Tension in the Beam

The previous derivation dealt with the case where there is no tension in the beam. If we include tension, and assume that external forces are still zero, then eq. (2.4) becomes

$$\rho A \frac{\delta^2}{\delta t^2}[u(z,t)] - T\frac{\delta^2}{\delta z^2}[u(z,t)] + EI_y \frac{\delta^4 u(z,t)}{\delta z^4} = 0 \tag{2.22}$$

And we must use the ansatz

$$u(z,t) = u_0 e^{\kappa z} e^{i\omega t} \tag{2.23}$$

which results in the modified eq. (2.9):

$$EI_y\kappa^4 - \rho A\omega^2 - T\kappa^2 = 0 \tag{2.24}$$

with imaginary solutions:

$$\kappa = \pm i\sqrt{\sqrt{\xi^2 + \lambda\omega^2} - \xi} = \pm i\eta \tag{2.25}$$

and real solutions:

$$\kappa = \pm\sqrt{\sqrt{\xi^2 + \lambda\omega^2} + \xi} = \pm\beta \tag{2.26}$$

Where

$$\xi = \frac{T}{2EI_y} \quad , \quad \lambda = \frac{\rho A}{EI_y} \tag{2.27}$$

The eigensolutions will be superpositions of $e^{\kappa_n z}$ satisfying the boundary conditions $\chi_n(0) = \chi'(0) = 0$ and $\chi_n(L) = \chi'_n(L) = 0$. The ansatz

$$u(z) = \alpha_n \chi_n(z) = \alpha_n \Big\{ a_n [\sin(\eta_n z) - \frac{\eta_n}{\beta_n} \sinh(\beta_n z)] + \cos(\eta_n z) - \cosh(\beta_n z) \Big\} \quad (2.28)$$

becomes

$$\cos(\eta_n L)\cosh(\beta_n L) - 1 = \frac{\xi}{\sqrt{\lambda}\omega_n} \sin(\eta_n L)\sinh(\beta_n L) \quad (2.29)$$

when the boundary conditions are applied, which has to be solved numerically. However, in the high tension limit

$$\xi \gg \sqrt{\lambda}\omega_n \quad (2.30)$$

the left hand side dominates and the condition becomes

$$\sin(\eta_n L) = 0 \quad (2.31)$$

Using

$$\eta_n \approx \omega_n \sqrt{\frac{A\rho}{T}} \quad (2.32)$$

gives the typical eigenfrequencies of a wave equation:

$$\omega_n \approx \sqrt{\frac{T}{\rho A}} \frac{n\pi}{L} \quad (2.33)$$

which shows us that the eigenfrequencies scale quadratically with tension, as expected for a string. Using typical stress values from Defoort *et al.* [19] we can calculate a frequency of 24 MHz for a 300 µm beam, a factor of 40 away from observed frequencies. However this calculation does not account for metal layers atop the resonator.

2.2 The Driven Resonator

In this project, the initial objective was to measure the thermal noise power in the resonator. To understand what to expect from a resonator driven by thermal energy, we first investigate the response of the NEMS to a generic drive.

Assuming that the driving force takes the form of

$$F(z,t) = F(z)e^{-i\omega_d t} \tag{2.34}$$

where ω_d is the driving frequency. From stationary at $t = 0$, we would expect the deformations to then be of the form

$$u(z,t) = u(z)e^{-i\omega_d t} \tag{2.35}$$

Which can be spectrally decomposed into $u(z) = \sum_n \alpha_n \chi_n(z)$ and inserted into the Euler-Bernoulli equation ignoring induced tension (eq. (2.1))

$$\sum_n \alpha_n(-\omega_d^2 + \omega_n^2)\chi_n(z) = \frac{1}{m}F(z) \tag{2.36}$$

where $m = \rho AL$, the mass of the resonator. Using the orthonormality condition

$$\alpha_m(-\omega_d^2 + \omega_m^2) = \frac{1}{mL}\int \chi_m(z)F(z)dz \tag{2.37}$$

we can see that the resonator follows the form of a harmonic oscillator, with α_m as an amplitude.

To find expressions for the Q and the frequency dependence, we will concentrate on a single mode with eigenfrequency close to ω_d for strong coupling. We will also include dissipation by considering $\omega_m \to \omega_m - i\gamma_m$ in the case $\gamma \ll \omega_m$.

$$\alpha_m(-\omega_d^2 - 2i\omega_m\gamma_m + \omega_m^2) = \frac{1}{mL}\int \chi_m(z)F(z)dz = \frac{F_0\eta_m}{m} \tag{2.38}$$

where F_0 is the force amplitude and η_m is the projection of the force onto the mode with eigenfunction $\chi_n(z)$

$$\eta_m = \frac{1}{L}\int_0^L \chi_n(z)\frac{F(z)}{F_0}dz \tag{2.39}$$

Considering that the Q-factor can be defined as

$$Q_m^{-1} = \frac{\mathrm{Im}(\omega_m)}{|\omega_m|} = \frac{\gamma^2}{\sqrt{\omega_m^2 + \gamma_m^2}} \overset{\gamma \ll \omega_m}{\approx} \frac{\gamma}{\omega_m} \tag{2.40}$$

Then we can express the imaginary component of the mode amplitude as a Lorentzian form as long as $\omega_d \approx \omega_m$

$$\mathrm{Im}(\alpha_m) \approx \frac{\eta_m F}{m}\frac{Q_m\omega_m^2}{\omega_m^4 + Q_m^2(\omega_d - \omega_m)^2} \overset{\omega_d \approx \omega_m}{\approx} \frac{\eta_m F}{m}\frac{Q_m}{\omega_m^2 + 4Q_m^2(\omega_d - \omega_m)^2} \tag{2.41}$$

So we can expect to see a Lorentzian response from the resonator to a drive frequency close to the resonant frequency. When the resonator is driven with thermal motion (or any power below a critical level, above which the resonator becomes non-linear), we see a Lorentzian signal from the NEMS as demonstrated in fig. 2.3.

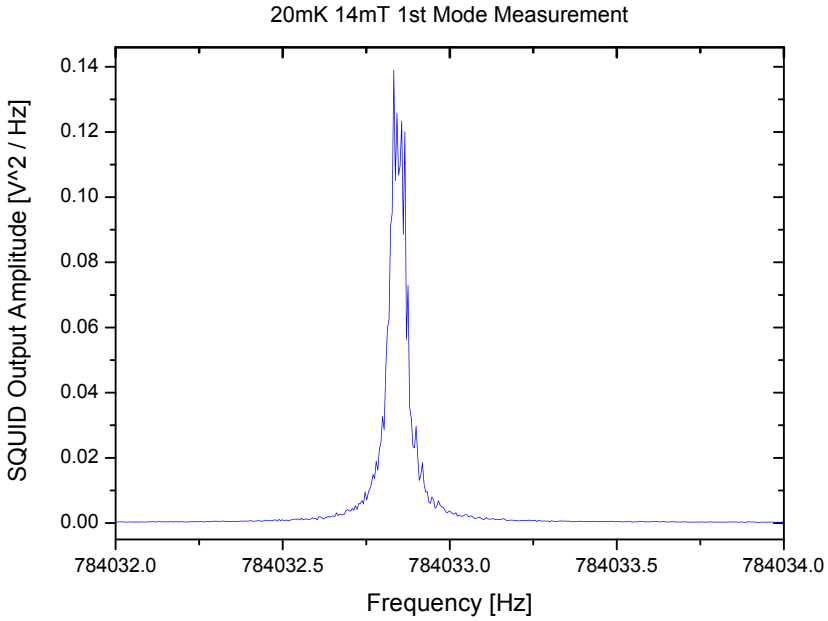

Figure 2.3: An example of the typical Lorentzian noise peak we see from the resonator. The resonator is driven by thermal noise at 20 mK, and we expect this to generate a Lorentzian.

Non-linearity in Beams Non-linear effects are seen in doubly clamped resonators when the beam reaches high displacement amplitudes, at which point the previous model starts to break down. The large amplitudes stretch the beam, adding length and increasing internal tension, which changes the overall elastic response of the beam - we can therefore no longer use the Euler-Bernoulli equation to describe the frequency response.

This non-linearity is characteristic of a Duffing Oscillator, and can be described by the driven Duffing equation:

$$x'' + \delta x' + (\beta x^3 \pm \omega_0^2 x) = \gamma \cos(\omega t + \phi) \tag{2.42}$$

where δ is the damping term, γ is the driving amplitude, ω_0 is the resonant frequency and ω is the drive frequency. The β term is the non-linearity condition which, if set to zero, reduces the Duffing oscillator to a simple damped driven harmonic oscillator as described previously.

In Cleland's '*Foundations of Nanomechanics*' [57] there is a NEMS-specific derivation using Lagrangian equations of motion, which results in a similar equation:

$$x'' + \delta x' + \omega_0^2(x + Kx^3) = \eta f(t) \tag{2.43}$$

where K is a constant specific to beam geometry and $f(t)$ is the driving force. We can see from this equation that the resonant frequency term now includes a non-linearity term, and that as the amplitude of the mode increases, the effective spring constant increases. This results in a 'stiffening' of the beam, so the resonant frequency increases as the amplitude increases. This then produces a hysteresis when sweeping the driving frequency, creating a bifurcation region where the resonator could either be at high or low amplitude depending on whether the drive frequency is being swept up or down. Duffing effects are not seen in the work presented here, and so it will not be discussed in further detail.

2.2.1 Thermal Noise Power

To investigate the response to thermal noise power of a resonator, it is helpful to first find the Langevin equation using statistical mechanics methodology. The approach used here is a mixture of the approaches used by Cleland [57] and Cowan [58].

We model the beam as a frictionless particle trapped in a local minimum of a potential, $U(x)$, which we assume is well-behaved and symmetric locally. Due to the constraint of a local minimum we can assert that:

$$U'(x) = 0, \tag{2.44a}$$

$$U''(x) = +\text{ve} \tag{2.44b}$$

Using a Taylor expansion, we can find a leading order expression for $U(x)$ about 0.

$$U(x) = U(0) + \frac{U'(0)}{1!}(x-0) + \frac{U''(0)}{2!}(x-0)^2 + ... \tag{2.45}$$

$$= U(0) + \frac{U''(0)x^2}{2} + ... \tag{2.46}$$

Where the 1st order term disappears because of eq. (2.44a). Using the standard relation for an undamped harmonic oscillator:

$$\omega = \sqrt{\frac{k}{m}} \tag{2.47}$$

where $k = U''(0)$ is the effective spring constant and m the effective mass. We can describe the motion of the beam as:

$$m\frac{d^2x}{dt^2} + m\omega_0^2 x = 0 \tag{2.48}$$

for small displacements. This has a solution of the form:

$$x(t) = x_0 \exp(-i\omega_0 t + i\phi) \tag{2.49}$$

We now define the driving force F_Σ, as a random drive with many degrees of freedom such that we cannot specify the direction of the force in any given period.

$$m\frac{d^2x}{dt^2} + m\omega_0^2 x = F_\Sigma \tag{2.50}$$

Without knowledge of the direction of the driving force, we must treat it as having two components: a driving component and a damping component. These are compatible with the expectation that the drive is in the same direction of the beam's motion and the damping against the beam's motion.

$$F_\Sigma = F_{\text{Drive}} + F_{\text{Damp}} \tag{2.51}$$

Because we define the force opposing the beam's motion to be damping, we describe it as appropriate for a damped oscillator, and describe the driving force as noise which averages to zero:

$$F_{\text{Damp}} = -m\gamma\frac{dx}{dt}, \tag{2.52}$$

$$F_{\text{Drive}} = F_N(t), \tag{2.53}$$

$$F_\Sigma = F_N(t) - m\gamma\frac{dx}{dt} \tag{2.54}$$

Thus we arrive at the Langevin equation for our system.

$$m\frac{d^2x}{dt^2} + m\omega_0^2 x + m\gamma\frac{dx}{dt} = F_N(t) \tag{2.55}$$

The driving force up until this point has been treated as a function that averages

to zero, but that is not the full picture. Thermally driven noise power, although uncorrelated, averages to the thermal energy of the resonator at long enough time scales. Thus we evaluate the integral of the ensemble average of the noise power as defined by Langevin equations to be the average thermal energy of the resonator for a short time t'. This is expressed here as the integral of the Gaussian:

$$\int_{-\infty}^{\infty} \langle F_N(t_0) F_N(t_0 + t') \rangle dt' = 2mk_{\mathrm{B}}T\gamma \tag{2.56}$$

If we further assume that the correlation time of the noise is much less than the time over which the resonator will respond to it (which is inversely proportional to the damping γ), we can further simplify the expression:

$$\langle F_N(t_0) F_N(t_0 + t') \rangle = 2mk_{\mathrm{B}}T\gamma\delta(t_0 - t') \tag{2.57}$$

The left hand side of eq. (2.57) can be described as the t_0 independent correlation function $G(t')$

$$G(t') = 2mk_{\mathrm{B}}T\gamma\delta(t') \tag{2.58}$$

for which the spectral density can be expressed as

$$S(\omega) = \frac{1}{2\pi} \int_{-\infty}^{\infty} G(t') e^{i\omega t'} dt' \tag{2.59}$$

$$= \frac{1}{2\pi} \int_{-\infty}^{\infty} 2mk_{\mathrm{B}}T\gamma\delta(t') e^{i\omega t'} dt' \tag{2.60}$$

which produces, for time $t_0 > 0$, a frequency independent spectrum:

$$S(\omega) = \frac{mk_{\mathrm{B}}T\gamma}{\pi} \tag{2.61}$$

This spectrum describes white noise, and indicates that the thermal noise power available to the resonator is equal at all frequencies.

2.2.2 Thermal Energy of a Harmonic Oscillator

The final conclusion to draw from the mechanical theory is the energy within a resonator driven by thermal power. The following derivation is described more thoroughly by Reif, Cleland and Cowan [57, 58, 59].

The energy in a one-dimensional simple harmonic oscillator is defined as the sum of its kinetic and potential energies,

$$E = \frac{1}{2}mv^2 + \frac{1}{2}kx^2 \tag{2.62}$$

where k is the spring constant and x is the oscillator's position. The theorem of equipartition, (proved on pp.248-249 [59]) states that the mean of each independent quadratic term in the expression for energy is $\frac{1}{2}k_{\mathrm{B}}T$. This then constrains the values of each of the terms in eq. (2.62):

$$\left\langle \frac{1}{2}mv^2 \right\rangle = \frac{1}{2}k_{\mathrm{B}}T, \quad \left\langle \frac{1}{2}kx^2 \right\rangle = \frac{1}{2}k_{\mathrm{B}}T \tag{2.63}$$

$$\langle E \rangle = \frac{1}{2}k_{\mathrm{B}}T + \frac{1}{2}k_{\mathrm{B}}T \tag{2.64}$$

and thus we arrive at the total thermal energy within an oscillator:

$$\langle E \rangle = k_{\mathrm{B}} T \tag{2.65}$$

As stated at the start of this section, one of the goals in this project is to cool a resonator in vacuum to its quantum ground state. To investigate the energy contained in the resonator at that point, we should use the expression for quantised energy levels in a harmonic oscillator:

$$E_n = \hbar\omega \left(n + \frac{1}{2} \right) \tag{2.66}$$

where n indicates the energy level of integer value, and ω the angular frequency is defined as before in eq. (2.47). Defining the partition function:

$$Z(N, V, T) = \sum_i e^{-E_i(N,V)/k_{\mathrm{B}}T} \tag{2.67}$$

$$Z = \sum_{n=0}^{\infty} e^{-(n+\frac{1}{2})\hbar\omega/k_{\mathrm{B}}T} \tag{2.68}$$

$$Z = \sum_{n=0}^{\infty} e^{-E_n\beta} \tag{2.69}$$

where $\beta = 1/k_{\mathrm{B}}T$, we take the mean energy of the oscillator:

$$\bar{E} = \frac{\sum_{n=0}^{\infty} E_n e^{-E_n\beta}}{\sum_{n=0}^{\infty} e^{-E_n\beta}} = -\frac{1}{Z}\frac{\delta Z}{\delta \beta} \tag{2.70}$$

So the mean energy of a quantised resonator can be expressed as:

$$\bar{E} = -\frac{\delta}{\delta\beta} \ln Z = \hbar \left(\frac{1}{2} + \frac{1}{e^{\beta\hbar\omega} - 1} \right) \tag{2.71}$$

As we are considering a quantised resonator for the purposes of low temperature experiments, it makes sense to make the assumption

$$\beta = \frac{1}{k_{\mathrm{B}} T} >> 1 \tag{2.72}$$

such that eq. (2.71) becomes our expression for the energy in the resonator at the lowest temperatures:

$$\bar{E} = \hbar\omega \left(\frac{1}{2} + e^{-\beta\hbar\omega} \right) \tag{2.73}$$

This result indicates that in order to reach the quantum ground state of the resonator, we obtain an expression for the temperature needed for a resonator of angular frequency ω.

$$k_{\mathrm{B}} T \approx \frac{1}{2} \hbar\omega \tag{2.74}$$

This expression is evidently useful, and informs us that in the best case scenario of achieving 150 µK, the resonator would have to have a resonant frequency above $\approx 6.25 \times 10^6$ Hz.

2.3 Electrical Modelling

We now take a different approach to describing the motion of the resonator, such that we use a well understood and widely used electrical analogue. We model the motion of the resonator as a driven damped harmonic oscillator, which we saw was a valid approximation in section 2.2. Given that the magnetomotive transduction method can only transduce one plane of motion of the resonator in our experiment, we treat the resonator as one-dimensional for simplicity. The equation of motion for the resonator is then:

$$\frac{d^2x}{dt^2} + \gamma\frac{dx}{dt} + \omega_0^2 x = \frac{F_0}{m}\cos(\omega t) \tag{2.75}$$

Where x is the displacement, γ is the damping factor, ω_0 is the natural frequency, F_0 is a unique damping factor, ω is the driving frequency and m is the mass of the resonator. This approximation has the ansatz:

$$x = A\cos(\omega t - \phi) \tag{2.76}$$

An important property measured in the experiment is the quality or 'Q' factor, which is given by $Q = \omega_0/\gamma$. We rewrite eq. (2.75):

$$\frac{d^2x}{dt^2} + \frac{\omega_0}{Q}\frac{dx}{dt} + \omega_0^2 x = \frac{F_0}{m}\cos(\omega t) \tag{2.77}$$

It can be shown that eq. (2.76) is a solution to eq. (2.77), and by substituting t for

values of $n\pi/\omega$ (where n is an integer) to find:

$$A = \frac{F_0/m}{\sqrt{(\omega_0^2 - \omega^2)^2 + \omega^2\omega_0^2/Q^2}} \tag{2.78a}$$

$$\phi = \tan^{-1}\left(\frac{\omega_0\omega/Q}{\omega_0^2 - \omega^2}\right) \tag{2.78b}$$

We now include the effect of a magnetic field applied perpendicular to the plane of motion such that an alternating current $I_0\cos(\omega t)$ will produce an oscillatory force on the resonator. The force is given by:

$$F = BlI_0\cos(\omega t) \tag{2.79}$$

Where B is the applied magnetic field and l is the length of the resonator. This must be modified to account for the shape of the resonator which is achieved by including a term m_{eff} (the effective mass, which will be discussed further in section 3.6) before introducing it to eq. (2.77):

$$\frac{d^2x}{dt^2} + \frac{\omega_0}{Q}\frac{dx}{dt} + \omega_0^2 x = \frac{BlI_0}{m_{\text{eff}}}\cos(\omega t) \tag{2.80}$$

This driving force will result in the resonator's displacement in the x direction, which indicates a change in flux along the resonator length. This induces a voltage across the resonator, given by:

$$v = \frac{d\phi}{dt} = Bl\frac{dx}{dt} \tag{2.81}$$

Where l here is an effective length of the resonator calculated from integrating the

deformation over the beam length:

$$l = \int_0^L \frac{du(z,t)}{dt} dz \tag{2.82}$$

Equation (2.81) can be rearranged to substitute into eq. (2.80)

$$\frac{dx}{dt} = \frac{v}{Bl} \tag{2.83a}$$

$$\frac{d^2x}{dt^2} = \frac{1}{Bl}\frac{dv}{dt} \tag{2.83b}$$

to describe eq. (2.77) in terms of voltage and current:

$$\frac{1}{Bl}\frac{dv}{dt} + \frac{v}{Bl}\frac{\omega_0}{Q} + \omega_0^2 x = \frac{BlI_0}{m_{\text{eff}}}\cos(\omega t) \tag{2.84}$$

Which, differentiating and collecting like terms provides an expression for the voltage induced across the resonator as a function of time:

$$\frac{d^2v}{dt^2} + \frac{\omega_0}{Q}\frac{dv}{dt} + \omega_0^2 v = -\omega\frac{B^2l^2I_0}{m_{\text{eff}}}\sin(\omega t) \tag{2.85}$$

From inspection of eq. (2.85) it is evident that the resonator behaves as a resonant circuit, and so we now compare its behaviour to that of a parallel resonant circuit, comprising a capacitor C, an inductor L, and a resistor R. The sum of all currents I_Σ in such a circuit is given by:

$$I_\Sigma = \frac{v}{R} + C\frac{dv}{dt} + \frac{1}{L}\int v dt = I_0\cos(\omega t) \tag{2.86}$$

Which differentiated with respect to time becomes:

$$\frac{d^2v}{dt^2} + \frac{1}{RC}\frac{dv}{dt} + \frac{v}{LC} = -\frac{\omega}{C} I_0 \sin(\omega t) \tag{2.87}$$

Now comparing the terms of eq. (2.87) with eq. (2.85), we find:

$$\frac{\omega_0}{Q} = \frac{1}{RC} \tag{2.88a}$$

$$\omega_0^2 = \frac{1}{LC} \tag{2.88b}$$

$$\frac{B^2l^2}{m_{\text{eff}}} = \frac{1}{C} \tag{2.88c}$$

Which is rearranged to find the model circuit parameters for a NEMS device in a magnetic field; model inductance L_{m}, model capacitance C_{m}, and model resistance R_{m}.

$$C_{\text{m}} = \frac{m_{\text{eff}}}{B^2l^2}; \quad L_{\text{m}} = \frac{B^2l^2}{m_{\text{eff}}\omega_0^2}; \quad R_{\text{m}} = \frac{QB^2l^2}{m_{\text{eff}}\omega_0^2} \tag{2.89}$$

The model circuit shown in fig. 2.4 is used throughout this thesis to represent the

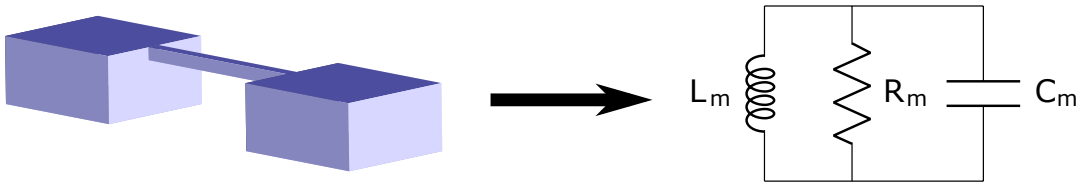

Figure 2.4: The model circuit described, showing the NEMS device as an LCR resonant circuit.

electrical behaviour of resonators in magnetic fields. This approach is widely used to model vibrating wires [60].

Chapter 3

Experimental Techniques

In this chapter the methods used to perform the experiments detailed in this thesis are described. It begins with a description of the fabrication of the NEMS samples, and moves onto the sensing technology, the most unique component of the measurement setup. The signal analysis protocols are then discussed before the thermometry methods, which will use the cumulative information from the rest of the chapter.

3.1 NEMS Fabrication

Aluminium coated - NEEL Institut

The resonators studied in this thesis in initial experiments were fabricated at the NEEL Insitut at CNRS Grenoble, by Dr. Kunal Lulla. They were fabricated using a top-down method, starting with silicon chips that were purchased from a manufacturer and culminating in suspended silicon nitride beams with a top layer of aluminium.

The stoichiometric layer of silicon nitride (Si_3N_4) was grown either by a manufacturer

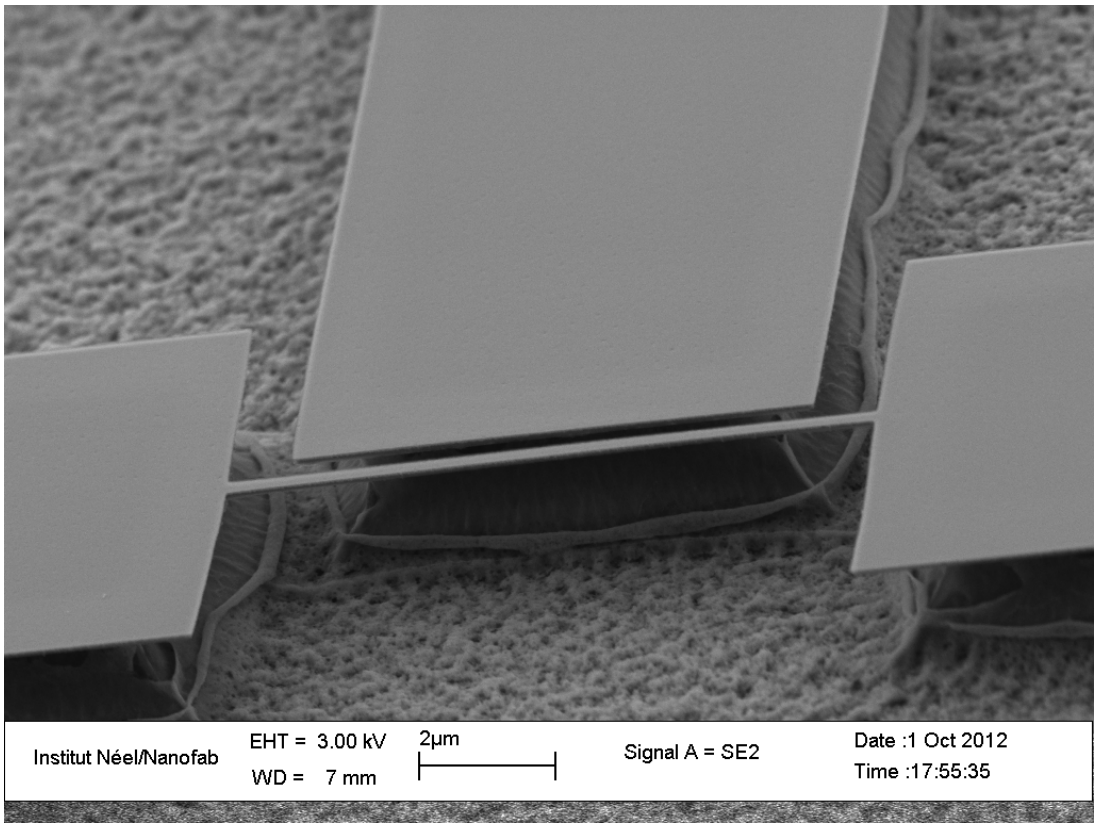

Figure 3.1: A Si_3N_4 resonator fabricated at the NEEL Institut, shown here including a gate electrode.

or by collaborators through the use of Low Pressure Chemical Vapour Deposition (LPCVD). The Si-N bonds are 'stretched' by the stoichiometry, resulting in an average internal stress of around 1.2 GPa [61], creating a desirably taut beam with a higher frequency and higher Q-factor.

The resist was a 100 nm thick layer of polymethyl methacrylate (PMMA), spun and then heated on a hot plate for 5 minutes at 180 °C to remove the residual solvent. A positive resist is used, meaning that Electron Beam Lithography (EBL) is used to project the negative image of the structures onto the resist. Following EBL the

sample was developed in an isopropanol / methyl isobutyl ketone (MIBK) mixture of ratio 3:1 respectively [19].

A thin aluminium layer is then evaporated onto the surface of the Si_3N_4, such that the resonator can be actuated and transduced electronically. The choice of metal used for this layer is limited by the properties desired; in this case aluminium is used because it is a superconductor below 1 K.

The lift-off typically takes two days; the sample is left in the solution for this period to ensure all the PMMA is removed and the aluminium not desired is removed. This 'lifted' PMMA and aluminium is then removed using an ultrasonic bath for a few seconds and then dried using compressed air.

The sample is put through two etching processes. The first uses SF_6 in Reactive Ion Etching (RIE) to anisotropically remove the Si_3N_4. This process must be carefully timed because SF_6 etches both Si_3N_4 and Si, so there is a danger of eroding the chip unintentionally.

The second etching process uses XeF_2, which etches silicon isotropically. The chip is intentionally etched until the beam is released and is free-standing. The structures are then preliminarily inspected under an optical microscope to see if the pads or gate (if present) are deformed.

Of these beams, some are normally fabricated with gate electrodes to allow capacitive actuation, transduction, and parametric pumping [62]. However, the gate can often

make the fabrication process less reliable and can result in a useless resonator.

The sample used for the milliKelvin vacuum experiments was 300 µm in length. Such a length was chosen because it is the longest that the beams can be reliably fabricated. At this length, the signal amplitude from thermodynamic vibrations is high due to the cross-sectional area of the beam cutting the magnetic flux during inductive transduction.

Niobium coated - Cornell

These resonators are very similar in construction to the resonators from NEEL, given that the substrate for both is manufactured at Cornell. In these resonators, however, two beams are fabricated on each pair of electrical contacts but at different lengths. It is then not possible to transduce either in isolation but their fundamental frequencies differ by some 1.5 MHz such that it does not pose a logistical issue.

This leads on to the significant differences in geometry of the chip compared to that of the Al resonators. There are six pairs of contacts, each with two resonators between them. In addition, the chip features a capacitive drive gate. By applying a drive to the gate one applies a drive to all of the resonators, providing an additional option for driving the resonators.

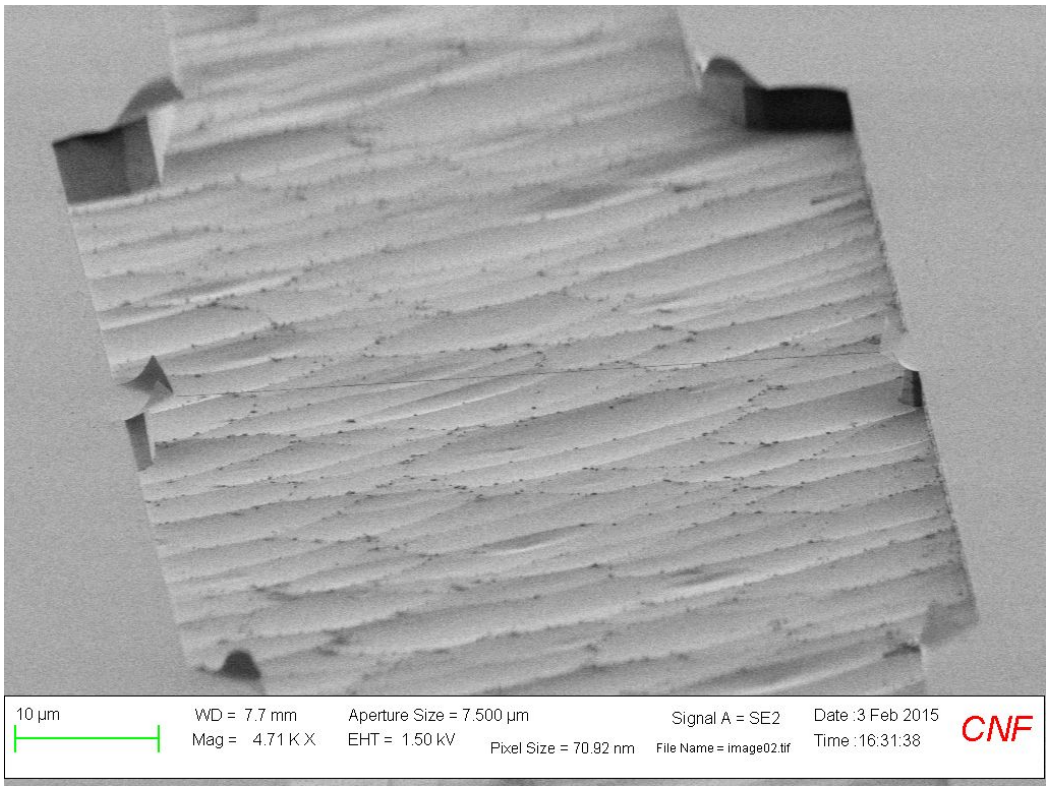

Figure 3.2: One of the 50 nm wide resonators from Cornell, the niobium and Si_3N_4 film can be seen to flex upwards at the clamped end of the beam, indicating additional stress.

One of the most immediate opportunities with these resonators will be to use them in liquid helium: the ability to explore the frequency range with one device is attractive, and the cross-section of the beams are of the order of the coherence length in superfluid ^{3}He (65 nm [7, 39]).

3.2 Superconducting Quantum Interference Devices (SQUIDs)

Superconducting Quantum Interference Devices (SQUIDs) are extremely sensitive magnetometers. In the London Low Temprature Laboratory we use two-stage SQUIDs fabricated at Physikalisch-Technische Bundesanstalt (PTB) with unprecedented sensitivity (coupled energy resolution of 8 h at 300 mK [8]) and versatility, allowing us to employ a 'plug and play' strategy.

3.2.1 SQUID Basics

A SQUID consists of a superconducting loop interrupted by two parallel Josephson junctions. In the superconducting state screening currents cause the material to expel magnetic flux, and limit the flux threading the loop to quantised values. The electrons inside the superconductor form a macroscopic wavefunction within the ring;

$$\Psi_{(\vec{r},t)} = |\Psi_{(\vec{r},t)}|e^{i\phi(\vec{r},t)} \tag{3.1}$$

with a single-valued $\phi(\vec{r},t)$ at all points. A phase discontinuity within the loop would reduce the supercurrent across a junction to zero, effectively causing the superconductor to behave resistively and develop a voltage across the superconducting ring. The current in a Josephson junction is described by:

$$I_s = I_c \sin(\delta) \tag{3.2}$$

where I_c is the critical current of the superconductor, and δ is the phase difference

across the junction [63]. When the external flux density changes around the ring, a screening current will develop as per the Meissner effect preventing any flux entering the ring. As the supercurrent increases the phase difference across the junction will increase as indicated by eq. (3.2), developing a voltage U until the phase becomes large enough to drive the junction normal:

$$\frac{d\delta}{dt} = \frac{2e}{\hbar}U = \frac{2\pi}{\Phi_0}U \tag{3.3}$$

where $\Phi_0 = h/2e \approx 2.07 \times 10^{-15}$ Wb is the flux quantum [63]. When the phase difference δ is large enough to cause the junction to become completely normal this section of the ring will no longer be generating screening currents and thus one Φ_0 can penetrate the conductor and enter the ring. The flux density at the edge of the ring then drops, and the screening current reverses direction now working against expelling the trapped flux. As the flux continues to increase the trapped flux will move to the centre of the ring and no longer generate screening currents, causing the phase difference across the junction to return to its minimum value, allowing the ring to become fully superconducting once more and U to drop to zero. This becomes a periodic effect with linearly increasing flux bias, which can be seen in fig. 3.3. This effect is known as flux quantisation, and the high sensitivity level of the SQUID to changes in magnetic flux is what makes it such a versatile measurement tool.

In normal operation the SQUID is placed in a magnetically shielded environment some distance away from the experiment. The experiment signal is coupled to the SQUID through an on-chip input inductor wound near to the SQUID. The input inductor

is superconducting to reduce losses and Johnson noise, and (for example) could be connected to a superconducting sensing coil which would then be a flux transformer arrangement. In the experiments described here we seek to measure current from the NEMS device through resistive bond wires. This allows us to use the SQUID to measure both the motion of the resonator, and (in B = 0 applied field) the temperature of the bond wires via current-sensing noise thermometry (CSNT).

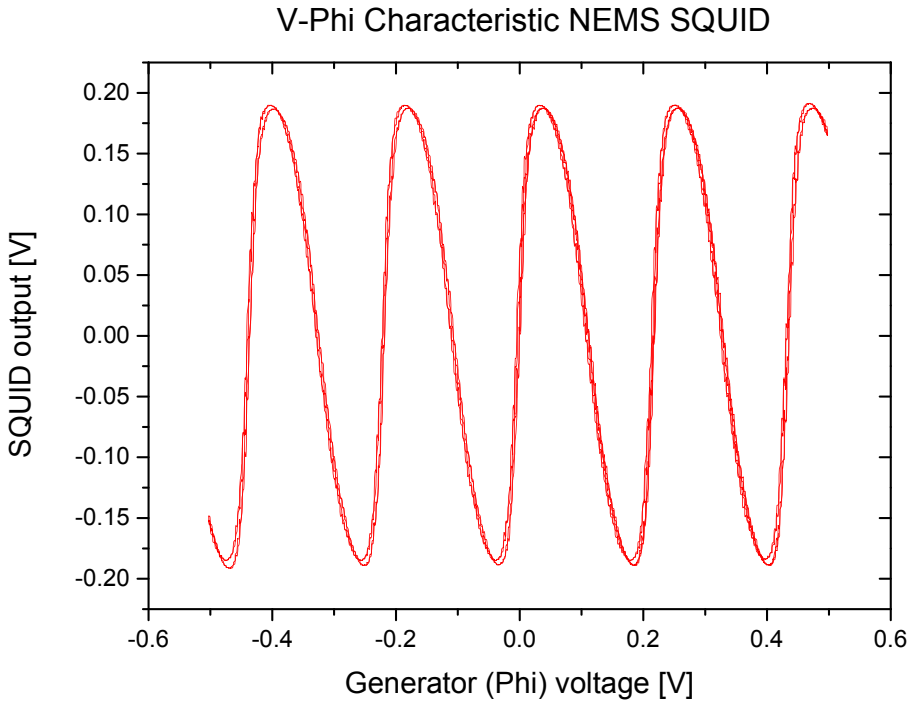

Figure 3.3: The V-Φ characteristic of the NEMS SQUID, showing the periodicity of the voltage across the device with applied flux, here represented by the voltage applied to the flux bias coil. The characteristic for our SQUID is asymmetric because of the additional positive feedback electronics.

3.3 Two-Stage SQUIDs

The SQUIDs used for the experiments described in this thesis (referred to hereafter as XXF SQUIDs) are fabricated at PTB in Berlin, and are described thoroughly by Drung [8]. These SQUIDs have high coupled energy resolution at 8 h and low flux noise of 3.6 fT/$\sqrt{\text{Hz}}$. They have been designed specifically for pulsed measurements such as NMR. This section will describe the features of these devices, which will be relevant in discussion of the results of the first experiments.

Figure 3.4 is a circuit diagram of the two-stage SQUID made by PTB. It shows the sensing SQUID (the uppermost of the SQUID symbols) coupled to the input coil, and its amplifier array of 16 SQUIDs below it. There is a second array of 16 SQUIDs on the right hand side of the diagram, which is a Q-spoiler, designed to go normal when the current through the input coil causes resonant currents to 'ring' in the SQUID. By going normal the resistance of the input circuit increases and the time constant of any resonant currents decreases, allowing the SQUID to return to operation in a shorter time period.

The relevant terminals on the left hand side of this diagram are:

- (+F, −F) — Current Φ_b, the flux bias for the sensing SQUID, is applied
- (+I, −IFX) — Sensing SQUID bias current I is applied
- (+FX,−IFX) — Second stage flux bias current Φ_x is applied
- (−V, +V) — Second stage bias voltage V_b and current I_b are applied

These are all the terminals that are used in controlling the SQUID and obtaining a signal. The terminals on the right hand side are the input terminals, where +IN is the connection for one end of the input coil, and the other two determine whether or not the Q-spoiler is used to safeguard the SQUID.

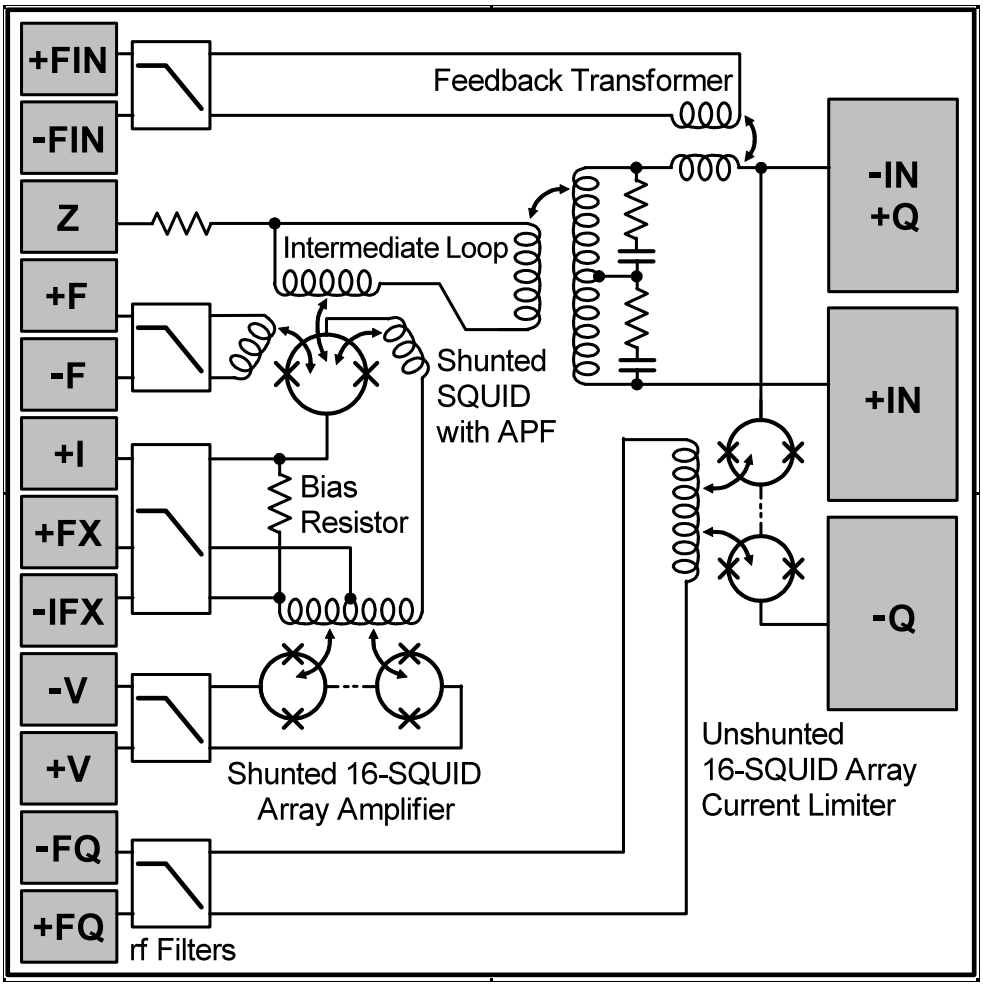

Figure 3.4: PTB SQUID circuit diagram, showing the separated sensing and amplification stages [8]. The right of the chip supports the contacts that are connected to the NEMS chip (-IN, +IN) and the left side supports the various connections to the Magnicon SQUID electronics system.

3.3.1 Flux-Locked Loop (FLL) Mode

As described in section 3.2.1 and shown in fig. 3.3, a SQUID has a periodic voltage characteristic under the application of changing flux. The voltage developed under application of flux is the output signal that is measured, and as such the range over which the signal gain through the SQUID is linear is limited to the maximum gradient of the slope, corresponding to about a half flux quantum. Furthermore, as shown in fig. 3.3, if the applied flux exceeds one half flux quantum the gain will not only be non-linear, but the voltage will decrease which makes measuring large flux variations unfeasible.

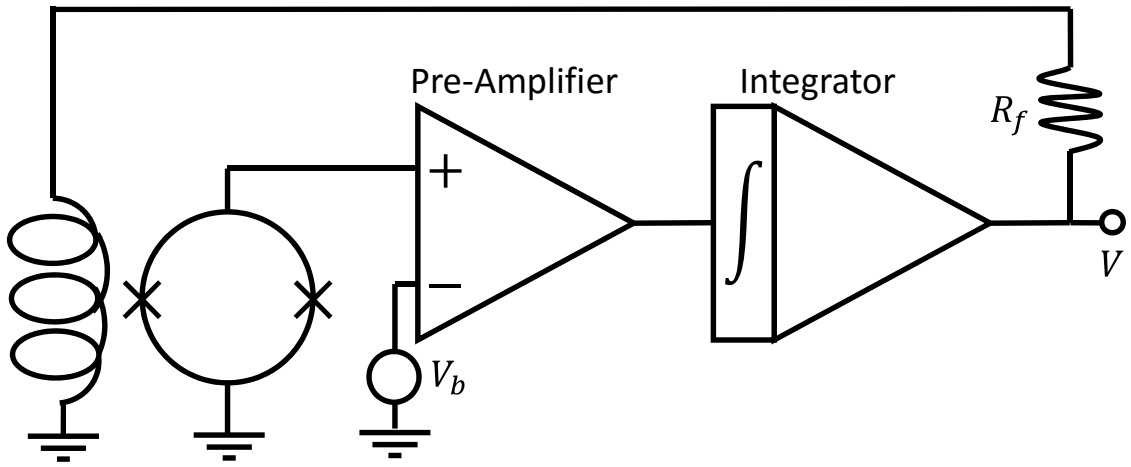

Figure 3.5: A diagram of the basic circuit for a Flux-Locked Loop (FLL).

The solution to this problem is to bias the SQUID with an external flux controlled by the measurement electronics, designed to null the incident flux, and instead use this circuit to measure the behaviour of the device. This is achieved by winding an inductor close to the SQUID connected to feedback electronics which will modulate

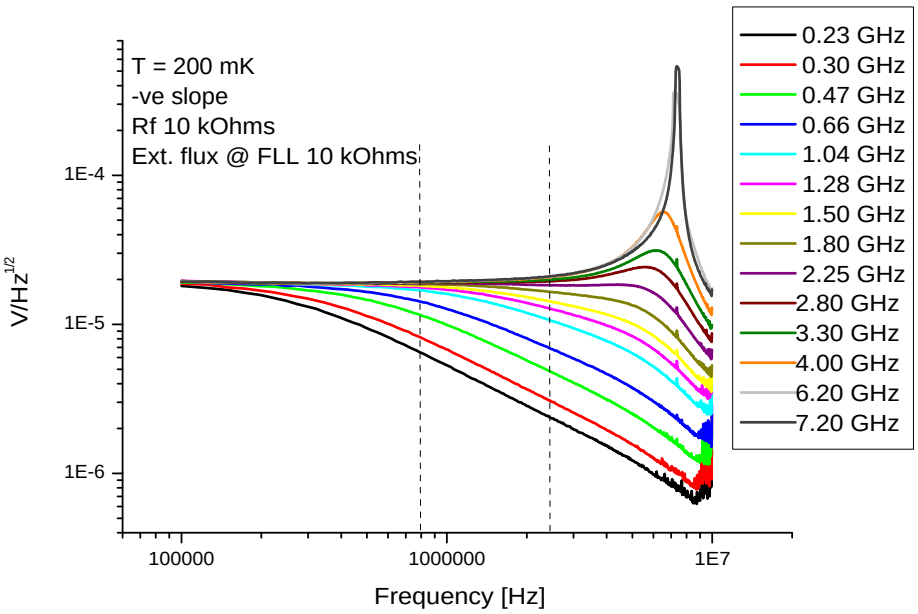

Figure 3.6: The gain profile of the SQUID for the different gain bandwidth products for a fixed feedback resistance. The vertical lines indicate typical resonance frequencies for the first and third mode of the 300 µm resonator.

the current in the inductor responding to voltage developed.

Figure 3.5 shows the basics of a circuit which would work for any SQUID with a non-hysteretic V-Φ relationship. The steepest part of the curve (shown in fig. 3.3) is selected to maximise the voltage developed for a given change in flux. The flux from the input coil (not shown) will develop a voltage across the SQUID, which is amplified by the preamplifier, integrated, and then fed back into the SQUID via a feedback inductor through a feedback resistor. The value of the feedback resistor can be changed via software in our system, but is usually kept at a high value such as 10 kΩ to render the impedance of the feedback inductor negligible. In normal measurements the variable we change in the SQUID electronics is the Gain Bandwidth

Product (GBP) which chiefly changes the gain profile as demonstrated by fig. 3.6. This is a discrete modifier without the option for continuous variation. Increasing the GBP decreases the capacitance in the integrator which reduces the time constant, effectively increasing the corner frequency of the circuit and thus increasing the bandwidth of the electronics.

Increasing the GBP does not affect the frequencies that the SQUID itself responds to, but changes the response of the feedback electronics such that the output will start to include the higher frequencies, and the higher frequencies will be fed back into the SQUID via the feedback inductor [64]. It is important to note that this also limits the frequency range that we are able to measure, and so the bandwidth that is available to us is only a fraction of the noise power truly incident on the SQUID.

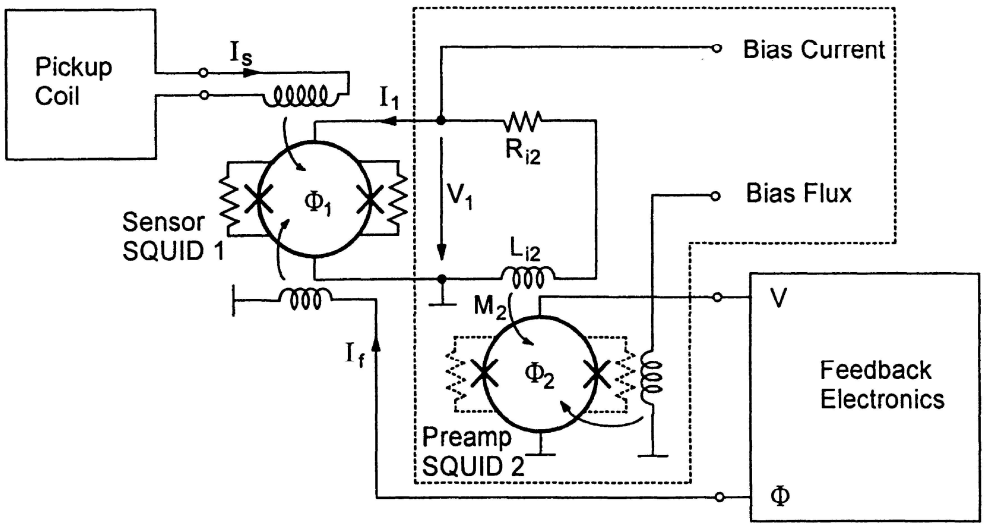

Figure 3.7: A schematic of a basic two-staged SQUID arrangement where the second stage is contained within the dashed line [65].

The preamplifier in the circuit described in fig. 3.5 is realised by using a series array of SQUIDs coupled to the sensing SQUID via an inductor, shown in fig. 3.7. The sensing SQUID is voltage biased such that an incident varying flux generates a varying current in the SQUID, which then flows through the input inductor of the second stage SQUID array which is current biased. It is important to note that the feedback electronics react to a changing voltage over the amplifier SQUIDs, but then act upon the sensing SQUID.

3.3.2 Additional Positive Feedback (APF)

Figure 3.3 refers to 'Additional Positive Feedback' (APF) as the cause of the asymmetric V-Φ curve that is characteristic of the SQUIDs used in this research. APF is a technique used in SQUIDs as a method to improve the signal to noise ratio by modifying the transfer coefficient such that output signal is voltage amplified without using an additional amplifier, effectively adding a low noise preamplifier to the circuit [63, 66].

3.3.3 Output Current Feedback (OCF) SQUIDs

The SQUID used in all experiments described in this thesis has a bandwidth of 10 MHz but the gain profile is only flat to 5 MHz, due to the effects of dual pole integrators in the feedback electronics. This was not an issue for resonators used for helium probes because the frequencies are well below 4 MHz. For experiments designed to reach the quantum regime however the resonators must have a frequency greater than 6.25 MHz, which was shown in section 2.2. For higher frequency resonators a SQUID

with a higher bandwidth is required, also produced by PTB, which is an 'Output Current Feedback' (OCF) SQUID.

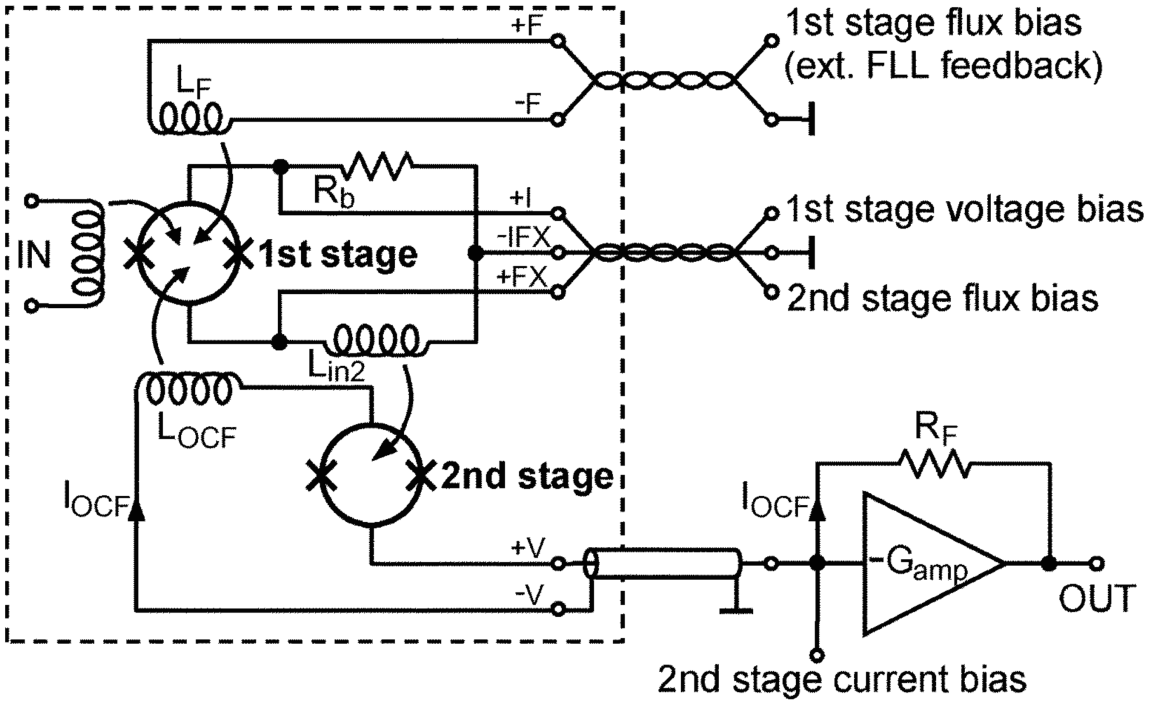

Figure 3.8: A simplified circuit diagram of the OCF SQUID, showing the differences in operation from the XXF SQUIDs; here, everything inside the dashed box is in a cryogenic environment [67].

On the SQUID chip previously discussed the first stage consists of only one SQUID whereas on the OCF SQUID chip there are 16. The second stage holds either 40, 160 or 640 SQUIDs, depending on the variant of the chip in use [67]. The input inductance of these SQUIDs is ≈ 40 nH, meaning in order to maintain optimal impedance matching the leads from the NEMS to the SQUID must be kept as short as possible to reduce stray inductance.

As explained in section 3.3.1, we measure a SQUID output through the use of a Flux-Locked Loop scheme. In the XXF SQUIDs, the circuitry for this is at room temperature, and as such there is a relatively large delay between the flux from the input coil affecting the sensing SQUID, and the feedback coil nulling the incident flux. In the OCF SQUID, the room temperature amplifier and integrator is replaced with an on chip SQUID array - in this case, the second stage array.

As shown in fig. 3.8 the feedback inductor is fed purely by the output current of the second stage, and the feedback resistor is mounted across an amplifier at room temperature. This allows the SQUID to 'see' a low impedance for the feedback inductor, where normally the feedback resistor would produce a large output voltage at the cost of a low feedback amplitude. Here the feedback resistor is still able to generate a large output voltage, but without reducing the feedback amplitude. These modifications allow the SQUID a much larger bandwidth, but at a sensitivity cost [67].

3.4 Measurement Scheme

These experiments are unique in the method used to couple the SQUID to the NEMS. There are two sets of experiments described in this thesis; the first using an electrically screened copper box to contain the NEMS, and the second using a purpose built cell. The cell constructed for the second set is described in detail later in this thesis, and the wiring is very similar between the two experiments. Here, the general setup will be discussed.

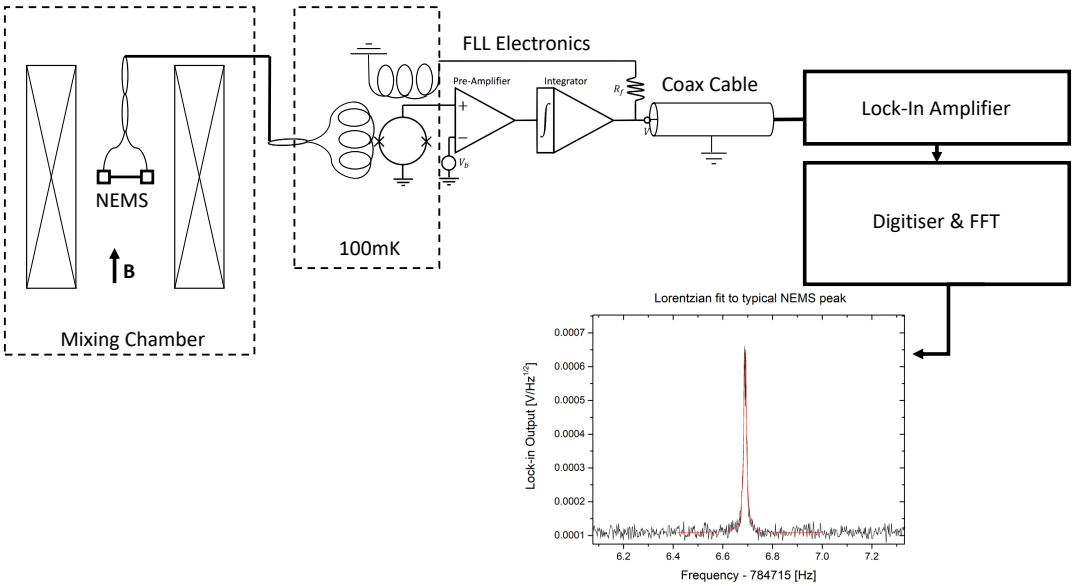

Figure 3.9: The basic arrangement of components for the first set of experiments described in this thesis. Although the second set of experiments were performed with a similar scheme, there are differences in temperatures and vacuum spaces.

Figure 3.9 shows the simplest electrical arrangement for the experiment, with the NEMS mounted perpendicular to an applied magnetic field produced by a magnet

mounted on either the mixing chamber stage, or the 3 K stage. The NEMS was initially mounted upon an extension to the mixing chamber with a large magnet intended for demagnetisation refrigeration supported from the 3 K plate. This arrangement had the advantage of a fast build time, and no new components were fabricated to be able to perform the experiment. This configuration was used for the majority of the measurements in fields above 10 mT, during which the exact field to current ratio of the magnet was uncertain, which will be discussed later in this chapter. Later measurements were performed with a smaller custom built magnet that could be mounted on the mixing chamber, allowing access to higher magnetic fields due to reduced stray field affecting the SQUID, and shorter thermal lag between stage temperature changes and the NEMS thermalisation.

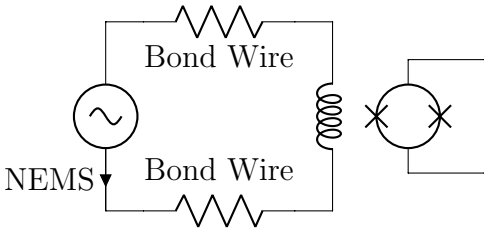

Figure 3.10: Electrical diagram of the SQUID input circuit.

The NEMS itself was grown on a silicon chip glued to the interior of the copper box with GE varnish. It was electrically connected to two solder pads with gold bond wires, which in turn were connected to a CuNi clad NbTi twisted pair via solder. The twisted pair was shielded with a Nb tube that was electrically grounded to the copper box and SQUID shield, and insulated from the twisted pair by a Teflon sheath. The twisted pair was connected to the SQUID input circuit with peek screw terminals, providing a superconducting joint. Notably the circuit is not entirely superconducting

because of the resistive bond wires, as described in fig. 3.10.

This setup allowed some key advantages over other SQUID coupling methods, such as those used by Hao [9] and Naik [28] which both involved the SQUID being in the same location as the NEMS. Those methods both require extensive work to change the resonator being investigated; the former was an extremely delicate setup with the NEMS being mounted directly over the SQUID on-chip, and the latter incorporated the NEMS into the SQUID itself such that replacing either involves replacing the SQUID. In this setup, the resonator was fabricated on a separate chip and in principle could be replaced in a short time period. This also allowed us to have an extremely well-characterised SQUID that we could keep between experiments, adding a useful control factor.

The NEMS being mounted on a different plate to the SQUID also allowed us to vary the temperature of the NEMS without changing the SQUID's temperature, which extended the temperature range over which we could measure the NEMS with consistent parameters. The distance between the NEMS and SQUID also extended the field range available to us in experiments, as (subject to the exact arrangement) it was possible to achieve fields that would have rendered the SQUID inoperable whilst measuring the NEMS with minimal stray flux affecting SQUID performance. In addition to distancing the SQUID from the magnet, the magnet was shielded with a superconducting shield to prevent excessive stray flux, as was the SQUID. Altering the bias flux settings of the SQUID could be used to adapt to any changes due to excess field, further improving reliability.

3.5 Thermometry

The cryostat used for most of the experiments described in this thesis was fitted with a range of well calibrated resistive thermometers, which were more than adequate for measuring temperatures above 20 mK. These thermometers are also used for temperature stabilisation, and as such the temperature of the cryostat when not at base temperature was more stable than otherwise. However, these thermometers were not accurate below 20 mK and the NEMS itself was always mounted on the coldest plate, designed to reach below 8 mK. As a result, we do not rely on the pre-equipped thermometers but on alternative methods shown to be more accurate. In addition, the thermometry methods described below are a key feature of the work in this thesis, as they allow us to measure the temperature of the stage, the temperature of the thermal connection to the NEMS and then the intrinsic temperature of the NEMS itself.

3.5.1 Current Sensing Noise Thermometry

When measuring the temperature of an experiment with a high degree of confidence primary thermometers are the instrument of choice. A primary thermometer is one which derives the thermodynamic temperature of an object by using fundamental constants and no unknown values. Current Sensing Noise Thermometry (CSNT) is such a method, deriving the temperature of a current carrying conductor from the voltage noise generated by the Brownian motion of the electrons within. The noise created by this Brownian motion was discovered and explained by Johnson [68] and Nyquist [69]. The mean square open voltage noise is described by:

$$\langle V_N^2 \rangle = 4k_{\mathrm{B}}TR \tag{3.4}$$

Where k_B is the Boltzmann constant, T is the thermodynamic temperature and R is the resistance of the conductor [68, 70]. The method for measuring this with a SQUID was developed by Webb, Giffard and Wheatley [71] by connecting an inductor across the resistor, and placing this inductor near to a SQUID to measure the flux noise generated.

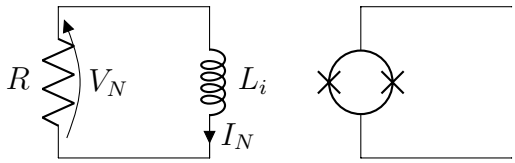

Figure 3.11: CSNT input circuit.

The mean squared current flowing through the input circuit shown above has a white spectral density due to being a consequence of Brownian motion, which itself has white spectral density as shown in section 2.2.1, and is described by:

$$\langle I_N^2 \rangle = \frac{4k_B T}{R} \left(\frac{1}{1 + \omega^2 \tau^2} \right) \tag{3.5}$$

Where $\omega = 2\pi f$ is the angular frequency and $\tau = R/L$, where L is representative of the inductance of the entire input circuit, including stray inductance, L_i, and the mutual inductance of the SQUID. By inspection of eq. (3.5) it is apparent that the amplitude of the current will decrease as the frequency increases, dependent upon the ratio of resistance R to inductance L. The measurement of the temperature using the SQUID then is essentially the measurement of the low frequency spectral power through a low-pass filter.

In practice, a PXI digitiser is used to sample the SQUID output at a sampling rate and record length large enough to capture the structure of the noise at low frequencies. This means that the capture time for the thermometer is long if the -3 dB point of the input circuit is low. It is possible to increase the bandwidth of the input circuit by increasing the resistance value, but this in turn reduces the noise amplitude which will eventually become comparable to the SQUID noise, at which point the thermometer is impractical.

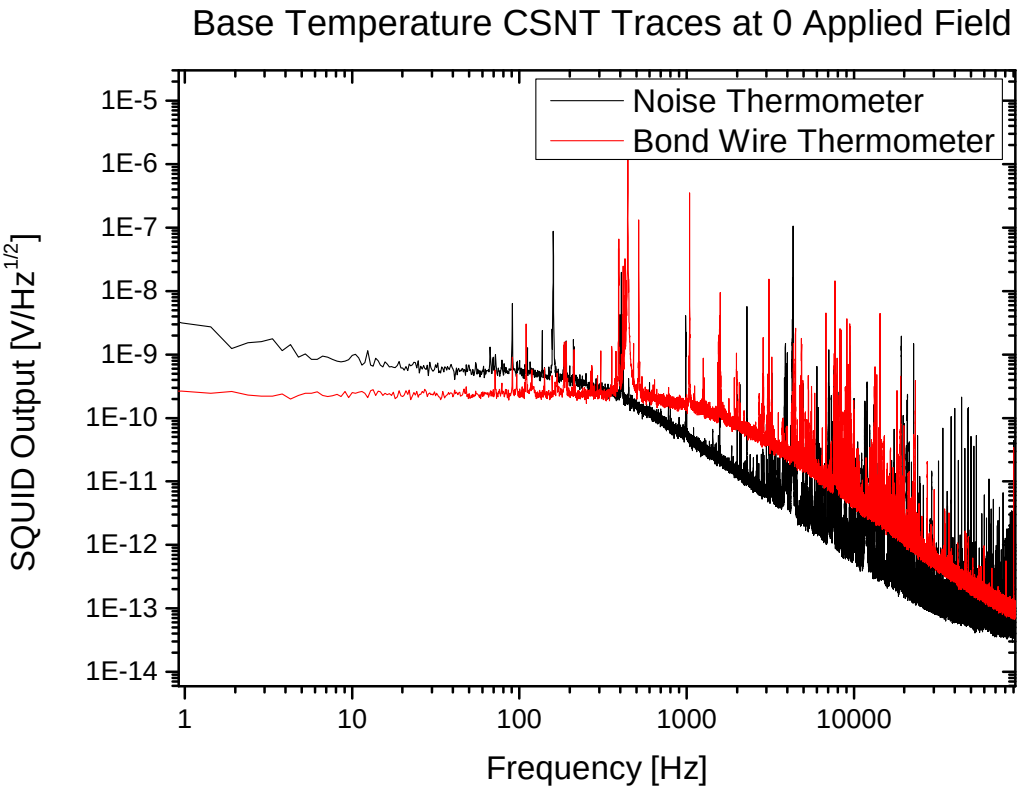

Figure 3.12: Thermometry traces from the noise thermometer mounted on the mixing chamber (black) and the experiment circuit when measuring the temperature of the bond wires (red).

The selection of thermometers used in these experiments evolved over the course of the project. Ultimately the thermometry used on the cryogen free cryostat was a CSNT thermometer mounted on the mixing chamber stage, and the bond wire noise thermometry of the experiment itself. The electrical path from the SQUID to the NEMS was not entirely superconducting; there were gold wire bonds between the NEMS chip and the twisted pair leading to the SQUID input coil. This was primarily for the thermalisation of the NEMS but had the added advantage of acting as a resistor of a CSNT circuit when the resonator was superconducting. Due to the high resonant frequencies of the resonators, they did not have an effect on the low frequency noise power and in theory thermometry measurements could be performed concurrently with resonator measurements. In practice however the presence of an applied magnetic field generated additional low frequency noise through magnetoacoustics, and so typically only one of the two measurements could be performed at any one time.

Figure 3.12 shows an example of noise traces taken from the noise thermometer and the experiment. The different resistance values between the two thermometers is demonstrated by the different -3 dB points of the two curves, and the different amplitudes. Here the bond wire resistance was higher than the resistor used in the noise thermometer, and so the amplitude appears lower even though the two thermometers are at the same temperature.

3.5.2 NEMS Area Scaling

As with CSNT, we are concerned here with measuring Johnson-Nyquist noise to determine temperature. However in this instance the resistance value used is not that of the bond wires, but of the resonator itself, which were calculated using its electrical analogue. The more complex input circuit must also be considered.

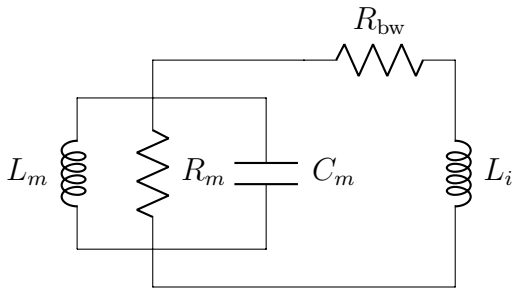

Figure 3.13: The input circuit for the experiment, including the NEMS as a parallel resonant circuit.

In order to calculate the noise, we first need to know the complex impedance of the parallel circuit, defined by:

$$\frac{1}{Z_{\mathrm{m}}} = \frac{1}{R_{\mathrm{m}}} + \frac{1}{i\omega L_{\mathrm{m}}} + i\omega C_{\mathrm{m}} \tag{3.6}$$

$$Z_{\mathrm{m}}(\omega) = \frac{i\omega/C_{\mathrm{m}}}{(\omega_0^2 - \omega^2) + i\omega_0\omega/Q} \tag{3.7}$$

Where R_{m}, L_{m} and C_{m} are the electrical analogue components for the resonator as derived in section 2.3, and Q is the quality factor of the resonator. This can be rationalised to:

$$Z_{\mathrm{m}}(\omega) = \frac{\omega_0\omega^2/QC_{\mathrm{m}}}{(\omega_0^2 - \omega^2)^2 + (\omega_0\omega/Q)^2} + i\frac{(\omega/C_{\mathrm{m}})(\omega_0^2 - \omega^2)}{(\omega_0^2 - \omega^2)^2 + (\omega_0\omega/Q)^2} \tag{3.8}$$

Recalling from eq. (2.89) that R_m can be expressed as $Q\omega_0 L_\mathrm{m}$, and C_m^{-1} as $\omega_0^2 L_\mathrm{m}$:

$$Z_\mathrm{m}(\omega) = \frac{R_\mathrm{m}(\omega_0\omega/Q)^2}{(\omega_0^2-\omega^2)^2+(\omega_0\omega/Q)^2} + i\frac{\omega(\omega_0^2 L_\mathrm{m})}{(\omega_0^2-\omega^2)^2+(\omega_0\omega/Q)^2} \tag{3.9}$$

Which can be written in terms of a frequency dependent resistance and inductance:

$$Z_\mathrm{m}(\omega) = R_\mathrm{m}(\omega) + i\omega L_\mathrm{m}(\omega) \tag{3.10}$$

Now we can substitute this value into eq. (3.4), remembering that only the real component is required:

$$\langle V_N^2\rangle = 4k_\mathrm{B}T \times \mathrm{Re}(Z_\mathrm{m}(\omega)) \tag{3.11}$$

$$\langle V_N^2\rangle = 4k_\mathrm{B}T\frac{R_\mathrm{m}(\omega_0\omega/Q)^2}{(\omega_0^2-\omega^2)^2+(\omega_0\omega/Q)^2} \tag{3.12}$$

Thus arriving at the mean squared open circuit voltage generated by the resonator at temperature T, where the dependence on applied magnetic field B is contained in the terms from the derivation of the electrical analogue in section 2.3.

To find the current that this voltage induces in the circuit, we must find the impedance of the input circuit as a whole, Z_Σ.

$$Z_\Sigma = Z_\mathrm{m} + R_\mathrm{bw} + i\omega L_i \tag{3.13}$$

$$Z_\Sigma = (R_\mathrm{bw} + R_\mathrm{m}(\omega)) + i\omega(L_i + L_\mathrm{m}(\omega)) \tag{3.14}$$

Where R_bw is the resistance of the bond wires and L_i is the inductance of the SQUID input inductor, both are shown in fig. 3.13. Recalling from eq. (3.4) the expression for

the mean squared Johnson noise of a resistor, we can express the sum Johnson voltage for the circuit as a linear combination of the NEMS and bond wire resistances:

$$\langle V_N^2 \rangle_\Sigma = 4k_\mathrm{B}(T_\mathrm{bw}R_\mathrm{bw} + T_\mathrm{m}R_\mathrm{m}(\omega)) \tag{3.15}$$

Where T_bw and T_m are the temperatures of the bond wires and NEMS respectively. Although we expect these two temperatures to be similar, they are treated as different values for the case that the wires continue to cool when the resonator does not. Finding the current in the input circuit is now a case of applying Ohm's law:

$$\langle I_N^2 \rangle_\Sigma = \frac{\langle V_N^2 \rangle_\Sigma}{|Z_\Sigma|^2} \tag{3.16}$$

$$= \frac{4k_\mathrm{B}(T_\mathrm{bw}R_\mathrm{bw} + T_\mathrm{m}R_\mathrm{m}(\omega))}{|(R_\mathrm{bw} + R_\mathrm{m}(\omega)) + i\omega(L_i + L_\mathrm{m}(\omega))|^2} \tag{3.17}$$

$$= \frac{4k_\mathrm{B}(T_\mathrm{bw}R_\mathrm{bw} + T_\mathrm{m}R_\mathrm{m}(\omega))}{(R_\mathrm{bw} + R_\mathrm{m}(\omega))^2(1 + \omega^2\tau^2(\omega))} \tag{3.18}$$

Where $\tau(\omega)$ represents the time constant of the resonant circuit, defined by:

$$\tau(\omega) = \frac{L_i + L_\mathrm{m}(\omega)}{R_\mathrm{bw} + R_\mathrm{m}(\omega)} \tag{3.19}$$

By knowing the SQUID gain and transfer function, it is then possible to calculate the temperature of the mode by measuring the temperature of the bond wires using CSNT, and then using the known (or previously measured) natural Q-factor of the resonator and other parameters.

3.6 Initial Tests and Calibration

In this section the procedures for beginning the NEMS measurements will be discussed. There are a number of parameters that must be established before any meaningful results can be taken, including the calibrations for the magnetic field applied and the stray magnetic field.

3.6.1 Magnet Calibration

In these experiments a total of three magnets were used, one commercial magnet intended for nuclear demagnetisation cooling and two custom made in-house magnets of much smaller volume and maximum field. The need for calibration of the in-house magnets is obvious: although we may be able to calculate the theoretical current-field ratio, there is a requirement to measure it precisely for our experiments. Previous work in this group has not required such precise measurements; due to the nature of Nuclear Magnetic Resonance (NMR) it is possible to calculate the field from the resonant frequency of the sample. The commercial magnet was provided with a calibration from the manufacturers, but as the magnet had shielding and was designed to operate at fields of order 1 T contrasted with the 30 mT we required, it had a non-linear field current ratio at low currents. This can be for a variey of reasons in large superconducting magnets, such as current leakage through the persistent switch at low currents or flux pinning in the superconducting windings of the magnet. To test the magnetic field of the large magnet, Hall probes were mounted to the NEMS plate (the NEMS cell having been removed).

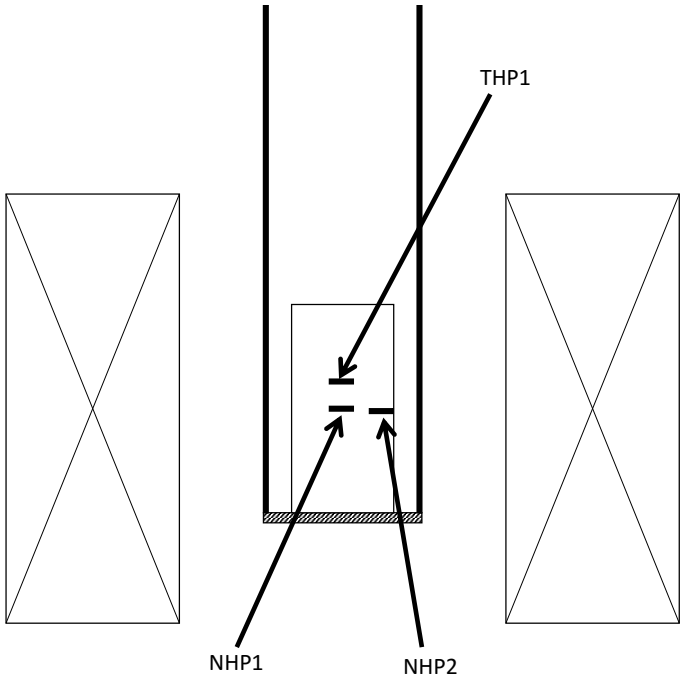

Figure 3.14: The positions of the three Hall sensors mounted on a copper plate at sample position in the magnet.

Figure 3.14 shows the position of the three Hall probes used in the calibration, mounted at the position of the NEMS chip (NHP1), the wall of the cell (NHP2), and the upper wall of the cell (THP1). The aim of the three sensors was to be able to determine the field profile and homogeneity, however ultimately only one, NHP1, was used for the field calibrations. The Hall probes used were Toshiba THS119 'crank shaft position monitors'. These were not designed for the purpose of high precision magnetic field measurements, but had a consistent field resistance relationship at 4 Kelvin.

To determine the Hall probe calibration, one of the devices was placed in a physical property measurement system which had a very well calibrated magnetic field, and was

able to reach temperatures between 1 K and 4 K. Figure 3.15 shows the calibration line acquired from these measurements, having first confirmed that the behaviour of the Hall probe was consistent between 1 and 4 Kelvin. It was determined that although temperature independent, the Hall probe required current supplied to it for the period of an hour before it was stable enough to measure. The current used in these measurements was 10 µA.

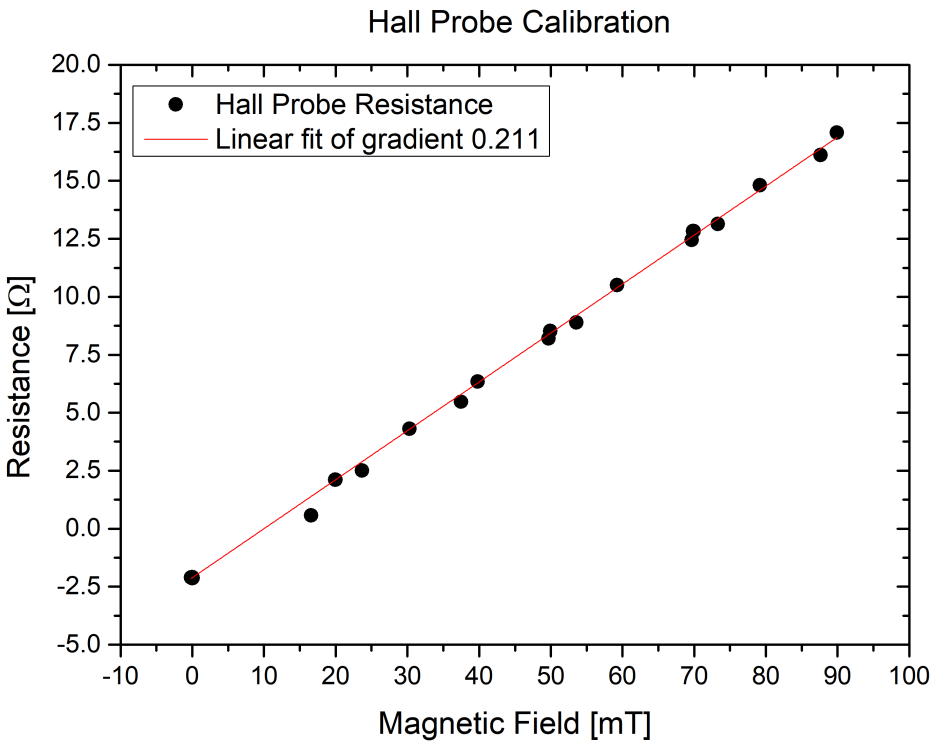

Figure 3.15: The Hall probe calibration, showing a result of 0.21103 Ω/mT.

Using this calibration for the Hall probes, the field of the large magnet was measured and was found to agree with its factory calibration at high fields, but disagree at low fields.

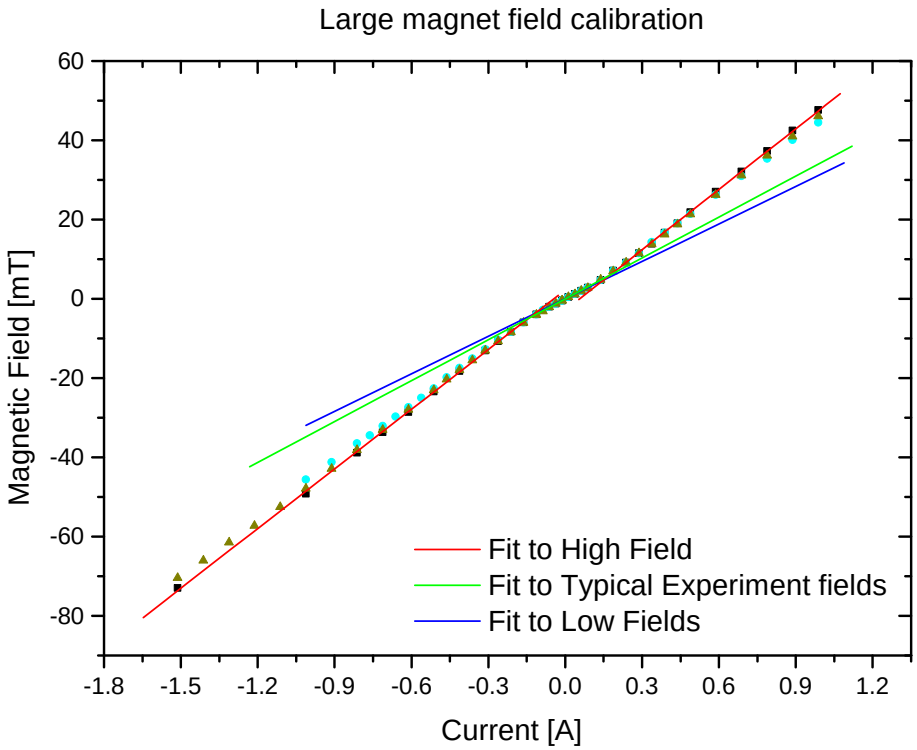

Figure 3.16: The current-field gradients found from NHP1 in the large magnet, there are three distinct trends: High field (red), Low field (Blue), and the fields typically used in the experiment (green).

Figure 3.16 shows the three possible linear fits to the magnet's field current ratio; one at high fields and two at low fields. This introduced a significant error in the NEMS calculations which are heavily field-dependent. Upon closer inspection of the low field results it was evident that a cubic can be used to fit the curve, which was then used as the calibration curve. The final calibration for this magnet is found in table 3.1.

Current Range	Formula
0 - 0.2 A	$32.59006 \times \mathrm{I} + 32.9814 \times \mathrm{I}^2 - 17.44241 \times \mathrm{I}^3 - 0.13805$
0.2 - 1 A	$50.18 \times \mathrm{I} - 2.24$

Table 3.1: Current-field calibration for the large magnet.

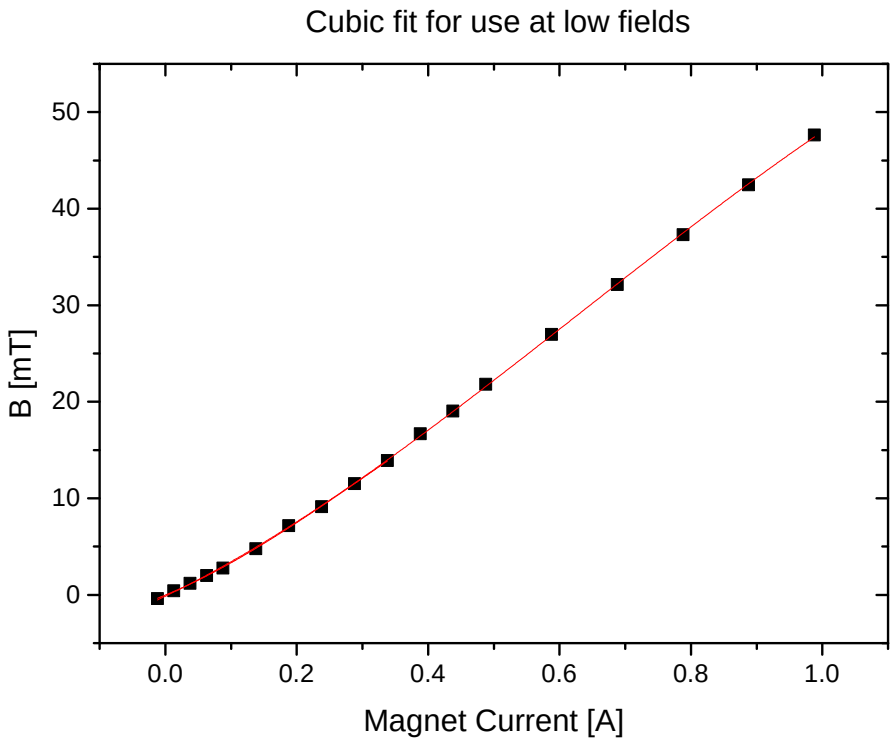

Figure 3.17: Cubic fit of large magnet for low fields.

This calibration is used throughout the rest of this thesis for experiments involving the 300 µm resonator, before the fabrication of the custom made magnet, with a well defined field current ratio:

$$\text{Small Magnet Field Current Ratio} = 33.6488 \text{ mT/A} \tag{3.20}$$

This magnet was well characterised with the same Hall probe, NHP1, as had been used with the large magnet for consistency. This Hall probe went on to be used to characterise the final magnet constructed for these experiments which had a smaller form factor and had better shielding. The final magnet field current ratio was deter-

mined as:

$$\text{ND2 Magnet Field Current Ratio} = 24.743 \text{ mT/A} \tag{3.21}$$

In the case of the later experiments the aluminium bond wires used as thermal breaks (described further in chapter 5) had a critical field of ≈ 10 mT. Having previously calculated the field profile of the magnet, knowing the position of the bond wires accurately allowed a final check of the field produced by the magnet. This was made possible by monitoring the low frequency noise generated by the bond wires using the same methods as decribed in section 3.5.

3.6.2 Finding the NEMS Resonance

Although it is possible to use the length and internal stress to calculate the ideal frequency of a NEMS resonator, thermal cycling and vacuum conditions can strongly affect the frequency response. For this reason it is not trivial to find the resonance of a NEMS for the first time, and every subsequent thermal cycle will likely change the resonant frequency by some amount.

For the purposes of finding the NEMS resonance a piezo shaker was glued to the exterior of the NEMS cell. By applying an alternating voltage drive, the shaker would vibrate at the frequency of the drive. For experiments with the 300 µm resonator it was sufficient to use a standard tracking generator and spectrum analyser to scan the frequency range in which the resonator was expected to respond. Some fine-tuning of resolution bandwidth was required, as the Q-factor of the resonator was high enough that too low a resolution would not detect the response of the NEMS to excitation.

Using the tracking generator was the coarse grain approach, and was not sufficient for detecting the response of the smaller, higher-frequency resonators. In order to detect these, a pulsed approach was used, reminiscent of pulsed NMR techniques. A pulse generator card in a National Instruments PXI chassis was set up such that it would trigger a second PXI card, a digitiser, to start acquisition concurrent with a burst of sinusoidal voltage applied to the piezo shaker. The pulse generator was also connected to the FLL reset of the SQUID, such that the SQUID only entered flux-locked loop mode once the pulse had finished. This was done to reduce the flux-jump noise from the SQUID in the measured trace. The length of the pulse was chosen such that the spectral weight was spread over a wide frequency range, in the form of a Sinc function in frequency space. These traces were taken in the time domain and then averaged, which improved the signal to noise ratio by averaging away any non-coherent signals. In addition, passive high-pass filters were used on the line to the piezo drive and from the SQUID to reduce the low-frequency noise that could not be part of the NEMS signal.

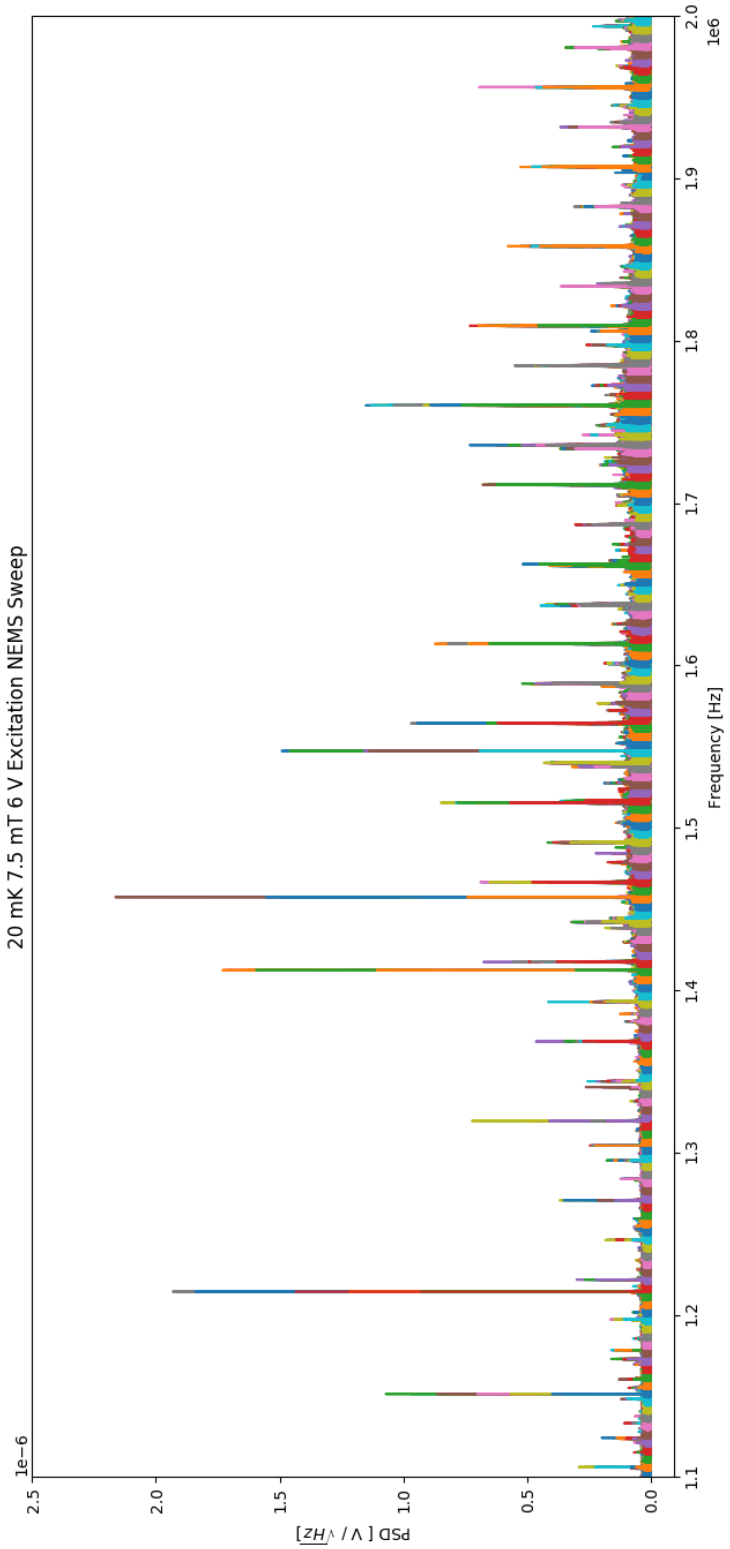

Figure 3.18: An example of a pulsed field sweep test, showing several NEMS candidates. Different colours indicate different data sets, where each data set was taken after a pulse at a different frequency, the pulse width indicated by each coloured region.

This process was not capable of determining that the signal seen is the NEMS, but it reveals a number of candidate signals as seen in fig. 3.18. To be certain that it was the NEMS, high-resolution traces of the response to thermal power and magnetic field were acquired. This was accomplished by introducing a lock-in amplifier with a stable frequency reference between the SQUID output and the PXI digitiser. This allowed the use of a much lower sampling rate with the same record length and thus the Fast Fourier Transform (FFT) had higher resolution than the previous traces, such that it is possible to accurately measure the properties of the narrow Lorenztian produced by the NEMS (Typically sub-Hz). From this point the signal must obey 5 patterns of behaviour:

- Area increase with pulse amplitude.
- Area increase with temperature.
- Frequency increase with magnetic field squared.
- Area increase with magnetic field squared.
- Q-factor decrease with magnetic field squared.

The first of these could be tested without using the lock-in amplifier, but the others were dependent on high resolution. If it was confirmed that a signal demonstrated these trends, then that signal was accepted as the resonator signal.

3.6.3 Stray Field Determination

Once the NEMS signal was confirmed it was necessary to identify the magnitude of any stray magnetic field around the cryostat, which was not magnetically shielded. In

order for this test to be valid the magnet must have been tested with inverted current with a Hall probe attached, to confirm that the field is symmetric. The probe itself could not determine absolute magnetic field due to a variable offset that changed with every thermal cycle and drifted with time, and so was only appropriate for measuring a relative change.

Using an inverted field at a fixed temperature at identical SQUID bias conditions, the area of the Lorentzian was used to identify the stray field. Knowing that (at low fields) the area was proportional to the magnetic field squared:

$$\mathbf{A} = k \times \mathbf{B}^2 \tag{3.22}$$

Where k is a constant of proportionality, by replacing $\mathbf{B}$ with a field produced by the magnet, $\mathbf{H}$, and a stray field, x, we have:

$$\mathbf{A} = k \times (\mathbf{H} + x)^2 \tag{3.23}$$

If we invert the field, then we should have the relation

$$\mathbf{A} = k \times (\mathbf{H} - x)^2 \tag{3.24}$$

Thus it is possible to find the stray field by inverting the applied field. Using subscript + and - to denote positive and negative applied field the expression is found for calculating stray field:

$$x = \frac{\sqrt{\mathbf{A}}_+ - \sqrt{\mathbf{A}}_-}{\sqrt{\mathbf{A}}_+ + \sqrt{\mathbf{A}}_-} \times \mathbf{H} \tag{3.25}$$

This procedure was used after every thermal cycle to ensure consistency.

3.6.4 NEMS Effective Mass

The electrical model used to predict the NEMS behaviour requires prior knowledge of the mass of the beam. This value is to an approximation known to us because we know the intended dimensions of the beam and also the composition of the materials used to construct it to a high degree. However, due to the beam being clamped at both ends the true mass is not what should be used in these calculations. Instead we use the effective mass integral [72, 73] defined as:

$$m_{\text{eff},n} = \rho A \int_0^L dx |U_n(x)|^2 \tag{3.26}$$

for a one dimensional resonator, where ρ is the mass density, A is the cross-sectional area, L is the resonator length and $U_n(x)$ is the mode shape, calculated in section 2.1. This effective mass is mode dependent and has been calculated to the tenth mode in Hauer *et al.* [72]. The effective mass as a function of the total mass for the first five modes is tabulated in table 3.2. Only the first five modes are tabulated as the bandwidth limitations of the experiment prohibit effective transduction of the higher modes of the resonators described in this thesis.

Mode	m_{eff}/m
1	0.3965
2	0.4390
3	0.4371
4	0.4372
5	0.4372

Table 3.2: The first five values for the effective mass of a doubly clamped beam.

Chapter 4

MilliKelvin Vacuum Experiments

In this chapter the experiments performed with the 300 µm Si_3N_4 aluminium coated resonator described in section 3.1 are discussed. These were the first successful experiments performed with the new measurement scheme, and were designed to investigate the properties of the new arrangement such that the system was well characterised. Following characterisation, work was to begin on the new cell. These experiments were performed in the first two of the three configurations described in chapter 3, using a non-isolated NEMS cell that shared a vacuum with the cryostat Outer Vacuum Chamber (OVC).

These experiments took place over the course of two years, with the bulk of the measurements being performed in the large magnet described in chapter 3 and then confirmed using the first of the smaller magnets designed to extend field range. As a consequence of this, the data were not fully analysed until the fields of the magnets were fully calibrated as described previously, and this had some impact on the design of the new cell described in chapter 5.

First, the chapter will review the fundamental characteristics of the resonator measured in a range of magnetic fields, and then go on to discuss interactions between the NEMS and the SQUID, which have some analogues in cavity optomechanics as mentioned in section 1.1.3. A theoretical model for the interaction is presented, and conclusions drawn about the effective mode temperature.

4.1 Vacuum Characterisation

As earlier described in chapter 2, the resonator was expected to demonstrate field and temperature dependent behaviour, based on fundamental characteristics such as the natural frequency and the Q-factor. This section will describe the properties of the 300 µm resonator in vacuum.

The collection of the data for these experiments was conducted by using a lock-in amplifier to mix down the SQUID signal and then digitising it with a National Instruments PXI card. From that card the data was transferred to a LabView program that performed the averaging (in the frequency domain) and then saved the data to ASCII files. These data were then plotted using spreadsheet software and fitted to a Lorentzian after the peak was identified 'by eye'.

Figure 4.1 is an example of the peak that would be identified as the NEMS, and then fit to a Lorentzian. The extracted parameters were then entered into a spreadsheet so that features such as frequency shift could be analysed efficiently, as is demonstrated in fig. 4.4. As has been mentioned, the frequency of the resonator varied with temper-

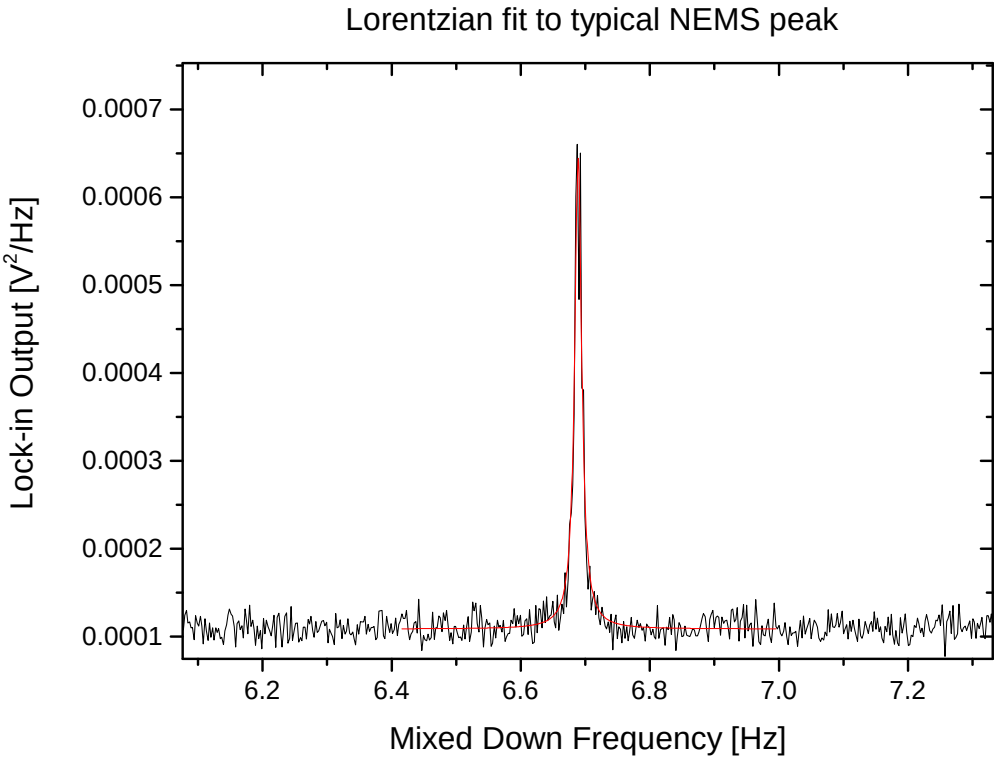

Equation	$y_0 + \frac{w2A/\pi}{(4(x-x_c)^2+w^2)}$
x_c	6.688 ± 0.002 Hz
w	$(1.31 \pm 0.05) \times 10^{-2}$ Hz
A	$(1.099 \pm 0.03) \times 10^{-5}$ V^2
y_0	$(1.085 \pm 0.001) \times 10^{-4}$ V^2
Reduced Chi^2	4.03×10^{-10}

Figure 4.1: A typical resonance lineshape for the 300 µm resonator $f_0 \approx 770$ kHz, shown with the fitting routine used to extract parameters such as the width and integrated area.

ature, magnetic field and upon thermal cycling. For this reason the frequency used to mix down the SQUID output was varied frequently enough that it was included in each of the spreadsheets as a parameter. The settings of the lock-in were broadly kept the same for all measurements, except for the preamplifier gain. This was changed to a lower value on occasion to prevent overload of the mixer and secondary amplifiers in the lock-in amplifier.

Figure 4.2 demonstrates the difference in signal size between a 'high' field (50 mT) and 'low' field (2 mT) signal (both taken at 20 mK). The contrast is stark, and so at higher temperatures the difference in output can be marked enough to warrant gain setting changes.

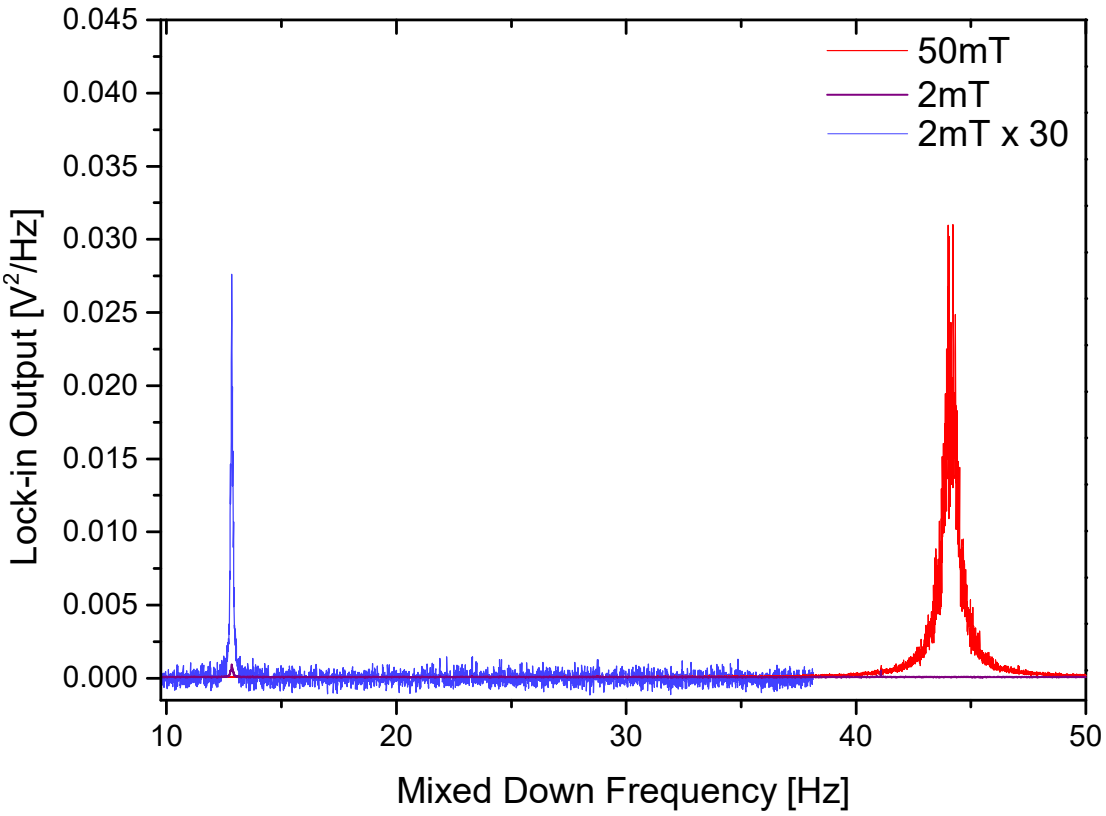

Figure 4.2: A comparison of a 2 mT (purple, blue) and 50 mT (red) measurement of the 300 µm NEMS fundamental mode lineshape. The blue trace is the same data as the purple trace, but multiplied by 30 so that the Q-factor change is apparent. For the same trace resolution there are fewer points resolving the lineshape and so the fitting to these features carry a higher error at low magnetic field.

4.1.1 Frequency Response

The resonator had a natural frequency around 7.84×10^5 Hz which varied significantly between thermal cycles. A resonator modelled as a parallel resonant circuit should have a frequency that is dependent on the applied magnetic field, as the resonance of the circuit will occur when the reactance of the inductor and capacitor are equal, where reactance is the imaginary component of the impedance.

$$X_C = X_L \tag{4.1}$$

$$\frac{1}{\omega C} = \omega L \tag{4.2}$$

$$\omega^2 = \frac{1}{LC} \tag{4.3}$$

The input circuit is described by fig. 3.11, which here we can consider equivalent to:

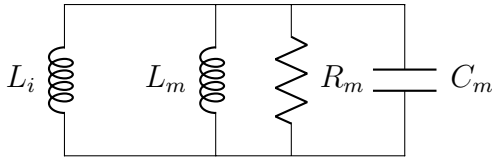

Figure 4.3: The equivalent circuit for describing the frequency shift given that R_{bw} is very small and so ignored.

Where R_{bw} is very small, and resistance is not important in eq. (4.3). We denote the total inductance to be L_Σ, and so eq. (4.3) becomes:

$$\omega = \frac{1}{L_\Sigma C_{\text{m}}} \tag{4.4}$$

where

$$L_\Sigma = \frac{L_\mathrm{m} L_i}{L_i + L_\mathrm{m}} \tag{4.5}$$

$$= L_\mathrm{m}\left(1 + \frac{L_\mathrm{m}}{L_i}\right)^{-1} \tag{4.6}$$

such that eq. (4.4) becomes

$$\omega^2 = \left(1 + \frac{L_\mathrm{m}}{L_i}\right)\frac{1}{L_\mathrm{m} C_\mathrm{m}} \tag{4.7}$$

The terms L_m and C_m multiply to form the field independent natural frequency of the resonator ω_0^2. Taking the square root of both sides and taking the leading order Taylor expansion of the right hand side yields:

$$\omega = \left(1 + \frac{L_\mathrm{m}}{2L_i}\right)\omega_0 \tag{4.8}$$

Where L_i is larger than L_m and is field independent. L_m is proportional to B^2 as defined in eq. (2.89) and as such it is expected that frequency will scale linearly with field squared.

The resonator frequency behaved as described by eq. (4.8) as shown in fig. 4.4, with very little temperature dependence. This is expected, as the only temperature dependent feature at low temperatures is the natural resonance of the resonator which will change due to differential contraction. The upper limit on magnetic field was due to the stray field affecting the SQUID. This was addressed in later measurements with a smaller magnet.

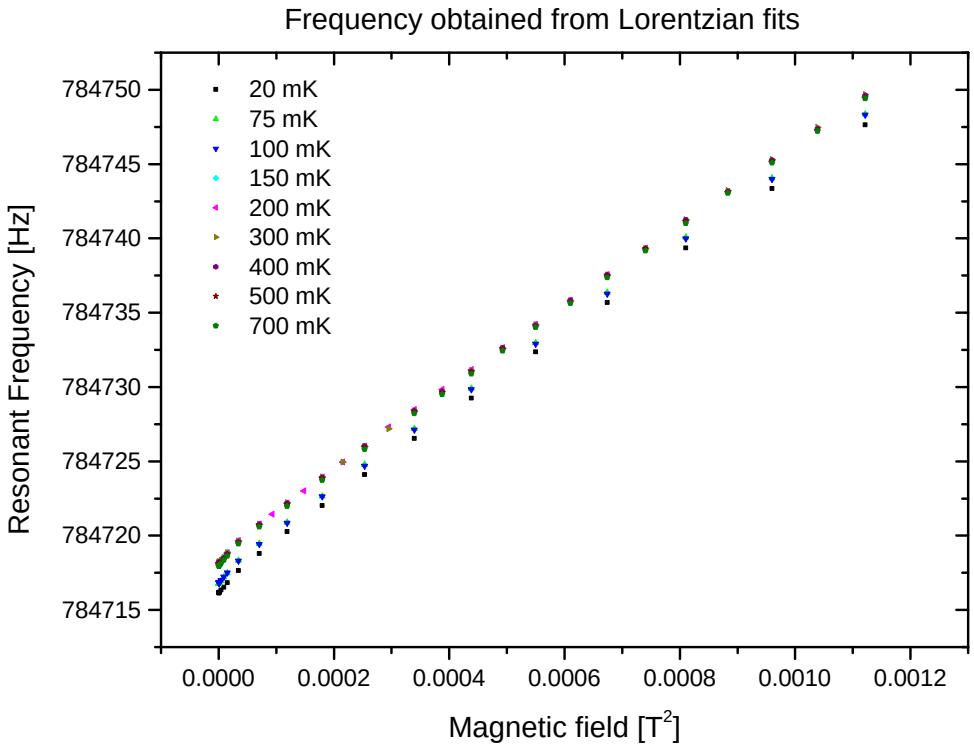

Figure 4.4: Frequency vs magnetic field applied to the resonator. The relationship between the frequency and field described by eq. (4.3) is demonstrated, and the gradient reproducible for a range of temperatures. There is a temperature dependence to the fundamental frequency ω_0 that is shown by the appearance of parallel data sets on the plot. This temperature dependent frequency shift is characteristic of the materials used to fabricate the NEMS.

4.1.2 Thermal Noise Power

As detailed in section 3.5 it was expected that the thermal power in the resonator would scale linearly with temperature, described by eq. (3.18):

$$\langle I_N^2 \rangle_\Sigma = \frac{4k_\mathrm{B}(T_\mathrm{bw}R_\mathrm{bw} + T_\mathrm{m}R_\mathrm{m}(\omega))}{(R_\mathrm{bw} + R_\mathrm{m}(\omega))^2(1 + \omega^2\tau^2(\omega))} \tag{4.9}$$

The terms here have already been described earlier, and it is important to remember that $R_\mathrm{m}(\omega)$ and $L_\mathrm{m}(\omega)$ are both field dependent, although they have been written more simply for convenience. The behaviour of the thermal power in the resonator with temperature was useful to determine that the resonator was thermalised with the experiment stage. For this experiment it was assumed that the bond wires were well thermalised to the experiment stage, such that we could set T_bw to the measured stage temperature. Re-arranging eq. (3.18) for T_m it was then possible to extract the mode temperature from the Lorentzian.

This resulting analysis demonstrated that our environment was free from additional noise power. The ability to observe a resonator behaving quantum mechanically is dependent on control of the energy that the resonator is exposed to. The phonon occupancy of the beam must be unitary, and so the energy available to the resonator must be less than one phonon of the resonant frequency of the beam, as shown in section 2.2. Being able to observe the result of a linear scaling between the temperature of the stage and the mode temperature of the NEMS would indicate that there is no non-thermal noise power available to the beam, and as such the quantum regime is achievable.

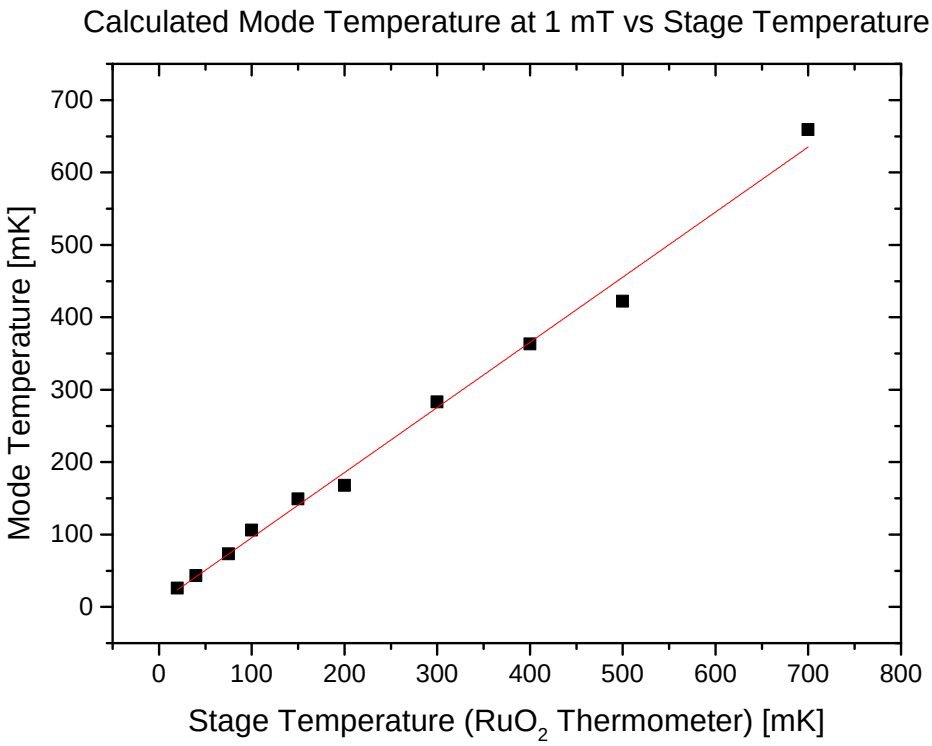

Figure 4.5: The fitted lineshape area was used to calculate the mode temperature of the resonator, here shown to have good linear dependence with stage temperature and good agreement at low temperatures, with a straight line fit giving a gradient close to unity.

This method for calculating mode temperature (with the assumption of no other drive applied to the resonator) provided good results for thermalisation of the resonator. However, it was observed that the resonator mode temperature would stop cooling at 26 mK even when the stage was at 20 mK. This was attributed to the thermalisation not being adequate for such low temperatures, as well as a heat leak from the experiment onto the mixing chamber plate which should have a base temperature of around 12 mK. However any such heat leak could not be well quantified, as the thermometry on the experiment stage was limited to a RuO_2 thermometer which is

unreliable below 20 mK.

The NEMS frequency under increasing field was expected to scale quadratically. This behaviour was a direct consequence of the resonator moving in a larger magnetic field and thus producing more signal power as it cut more flux lines. The behaviour of the NEMS in series with a resistance and under magnetic field is here referred to as the 'loaded' behaviour, such that the frequency of the NEMS at a given non-zero field is referred to as the loaded frequency and the area corresponding to that, the loaded area.

As shown previously, the current in the input circuit was described as:

$$\langle I_N^2 \rangle_\Sigma = \frac{\langle V_N^2 \rangle_\Sigma}{|Z_\Sigma|^2} \tag{4.10}$$

$$= \frac{4k_\mathrm{B}(T_\mathrm{bw}R_\mathrm{bw} + T_\mathrm{m}R_\mathrm{m}(\omega))}{(R_\mathrm{bw} + R_\mathrm{m}(\omega))^2(1 + \omega^2\tau^2(\omega))} \tag{4.11}$$

From inspection the input circuit current is maximum when $\omega^2\tau^2(\omega) << 1$, and when $\omega = \omega_0$, the resonance frequency. If this term is solved for 0, two roots are revealed; the first as $\omega = \omega_0$ and the second at $\omega = \omega_0 + \delta\omega$. The first of these roots is never experimentally observed, as the application of magnetic field shifts the frequency to the second root. The assumption is now made that $T_\mathrm{m} = T_\mathrm{bw} = T$, which has been demonstrated to be true above 25 mK. Recalling that the current can be expressed as:

$$\langle I_N^2 \rangle_\Sigma = \frac{\mathrm{Re}(Z_\Sigma)4k_\mathrm{B}T}{|Z_\Sigma|^2} \tag{4.12}$$

It is advantageous to know the expression for Z_Σ in the limiting case of high Q-factor

and the roots described above. The total impedance for the input circuit is described by:

$$Z_{\Sigma} = \left(R_{\mathrm{bw}} + \frac{R_{\mathrm{m}}}{1 + (\frac{\delta\omega}{\Delta\omega})^2} \right) - i \left(\omega L_i - \frac{2\delta\omega L_{\mathrm{m}} Q^2}{1 + (\frac{\delta\omega}{\Delta\omega})^2} \right) \tag{4.13}$$

Where $\delta\omega = \omega - \omega_0$, the shift between the true resonant frequency and the observed frequency, and $\Delta\omega = \omega/2Q$ describing half the width of the resonance. By making assumptions about the relative sizes of terms arising from the observations, it follows that when the second root ($\omega = \omega_0 + \delta\omega$) is substituted into the expression it can be expressed as:

$$Z_{\Sigma} = \frac{R_{\mathrm{bw}}(\omega_0 L_{\mathrm{m}}/2L_i)^2 + (R_{\mathrm{bw}} + R_{\mathrm{m}})(\Delta\omega)^2}{(\omega_0 L_{\mathrm{m}}/2L_i)^2} + i\frac{\delta\omega\omega_0^2(L_{\mathrm{m}}/2)}{(\omega_0 L_{\mathrm{m}}/2L_i)^2} \tag{4.14}$$

If as suggested previously we take eq. (4.11) and set the time constant term to zero, then computing the term $R_{\mathrm{m}}(\omega)$ for the resonance condition results in the expression for the current noise:

$$\langle I_N^2 \rangle_{\Sigma} = \frac{4k_{\mathrm{B}}T(L_{\mathrm{m}}/L_i)}{\omega_0 L_i[(R_{\mathrm{bw}}L_{\mathrm{m}}/\omega_0 l_i^2) + (1/Q)]} \tag{4.15}$$

Where the term in the square brackets in the denominator can be equated to the inverse of a loaded quality factor Q_l such that:

$$\frac{1}{Q_l} = \frac{R_{\mathrm{bw}}L_{\mathrm{m}}}{\omega_0 l_i^2} + \frac{1}{Q} \tag{4.16}$$

Using this substitution it is possible to reduce the expression for the current to:

$$\langle I_N^2 \rangle_\Sigma = \frac{4k_\mathrm{B}T(L_\mathrm{m}Q_l/\omega_0 L_i^2)}{1+4Q_l^2(\delta\omega/\omega_0)^2} \tag{4.17}$$

This expression can be written in terms of the frequency $f_0 = \omega_0/2\pi$ and integrated over frequency space to give the area under the Lorentzian:

$$\text{Area} = 4k_\mathrm{B}T\left(\frac{L_\mathrm{m}Q_l}{2\pi f_0 L_i^2}\right)\int_0^\infty \frac{(f_0/2Q_l)^2}{(f-f_0)^2+(f_0/2Q_l)^2}df \tag{4.18}$$

$$= 4k_\mathrm{B}T\left(\frac{L_\mathrm{m}Q_l}{2\pi f_0 L_i^2}\right)\left(\frac{f_0}{2Q_l}\right)^2\left(\frac{2\pi Q_l}{f_0}\right) \tag{4.19}$$

$$= \frac{k_\mathrm{B}TL_\mathrm{m}}{L_i^2} \tag{4.20}$$

which shows that the area is proportional to $L_\mathrm{m} \propto B^2$, which is observed experimentally. Figure 4.6 demonstrates the field area relationship obtained from the resonator under idealised bias conditions. The loaded area scaled with field quadratically as expected for this configuration. The agreement with theory is much stronger for lower magnetic fields than for higher values, which could be a consequence of being more susceptible to vibrational noise at these fields. Additionally, as will be discussed later in this chapter, there could be an interaction between the SQUID and NEMS causing this instability.

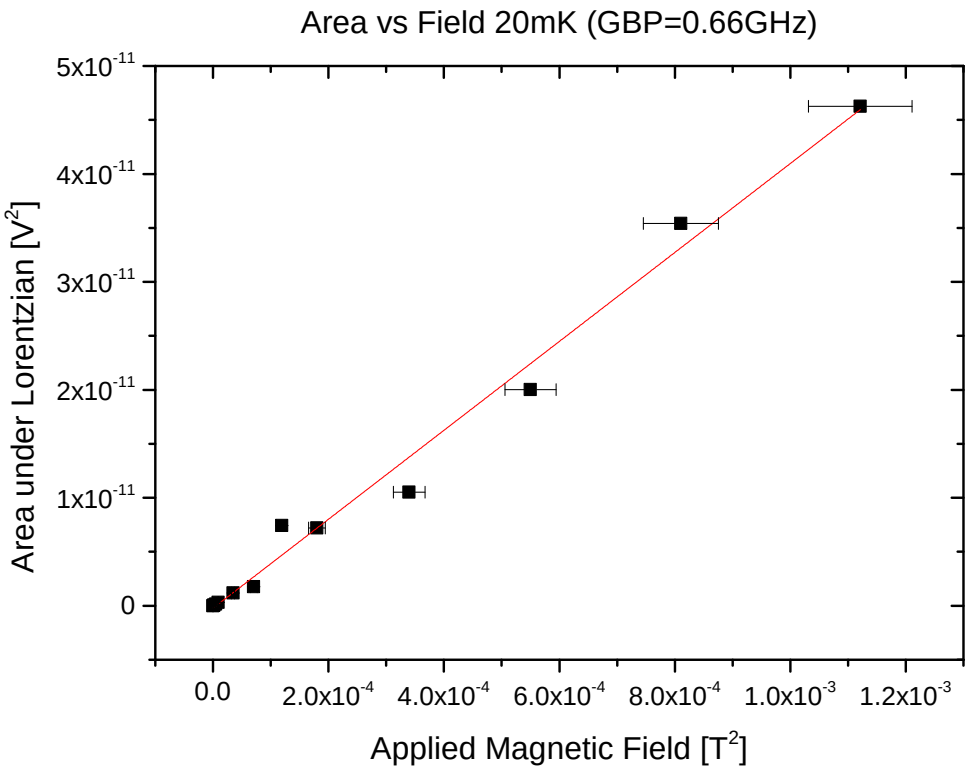

Figure 4.6: The field area relationship was shown to be quadratic, as expected. In this plot it is evident that at higher magnetic fields there is greater variation in the measured area.

4.1.3 Quality Factor Response

As discussed briefly in the previous subsection, the loaded Q-factor is described by:

$$\frac{1}{Q_l} = \frac{R_{\mathrm{bw}} L_{\mathrm{m}}}{\omega_0 L_i^2} + \frac{1}{Q} \tag{4.21}$$

which similarly to the area and frequency shift is proportional to the model inductance parameter for the NEMS, L_{m}.

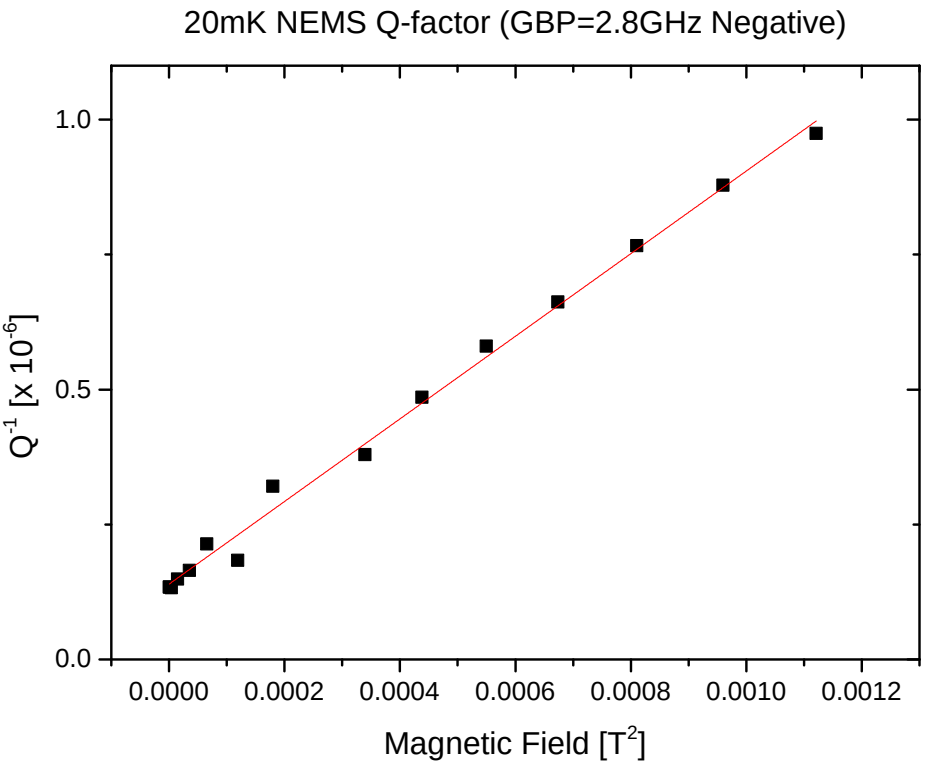

Figure 4.7: The inverse loaded Q-factor Q_l^{-1} plotted against applied magnetic field squared satisfies a linear relationship as predicted by eq. (4.21).

This makes the Q-factor proportional to B^2, so the sum effect of increasing magnetic field should shift the Lorentzian higher in frequency whilst increasing the area of the

peak, and broadening the width, given a constant drive power. This is demonstrated in fig. 4.2.

The Q-factor of the resonator was found to be as high as $Q_l \approx 7 \times 10^6$ at low fields and low temperatures, although the true unloaded Q-factor should be slightly higher than any measured value due to the loading by the magnetic field (Estimated at 7.2×10^6 from extrapolating to zero magnetic field). The consequences of this loaded Q were a sensitivity cost with increasing signal size. In order to obtain a strong output signal when the thermal drive power is minimal a larger magnetic field would have to be applied, increasing the linewidth of the resonator. Q-factors were not inherently important for the purposes of this project, but the possible applications of NEMS devices extend to high sensitivity sensing applications in which high Q-factors are desirable, such as mass sensing [74]. High Q-factors are also desirable in the field of quantum computing, where the lifetime of a state is tied to the Q-factor of its storage medium. One of the applications for a high-Q NEMS resonator would be such a component of a quantum computer [75].

The three behaviours described up to this point were characteristic of our setup, and as such the observation of these confirmed that the signal we were observing was indeed the resonator. However, these characteristics are not all independent of the SQUID bias settings. During the initial experiments it was discovered that different Gain Bandwidth Product (GBP) settings could illicit different patterns of behaviour from the NEMS, as well as changing the slope of the working point for the SQUID.

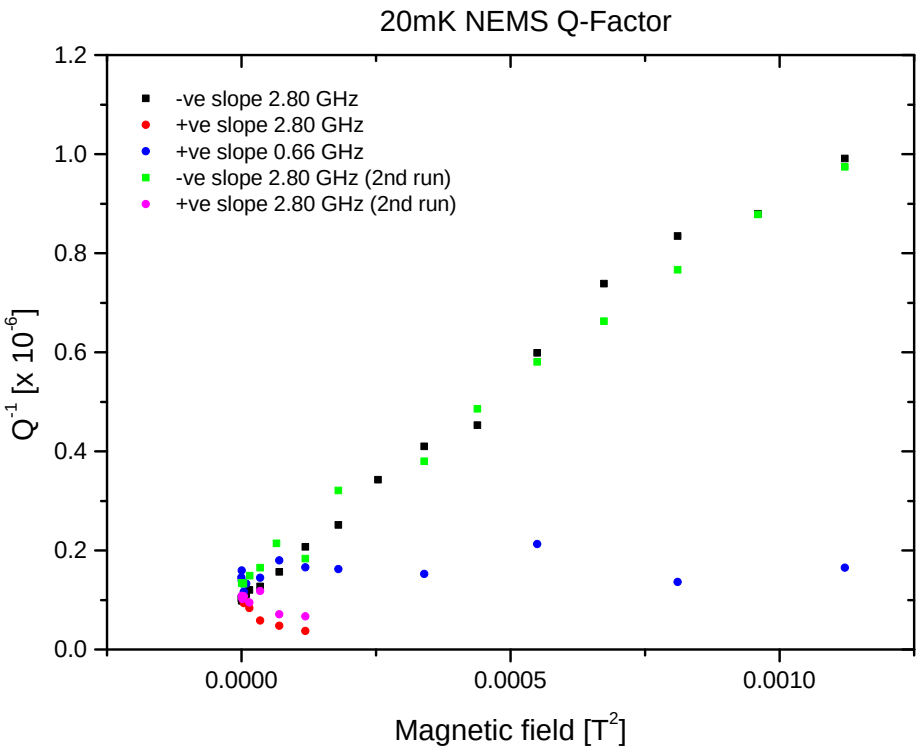

Figure 4.8: The inverse loaded Q-factor Q_l^{-1} plotted against applied magnetic field squared for varied SQUID bias conditions.

Figure 4.8 shows the effect on the resonator from changing SQUID bias conditions with increasing magnetic field. This plot only shows the GBP values that had the strongest and weakest effects. The three behaviours could initially be grouped into: no response to magnetic field (0.66 GHz Positive), expected response (2.80 GHz Negative) and opposite response (2.80 GHz Positive). These three behaviours are investigated in more depth in the following section, but are not observed for all modes. These features are not present in the data for the third and fifth mode, which instead follow the behaviours predicted by the model resonator.

The higher order modes are more difficult to detect in a magnetomotive scheme than

the first mode, as a consequence of the flux density 'cut' by the moving beam. For the same reasons that only the odd modes can be detected, the portion of the beam that generates a current for us to measure is reduced for each mode. In addition, the total energy in the resonator is the same for each mode and as such the power for beam displacement is split into the number of anti-nodes for a given mode. Eventually this means that we can only expect the third mode to generate at most one third of the noise power of the first mode, and then even less due to the lower displacement.

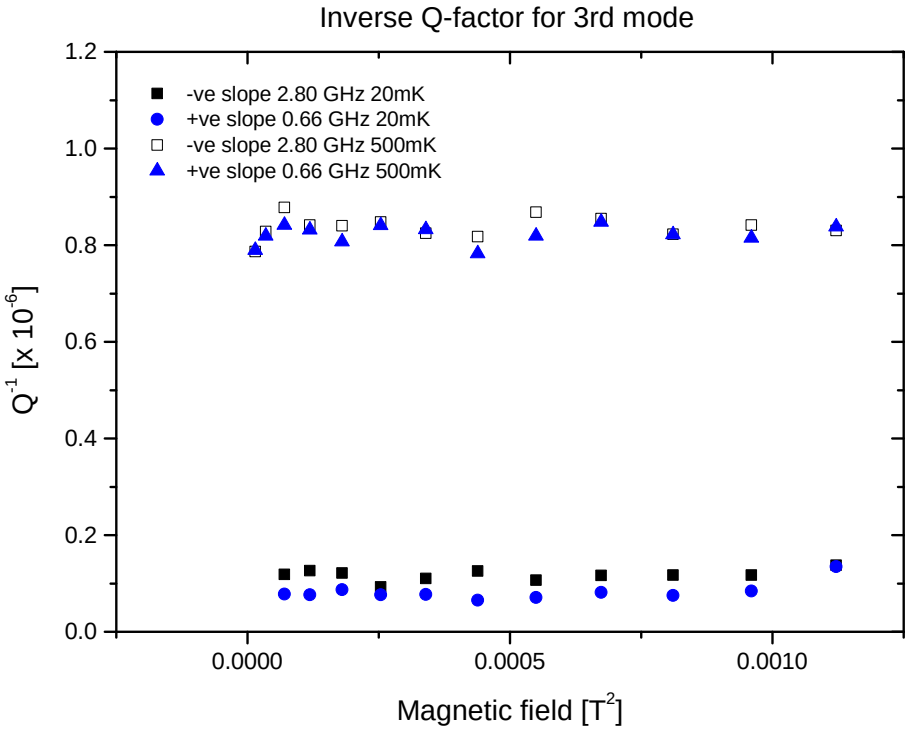

Figure 4.9: The inverse quality factor Q^{-1} of the third mode is not dependent on SQUID bias conditions and behaves as expected for a resonator of this type. This is also reproducible for the fifth mode. The third and fifth modes have much lower amplitudes than the first mode due to the portion of the beam moving in magnetic field that is detected.

4.2 SQUID NEMS Interaction

In the previous section the expected NEMS behaviour was described in terms of the resonant characteristics of the input circuit. It was indicated that there were emergent properties that were not expected, primarily affecting the behaviour of the loaded Q-factor Q^{-1}. It is the case that as the conducting body of metal atop the resonator moves through the applied magnetic field, the NEMS develops a voltage across it, which induces a current that flows through the SQUID input circuit. It is posited that a current flowing through the NEMS caused by interaction with the SQUID interacts with the magnetic field to develop a force against or in concert with the NEMS motion, which is a significant deviation from the initial theory. In this section the deviations from expected behaviour will be more fully detailed, followed by the model with which we have analysed this data. Conclusions about the nature of these deviations will be discussed in the last chapter of the thesis.

4.2.1 Observed Deviations from Theory

Previously it was demonstrated that the Q-factor behaviour with magnetic field was different to the expected behaviour, depending on the settings for the SQUID. The behaviour was previously classed as 'expected', 'no response' or 'opposite response' with respect to the behaviour predicted by theory. However, this description is not entirely accurate. When looking at the Q-factor of the resonator with different bias conditions it appears that the 'expected' Q_l^{-1} was greater than the predicted values with increasing magnetic field. There was a low field region where the responses did not differ. Figure 4.10 shows the behaviour of the Q-factor at low fields as being broadly the same before diverging above 10 mT. There is a clear mismatch between

the gradients of the two trends shown in this plot, and this in part speaks to the fact that in one regime the Q-factor increases (which is not expected) and in another it decreases but more rapidly with field than expected. The implications of this can be seen by recalling that the Q-factor is an expression of the energy lost per cycle for an oscillator. It would follow then that an increase in Q-factor indicates less energy being lost per cycle from the resonator. As there is no immediate source of energy other than the SQUID (as the thermal power has already been accounted for) then it follows that there is energy injected per cycle by the SQUID. By symmetry, in the opposite scenario where we should see a decrease in NEMS Q with field we can model that as a reduction (beyond the expected reduction) in energy per cycle.

It is instructive then to investigate the effects that this behaviour has on the integrated area under the lorentzian, which has been shown to indicate the noise power in the resonator.

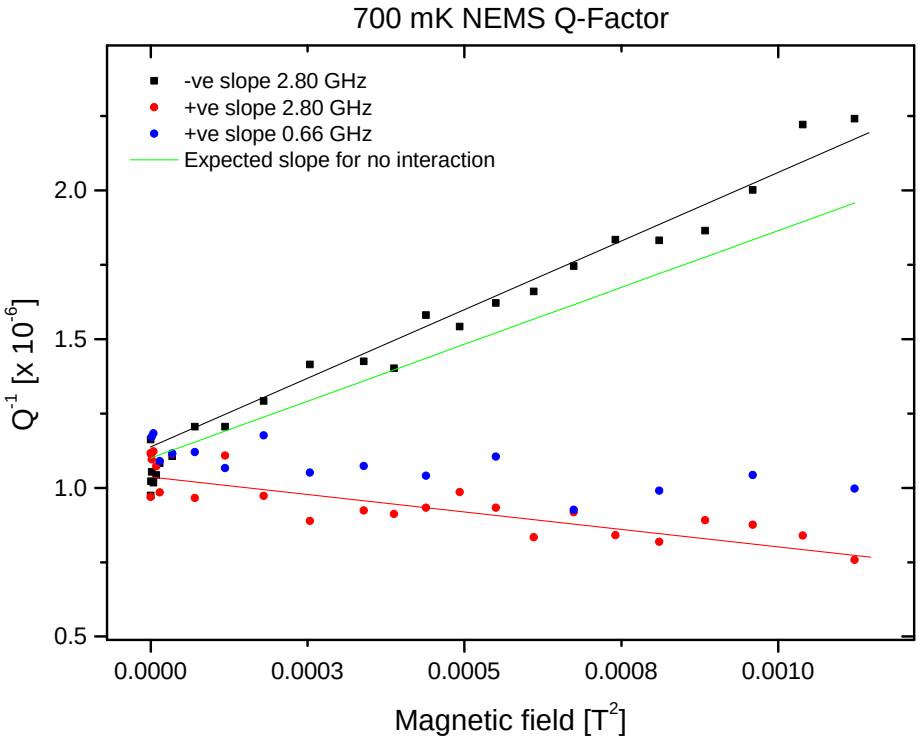

Figure 4.10: The inverse loaded Q (Q_l^{-1}) for 700 mK with different SQUID bias conditions. The red and black lines are a guide to the eye to illustrate the two differing SQUID-NEMS interactions, whilst the green line shows the expected slope for no interaction.

The area of the resonator should scale with power, but also scales with magnetic field squared (as previously shown). A relative increase or decrease in noise power with magnetic field then would present as a deviation from a linear relationship with B^2.

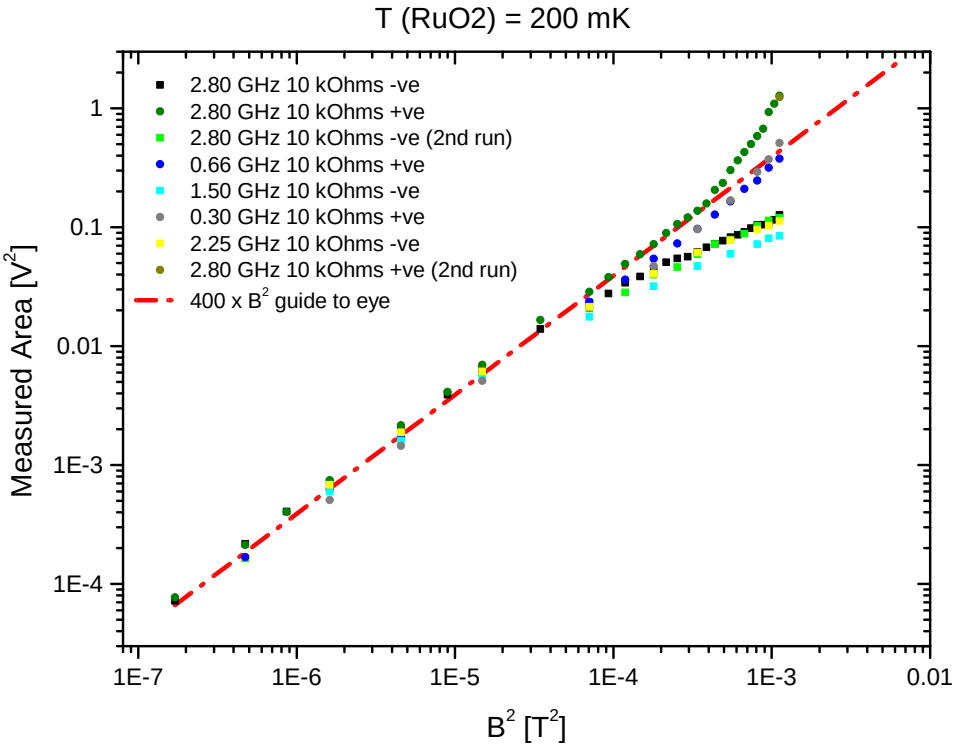

Figure 4.11: NEMS area with increasing magnetic field for different SQUID bias conditions, a guide to the eye line of B^2 with a shifted intercept is shown by a dashed red line.

Figure 4.11 demonstrates the deviations from the linear trend expected at fields above 10 mT. There is also demonstration that the behaviour that shows no Q-factor response also demonstrates the expected area-field proportionality. Data for 2.8 GHz GBP elicits the unexpected behaviour, and the slope of the working point selected then determines if the effect is increasing or decreasing the Q-factor. Data for the negative slope of 2.8 GHz peels away from the linear behaviour but then resumes a linear trend, implying that this effect reaches a limit quite quickly or that we lose sensitivity

to it. The data for the positive slope however appear to increase continuously. Both of these observed behaviours agree with the assertion that the behaviour of Q_l^{-1} is indicative of a change in the expected power in the resonator. It is interesting to note that as indicated in fig. 4.8 and fig. 4.10, the inverse loaded Q-factor Q_l^{-1} is tending towards zero in the 2.8 GHz positive slope regime. It is possible to cross this limit and observe the emergent behaviour, but this is reserved for a later section dealing with the resulting self-sustained oscillations. In this section we will consider only the data for the negative slope that implies a reduction of power.

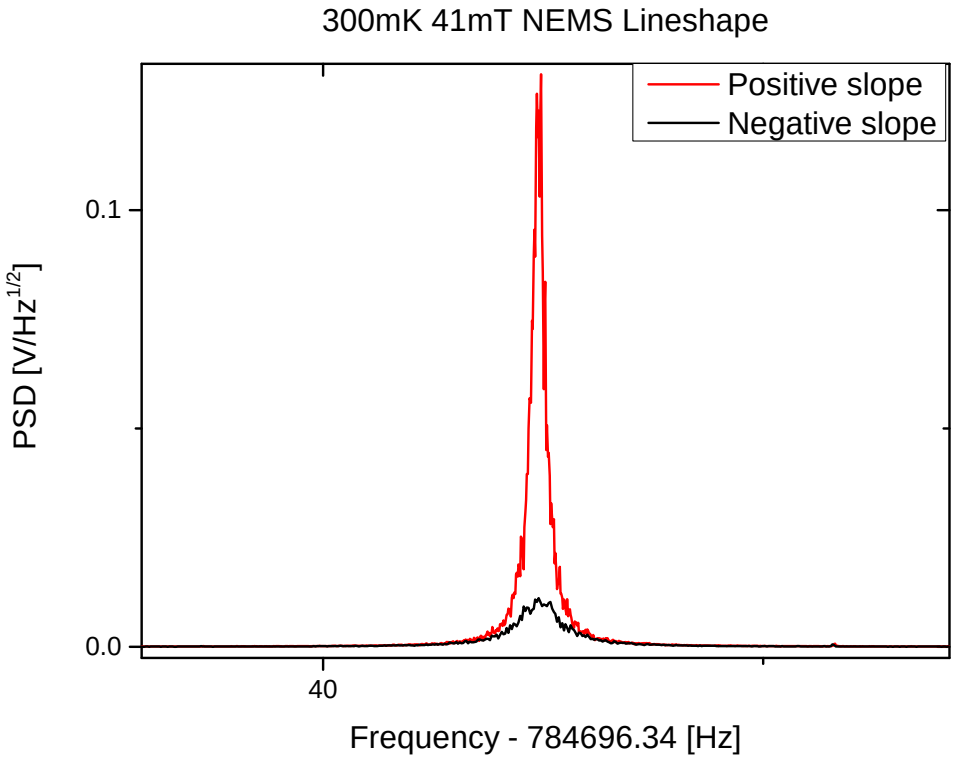

Figure 4.12: The NEMS lineshape change under different bias conditions at 2.8 GHz GBP.

As previously demonstrated in fig. 4.4, the frequency shift of the resonator is not affected by the changes in SQUID bias condition. This is to be expected, as the loaded

frequency is a function of the effective inductance which itself is only a function of field. It is worth noting that there is a weak temperature dependence to the frequency, but this shift is negligible over the ranges discussed here.

Figure 4.12 shows the net effects of the change between positive and negative slope for a field large enough for the effects to be present, but not so large that the resonator starts to self-oscillate. The area is larger under the positive slope data, and the Q is demonstrably larger. The curve for the negative data is much broader and the integrated area is less. Both curves are centered on the same frequency.

Having seen that there would seem to be control over mode power using bias conditions, the techniques described in section 3.5 were used to extract the effective temperature of the resonator on the negative slope.

Figure 4.13 shows the mode temperature T_{eff} for all temperatures that were studied, with increasing magnetic field. The implication from this data was that the SQUID interaction with the NEMS was extracting thermal energy from the mode, inducing effective cooling by large factors, typically by a factor of four. The plot does show that at reduced temperatures, the quality of the data decreases. This is due to a reduction of signal size when compared to the background noise level, and as such the error on the fitting parameters increases. Similarly the data at low fields is not as reliable as the data from high fields.

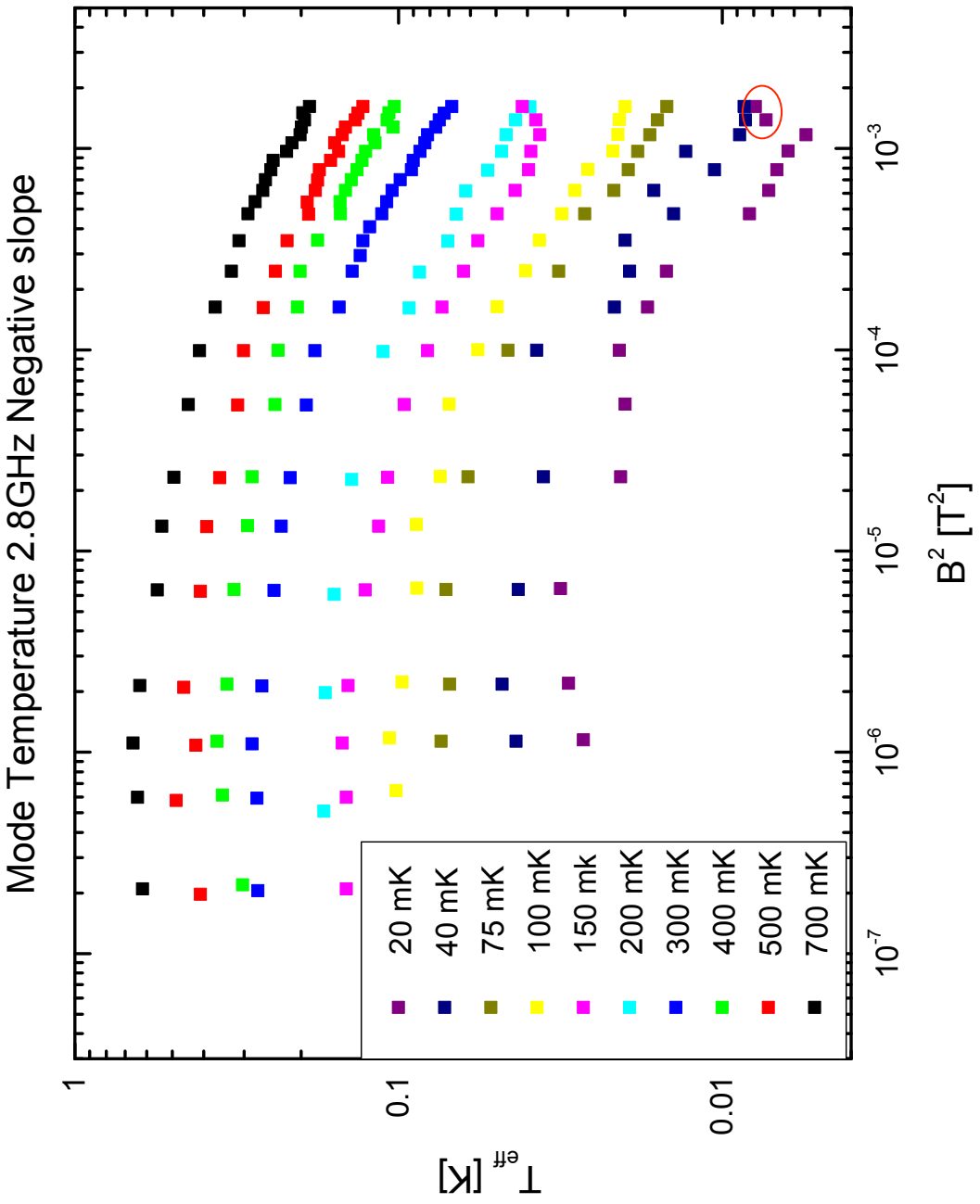

Figure 4.13: The effective temperature of the mode for the negative slope. The temperature of the mode is the same as the bond wire temperature at low fields, but drops as the field strength increases. The upturn as high field (red circle) for the low temperature data was found to be anomolous in further experiments (see fig. 4.15)

The curves for each temperature were similar enough that they could be collapsed to form a single curve, demonstrated in fig. 4.14.

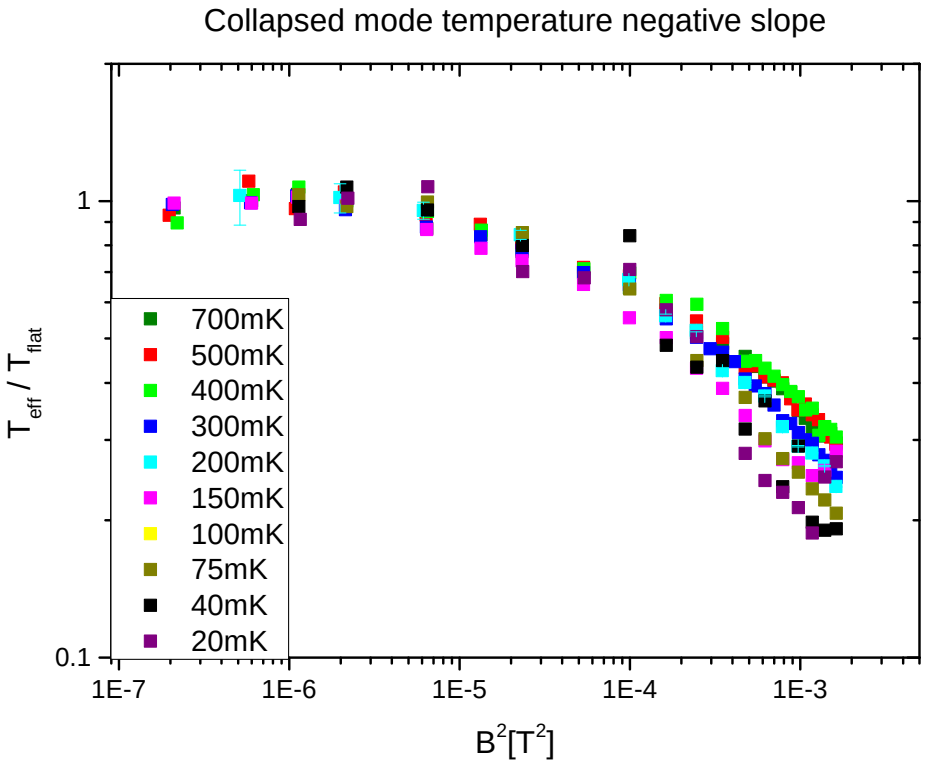

Figure 4.14: Mode temperature scaled by the mode temperature in low fields, T_{flat}. There is a self-similar curve at all temperatures observed, showing that to reach the lowest mode temperature it is necessary to reduce the initial temperature as much as possible.

This collapsed curve shows that the cooling factor is similar for all temperatures and so, to maximise the effect reducing the initial temperature is desirable. Following from these calculations it was decided to construct a smaller sized magnet that could achieve larger magnetic fields without disrupting SQUID performance, to allow investigation of any cooling limit there may be.

Figure 4.15 shows the data for the lowest attainable temperature and highest attainable magnetic fields for the negative slope. It is clear that there is a maximum cooling limit after which the mode temperature remains constant with magnetic field. The results shown here are promising as they indicate that there could be a method to cool the mode of a resonator without using additional refrigeration techniques. This would be useful in the case that a resonator has a frequency that forbids it from entering the quantum regime within the temperature ranges available to nuclear demagnetisation, but could be cooled further using this technique such that the quantum regime becomes achievable. These data suggest exciting physics discovered from a set of ex-

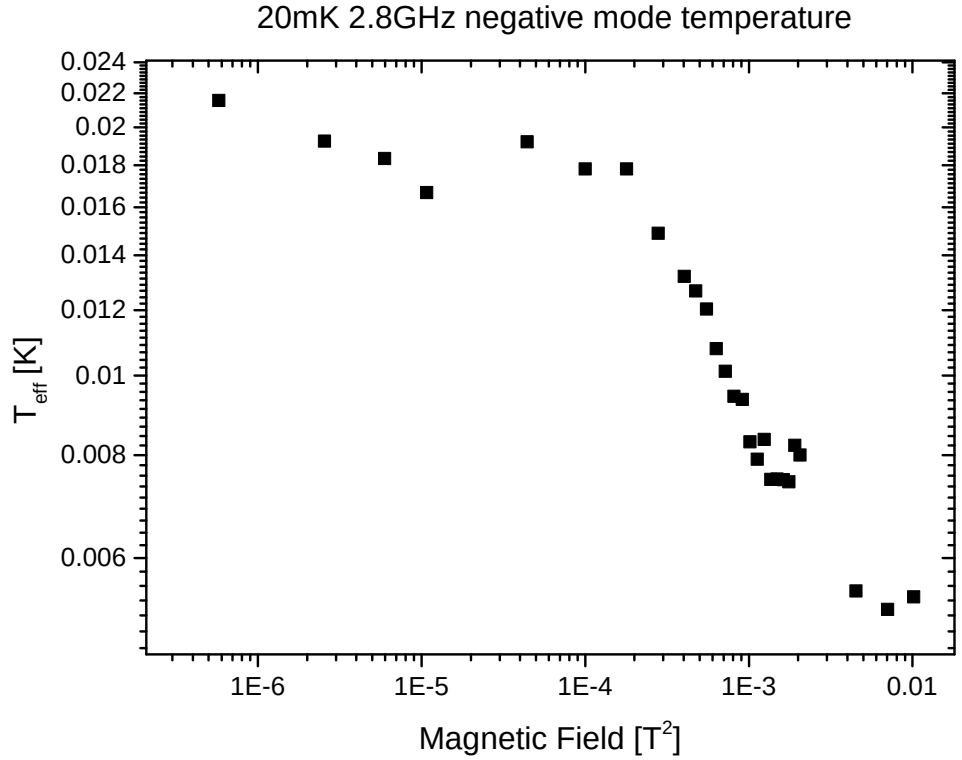

Figure 4.15: The attempt for maximum effective mode cooling using higher magnetic fields demonstrated that mode temperature reaches a minimum at high fields that is not reduced under increasing field.

periments initially planned for characterisation of the NEMS-SQUID experiment. In the next subsection we shall propose a theory developed by Dr C. Lusher for modelling this data, to investigate whether or not this can be treated as true mode cooling.

4.2.2 Theoretical Description

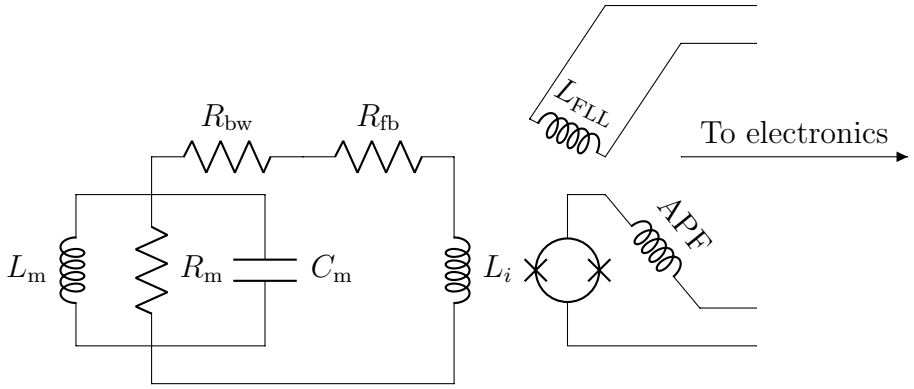

Figure 4.16: The complete model input circuit, here including the parts of the circuit implicated by changing gain bandwidth products, the FLL feedback inductor and the Additional Positive Feedback inductor. The functions of these components has been described in section 3.3.3. There is an additional resistance, R_{fb} that is introduced for modelling purposes, but does not represent a physical resistor. Its purpose is described in this section.

As in section 2.3 we model the NEMS as a parallel resonant circuit [76] with model circuit parameters denoted by subscript 'm'. L_i is the SQUID input inductance and L_{FLL} marks the feedback inductor which whilst not being directly included in calculations is important for the discussion. APF is the additional previous feedback inductor that was described in section 3.3.3 and is directly affected by changing working point slope, as such it is included here for later discussion. R_{bw} is the resistance of the bond wires between the superconductor and the NEMS, and R_{fb} is the 'feedback re-

sistance' that will be referred to in the model discussion, but is not a physical resistor.

In order to describe the model's development, we must consider the results from the experiment. The results described in the previous section are qualitatively consistent with feedback effects seen in other experiments, analagous to laser feedback methods [77, 78]. In these experiments a laser beam is used to feed a resonant frequency to the NEMS that is in or out of phase with the NEMS itself, thus driving or damping oscillation.

Backaction between a SQUID and its input circuit is not uncommon, and effects of this backaction on NEMS devices have been reported before [17]. When operating in the negative feedback mode, other experiments have observed effective cooling of the resonator mode [33]. This model was developed to investigate the possibility of backaction cooling as seen by Schwab *et al.*[28].

As described in the previous section, there was a decrease in noise power under certain bias conditions that could be construed as cooling via a reduction in mode power. It is accompanied by an increase in dissipation beyond what is expected. In our model this decrease in dissipation is characterised by an additional noiseless resistance in the input circuit which damps the resonator. This resistance is shown in fig. 4.16 as R_{fb}. It is important to note that this resistance is a model parameter and not a real resistance, and as such is modelled with a temperature of 0 Kelvin such that there is no Johnson-Nyquist noise generated by the component.

As derived in section 3.5 the thermally driven current in the input circuit in absence

of feedback can be described by:

$$\langle I_N^2 \rangle_\Sigma = \frac{\langle V_N^2 \rangle_\Sigma}{|Z_\Sigma|^2} \tag{4.22}$$

$$= \frac{4k_\mathrm{B}(T_\mathrm{bw}R_\mathrm{bw} + T_\mathrm{m}R_\mathrm{m}(\omega))}{|(R_\mathrm{bw} + R_\mathrm{m}(\omega)) + i\omega(L_i + L_\mathrm{m}(\omega))|^2} \tag{4.23}$$

From inspection, it is evident that the input circuit current noise consists (with frequency dependent scaling) of the noise of the NEMS, and the noise from the bond wires. The noise from the NEMS is dependent of the behaviour of $R(\omega)$.

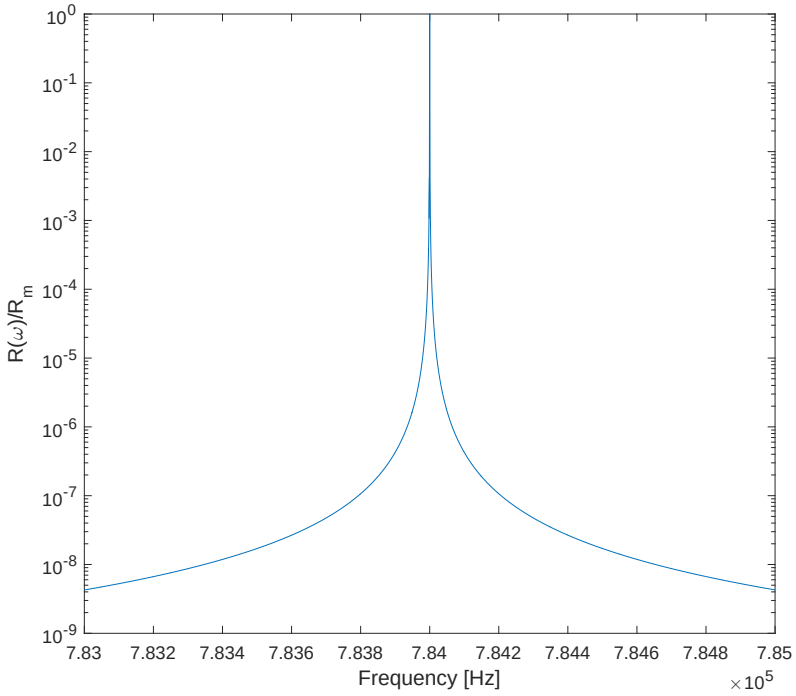

Figure 4.17: The frequency dependence of the NEMS model resistance, showing that as the loaded resonance moves away from the natural resonance the real component of the resistance reduces to many times less than the bond wire resistance ($\approx$ 80 mΩ).

Figure 4.17 shows the frequency dependence of the NEMS resistance relative to its

natural resonance (here modelled as approx. 784000 Hz). As the loaded NEMS frequency is shifted further away from the natural frequency, its resistance decreases. As the frequency of the NEMS is linearly dependent on B^2, there is then only a small range of field in which the NEMS resistance is larger than the bond wire resistance, and thus a region where we actually observe thermal noise power.

The derivation of the area under the lorentzian in the absence of feedback was performed in the previous section. Here we do the same but now assume that the NEMS and bond wires do not have the same temperature, such that the area can be expressed as a linear combination of the two noise terms:

$$\text{Area} = \frac{k_{\text{B}} L_m^2 Q_l}{\omega_0 L_i^4} \left\{ T_{\text{bath}} R_{\text{bw}} + T_{\text{eff}} \frac{\omega_0 L_i^2}{L_m Q_u} \right\} \tag{4.24}$$

This illustrates that as the magnetic field increases, the contribution of the noise power from the NEMS itself decreases whilst the contribution from the bond wires remains constant. For a NEMS at constant temperature equal to the bond wire temperature this comparative noise temperature contribution can be plotted using real data, as shown in fig. 4.18.

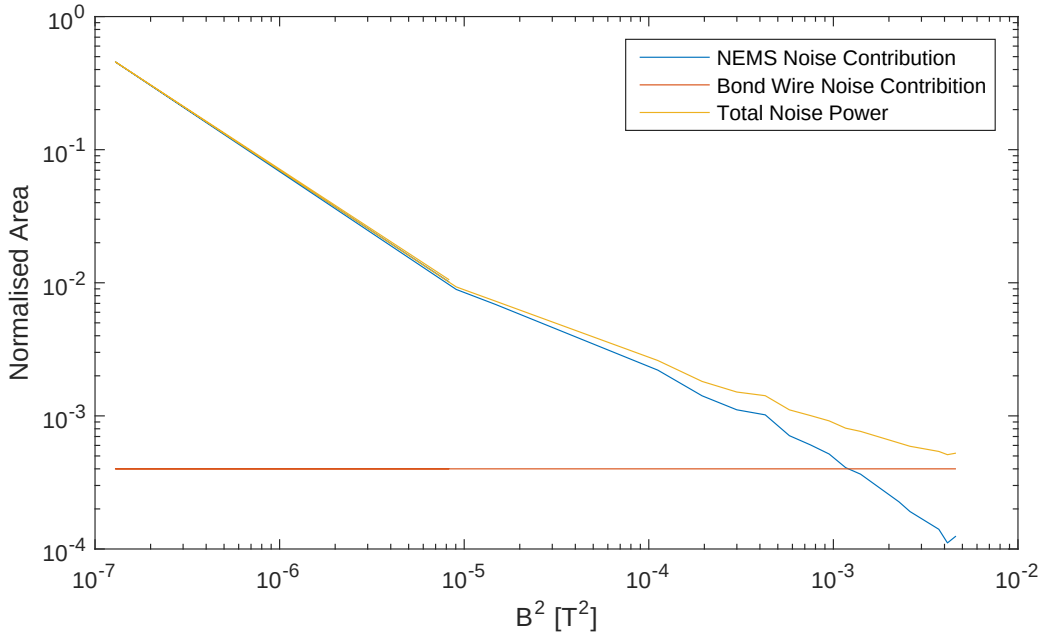

Figure 4.18: The contributions from the bond wires and the NEMS impedance to the total noise as a function of magnetic field at 20 mK using real data.

Figure 4.18 shows that the total noise power is in fact expected to decrease with increasing magnetic field for a given temperature. Furthermore, beyond $\approx$ 30 mT the contribution to the noise power from the NEMS is less than that of the bond wires, and so we cannot use any data above that field to calculate mode temperature. However, there are data that suggest it was possible to measure the NEMS at fields exceeding this limit. This is attributed to the NEMS 'shaping' the noise from the bond wires, acting as a bandpass filter with the NEMS' linewidth. Much as the input circuit has a natural bandwidth that is used to measure the noise temperature, the NEMS can be viewed as a very narrow bandpass filter at its loaded frequency ω_l. Because of this effect it was still possible to measure the properties of the beam after it was not possible to measure its thermal noise directly.

This model allowed us to predict the behaviour of the NEMS in absence of additional damping, such that we could determine whether or not there was evidence of mode cooling in the data.

The presence of a feedback effect would exhibit values for the area less than that of the predicted values. For the following analysis the expression for area was rearranged such that it was possible to plot the expected 'Scaled Area' in Ohms. Equation (4.25) shows the rearrangement before the effective temperature $T_{\rm eff}$ is set equal to the bond wire temperature $T_{\rm bw}$.

$$\text{Area}\frac{\omega_0 L_i^4}{k_{\rm B} L_m^2 Q_l} - T_{\rm bw} R_{\rm bw} = T_{\rm eff}\frac{\omega_0 L_i^2}{L_{\rm m} Q} \tag{4.25}$$

This serves to illustrate that if $T_{\rm eff} \neq T_{\rm bw}$ then the relationship:

$$\frac{\text{Area}}{T_{\rm bw}}\frac{\omega_0 L_i^4}{k_{\rm B} L_m^2 Q_l} - R_{\rm bw} = \frac{\omega_0 L_i^2}{L_{\rm m} Q} \tag{4.26}$$

will not hold. Instead the experimental scaled area data would be seen to deviate by decreasing more than the theoretical value calculated using eq. (4.26), and the fraction of the expected value here scales with the ratio of the bond wire temperature to the mode temperature.

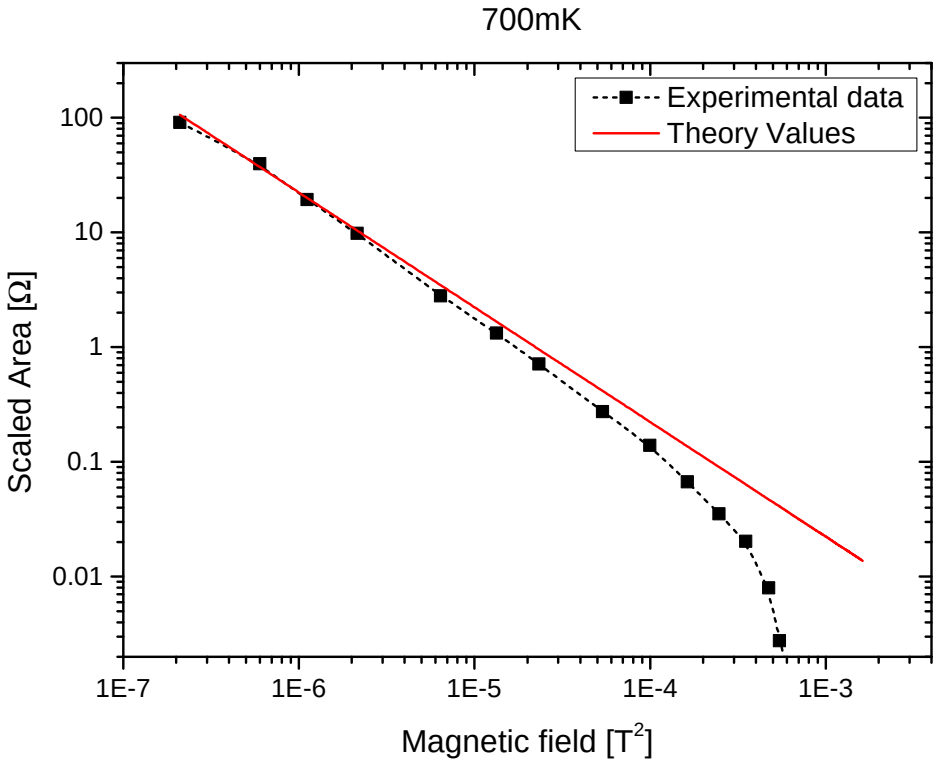

Figure 4.19: The theoretical (red) and experimental (black) scaled area as a function of magnetic field. At low magnetic fields there is agreement between theory and experiment, which is reflected in the data for inverse quality factor. At fields approaching 10 mT, however, the experimental data deviate from the theoretical line, indicating a reduction of noise power beyond that expected for the circuit.

Figure 4.19 is such a plot of the scaled area for theoretical and experimental data. The experimental data deviates from the theoretical data in such a way as to indicate mode cooling as previously described, showing that the mode temperature T_{eff} was less than the bond wire temperature T_{bw} at higher fields. It is important to consider the field limit in which the resonator mode temperature can still be accurately transduced due to the frequency dependence of the resistance described earlier in this section. Even excluding this field range as shown in fig. 4.20 there is still a degree of mode

cooling observed.

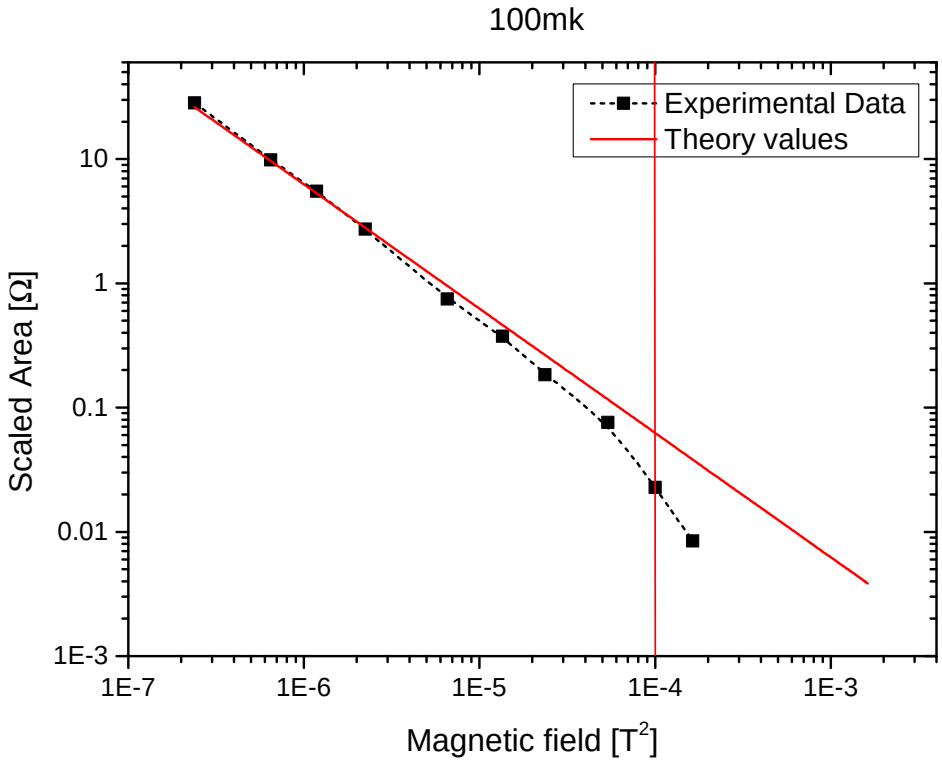

Figure 4.20: Theoretical (red) and experimental (black) scaled areas for 100 mK low fields. The red vertical line indicates the limit at which the NEMS is generating less than half the noise power in the circuit, and so the data above this limit is for the moment discarded.

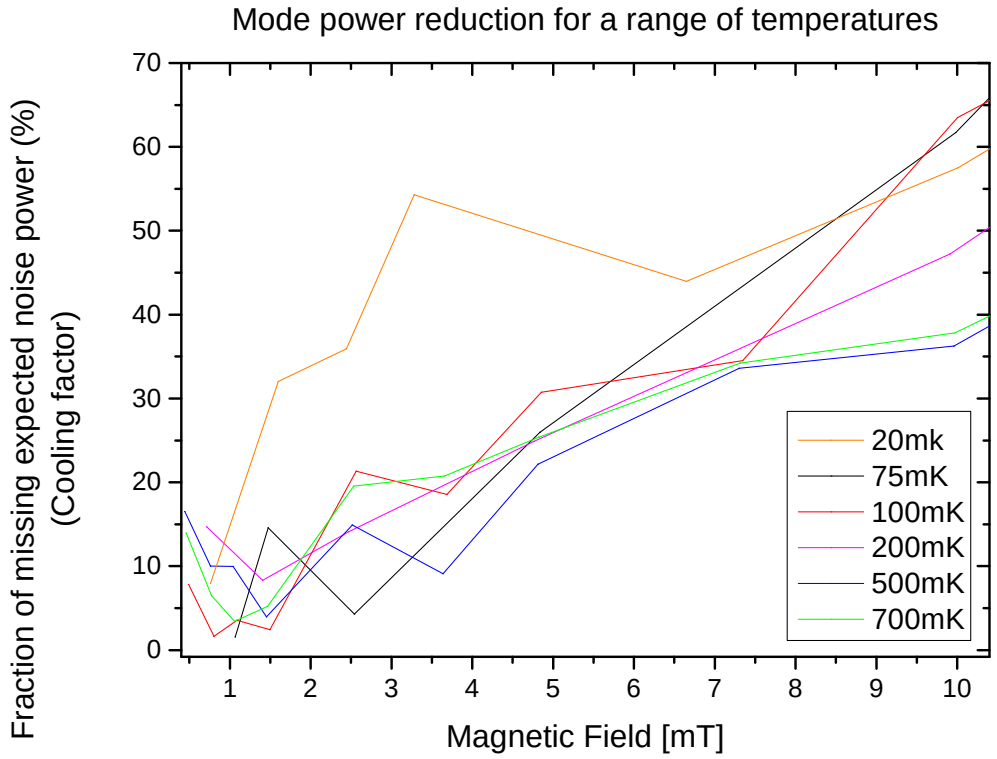

Figure 4.21: The difference in expected scaled area to observed, expressed as a percentage for a range of temperatures over the valid field range. This percentage can be considered a mode cooling factor and is shown to have a similar gradient at a range of temperatures.

Figure 4.21 shows the fraction of 'missing' noise power as a percentage of the expected scaled area (i.e. the difference between the experimental data and theory values in fig. 4.20) for a range of temperatures, which is equivalent to a mode cooling factor. The data for higher temperatures has much less scatter than the data for low temperatures and this is attributed to the difficulty of low temperature capture. The cooling factor is higher at lower temperatures, which is consistent with the model of an increasing resistance in series with the NEMS as modelled in fig. 4.16. This indicates that the circuit can be modelled as having an additional resistor that contributes no noise, but increases in resistance as magnetic field is applied such that the current in the input

circuit can be expressed as:

$$\langle I_N^2 \rangle_\Sigma = \frac{\langle V_N^2 \rangle_\Sigma}{|Z_\Sigma|^2} \tag{4.27}$$

$$= \frac{4k_\mathrm{B}(T_\mathrm{bw}R_\mathrm{bw} + T_\mathrm{m}R_\mathrm{m}(\omega))}{|(R_\mathrm{bw} + R_\mathrm{m}(\omega) + R_\mathrm{fb}(B)) + i\omega(L_i + L_\mathrm{m}(\omega))|^2} \tag{4.28}$$

where $R_\mathrm{fb}(B)$ is the field dependent feedback resistance that is considered to be at absolute zero, hence its exclusion from the numerator of eq. (4.28).

4.3 Self-Sustained Oscillations

In section 4.2 the nature of the relationship between the inverse Q-factor and magnetic field for different gain bandwidth products was described. Until now only the emergent increase in damping has been considered, now we turn to the reduction in damping with apparent increase in noise power.

It is helpful now to characterise the two behaviours as 'driving' or 'damping' where the damping behaviour reduces noise power and the driving behaviour increases it. As with the damping behaviour, the driving behaviour did not affect the loaded frequency ω_l, and its effects were not seen in the third or fifth mode. The driving behaviour increased the measured area under the lorentzian as well as driving the dissipation (inverse Q-factor Q^{-1}) towards zero. Once the dissipation was driven past zero the NEMS began to behave as though driven by a large external source and 'rang up' to a fixed amplitude.

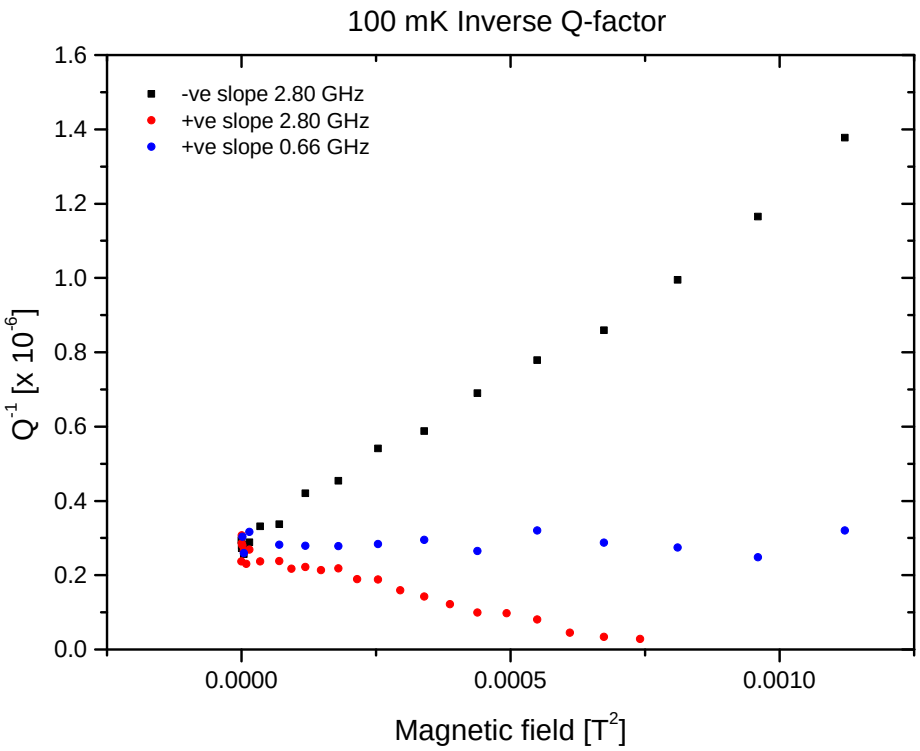

Figure 4.22: Dissipation for the positive slope of 2.80 GHz GBP (red) trends towards zero under increasing magnetic field. Close to zero applied magnetic field, it is possible to recover the intrinsic Q-factor of the device as the behaviours converge.

The dissipation for the resonator decreased under applied magnetic field for all temperatures. Figure 4.8 is a plot of the dissipation with increasing magnetic field that does not show values for the positive slope beyond 15 mT. This is because above these fields the resonator's behaviour was not measurable with the same scheme. Figure 4.22 is a similar plot but for a higher temperature where the intrinsic Q-factor is lower, thus creating a greater range over which to observe the measurable behaviour of the oscillator. This indicated that the immeasurable behaviour was limited not by frequency but by loaded Q-factor. At higher temperatures this behaviour did not occur and the dissipation did not cross through zero. To study this phenomenon in

detail the temperature was set to base (≈20 mK) such that the behaviour could be measured over a range of magnetic fields.

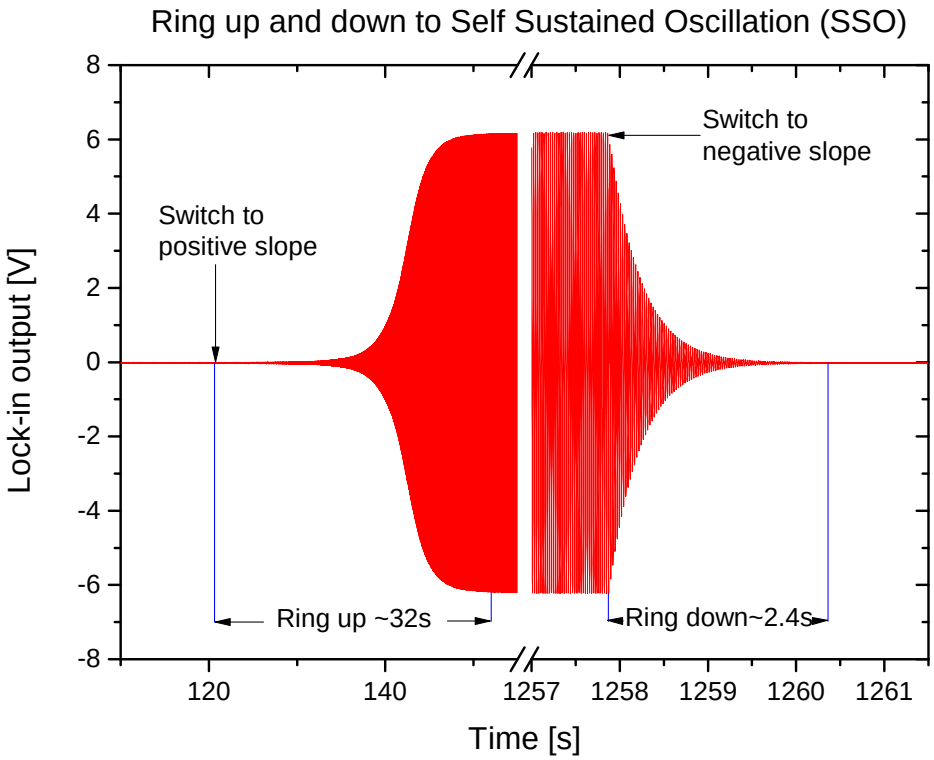

Figure 4.23: An example of a time-domain trace of the resonator's motion captured through a lock-in amplifier. The time axis has been truncated by removing the majority of the region where the behaviour was stable at constant amplitude and frequency. The time axis scale is also much smaller on the right hand side of the plot to ensure that the ring-down is visible, having a duration roughly ten times less than the ring up. Annotated are the points at which the SQUID bias conditions were changed from the damping to driven behaviours.

This strange behaviour shows strong similarities to self sustained oscillations (SSO), which have been observed in other experiments using SQUIDs [32], but also when using a laser drive [77]. Figure 4.23 is an example of the ring-up and ring-down from the SSO behaviour. The amplitude of this effect compared with thermal motion is

evident in that the gain settings on the lock-in amplifier had to be adjusted such that the thermal motion was not detectable. The change in Q-factor between the positive and negative slopes of the 2.90 GHz GBP is substantiated by the difference between the ring-up duration and the ring-down, with the former being roughly ten times longer. The section of data cut out of the plot is of uniform amplitude and frequency, and there is no frequency change between the two behaviours.

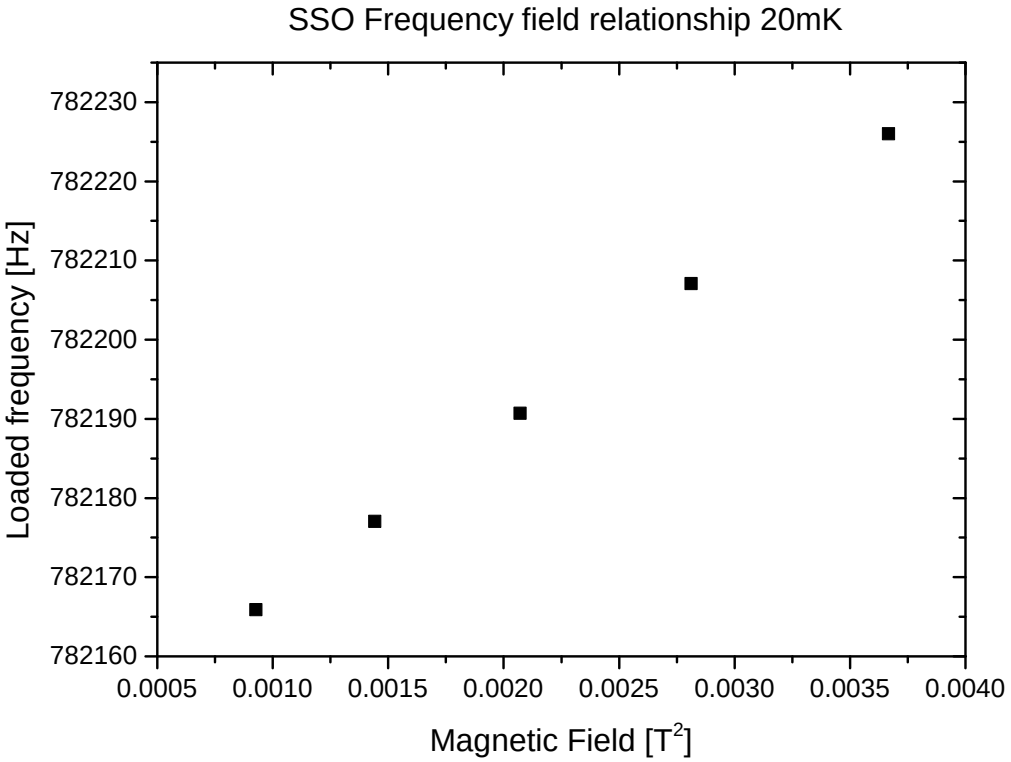

Figure 4.24: Frequency field relationship for the NEMS in self sustained oscillation, maintaining the linear relationship with field squared expected for the input circuit.

Figure 4.24 demonstrates that the SSO behaviour does not affect the frequency field relationship of the NEMS as is the case with the damping behaviour. Due to the amplitude of the signal it was not possible to obtain a meaningful fit to the lorentzian,

hence removing our direct ability to measure the Q-factor. In order to obtain these measurements time-domain traces were recorded and sections of it fitted to a sinusoid yielding a frequency and amplitude.

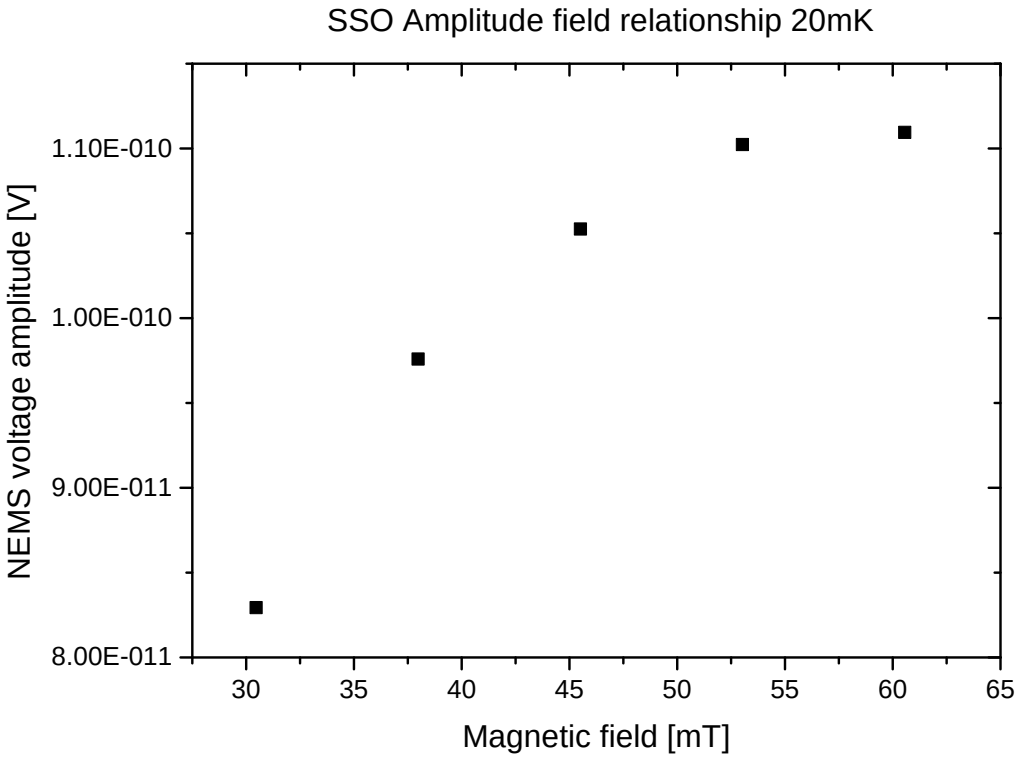

Figure 4.25: Amplitude field relationship for SSO behaviour. The amplitude seems to saturate approaching the maximum accessible field.

The amplitude however did not behave linearly with magnetic field but instead appeared to approach saturation at high fields. This is demonstrated in fig. 4.25 where the amplitude of the oscillations does not increase much above 110 pV. The highest magnetic field measured was 60 mT, at which point the SQUID was no longer able to hold lock due to the NEMS behaviour. This is assumed as this problem did not present for other gain bandwidth products, thus it is unknown if the behaviour continued and it was simply not possible to measure it.

To investigate the stability of the SSO the in-phase and quadrature responses of the SSO were recorded through a lock-in amplifier and then analysed by using a computational band-pass filter to remove harmonic distortion added by the amplifiers on the two channels. Then the two responses were plotted against each other, and an ellipticity correction applied to restore the original signal. Finally, the responses were manipulated by applying a rotation described by:

$$X_i = x_i \cos(2\pi f t_i) + y_i i \sin(2\pi f t_i) \tag{4.29}$$

$$Y_i = y_i \cos(2\pi f t_i) - x_i i \sin(2\pi f t_i) \tag{4.30}$$

Where x_i, y_i are the raw data for in-phase and quadrature respectively, X_i, Y_i are the rotated data, f is the frequency of the SSO and t_i is the time index. This rotation transforms the data such that it can be plotted on an amplitude-phase diagram where the distance from the origin represents the amplitude of the signal and the rotation about the origin represents the phase. On such a plot, a completely stable frequency source would be represented by a singular point displaced from the origin by the amplitude of the signal. Figure 4.26 is an example of the result of these calculations, where it is plotted for the entire length of the time trace unlike fig. 4.23. This plot shows the switch from negative slope to positive, whereupon the phase and amplitude increase rapidly. Once the NEMS has reached maximum amplitude the phase drifts slowly in the opposite direction to its rapid increase during ring up. It does this in a uniform fashion for roughly 200 seconds before beginning a period of erratic change during which the direction of phase drift does not remain constant. Upon ring-down, the phase rotates rapidly in the same direction as it had during ring-up.

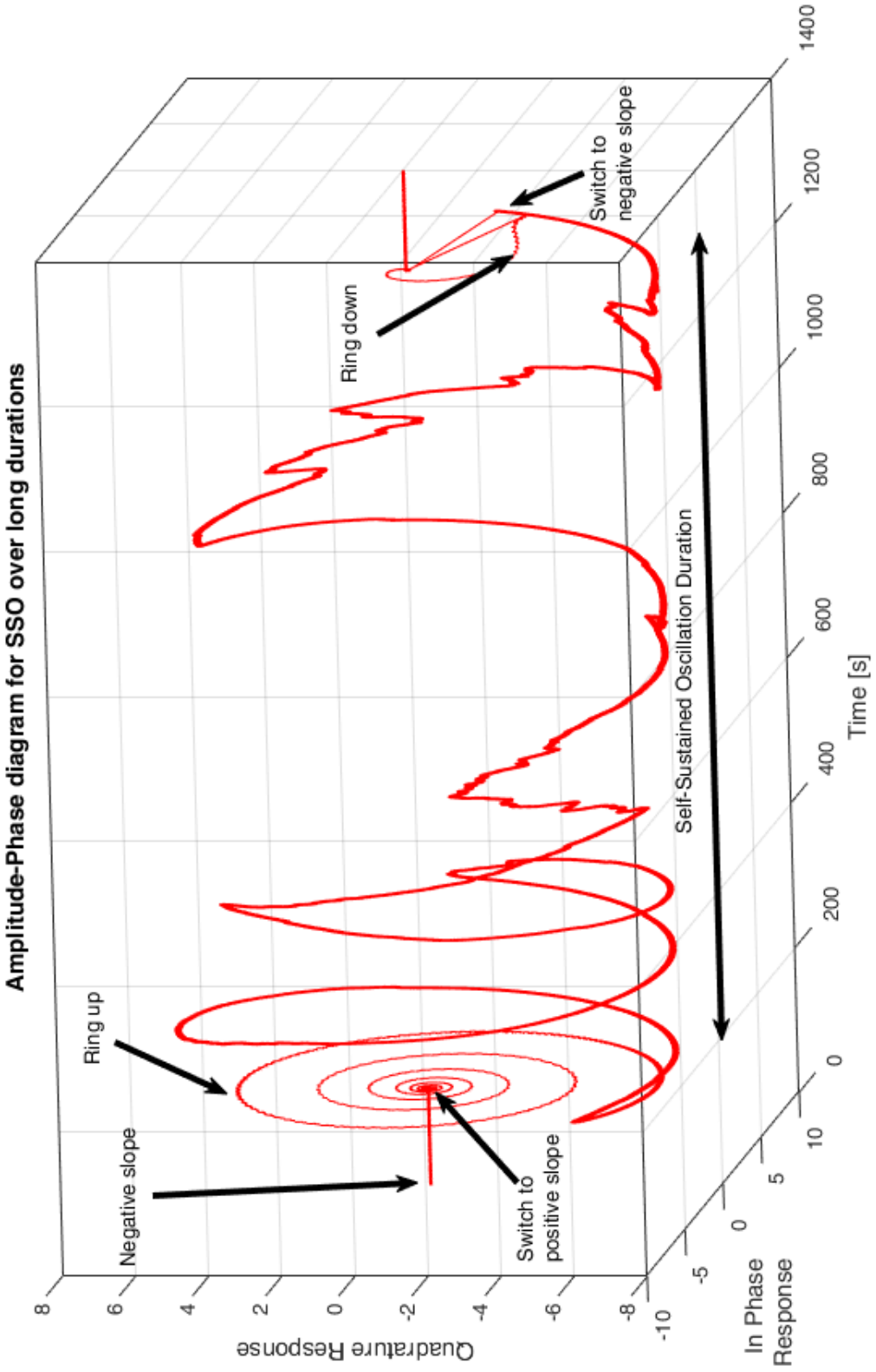

Figure 4.26: Amplitude-Phase plot of the Self Sustained Oscillations (SSO) over the course of a measurement, showing ring up and ring down.

This phase instability implicates SSO as seen by De Alba *et al.* [79] which also describes a drifting of the frequency once exhibiting self-sustained oscillation. It was not possible to replicate their entrainment however, as there was no readily available way to couple a weak pilot signal without overdriving the SQUID input. The instan-

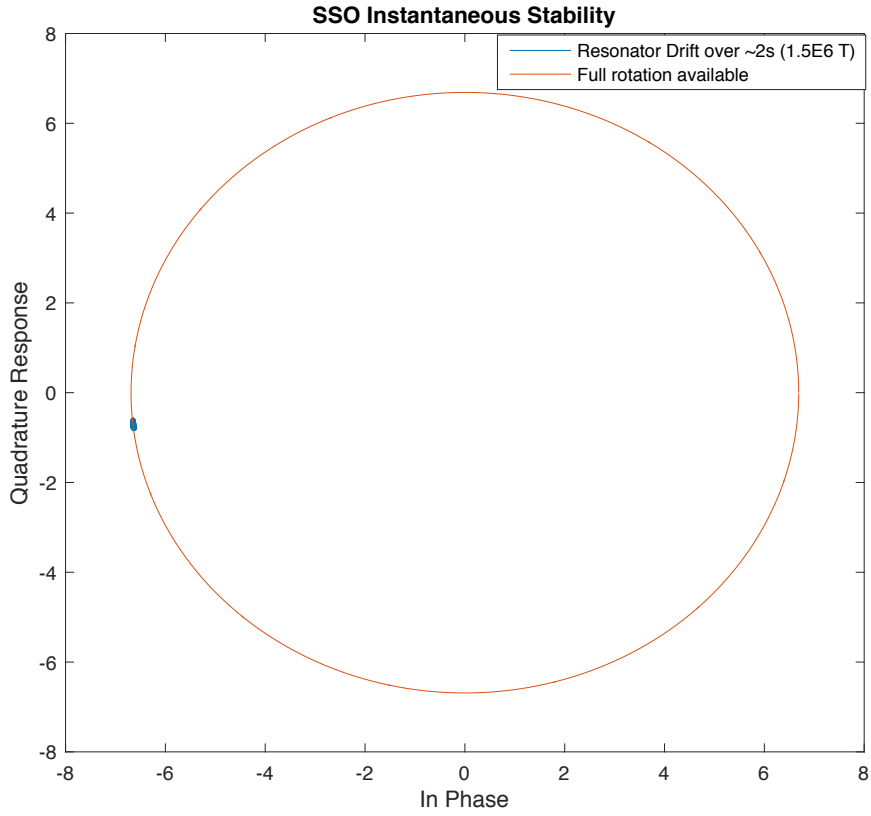

Figure 4.27: Amplitude-phase plot for SSO over a 2s period, equating to roughly 1.5×10^6 cycles. Over this period, the resonator does not deviate significantly. This small drift is equivalent to an instantaneous stability of 3.6 ppb.

taneous stability of the resonator can be calculated by comparing the frequency drift to the period of the NEMS, and this gives a stability of 3.6 ppb at the lower fields and therefore lower Q-factors. This should not be taken as the absolute stability, but

as an indicator of how stable this signal could become if entrained to a pilot signal.

4.4 Discussion

The behaviour of the NEMS under both sets of SQUID conditions must be a product of the same phenomena, which cannot be explained using a model resistor without making the assumption of negative resistance. Therefore instead we use a model current source that has sinusoidal current that is in-phase or anti-phase to the NEMS depending on SQUID parameters.

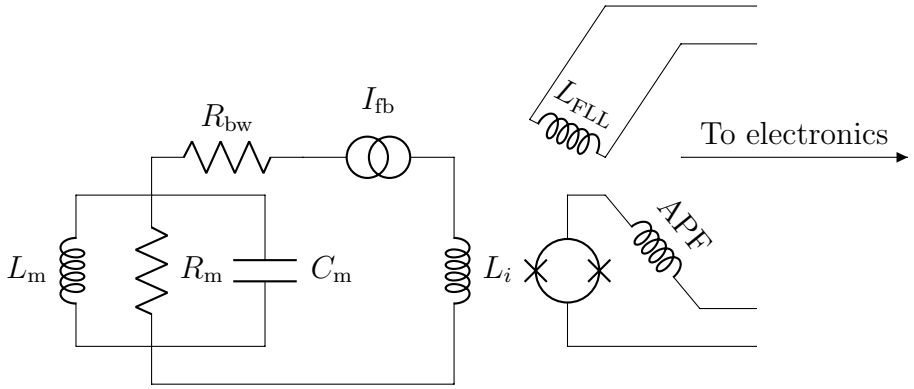

Figure 4.28: An adjusted feedback model circuit now including a current source I_{fb} instead of the model resistor R_{fb} from earlier.

Figure 4.28 illustrates the amended circuit with a current source replacing the noiseless resistor. This is a qualitative model that attempts to explain the nature of the interaction between the NEMS and the SQUID but is not yet capable of fully describing all of the effects. The summary of the effects seen are:

- 1st mode Q-factor dependence on gain bandwidth product.
- 1st mode Q-factor dependence on working point selected.

- The nature of the Q-factor dependence on gain bandwidth product is reversed by changing working point.
- Noise power for the first mode reduction for 2.80 GHz negative GBP.
- Equivalent noise power increase for 2.80 GHz positive GBP.
- Dissipation can be driven through zero, leading to self-sustained oscillations.

4.4.1 GBP Interaction

To explain these effects we must examine the nature of the SQUID FLL electronics more carefully. As described in section 3.3.3 the GBP controls the effective bandwidth of the FLL circuit by changing the capacitance value of the integrator, but this does not affect the input circuit bandwidth, meaning the noise spectrum truly incident on the SQUID is unknown to us outside of the FLL bandwidth. Within this bandwidth, the FLL circuit works to null flux at the SQUID. The SQUID chip is designed such that there is minimal coupling between the FLL inductor and the input inductor, but both are well coupled to the SQUID. It is feasible that a coupling of the input inductor to the FLL inductor (possibly via the SQUID) could present as an apparent current source in the input circuit. Such a current's spectral profile would be dependent upon the GBP selected which would go some way towards explaining the GBP dependence of the effect. This would predict that there should be a frequency dependence of the effect on GBP which is hard to confirm without resonators of different frequencies to study. However without further mechanism this should not be dependent on the working point selected for the SQUID, as this should only change the direction of current flowing through the sensing SQUID for a given polarity on incident flux.

It is now important to consider what the implications are to changing the SQUID working point. The act of changing working point alters the slope of the V-ϕ characteristic that the SQUID is biased on. This has two immediate effects on the SQUID: the transfer coefficient will change sign, and the value of the transfer coefficient decreases by roughly a factor of four due to the asymmetry of the V-ϕ characteristic caused by the additional positive feedback coil. The SQUID chip however has two stages, so the sign of the transfer coefficient of the sensing SQUID should only affect the phase of the flux incident on the second stage SQUID array. This phase change must be accounted for, either by changing the working point of the second stage or by introducing a phase shift in the feedback circuit, otherwise the FLL circuit would not function.

4.4.2 APF Interaction with Flux-Locked Loop

We now consider the Additional Positive Feedback (APF) components of the SQUID and define an arbitrary direction of flux that we call 'positive', which is important for the discussion of the APF coil. As previously mentioned the APF coil has the end result of acting like a noiseless amplifier on the output of the sensing SQUID. It does this by using the change of current in the SQUID to generate additional positive flux at the SQUID. This additional flux adds to the positive incident flux on the SQUID, increasing the transfer coefficient which results in the asymmetric V-ϕ characteristic of the first stage of the SQUID. The effect of the APF coil not only causes the positive slope to be steeper, but the negative slope to be shallower as the added positive flux will reduce the overall flux incident on the SQUID if the initial incident flux was negative. This change in the transfer coefficient is a product of the change in

direction of current flowing in the APF coil, which is itself the consequence of changing working point slope. The FLL circuit in fact works to eliminate the resultant flux at the SQUID which includes the additional APF flux. If there is a coupling between the FFL or APF coils to the input inductor, then this would complete the list of observed effects where the phase and amplitude of the interference between the SQUID and NEMS is dependent on the range of frequencies the SQUID is exposed to, and the selection of the SQUID working point.

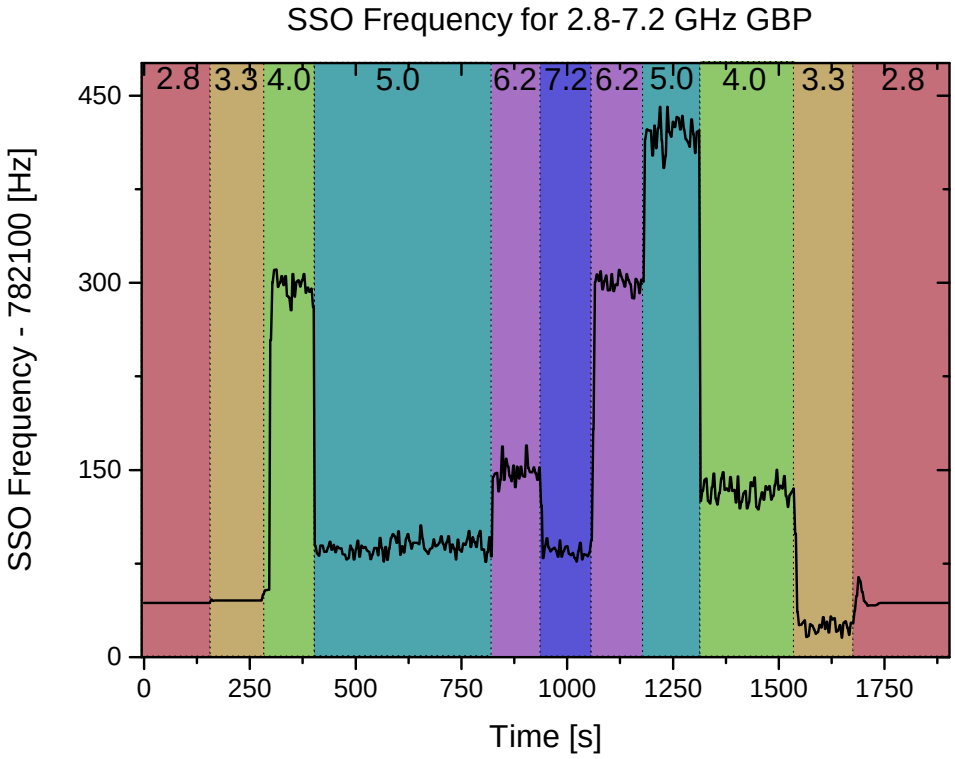

Figure 4.29: The behaviour of the NEMS frequency has been seen to be independent of GBP for non-SSO regimes, but here is seen to deviate significantly during SSO. This plot shows the behaviour of the NEMS frequency as a function of time, and the coloured boxes denote the gain bandwith product selected (which is written at the top of the plot).

This qualitative theory is supported by GBP dependence of SSO frequency demonstrated in fig. 4.29. This data was taken by using an HP counter to record the period of the oscillation fed into it via a lock-in amplifier such that the frequency is close to zero to increase resolution. There is no discernable pattern to the frequency behaviour apart from only 2.80 GHz is stable and consistent, whilst all other settings are unstable and unpredictable. There is perhaps evidence of hysteretic behaviour whilst the GBP is being reduced (Time $\approx$ 1000 s and greater) whereupon the frequency of the SSO increases in steps until 5.0 GHz, and then goes back to unpredictable behaviour. This hysteresis is consistent with the idea of a Duffing oscillator (briefly mentioned in section 2.2) which would be expected for a resonator being driven at maximum amplitude.

Chapter 5

Development of an Ultra-Low Temperature Environment

One of the primary uses of resonators on small length scales has been to probe the properties of liquid helium. In order to perform experiments of this nature, we needed to create an environment in which the resonator is submerged in helium at low temperatures, and to ensure that all the components are thermalised to the helium in the cell.

There are a number of requirements for the cell that can be broken down into five key features; modularity, screening from noise, thermalisation, efficiency and flexibility.

Modularity In order to make the electrical connections to the chip, the component the chip is attached to must fit into a wire bonder. For a cell with no capacity to hold helium this is a requirement that is easily met - these types of enclosure need nothing more than a pair of well positioned electrical contacts to fulfil their purpose. Such a cell design was used in the previous experiments purely in vacuum. For a cell

that must contain liquid helium, however, this raises the complication of thermally grounded but electrically isolated contacts, as well as low temperature seals and fill lines. These features are rarely compact and must interface intimately with the cryostat, and as such they are usually not convenient to remove. To this end the cell will have a modular design, whereby the parts of the cell that perform the sealing, screening and electrical feed-throughs are made separate to the chip holder. This allows the chip holder to be de-mounted and used in a wire bonder without disrupting the complex components of the cell.

Screening To prevent radio-frequency noise delivering thermal power to the chip the cell enclosure must be properly screened. This is done for the most part by creating a conducting metal enclosure and using a metallic vacuum seal. However there are routes into the enclosure that cannot be fully conducting, for example the route into the cell carrying liquid helium and the electrical lines. This is solved through two methods; insulating but RF-tight epoxy, and sintered silver. The former involves mixing copper powder with an epoxy, which is best suited for vacuum-tight seals such as feed-throughs for wiring. The metal fragments suspended within the epoxy filter high frequencies by capacitive coupling, and via eddy current dissipation [80]. The latter is not vacuum-tight, which makes it ideal for helium fill lines, taking the form of heat exchangers along the path of the helium from room temperature to the cell. The silver sinter acts as a conducting 'wall' through which is reflective to high frequency radiation, but allows the passage of matter.

Thermalisation The NEMS itself must be thermalised to the fridge stage for successful measurements. This is achieved by using liquid helium as the thermal link between the stage and the chip. When immersing the resonator in helium, this thermalisation is achieved through exchanges between the resonator and the helium directly. However, in vacuum the thermal ground for the NEMS is the electrical contact to the SQUID. In both cases the helium itself needs to be strongly thermally linked to the fridge stage, and this is achieved with a large volume sintered silver heat exchanger. The thermalisation of the NEMS in vacuum is achieved using electrical contact pads that have sintered silver packed onto them, in a separate enclosure. This allows the pads to be thermalised to helium whilst the NEMS is in vacuum.

Efficiency The cell is designed to use liquid helium, but the less bulk helium in the cell the less thermalisation we need to achieve thermal equilibrium between the helium and the fridge. To optimise this, the enclosures must have a low volume compared to the surface area of the heat exchangers. This presents a challenge in the cylindrical form factor defined by the magnet shields, and so the main enclosure contains a displacer, which is there to reduce the helium volume in the cell.

Flexibility The cell must be compatible with the existing structures on two nuclear demagnetisation cryostats; ND2 and ND4. ND4 at the time of writing does not have a demagnetisation stage fitted, and as such there are additional parts made for the test runs on ND4 that will not be used on ND2. The cell must also be able to function both in vacuum and filled with helium on the same run. That is to say that it should

not be the case that in order to change the nature of the experiment, we have to make physical changes to the cell structure. There should also be flexibility in the driving options for the resonator, so there should be ample electrical access and space for a piezo shaker.

On ND2 (Nuclear Demagnetisation cyrostat 2), magnets are required to have superconducting shields, which will prevent the field extending to other experiments on the nearby stages. The size of these shields is preset, to an outer diameter of 35 mm. In order to fit the cell onto the fridge, the magnet and cell must both fit into this shield. The length of the shield is not preset, so we have selected a magnet length of 10 cm. This should allow enough length to create a field that is uniform over the length of the resonator, whilst maintaining a compact form factor.

The cell consists of six components: the magnet, base, lid, displacer, heat exchanger, and sample holder. The intent behind the design is to allow re-use of the more complex components without arduous dismounting from the cryostat. As such, the cell base and heat exchanger are the only two parts designed to interface with the nuclear stage plate.

5.1 Ultra-Low Temperature Immersion Cell

The form factor of the cell needs to be cylindrical, to be able to fit into a magnet which can fit onto the nuclear stage of ND2. The chip itself must be held in the centre of the magnetic field, so the chip holder takes the form of a half cylinder with a recessed groove for the chip to sit in. The other half of the cylinder is designed to fill as much volume as possible whilst also providing a protective shield when the cell is open to atmosphere.

The internal structure of the chip holder consists of recessed pockets and connecting channels of 2 mm diameter. The pockets are designed in such a way that they can be filled with a sintered 'plug', that itself is electrically isolated from the copper body of the chip holder and forms a leak-tight seal between the channels within the chip holder and the vacuum space that the NEMS occupies.

The volume of the sinter pockets is determined by the desired ratio of thermal resistance between the gold bond wires and the sinter pad. We can relate the expression for the electrical conductivity of a material to the thermal conductivity, using the Wiedemann-Franz-Lorenz law. First, we define the electrical conductivity:

$$\sigma = \frac{l}{RA} \tag{5.1}$$

where σ is the conductivity, R is the resistance, A is the cross-sectional area of the conductor and l is the length of the conductor.

Then define an expression for the thermal conductivity, κ, using the Wiedemann-

Franz-Lorenz law to relate the thermal and electrical conductivities:

$$\kappa = \sigma L_N T \tag{5.2}$$

where T is the temperature of the conductor, and $L_N \approx 2.44 \times 10^{-8} \mathrm{V}^2/\mathrm{K}^2$ is a constant [81]. Combining these allows us to calculate the thermal resistance from the electrical properties:

$$\kappa = \frac{l L_N T}{RA} \tag{5.3}$$

$$\rho = \frac{1}{\kappa} = \frac{RA}{l L_N T} \tag{5.4}$$

The electrical resistance of the gold bond wires from the previous experiment is already known to be 20 mΩ. The bond wire length, l_1 was 5 mm, we shall assume 7 mm as worst case length for the new cell, l_2. Using these variables it is possible to arrive at an expression for the thermal resistance, R_k:

$$R_k = \frac{R A_1 l_2}{l_1 L_N \Delta T A_2} \tag{5.5}$$

Using a temperature of 1 mK across the bond wire, we arrive at a thermal resistance of $\approx 585 \times 10^6$ K/M. We aim to make the thermal resistance of the sinter plugs an order of magnitude less than that of the bond wires.

Pobell [40] cites a thermal resistance for silver sinter of $AR_k \approx 10^7$ K/M at 1 mK. The cross-sectional area of the sinter plugs is 8.8357×10^{-6} m^2, given a density of 10 g/cm^3. Knowing the cross-sectional area and the thermal resistance allows us to

calculate the maximum depth of the sinter plugs to be 5.65 mm.

The structure of the sinter plugs is such that there is a solid high-purity silver face and core, onto which silver powder is pressed to form sinter.

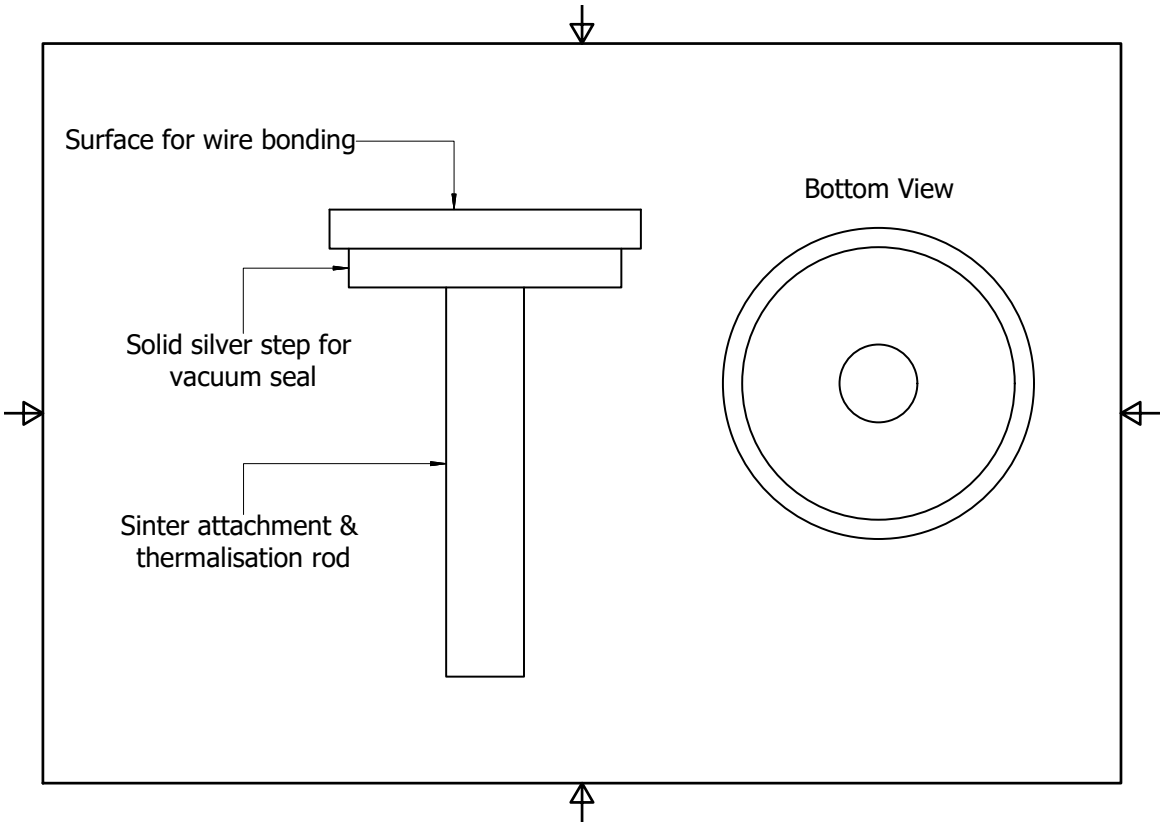

Figure 5.1: Features of the sinter plugs, showing the 'pin' used to attach the sintered silver, and the step that forms part of the seal described in fig. 5.5.

Gold bond wires were used between the NEMS and the sinter plug for the purpose of thermalisation and so we chose a material that has no superconducting phase. There is no advantage in a good thermal link between the sinter plugs and electrical lines from the SQUID, and thus aluminium bond wires were installed leading from the sinter pads to the niobium tracks used to electrically connect the SQUID to the NEMS.

The surface of the plug is coated in gold, for the purpose of preventing contact resistance between aluminium bond wires and the silver body.

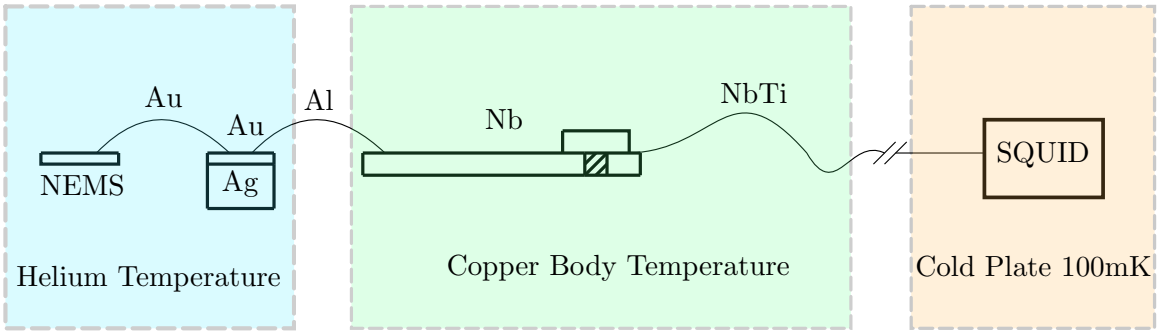

Figure 5.2: The thermal path for the cell wiring, from the SQUID mounted on the cold plate to the cell on the nuclear stage.

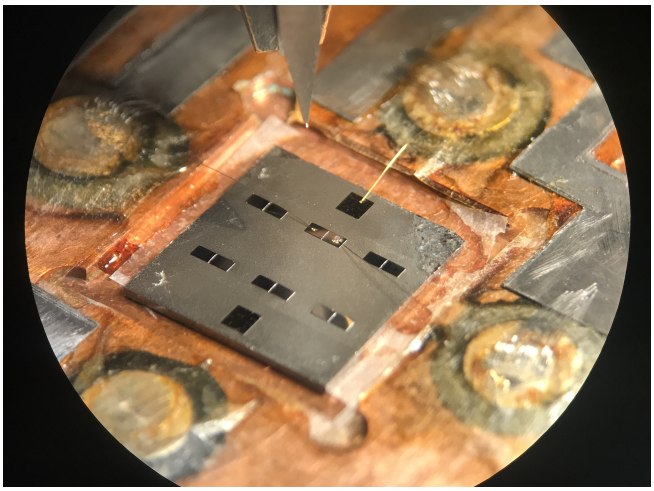

Figure 5.3: The NEMS chip in situ, showing the gold bond wires to the sinter plugs, and aluminium contacts to the niobium tracks.

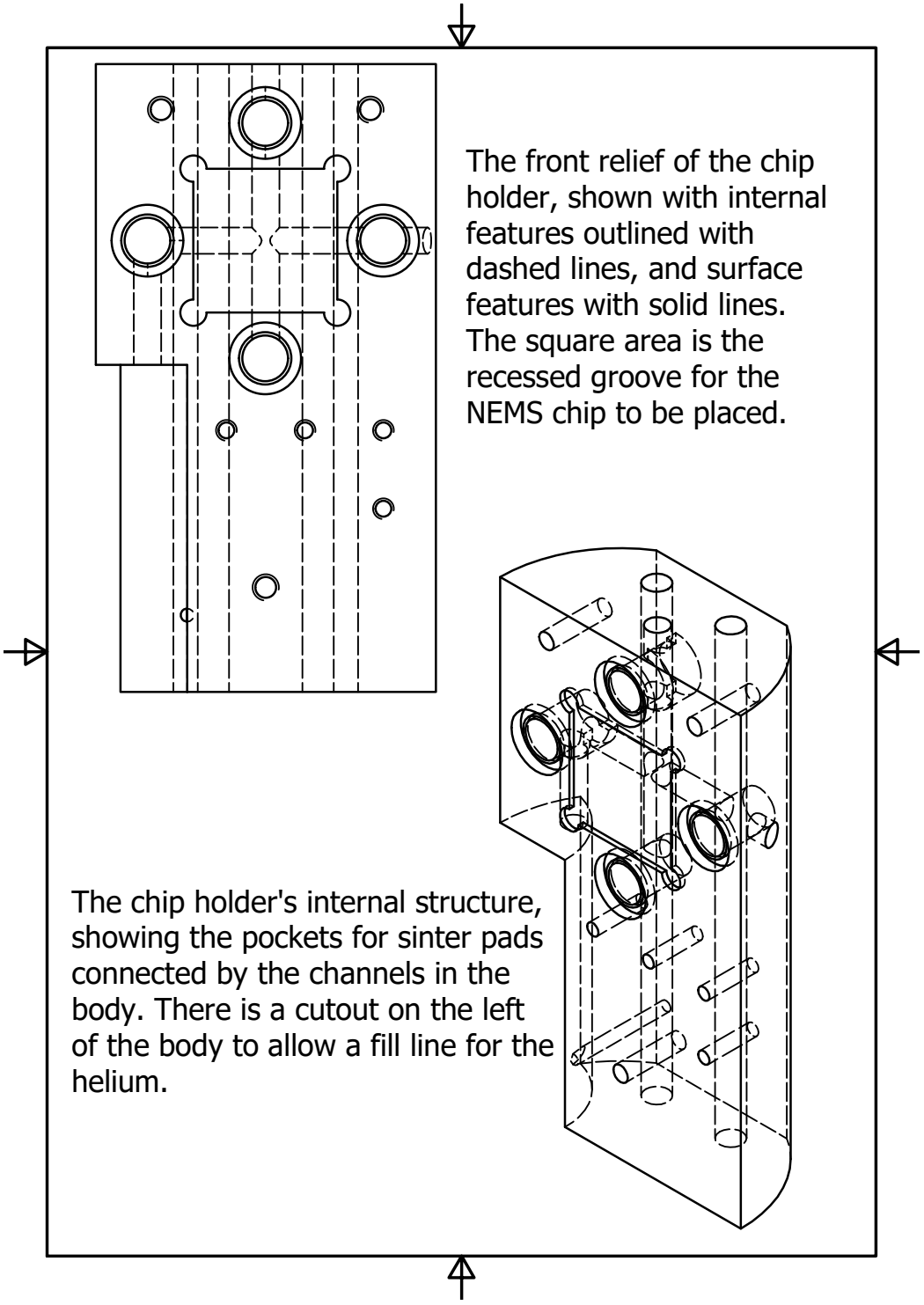

Figure 5.4: Schematic diagram of the chip holder.

Once the sinter plugs were fabricated, they needed to be electrically isolated from the copper body of the chip holder. This insulation must also form part of the vacuum seal around the plug, and must be resistant to both normal gas and superfluid leaks.

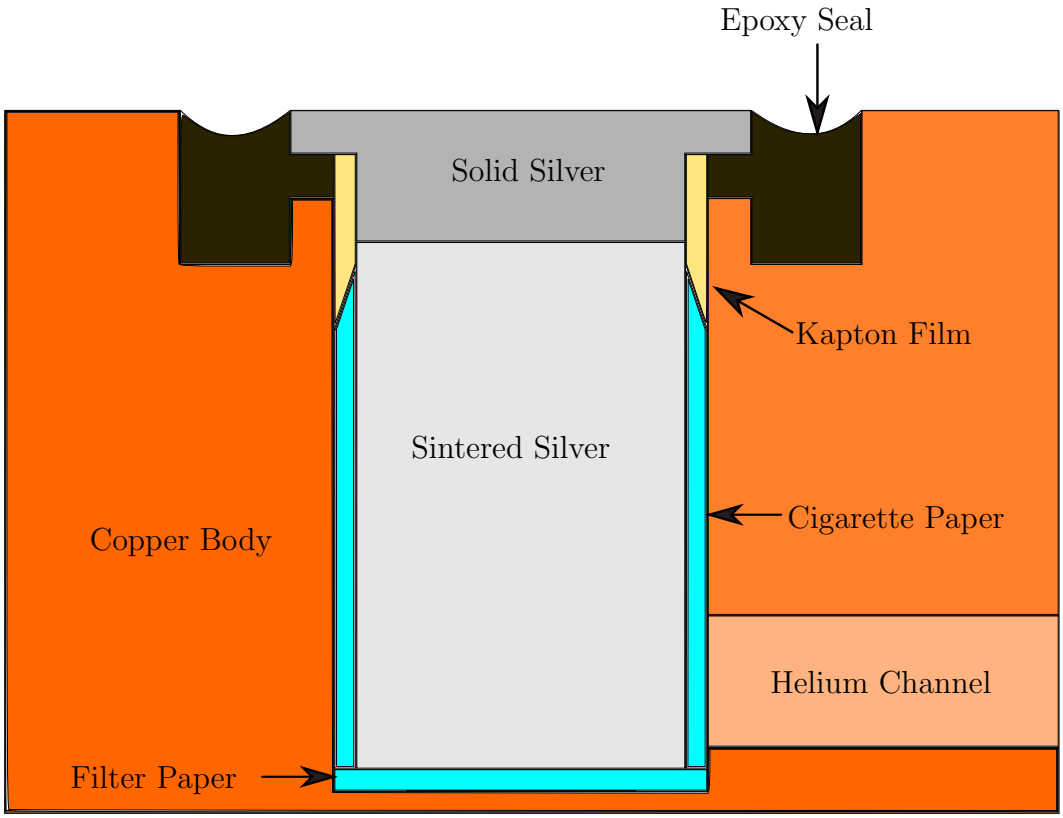

Figure 5.5: Schematic of the electrical isolation and vacuum seal on the sinter plugs (not to scale).

The insulation depicted in fig. 5.5 consists of three components. The topmost layer of insulation is a ring of Kapton film, carefully placed so as to be one layer thick and overlapping the solid silver and the start of the sintered silver parts of the plug. When the plug is inserted, this film is squeezed between the solid silver and the sinter, creating a weak liquid-resistant barrier but also insulating the plug. The second component is a layer of cigarette paper, this time between 1-2 layers thick, wrapped

around the rest of the sintered section of the plug. Cigarette paper is used because it is permeable to helium, and will not create a seal over the helium channels - a problem that we had encountered in earlier fabrication attempts. The third component is a disk of filter paper, pushed down into the base of the pocket. This forms the final insulating component, and accounts for any differential thermal contractions that may move the plug up and down, creating an electrical short.

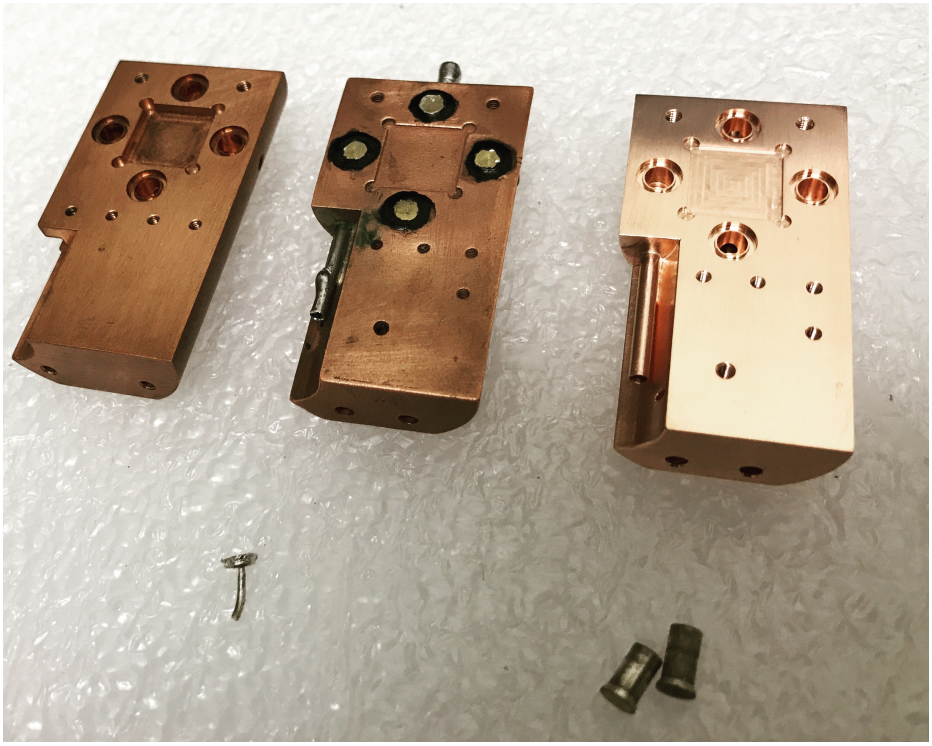

Figure 5.6: The three build attempts of the chip holder, the successful build is the furthest right. Visible is the new copper fill line that replaces the copper-nickel line originally used, which was added to allow vacuum brazing.

During the fabrication of this component, the design was altered significantly to resolve issues that arose in early attempts. Figure 5.6 shows the first three attempts, showing the changes primarily to the fill line placement and material. Not shown ei-

ther in the drawings or photographs are the small grooves tooled into the sinter pocket walls, placed to prevent the cigarette paper forming a liquid resistant seal around the sinter plug.

5.2 NEMS Cell Main Superfluid Heat Exchanger

Having designed the sintered electrical contacts for the chip holder, there was now a route to thermally link the NEMS to some helium, without immersion. The next stage was to control the temperature of that helium, and for that a thermal path from the helium to the copper of the fridge stage was needed. For this, we designed a large sintered heat exchanger that is designed to sit next to the immersion cell.

At ultra-low temperatures the thermal conductivity of most materials used in cryogenics drops dramatically [40]. However, the thermal conductivity of ^{3}He starts to increase in the low temperature limit, as shown in fig. 5.7.

There is, however, an acoustic mismatch between liquid helium and solids at low temperatures, which heavily impedes phonon transmission between the two materials. The arising thermal boundary is referred to as the Kapitza Resistance [40, 84], and is heavily dependent on temperature, as:

$$R_k \propto \frac{1}{AT^3} \tag{5.6}$$

where R_k is the thermal boundary resistance, T is temperature, and A is the area of contact. The sinter provides a large contact area for a small volume - reducing the

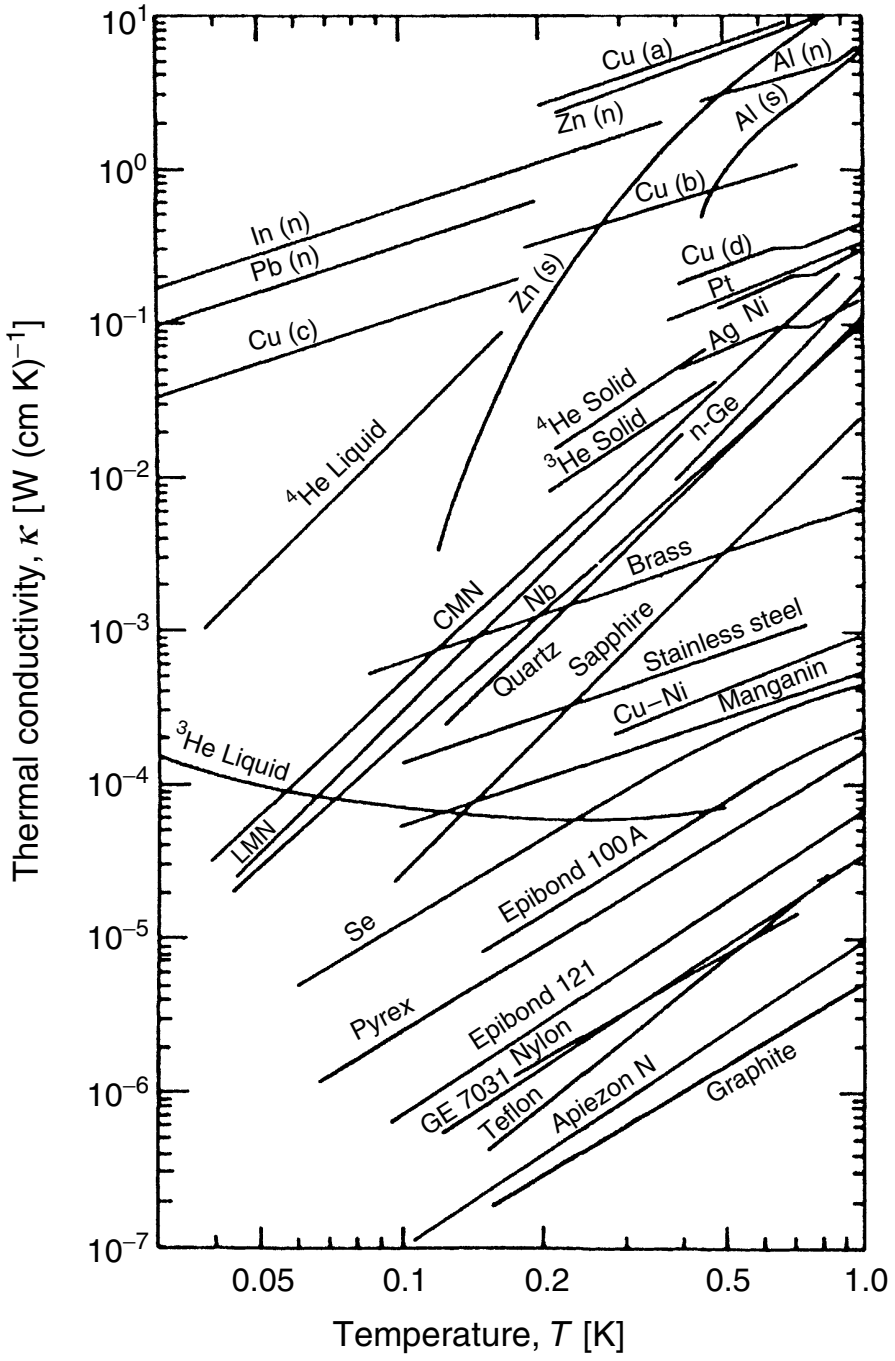

Figure 5.7: Thermal conductivities of common materials below 1 K, demonstrating the increasing thermal conductivity of ^{3}He at very low temperatures due to the high conductivity of the Fermi fluid [82, 83].

thermal resistance. In order for the sinter to be effective, the sinter itself must never be more than 1 mm away from the bulk silver - and the helium must never be further than 1 mm from the sinter [85].

To ensure this, the heat exchange has been designed with thermal contact fins that extend the length of the heat exchanger, and are separated by 2 mm gaps that will be filled with sinter, as detailed in fig. 5.8.

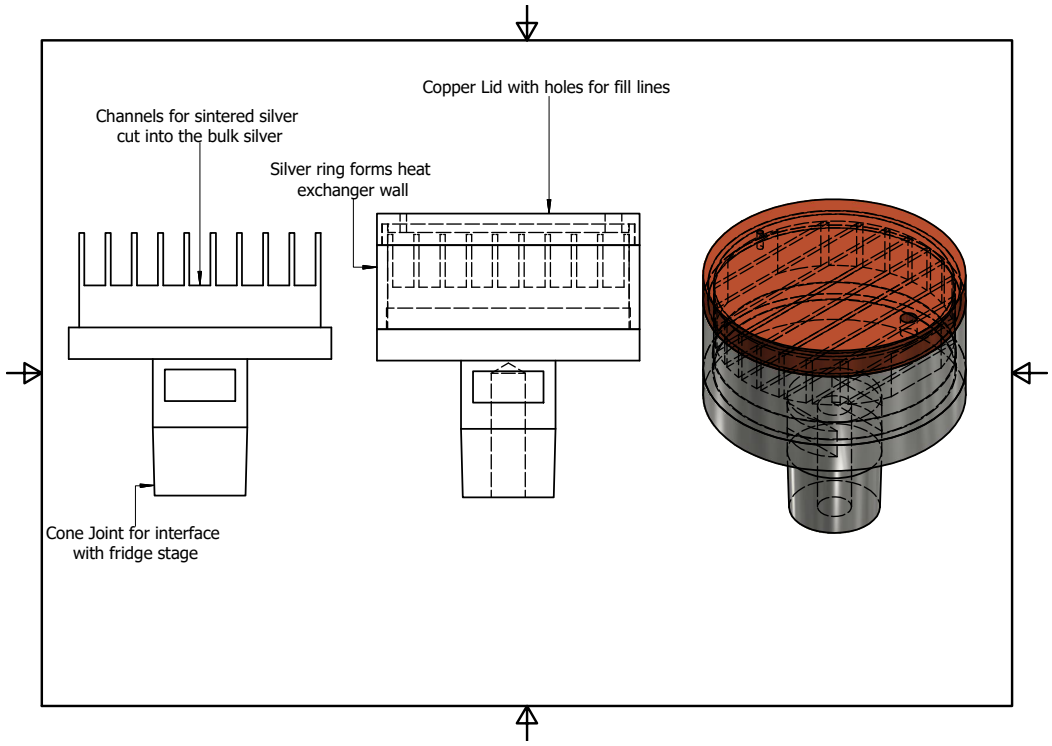

Figure 5.8: The design for the core of the NEMS heat exchanger, detailing the thermal contact fins extending from the bulk silver.

In this configuration, the sinter will have a surface area of ≈13.7 m^2 which is a factor of 4 orders of magnitude higher than if simple bulk silver were in its place, at $\approx 1 \times 10^{-3}$ m^2. The above numbers come from estimations using the results from Robert Bennett's thesis [86], from which the group has derived a sintering process with reproducible results.

5.3 Sintering Process

This procedure for making sintered silver is adapted from the methods detailed in Robert Bennett's thesis [86].

Sinter Jigs In order to press the sinter reliably, a 'jig' must be constructed to hold material you are pressing sinter onto, and also to maintain pressure on the sinter itself. In this project, two different jig designs were produced: one for the sinter plugs and one for the heat exchanger. In both cases, these comprised a brass body that could be disassembled, and a press piece.

Preparation The material the sinter will be pressed onto must be cleaned thoroughly in acetone, then isopropanol. In order for the sinter to 'grip' the bulk material, a sharp blade is used to roughen the binding surface of the bulk material. Following this, it is advisable to clean the material in acetone and isopropanol again, being sure to use refreshed supplies of each to avoid contamination of the newly scratched surface. Both the bulk material and the silver powder used are then placed in a desiccator and pumped on with a pumping trolley overnight, at 55 °C. For this process, a pump with a turbo-molecular option is favoured, because this reduces the chance of

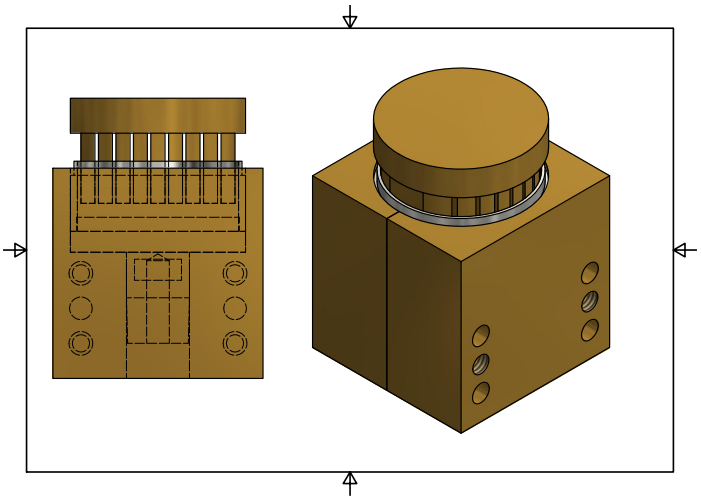

Figure 5.9: Sinter jig and press for the 25 mm heat exchanger, showing the cross-section and the fastenings for disassembly.

oil contaminating the desiccator during pumping. The following morning, a hydrogen atmosphere of $P \approx 0.41$ Bar is applied to the desiccator, and then left for approximately an hour before the desiccator is then vented and the materials are ready for the sintering process.

Pressing the sinter The true 'sintering' is performed by highly compressing the silver powder onto the surfaces of the supporting bulk. The pressure used is generally 750 Bar at the surface of the sinter - this means the pressure delivered by the end of the brass pressing piece. The limitations on the device used to compress the sinter are accuracy and contamination. Typically, contamination can be handled with control measures, but accuracy can be an issue. Depending on the size of the sinter being made, one of two methods was used in the fabrication of this cell. For the larger sinters, such as this heat exchanger, a hydraulic press was used, and the pressure reading converted accordingly. The calculation was as follows:

$$P_{\text{Gauge}} = \frac{A_{\text{Sinter}}}{A_{\text{Press}}} \times 750 \text{ Bar} \tag{5.7}$$

where A_{Sinter} is the area of the sinter being pressed, and $A_{\text{Press}} = 2468$ mm^2 is the surface area of the face of the hydraulic press. However, the resolution of the hydraulic press gauge is too low to be able to resolve less than 10 Bar, and for the smaller sinter plugs the applied pressure using the hydraulic press would have to be 1.045 Bar. For the smaller plugs then a different hydraulic press was used, which had no gauge. Instead, a set of domestic scales was placed under the jig and the pressure needed was converted to an equivalent mass at 1 g.

$$\frac{750\text{Bar} \times 100 \times 10^3\text{Pa} \times A_{\text{Sinter}}}{9.8\text{Nkg}^{-1}} = \text{Effective Pressing Mass} \tag{5.8}$$

This allowed much finer control of the sinter packing. To ensure the sinter was properly bound to the surface of the bulk, the first layer of powder would be compressed approximately 50% more than the normal pressure. This base layer of sinter then is not as permeable to liquid helium, but is much more solid as a base. The rest of the sinter is then pressed normally to fill the desired volume, in steps of around 2 mm deep powder layers.

Once the sinter was fully packed into the jig, the now sintered material was put back in the desiccator, and gradually warmed to 170 °C. Once at temperature, the desiccator was evacuated for about an hour and then filled with a 0.41 Bar atmosphere of hydrogen. This was left for about 40 mins, and then vented. It is important to immediately remove the sintered materials from the brass jig as once cool it may be difficult to remove them safely. Once the material had cooled, the sinter was immersed

in acetone for two days to remove unwanted by-products.

For maximum thermal contact with the liquid helium, the helium inside the sinter must not be more than 1 mm away from the bulk helium. Similarly, the sinter itself should not be more than 1 mm away from the bulk silver. This is resolved by drilling a series of 0.66 mm diameter holes in the sinter at intervals of 1.8 mm centre to centre. The holes should not penetrate all the way to base of the sinter, to make sure the structure of the sinter is not compromised.

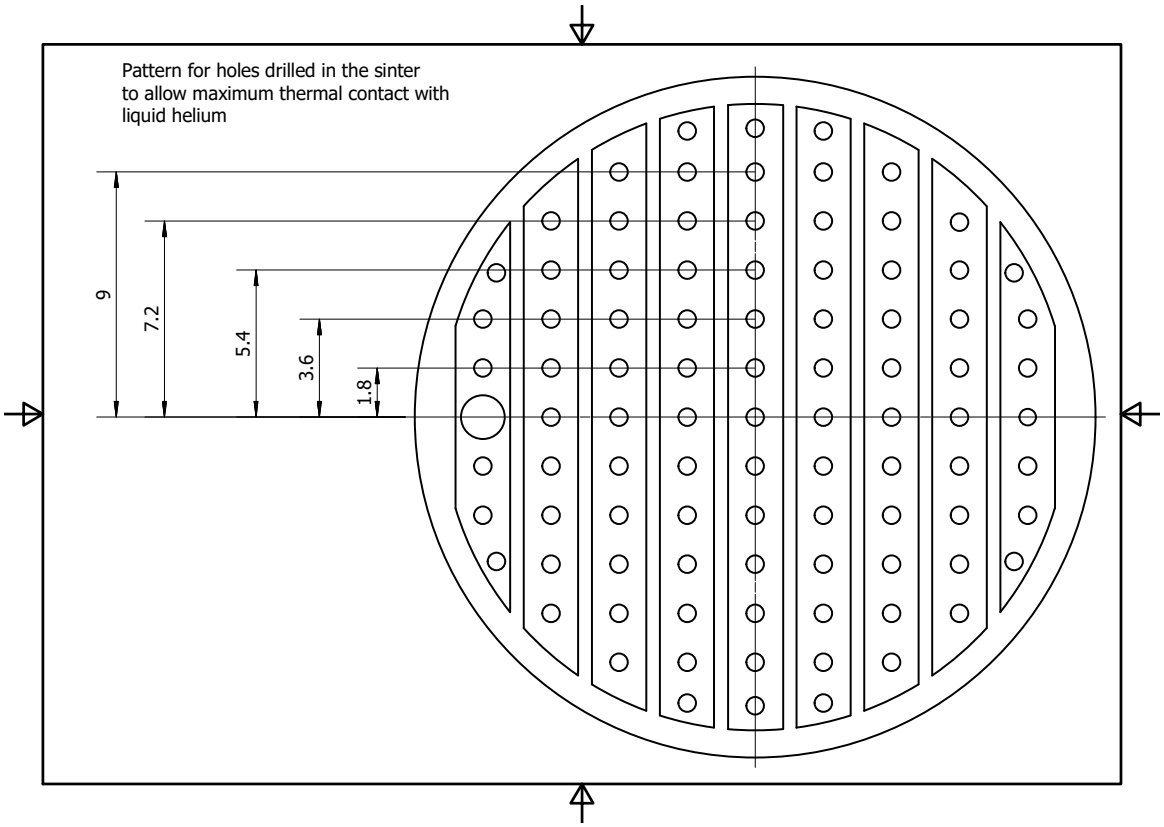

Figure 5.10: A schematic showing the pattern of the holes drilled into the heat exchanger to allow maximum thermal linkage to bulk liquid helium. At each end of the heat exchanger there are drilled holes made to accommodate fill lines, but also fulfil the purpose of the increased thermalisation.

Figure 5.10 shows the pattern of the drilled holes in the sinter. There are holes drilled into the sinter to allow the fill lines to be inserted. These penetrate the sinter such that there is no direct thermal path through the helium that does not go through the sinter, and also acts as a filter for radio frequency radiation in the fill line.

5.4 Assembly

Once the main components are completed the assembly itself must be made radio frequency isolated and leak tight. In order to access the helium space at the back of the chip holder, and the vacuum space in the enclosure, we brazed two silver pipes of appropriate length into the base of the cell.

These pipes are brazed because they will have a high thermal conductivity, and will be regularly soldered to. To avoid the pipes coming loose, we use hard solder which has a higher melting temperature than soft solder. An additional three copper-nickel pipes are soft soldered into the base; these will be the electrical access lines. These lines are detailed in fig. 5.11.

The electrical lines are made of a twisted pair of NbTi wires inside a Teflon sheath, then inserted into a niobium pipe. The niobium will be superconducting at low temperatures and thus provides an excellent electrical screen. However, niobium cannot be soldered, so we use a radio frequency reflective epoxy to form a leak tight seal between the niobium pipe wall and the copper-nickel bush. The same epoxy is used to seal the inner of the niobium tube, allowing the wiring to pass into the cell.

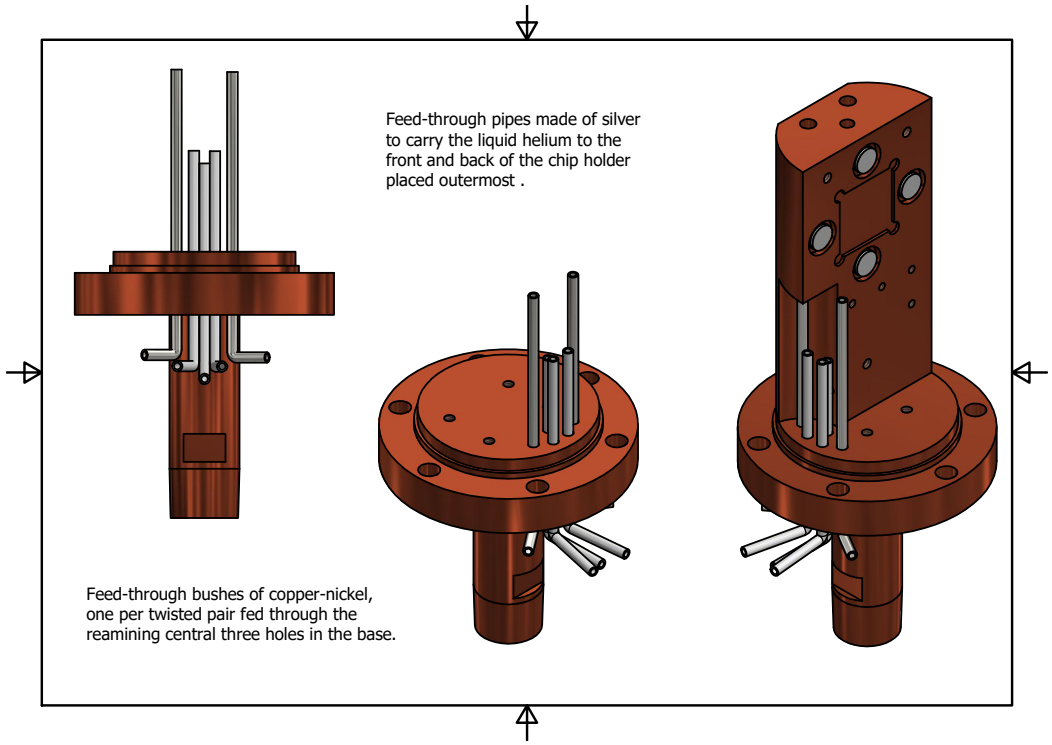

Figure 5.11: The cell base, including the silver fill lines and the copper-nickel electrical feed-throughs.

5.4.1 Copper Loaded Epoxy

The epoxy used here is Stycast 1266 loaded with copper powder, which is difficult to make leak tight due to the powder introducing air bubbles into the mixture. The procedure for successfully mixing leak-tight epoxy is as follows:

Before starting, clean two or more small Pyrex beakers in the ultrasonic bath with both acetone and isopropanol, making sure that they have both been dried completely before starting the mixing. The reason for selecting two or more beakers is that when pumping on the mixture, it will expand very swiftly. This can be managed by the separation of the mixture into smaller volumes after the initial mixing. This should

not be done before the mixing however, as the success rate of measuring the correct quantities of part A and part B is greatly increased by mixing larger volumes.

Copper loaded Stycast Procedure

- Place part A into the oven, set to 50 °C for 20 mins.
- Once heated sufficiently, decant the desired quantity of part A into one beaker.
- Add the appropriate amount of part B, this is usually measured by mass rather than volume.
- Use a glass or metal rod that has been appropriately cleaned to mix the parts A and B together until the strata in the mixture are no longer obvious.
- Place the mixture in a desiccator, with a clean loose cover to prevent debris from the vent line contaminating the mixture, and evacuate using only the rotary pump of a pumping trolley.
- Pump on the mixture for 5 mins, or until bubbling stops.
- Vent the desiccator and add to the mixture an equal mass of copper powder, being careful to use personal protective equipment as appropriate.
- Mix the copper powder into the mixture until it appears uniform, then divide the mixture equally amongst the beakers you have prepared.
- Again place the beakers in a desiccator, and evacuate whilst throttling the pressure in gentle steps.

- At a pressure below 0.5 Bar the mixture will start to expand swiftly, at which point the pressure must be reduced very slowly until the expanded liquid surface 'pops', and the liquid returns to the original level.

- Once the base pressure of the rotary pump is reached, turn on the turbo pump and leave for about 10 mins after the turbo is up to speed, or when the mixture ceases to bubble.

- Vent the desiccator gently, and then stir the mixture very gently with a fresh clean rod. The mixture is now ready for application, which should be done either with syringe or with the end of a needle / clear rod. Do not use a paintbrush, as this will introduce air bubbles and debris.

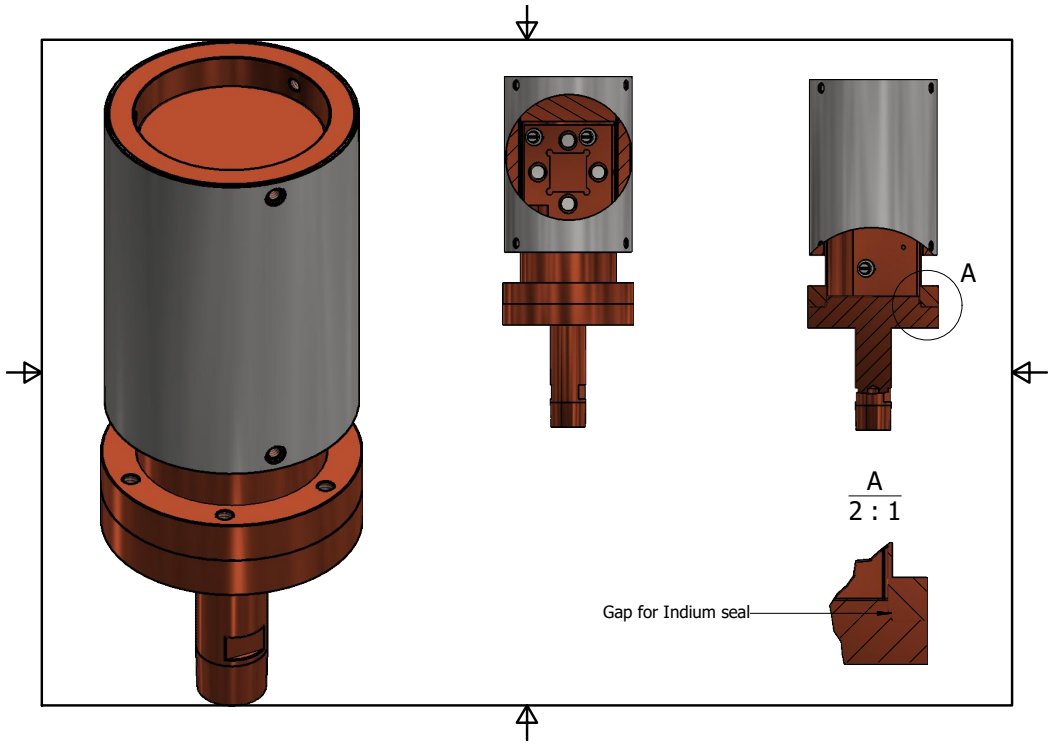

Figure 5.12: A schematic diagram of the full cell enclosure, showing the magnet and cell body. In the detail view, the step for the indium seal is detailed.

Once lines into the cell have been completed, the cell must be sealed using an indium seal. This is chosen as it is a reliable seal at ultra low temperatures, is robust to high pressure and is easily reproducible. Once the cell is closed, it can be opened again with relatively little effort. Incorporated into the design of the cell base and lid, is a gapped step that is designed to trap and compress the indium wire we place around the base of the seal, shown in fig. 5.12.

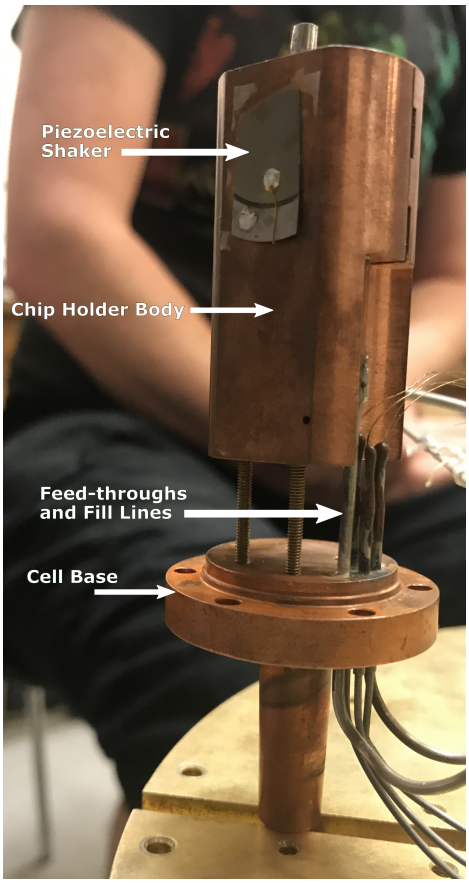

(a)

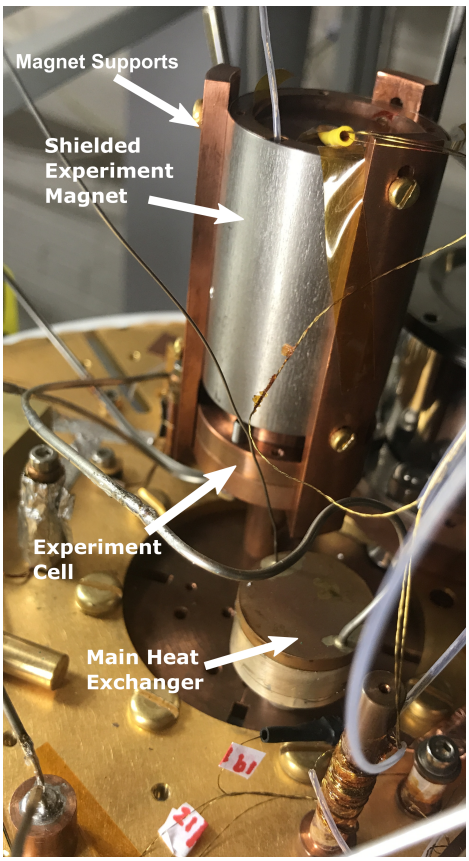

(b)

Figure 5.13: (a): The chip holder and displacer being mounted onto the cell base, visible in this picture is the piezoelectric buzzer, stuck to the back of the chip holder with varnish. (b): The full cell and heat exchanger mounted on the fridge stage. The magnet is supported by struts that are removable, but necessary for dry fridge operation.

5.4.2 Design Notes

There are a number of design elements that are not intuitive, and indeed are not the simplest implementation that one might use to create a similar cell. There are, however, reasons for these elements that shall be addressed here, to emphasise their importance.

Sinter plug insulation The insulation for the sinter plugs described in fig. 5.5 seems overcomplicated, but from frequent testing it is the most successful model. The first test pieces were insulated using only Kapton film, which insulated the plug well and had no negative impact on the epoxy seal. However, when the second iteration of the chip holder was built, it turned out that the Kapton film formed a seal against the inner helium channels, which prevented them from being evacuated, or filled with helium. The next attempt used only cigarette paper, however this seemed to make the epoxy seal far more likely to leak, whilst still restricting the helium flow. Our assumption is that the compression of the kapton film in conjunction with the epoxy creates a more cohesive seal. Finally, we used a combination of the two approaches, with the addition of a separate insulating layer at the base of the plug to allow for any gaps in the cigarette paper. It should be noted that during this process, we identified that the sealing surface - where the epoxy seal is made - must be kept free of any scratches or divots. Any damage to this surface severely lessens the likelihood of a strong seal.

Fill line brazing In normal use of the chip holder, the fill lines will be regularly soft-soldered to the lines on the cryostat. Consequently, we cannot use soft solder to attach them to the chip holder body, because the seal would then be at risk every

time the pipe was heated, so we use hard solder instead. Initially the fill line was brazed in normally, and was made of copper-nickel of a standard diameter. However, the process left trace amounts of hard solder lining the sinter pocket above it, and the subsequent sand blasting damaged the sealing surface. We found that following this damage it was difficult to make a good seal with the epoxy, as well as difficult to properly insulate the plug. To resolve this, a copper tube of the appropriate size was machined, which could be vacuum brazed into place using the furnace. In addition to reducing the amount of solder used, and making a cleaner seal, the chip holder could now be cleaned sufficiently using only ethanoic acid, which was far less abrasive.

Sinter pocket grooves If the pockets for the sinter plugs are machined as described in section 5.1, as previously mentioned, a flow restriction develops between the fill line and the spare fill port at the top of the cell holder. To resolve this issue, we created very small grooves around the inner of the pocket, at the level of the helium fill channel, such that the smooth surface that forms the seal was undamaged. This is represented in fig. 5.4 by large extensions to the sinter pockets - although these extensions are not realised. In particular these grooves must be placed around the pocket to which the fill lines are attached. The other pockets are not depended upon for helium throughput, and as such we do not risk damage to them by making these grooves.

Epoxy seals Not detailed was that the initial choice for epoxy seal on the chip holder was copper loaded epoxy. It was believed that using this would further screen the cell from RF noise. However, there were a few issues with the conductivity of the mixture. Although initially it appeared that the epoxy was insulating, it later

proved to be unreliable. The curing time for the epoxy was on the order of days, even when baked at around 40 °C, and whilst the mixture was curing it was conductive. Depending on how long the mixture took to cure, the quality of insulation was seen to vary. Ultimately it was decided something to do with the form factor must have been adversely affecting the curing process, perhaps that the seal itself was approaching the length scale of the copper particles, and to use Stycast 2850 instead.

Chapter 6

Megahertz Range Devices

The new cell described in chapter 5 was tested by attempting to measure the Cornell fabricated niobium coated devices described in section 3.1 on the cryo-free Triton cryostat (ND4). ND4 was used because of the quick turnaround time, such that any faults could be addressed and the cryostat returned to operation in roughly five days at best, whereas this is on the order of weeks for ND2 (the intended location). The cell is designed for use on a different nuclear demagnetisation cryostat and as such some modifications were made to ND4 to enable testing; the details of these modifications and the subsequent tests are discussed in this section.

6.1 Preparation

6.1.1 Configuration of the Cell

The testing configuration was different to the intended configuration because of the restrictions of ND4 compared to ND2 (the intended location of this experiment). The cone joints on the new cell and heat exchanger were not used; instead the tapped holes

in the cone joint were used to secure them to the mixing chamber plate. This meant that thermalisation would not be as high as intended, but this should not have caused an issue at temperatures above 10 mK, and the base temperature of ND4 (without nuclear demagnetisation) is 12 mK. The magnet was also designed to be supported on struts descending from the plate above to prevent additional heat leak. This was unnecessary on ND4 because of the temperatures accessible and so the magnet was mounted on copper struts that thermalise and support the magnet on the main cell base. These struts were designed by a master's student, Florence Roberts, visible in fig. 5.13b.

The main heat exchanger was connected to the fill line for the sintered pads in the cell, and a vent line was left open between the helium channels in the chip holder and the main vacuum space of the cell. This ensured that the helium around the NEMS beam itself was well thermally connected to the helium in the main heat exchanger. In addition, a much smaller heat exchanger was placed on the mixing chamber plate and linked to the pump-out port of the main vacuum space of the cell to further thermalise the helium around the NEMS. To supply helium to the cell fill lines were installed on a removable set of inserts designed to hold bobbins to which both the fill lines and electrical wiring could be thermalised. The fill lines were thermalised by winding them around copper bobbins and then vacuum brazing them in place, ensuring good thermalisation and mechanical support. The lines were vacuum brazed rather than soldered because conventional solder superconducts [87] and thus is unsuitable for thermalisation. The bobbins were then secured to the insert plates with brass screws and soldered to feedthroughs from the lab to the OVC. These can be seen in fig. 6.1.

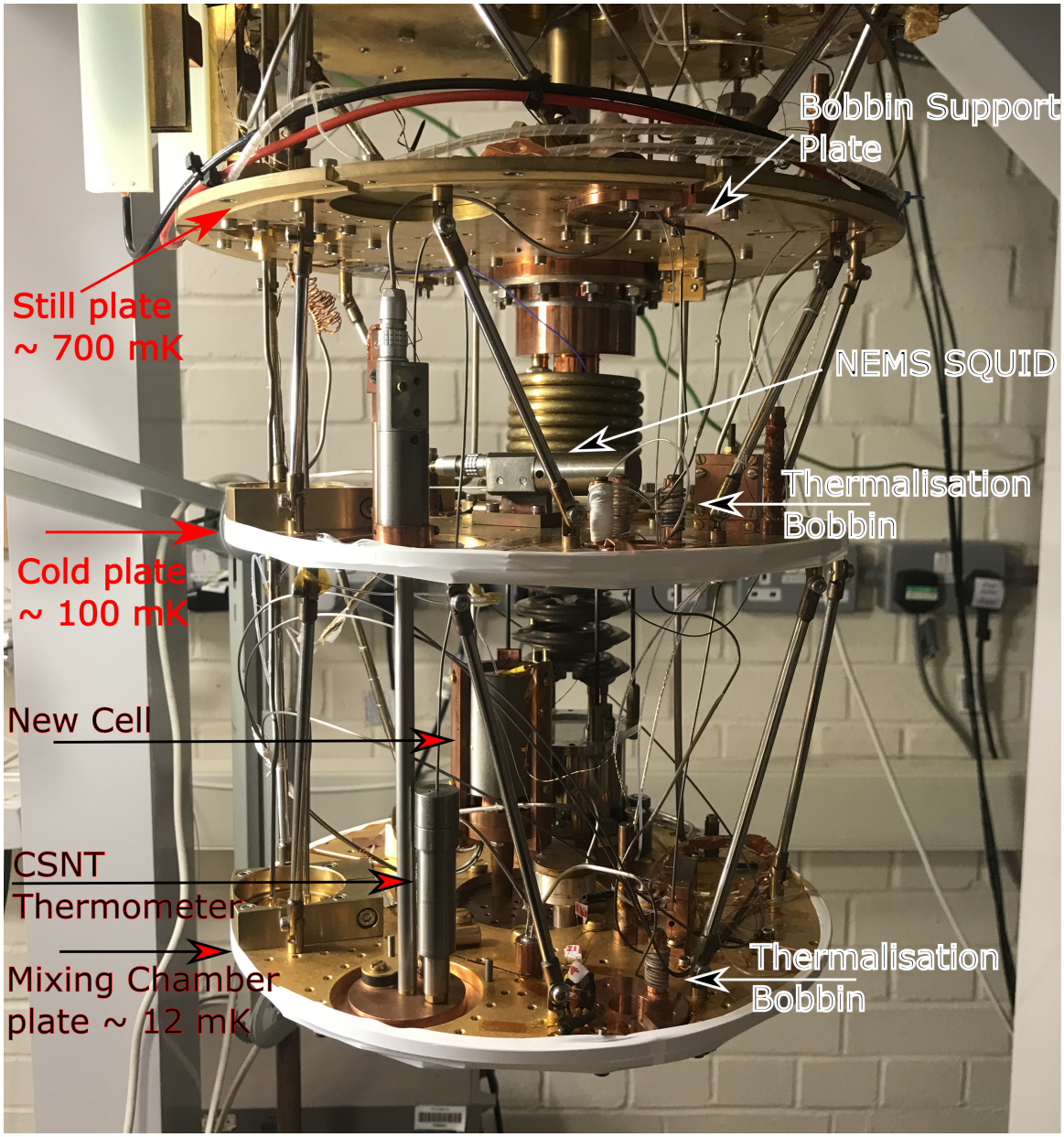

Figure 6.1: The configuration of the cryostat for the testing of the new cell. Pictured is ND4 from the still plate down, with a newly installed CSNT thermometer and cell on the left. On the right the thermalisation bobbins and support plates are annotated, and the NEMS SQUID shown mounted on the cold plate.

The fill lines were of two different diameters: 0.5 mm and 2.5 mm. The smaller diameter line feeds the main heat exchanger, and is smaller so that the volume of helium linking the cold plate to the mixing chamber plate is minimised. By contrast, the larger fill line is intended to be a pump-out port and so has a large diameter to reduce the time taken to reach a vacuum. However, for these experiments the pump-out line was used as a fill line and so had additional thermalisation on the mixing chamber plate to account for it.

To accurately measure the stage temperature a CSNT thermometer was installed on the mixing chamber, giving a reliable temperature measurement to well below the range of the RuO_2 resistive thermometers previously used for thermometry. The lines for the capacitive drive were left unconnected to avoid radio-frequency heat leaks or noise affecting the test measurements and the piezo drive was connected to superconducting lines that lead to normal room temperature connections.

6.1.2 NEMS Identification

To identify the NEMS the techniques described in chapter 3 were used to excite and measure the response across a 4 MHz range, and the peaks that responded to both pulse amplitude and magnetic field were investigated. The pulsing technique used could not acquire data in any higher resolution than 10 Hz, so parameters such as the Q-factor could not be extracted initially. These methods allowed the response from the 50 µm and 40 µm beams to be identified at 1.49 MHz and 3.33 MHz respectively.

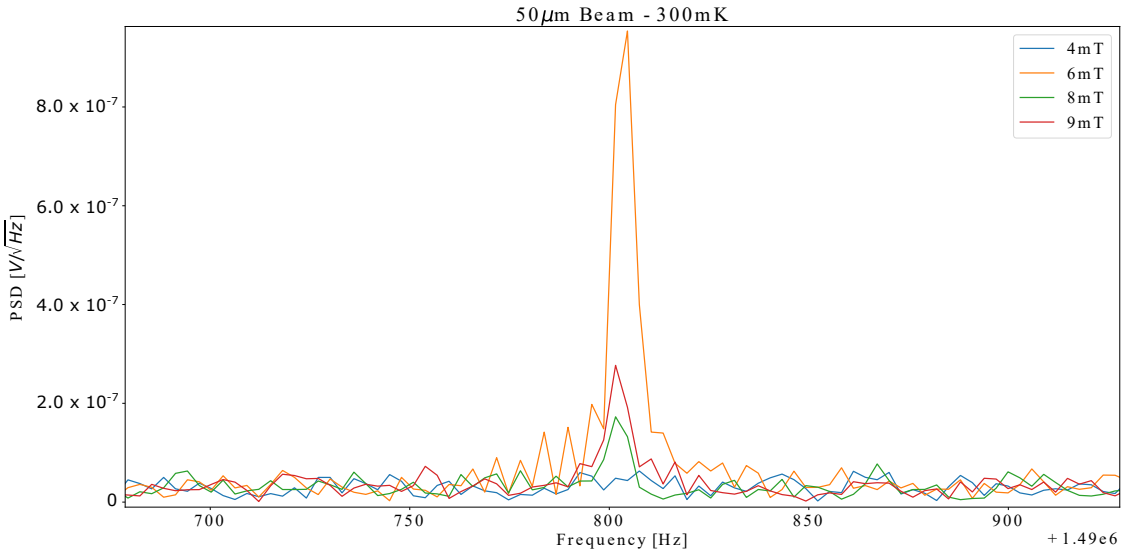

Figure 6.2: The amplitude response of the 50 µm beam for varying pulse amplitudes.

Figure 6.2 shows the amplitude response of the 50 µm NEMS to a broadband pulse at a nearby frequency, with the increase in amplitude that is expected with increasing magnetic field. There is a large drop in amplitude when the NEMS is subjected to 9 mT compared to 6 mT. This is explained by considering that the aluminium bond wires designed as thermal breaks have a critical field of 10 mT, and the field profile of a solenoid is such that the field is weakest in the radial centre, where the NEMS is located. The field here was known to be 9 mT, which indicates that the magnetic field around the aluminium bond wires must be greater and as such they will be normal. This increased the resistance of the input circuit significantly, thus linearly reducing the current induced by the voltage developed across the NEMS.

6.2 Preliminary Results

After the new cell had been successfully cooled to the operating base temperature of the cryostat and the NEMS signals identified, a limited range of experiments were performed. These experiments were to provide evidence of the feasibility of further studies using the new cell and the first data for NEMS devices of this type at milliKelvin temperatures.

6.2.1 Thermal Measurements

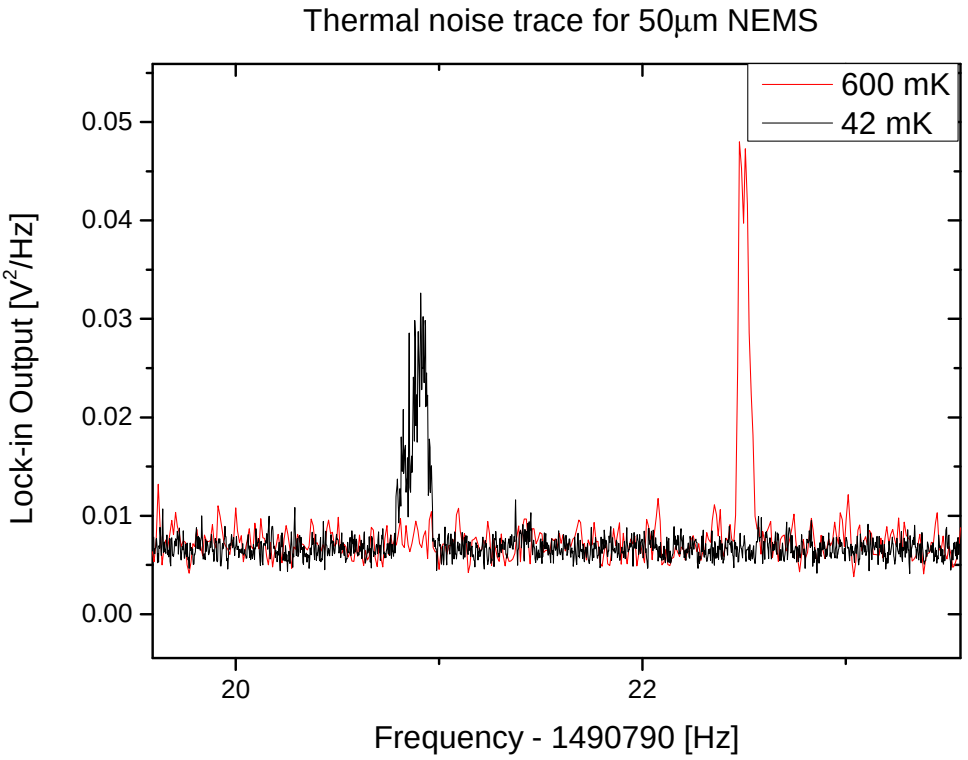

Figure 6.3: Thermal noise power traces for 600 mK (red) and 42 mK (black) for the 50 µm NEMS.

To be able to measure the Q-factor of the resonator, the noise was captured using a lock-in amplifier in the same configuration as used for the experiments with the

300 µm NEMS and described in chapter 3.

Figure 6.3 is a plot of two traces resulting from the measurement described, one for the highest temperature used in these experiments, 600 mK, and one for the lowest, 42 mK, due to an unexpected heat leak on the cryostat. On first inspection the lower temperature data appeared to have a much broader peak than the data for high temperature. This was believed to be an artefact of an extremely high Q-factor. The Q-factor measured from these traces indicated Q-factors as high as 500×10^6, which is two orders of magnitude larger than the largest Q-factor for the 300 µm NEMS. It is suspected that the Q-factor is higher still, but we were unable to measure it with current equipment. Such a high Q-factor could lead to phase instability as described in section 4.3, and as such could appear to be a wider, noisier peak than the true signal.

6.2.2 Helium Immersion

To test the solder joints and epoxy feedthroughs for superleaks, and also to gain an initial understanding of the effect of liquid helium on the NEMS, the cell was filled with ^{4}He. There was a danger to the NEMS from a moving liquid surface where wetting of the chip could form a liquid layer between the NEMS and the surface of the chip. This could then break the NEMS via surface tension pulling the NEMS towards the chip surface. To avoid this the cell was filled super-critically such that there was no moving liquid boundary in the cell during filling.

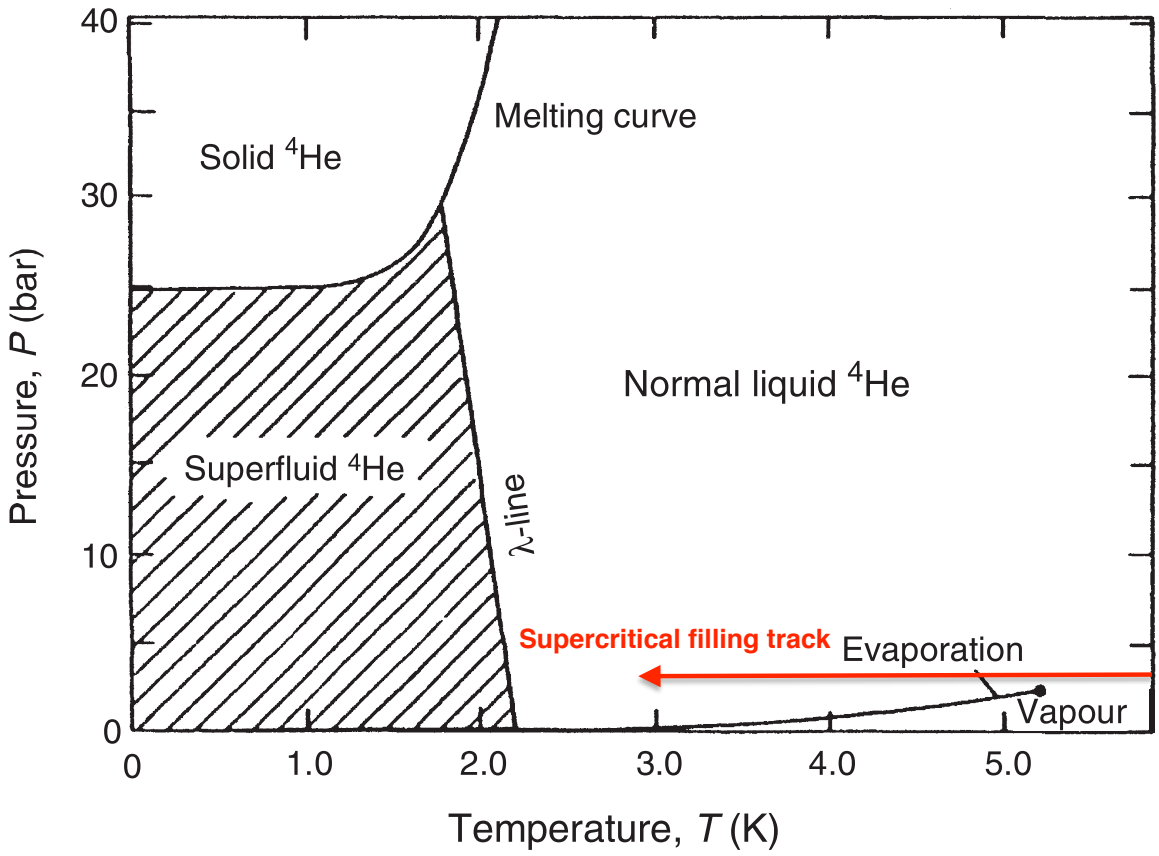

Figure 6.4: Phase diagram of ^{4}He [40]. Annotated is the path used to ensure no moving liquid phase boundary in the cell.

This was achieved by warming the cryostat to approximately 15 K by collecting the mixture (using an automated process). The cell pump-out line and fill line were then both pressurised with helium from an adsorption pump that was heated to provide 2.5 Bar of pressure to the cell. This pressure was chosen to make sure that the transition between gas and liquid on cooling was continuous rather than discrete, passing above the critical point on the phase diagram for helium 4, fig. 6.4. The critical point can be seen in the lower right of the figure, at 2 Bar and 5.2 mK. During the initial stages of this process the SQUID had to be turned off due to the cryostat exceeding its critical temperature of 9 K. The cryostat does not have a means of stabilisation

above 1 K, so it was not feasible to observe the transition between normal liquid and superfluid during this experiment.

Once the cell was filled with ^{4}He and cooled to base, the SQUID was turned back on and thermal noise measurements were repeated to identify the NEMS peak. The signal for the 50 µm NEMS was identified but no signal was found for the 40 µm for thermal or pulsed measurements. Focussing on the 50 µm beam the response amplitude was found to increase with pulse amplitude until a critical point at 1.5 V excitation, at which point the amplitude of the NEMS dropped to zero. It was thought that this was due to the method of exciting the NEMS; that the piezoelectric shaker that was also immersed could generate conditions that would cause the fluid around the NEMS to behave like a normal fluid. This behaviour is illustrated in fig. 6.5.

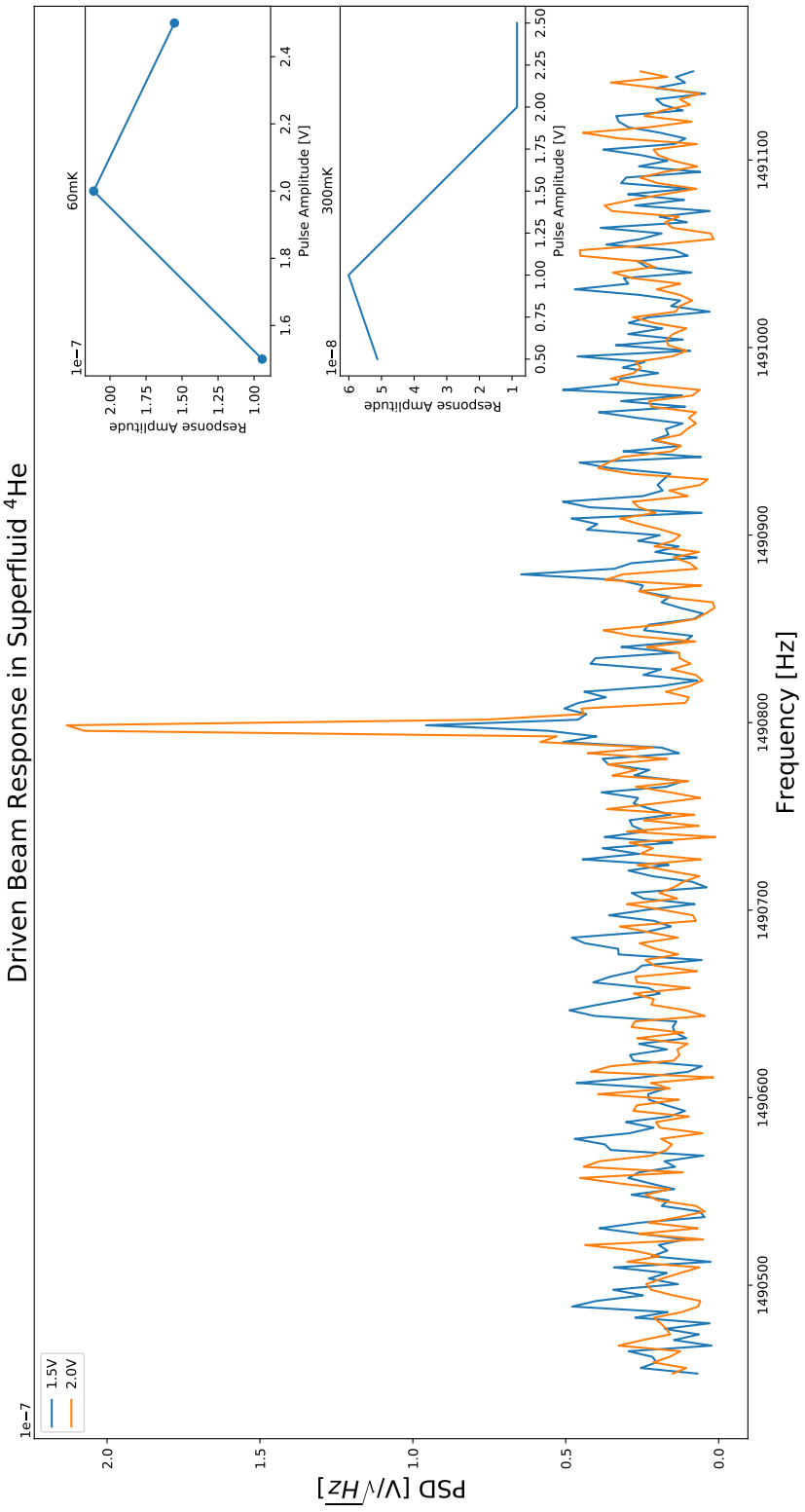

Figure 6.5: Driven response of the 50 µm NEMS in superfluid ^{4}He, showing the decrease in amplitude at 1.5 V excitation at different temperatures (right).

Using the thermal traces to extract parameters of the NEMS the Q-factor was measured for a range of temperatures whilst immersed and in vacuum. It was found that the Q-factor was lower in liquid and this would be expected from the excitation momentum exchanges between the superfluid and the resonator.

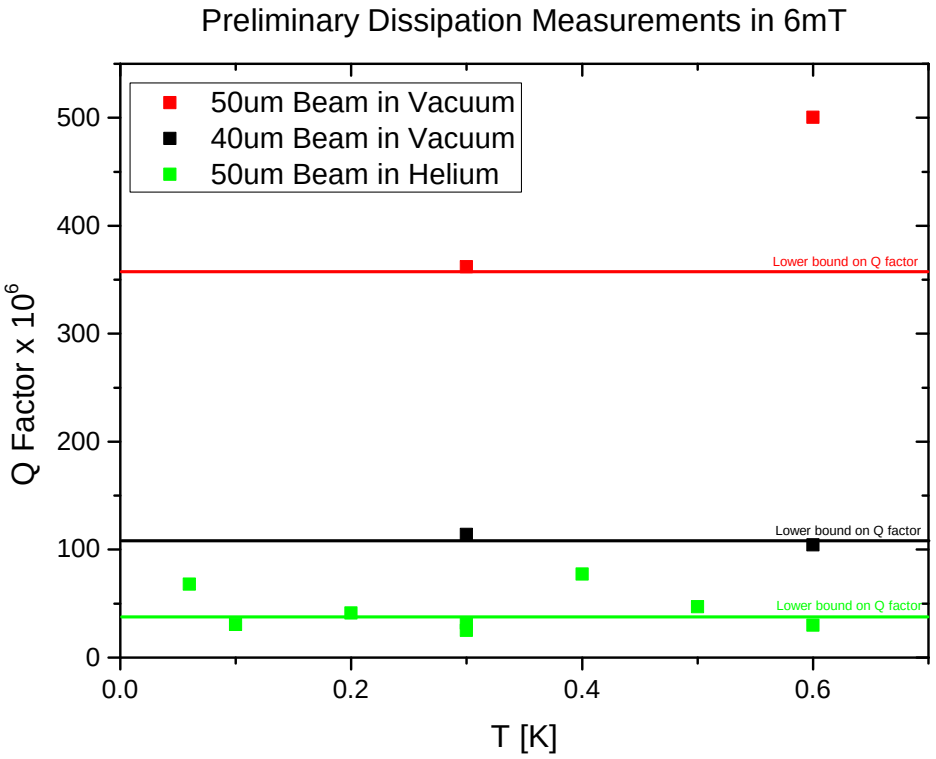

Figure 6.6: Collective measured Q-factor for the NEMS in vacuum and in superfluid ^{4}He. The 40 µm beam was not observed in liquid, whilst the 50 µm NEMS was seen both in vacuum and in liquid. The Q-factor of the 40 µm was lower than that of the 50 µm in vacuum and this is expected for lower volume beams.

The cryostat was then allowed to cool to base temperature, whereupon the signal from the 50 µm NEMS disappeared and was no longer visible. This was reversed by heating the stage back up to 60 mK which was the lowest temperature at which the thermal motion of the resonator was visible. The reason for this behaviour is unknown and it was not investigated due to time constraints.

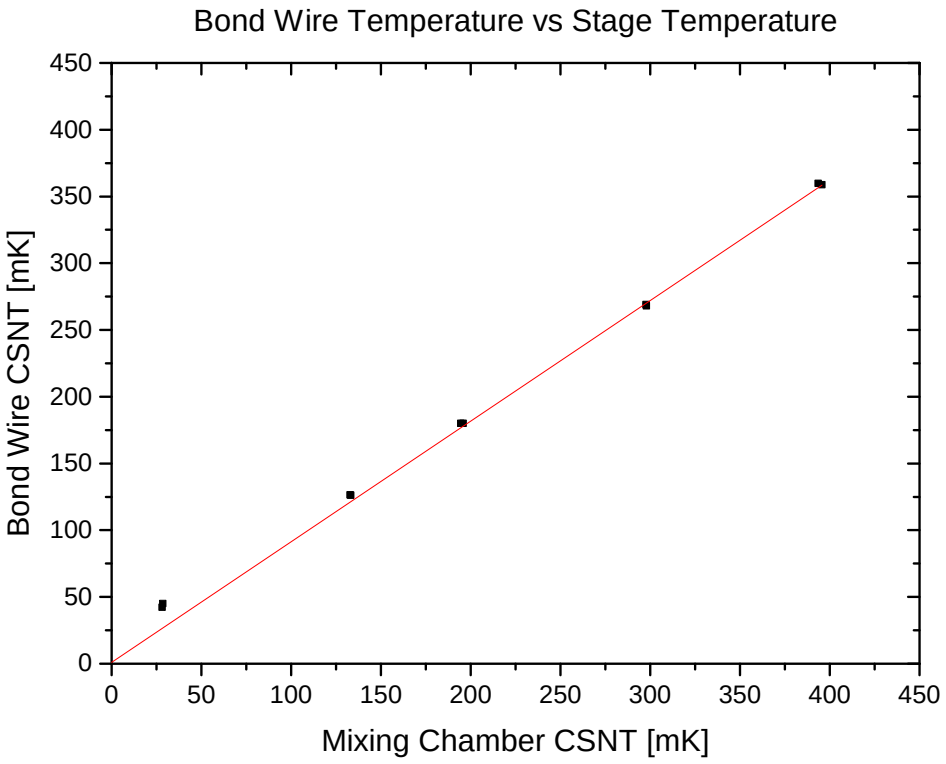

Figure 6.7: The bond wire temperature as determined through CSNT plotted against the mixing chamber place temperature as determined from a noise thermometer. At temperatures above 100 mK the cell does not deviate in temperature from the mixing chamber as indicated by the red line to guide the eye, however when left to cool to base the bond wires do not cool beyond 42 mK.

By heating the mixing chamber it was possible to vary the stage temperature and measure the temperature with the newly installed noise thermometer and by using the bond wire thermometry discussed in section 3.5. The two thermometers agreed for temperatures above 100 mK indicating good thermalisation of the NEMS. At base temperature the cryostat stopped cooling at 28 mK; 14 mK above the normal base temperature. The bond wires stopped cooling at 42 mK indicating a breakdown in the thermal connection between the NEMS and the stage. This behaviour indicated an

unexpected heat leak to the mixing chamber stage, which could have been delivering more thermal power to the cell than it was capable of transferring to the stage. This was not wholly unexpected due to the low contact area between the cell, the heat exchanger, and the mixing chamber plate, given that the plate holding the cell and heat exchanger was itself bolted to the mixing chamber plate separately, increasing the thermal resistance via acoustic mismatch.

6.2.3 Conclusion of Tests

At the conclusion of these tests the cryostat was warmed and opened and it was found that the NEMS chip had separated from the wall of the cell during thermal cycling and had fallen out of its mounting, breaking the bond wires. On examination of the chip, it appeared that the 40 µm beam was broken but the 50 µm beam was intact, as were most other beams on the chip. It is thought that the 40 µm beam had broken during the experiment, hence the signal vanishing. Although attempts were made to reconnect the NEMS, the difficulty in bonding gold to niobium without heating resulted in the destruction of the devices that had been studied in the preliminary measurements. In order to continue measurements, bonds to a new pair of resonators were required.

6.3 Characterisation Run for MHz Beams

This section describes the preliminary measurements on a new set of resonators on the same chip as described in the tests. However, the resonators studied in this section are 80 nm wide, rather than the 50 nm wide resonators initially studied on this chip. This is due to the challenging fabrication process.

6.3.1 New Bonding

Following the conclusion of tests on the new cell, the NEMS chip had to be re-bonded for further experiments.

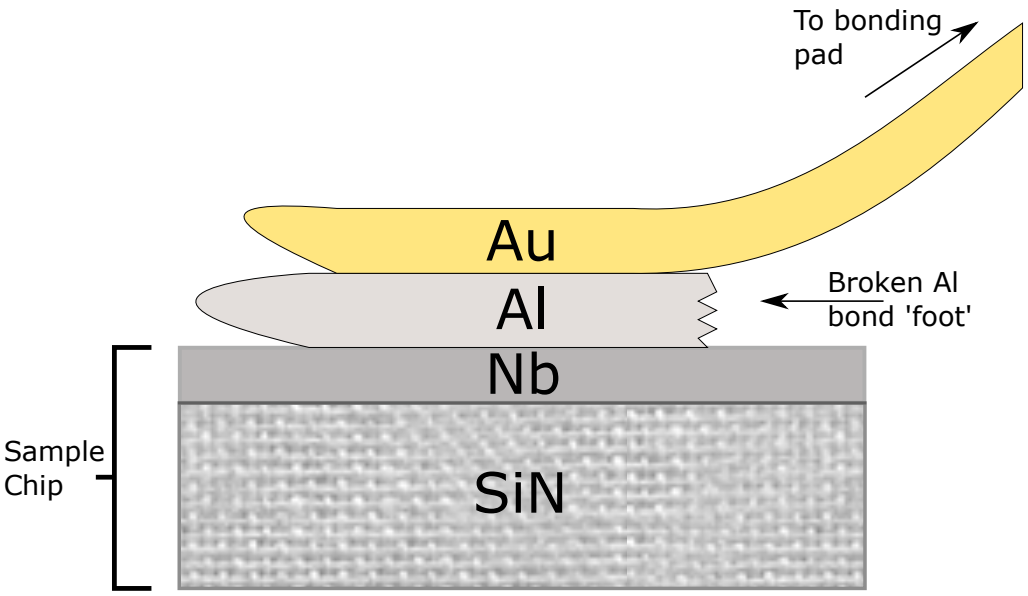

Figure 6.8: A schematic of the new method for bonding the NEMS chip using Au bond wires. Au wires will not easily bond to Nb films without heating, so Al was used as an interface between the Nb and Au to provide a robust contact.

The previous attempts at bonding Au wires directly to the Nb film on the chip demonstrated that relying on these types of bonds was not sustainable. Instead, Al bonds were made to the chip and the length of wire then deliberately removed leaving only a 'foot' of the bond on the chip. The Al bonded well to the Nb film, and then the Au bond was made by bonding to the Al foot. These new bonds were more robust and did not fail during subsequent experiments. These new bonds are depicted in fig. 6.8.

6.3.2 ^{4}He Immersed Resonator Measurements

The search for the resonators for the characterisation run was prolonged due to a lack of visible response in vacuum. The reasons for this apparent lack are not known, but it is not unreasonable to suggest that high Q-factors caused by changes in the beam geometry could have affected response. With this being the assumption, the cell was then super-critically filled with ^{4}He once again in the hopes of damping the resonator enough to be able to excite it with a broadband pulse. In addition, the interval of frequency step in the pulse sweep was reduced and the pulse duration increased such that the spectral power density was increased.

A signal was found at 2 763 250 Hz that decreased in frequency with increasing temperature and increased in Q-factor with reducing temperature. This signal, shown in fig. 6.9, was determined to be a likely NEMS candidate signal due to following the behaviours expected for the input circuit as described in chapter 4. From the results obtained earlier in this chapter, the NEMS resonances are expected at around 3 MHz for the 40 µm resonator, and 1.5 MHz for the 50 µm resonator. The increased width of

these resonators would have reduced the frequency because of the increased mass and, in addition, a higher cross-section moving through the helium should have increased the hydrodynamic effective mass through backflow. It was decided that the observed signal was from the 40 µm resonator due to the frequency being below 3 MHz and above 1.5 MHz.

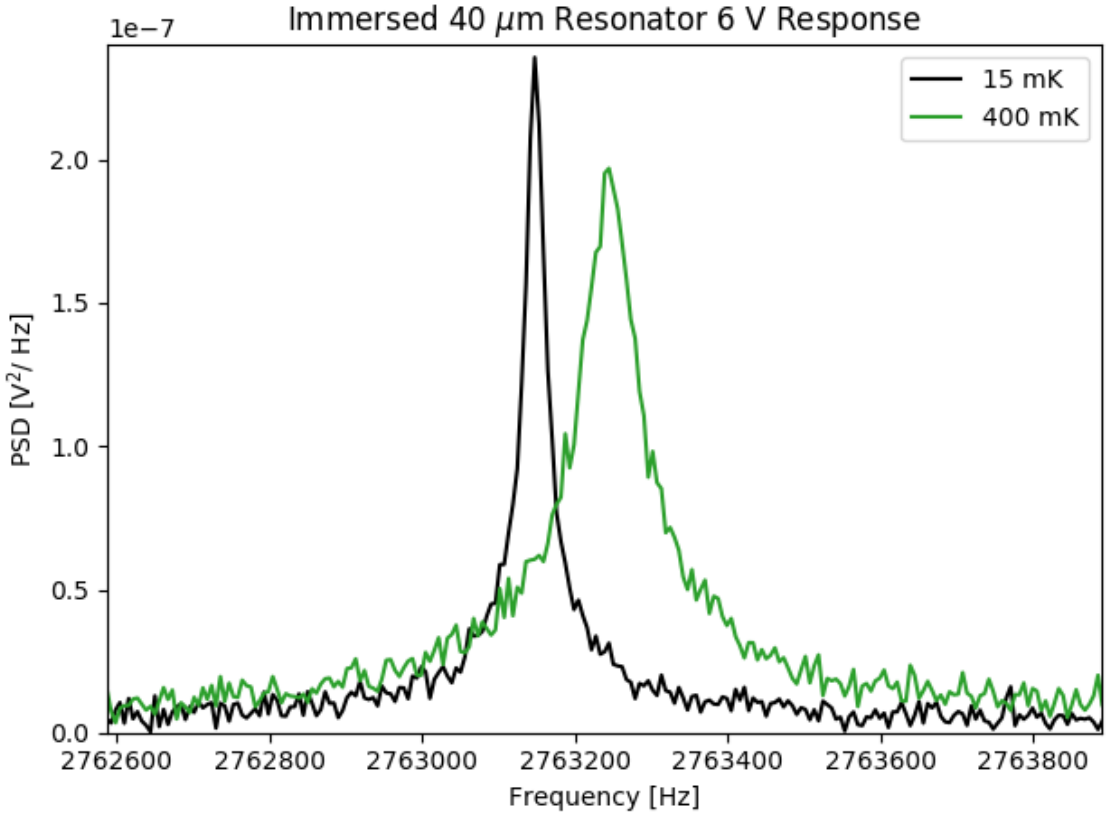

Figure 6.9: The driven response of the 40 µm resonator to a 6 V AC drive to the piezoelectric shaker at 2 765 000 Hz in a 22 mT field, at 15 mK (black) and 400 mK (green). The shift in frequency due to temperature change is expected for a NEMS, as is the change in Q-factor.

The amplitude response of the resonator in helium with changing magnetic field was then measured, where the expected frequency shift due to magnetic field is low due to the low inductance of the resonator. In contrast to the 40 µm resonators studied in the cell tests, the Q-factor of this resonator was much lower when driven, averaging around 14×10^4 for any given measurement. The Q-factor for driven measurements did not change significantly with field, shown in fig. 6.10, which was reflected in the test measurements. This could have been due to the viscosity of the ^{4}He dominating

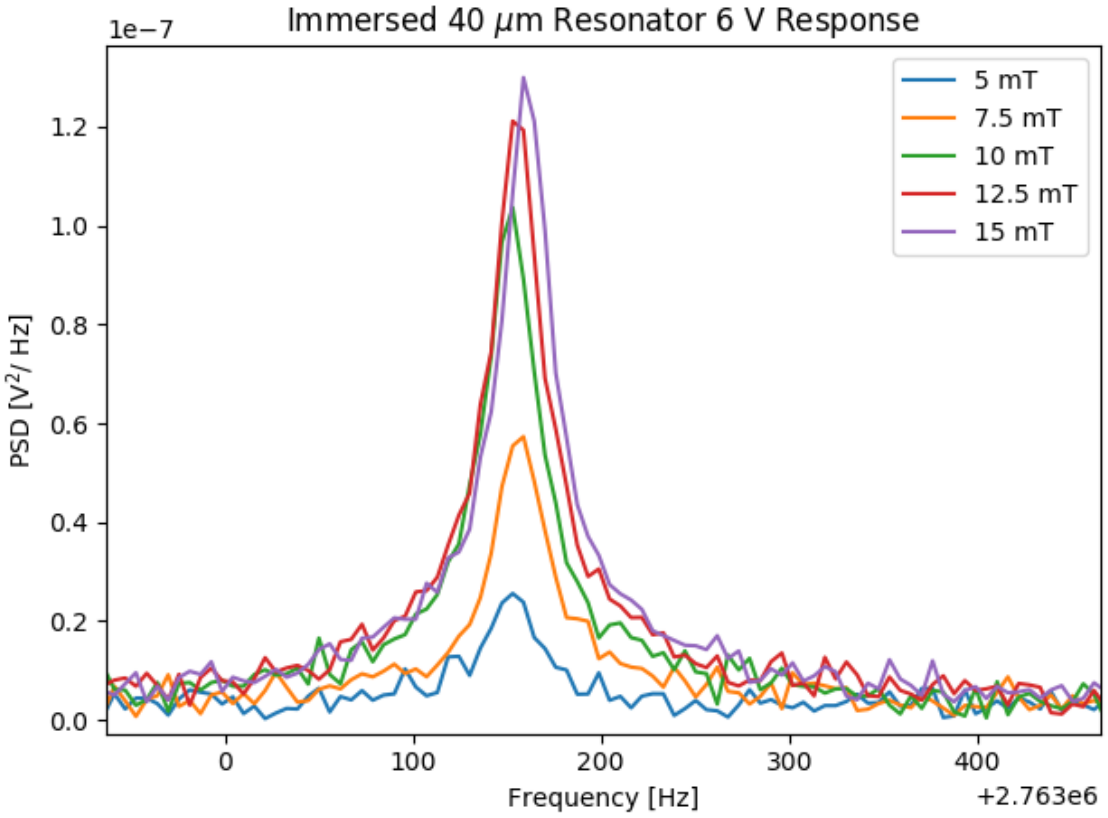

Figure 6.10: The field dependence of the resonator response to a 6 V pulse supplied to the piezo shaker in ^{4}He, showing the slight frequency shift expected and the large change in amplitude.

the dissipation thus suppressing the effects of the input circuit. As magnetic field

was increased it was expected that there would be a discontinuity in the area of the Lorentzian due to the Al bond wires exceeding their critical field and thus increasing the resistance of the input circuit. This discontinuity is observed in fig. 6.11, and allowed us to calibrate the magnetic field appropriately using the field profile of the magnet generated by design software.

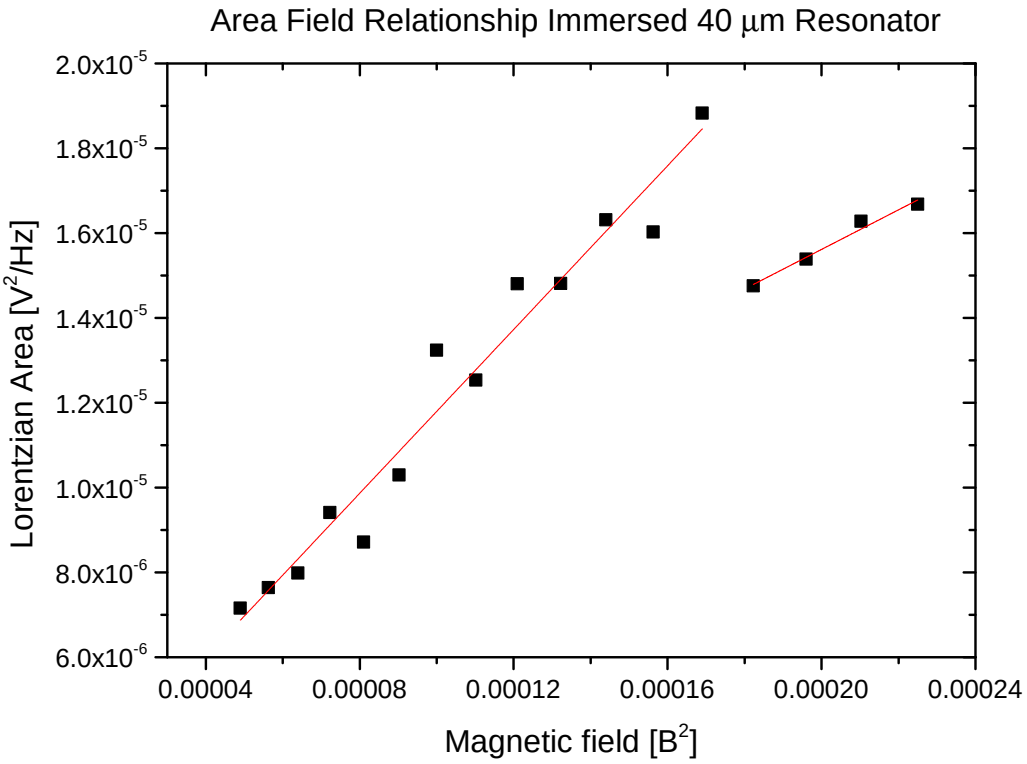

Figure 6.11: The area under the Lorentzian increased linearly with magnetic field squared as expected, before a discontinuity caused by the Al bond wires going normal changes both the gradient and noise power observed. After the bond wires go normal, the area continues to increase linearly with field as expected.

Preparation for the characterisation run also involved work to reduce optical heat leaks on the cryostat to the mixing chamber plate. Gaps in the cryostat plates were covered by using copper tape or by inserting screws into threaded holes to reduce

any potential heat leak and identify the poor thermalisation performance from the test run. The result of these changes was that the cell thermalisation performed far better than in the tests, and exceeded the minimum cooling previously achieved with the first cell. The bond wires reached 14.53 mK in contrast to the 20 mK minimum previously achieved. However, the stage temperature continued to reduce to 11.4 mK as shown in fig. 6.12, indicating that the thermalisation was still not optimal.

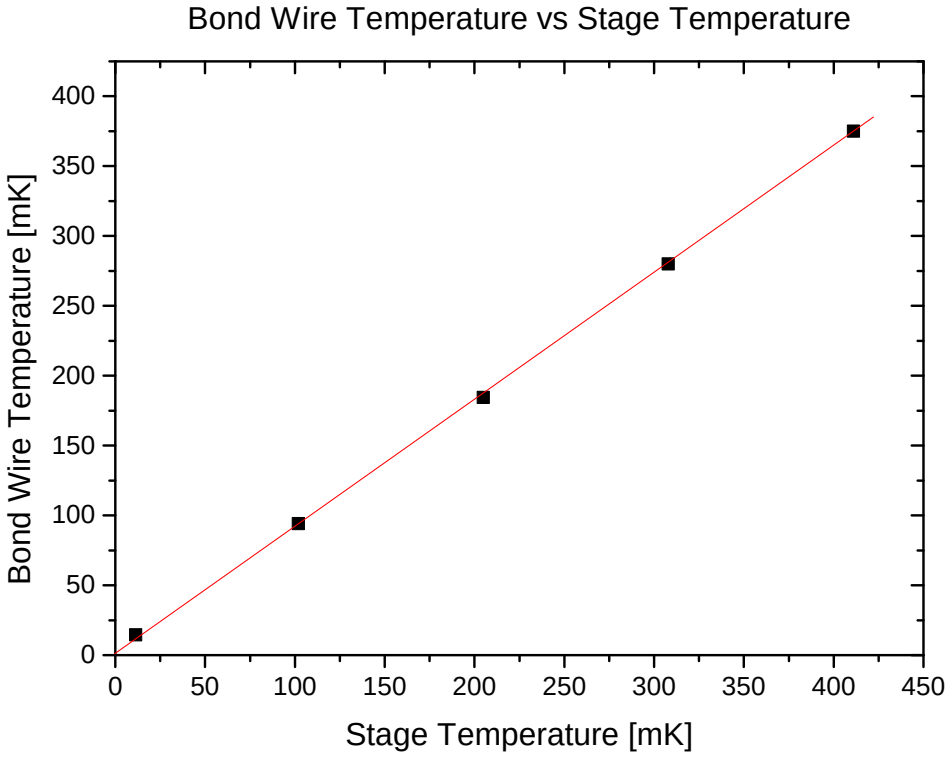

Figure 6.12: Thermalisation of the bond wires demonstrated by a gradient approaching unity when bond wire temperature and stage temperature are plotted against each other. The red line is a guide to the eye, to illustrate the thermal disconnect between the bond wires and stage temperature below 15 mK.

The improved thermalisation allowed observation of the thermal noise power in the resonator whilst immersed in ^{4}He, which was observed with Q-Factors of 22.2×10^6 at 21 mT at 14.5 mK.

6.3.3 Viscous Damping in Superfluid ^{4}He

The Q-factor of the resonator in vacuum is dependent on temperature due to the increased tension in the beam resulting from differential thermal contractions. However, the intrinsic Q-factor at low temperatures appeared to be dominated by the helium rather than by the properties of the resonator. By extracting the damping from the Lorentzian it was possible to observe features of viscosity in He II as discussed in section 1.1.4, demonstrated in fig. 6.13.

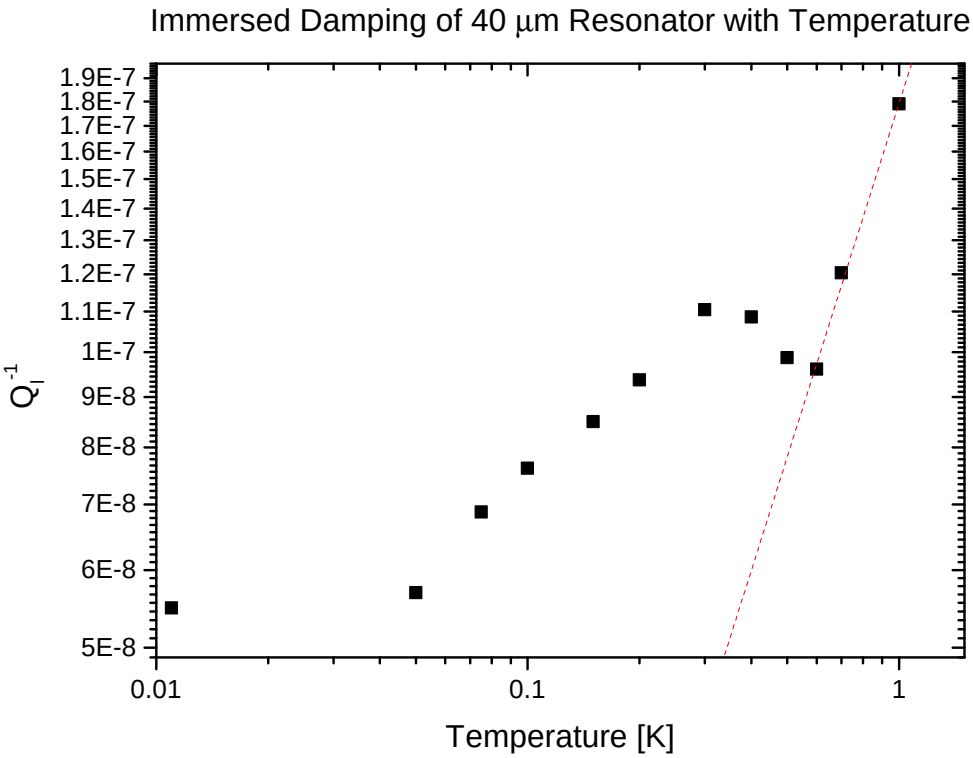

Figure 6.13: Damping of the resonator due to He II viscosity. The data below 600 mK replicates the trend observed in fig. 1.9, showing the peak viscosity and roll off above 300 mK due to the drop in roton viscosity, and then the fall due to the extension of the phonon mean free path. Above 600 mK the resonator intrinsic Q-factor drops below the viscous damping, and the temperature dependence of the resonator Q is observed. This is illustrated with the red dashed line as a guide to the eye.

Near 1 K the damping of the resonator is dropped rapidly with temperature due to increasing stress in the beam. As the temperature reduced further the intrinsic damping of the resonator dropped below the viscous damping of the superfluid, allowing observation of viscous damping. As the temperature reached 500 mK the viscosity of the superfluid plateaued as the roton component reduced. Below 400 mK the viscosity dropped further as the mean free path of the phonons grew to the length scale of the resonator. When the the temperature reduced to 11 mK the viscosity had stopped decreasing. At this temperature the highest Q-factor of the resonator was observed at 18×10^6 and it was assumed that the resonator was no longer interacting with quasiparticles, which resulted in the high Q-factor observed.

This final observation provides enough evidence to confirm that the observed signal was indeed a NEMS in a quantum fluid, and provided proof of concept for further experiments in ^{3}He where the dimensions of these resonators are the same as the coherence length. This will hopefully allow for investigation of new physics; probing helium on the order of the quantum mechanical interactions.

Chapter 7

Conclusions

This thesis documents the work towards the use of NEMS as probes in quantum fluids. There are two main experiments: the first in vacuum to characterise the properties of the SQUID-NEMS system, and the second to test a newly constructed enclosure for helium experiments. The conclusions drawn from these experiments are summarised in this chapter.

7.1 Vacuum Experiments

In chapter 4 the vacuum characterisation of the NEMS was described. Feedback effects between the SQUID and NEMS were observed, the behaviours described and a qualitative theory presented.

7.1.1 Mode Cooling

The feedback interaction that increases damping for a mode beyond that which is expected presents convincing evidence that the mode is being cooled by the same

action. It was shown that the damping was consistent with a modelled noiseless resistor being placed in series with the NEMS, indicating the presence of a direct feedback coupling between the flux-locked loop electronics and the NEMS. As seen

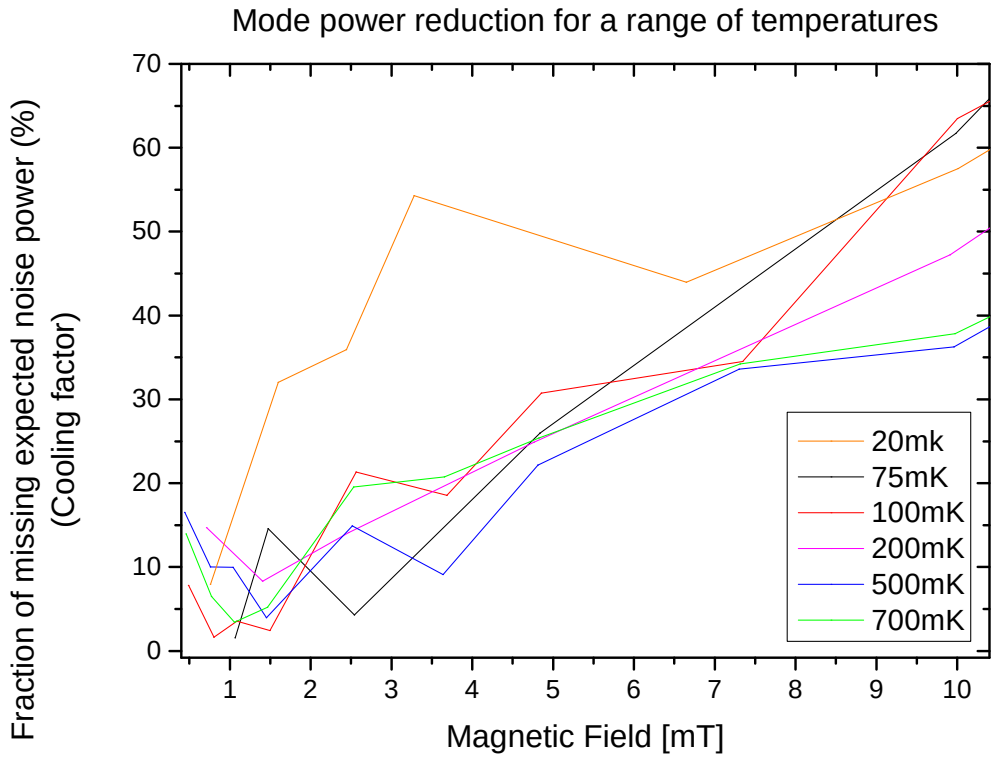

Figure 7.1: The plot showing cooling factor from section 4.2.2, indicating a replicable cooling power at all temperatures.

in fig. 7.1 the effect of the feedback was to reduce the measured noise temperature of the mode, even after accounting for expected signal loss due to magnetic field increases effecting the resistance of the NEMS. This feedback effect is only observed above 2 mT whilst the SQUID is set to a 2.8 GHz Gain Bandwidth Product with the working point on the negative slope of the transfer function.

7.1.2 Self-Sustained Oscillations

In contrast to the mode cooling behaviour, when the working point is switched to the positive slope of the transfer function the damping is reduced under increasing magnetic field. This results in self-sustained oscillations once the inverse Q-factor is reduced below zero, indicating the presence of additional power in the NEMS. These self-sustained oscillations are similar to those seen in the literature [32, 62, 77] but it was not possible to search for entrainment of the NEMS due to the limited nature of the experiment. The behaviour observed modifies the working theory to explain these effects by replacing the noiseless resistance in the input circuit with an AC current supply of similar frequency but different phase to the NEMS. This coupling of current to the input circuit is possible a result of the Additional Positive Feedback (APF) coil coupling to the input circuit though the FLL electronics. This then provides more confidence in the notion that the mode is being cooled by the damping behaviour, in a fashion analogous to laser feedback cooling.

7.2 New Immersion Cell for NEMS Experiments

A new type of cell for testing NEMS in vacuum and in superfluid helium was constructed using a combination of techniques developed within the group, and using a unique modular design that allows changing of sample with relative ease. A key feature of this design is that it can be used for both vacuum and immersion experiments in the same temperature ranges without the requirement for thermal cycling to room temperature to change configuration. An accompanying sintered silver heat exchanger was also designed, that allows the thermal ground of the cell to be displaced from the cell enclosure and therefore minimise risk of damage to delicate elements during

sample change.

7.3 Probing Superfluid Helium 4

The new cell described in chapter 5 was tested by filling it with ^{4}He and cooling it through the superfluid transition temperature whilst pressurised to prevent a moving phase boundary within the cell. The cell proved to be leak-tight to superfluid ^{4}He under an applied 2.5 Bar of pressure, which confirms it will be leak-tight for ^{3}He in future experiments. NEMS resonances were found and measured in vacuum and in liquid, with an apparent dependence of NEMS response of excitation amplitude in superfluid that implies the presence of quasiparticles within the superfluid due to the piezoelectric shaker's influence.

Further experiments with a different set of resonators verified the results seen in testing, and allowed measurements of the Q-factor and resonator noise power to be measured directly for characterisation. This work demonstrated the functionality of a NEMS as a viscometer for quantum fluids, mirroring measurements previously performed using quartz tuning forks and vibrating wires. Work on using a capacitive drive for the resonator has begun, with the adaptation of the capacitive drive lines to a coaxial connector for low-loss RF transmission.

7.4 Further Work

To complete the testing of the new cell, the capacitive drive should be connected via filtering to a high-frequency line such that the NEMS can be driven in the superfluid

without disturbing the liquid with any other drive. The cell is designed to be used on ND2, and following the completion of testing the natural progression of these experiments is to fit the cell and heat exchanger to this cryostat. ND2 is fitted with a nuclear demagnetisation stage and so will be able to cool the cell to low enough temperatures to investigate liquid ^{3}He in both its normal and superfluid state, as the new cell is designed to achieve. Work on cooling a NEMS into the quantum regime is also planned, first replacing the Cornell resonators presently mounted with higher frequency NEMS such that the single phonon energy is achievable.

Appendix A

Chip Holder Drawings

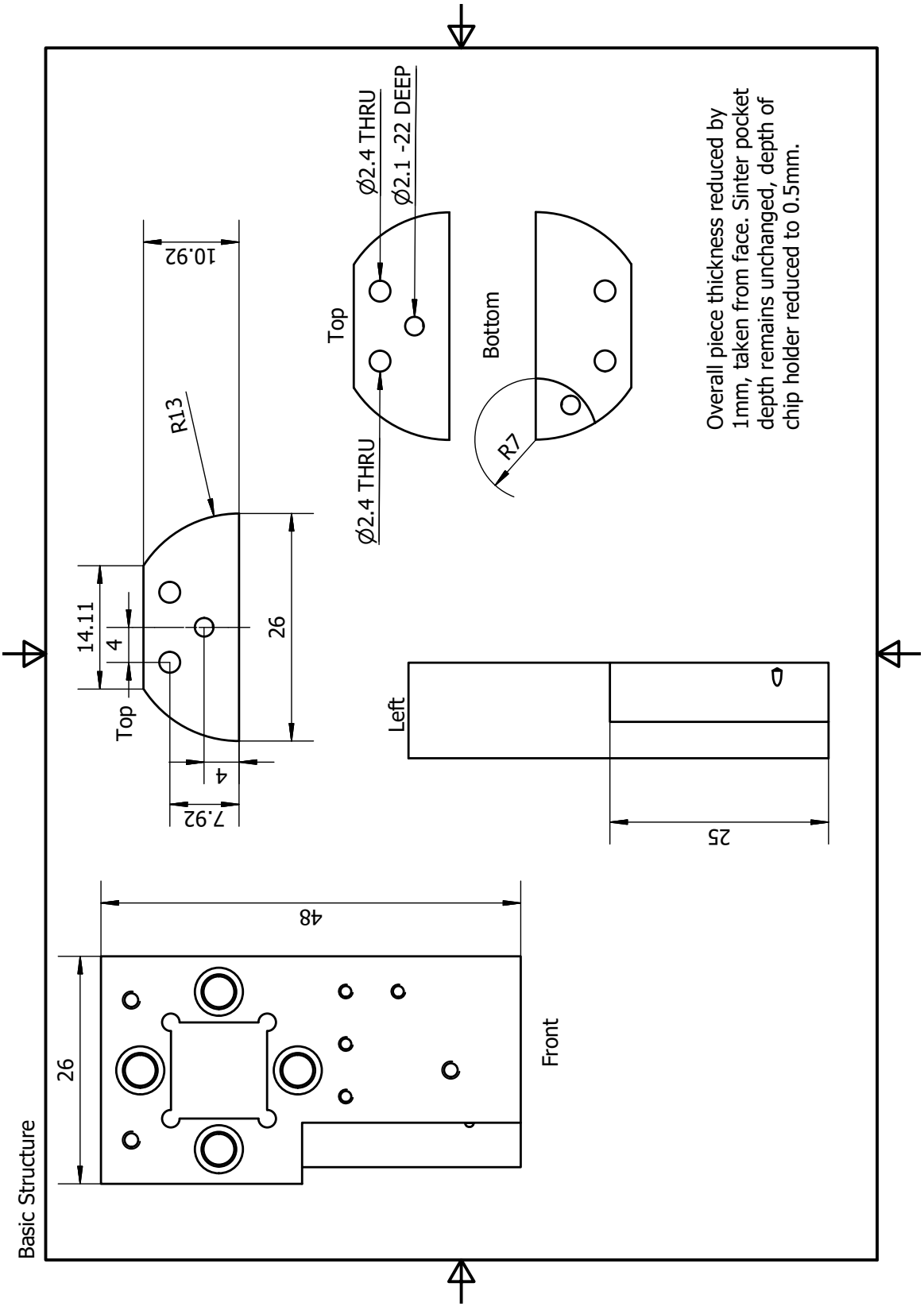
Basic Structure
48
26
Front
Left
25
Top
Ø2.4 THRU
Ø2.1 -22 DEEP
Ø2.4 THRU
Bottom
R7
Overall piece thickness reduced by
1mm, taken from face. Sinter pocket
depth remains unchanged, depth of
chip holder reduced to 0.5mm.
10.92
R13
14.11
4
26
Top
4
7.92

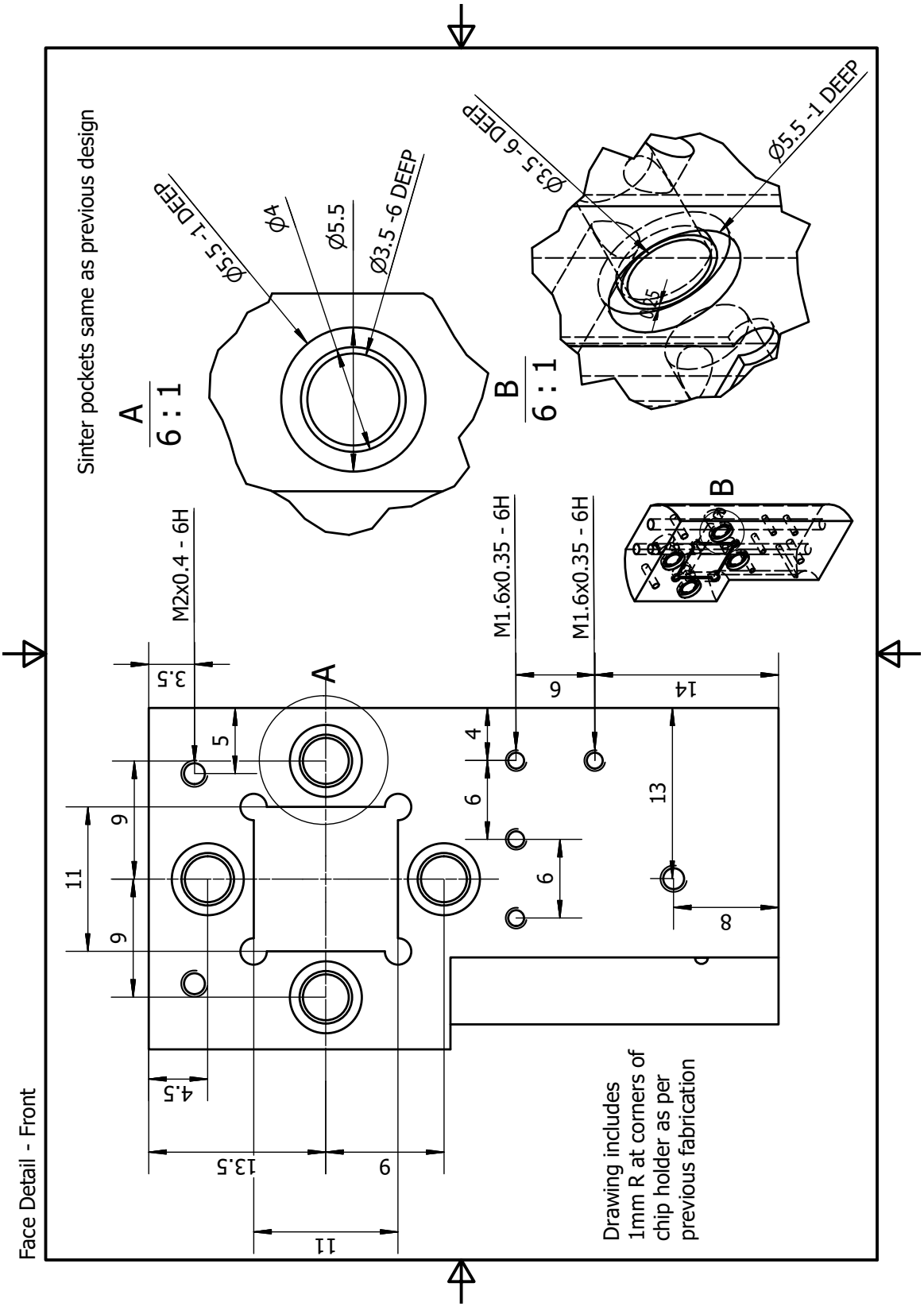
Face Detail - Front
Sinter pockets same as previous design
A
6 : 1
B
6 : 1
Ø5.5 -1 DEEP
ϕ4
Ø5.5
Ø3.5 -6 DEEP
Ø3.5 -6 DEEP
Ø5.5 -1 DEEP
M2x0.4 - 6H
M1.6x0.35 - 6H
M1.6x0.35 - 6H
3.5
5
4.5
13.5
9
11
11
9
6
9
4
6
6
13
14
8
Drawing includes
1mm R at corners of
chip holder as per
previous fabrication

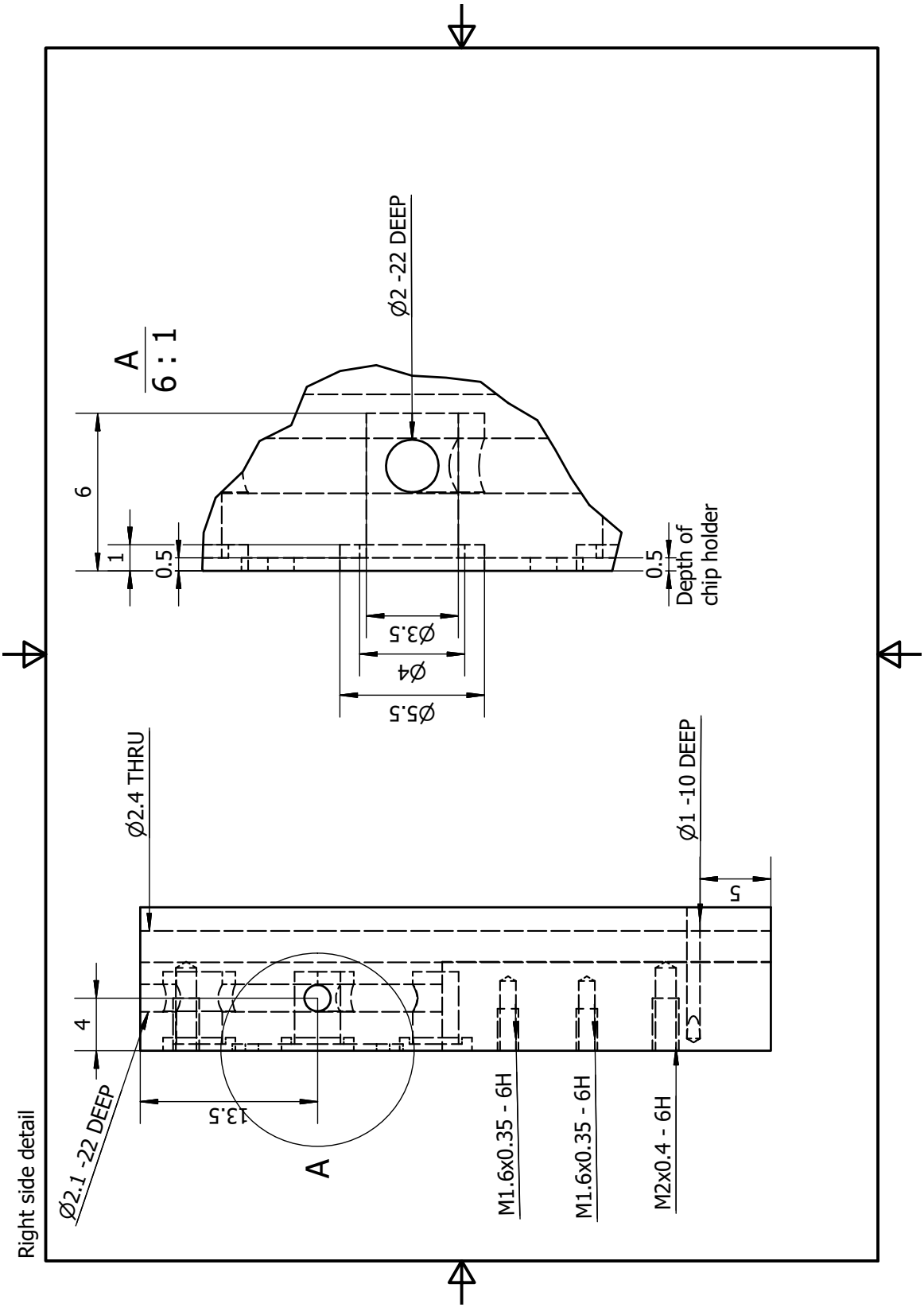
Right side detail
Ø2.1 -22 DEEP
13.5
A
M1.6x0.35 - 6H
M1.6x0.35 - 6H
M2x0.4 - 6H
Ø2.4 THRU
Ø1 -10 DEEP
5
4
2
Ø5.5
Ø4
Ø3.5
Depth of chip holder
0.5
0.5
1
6
Ø2 -22 DEEP
A
6 : 1

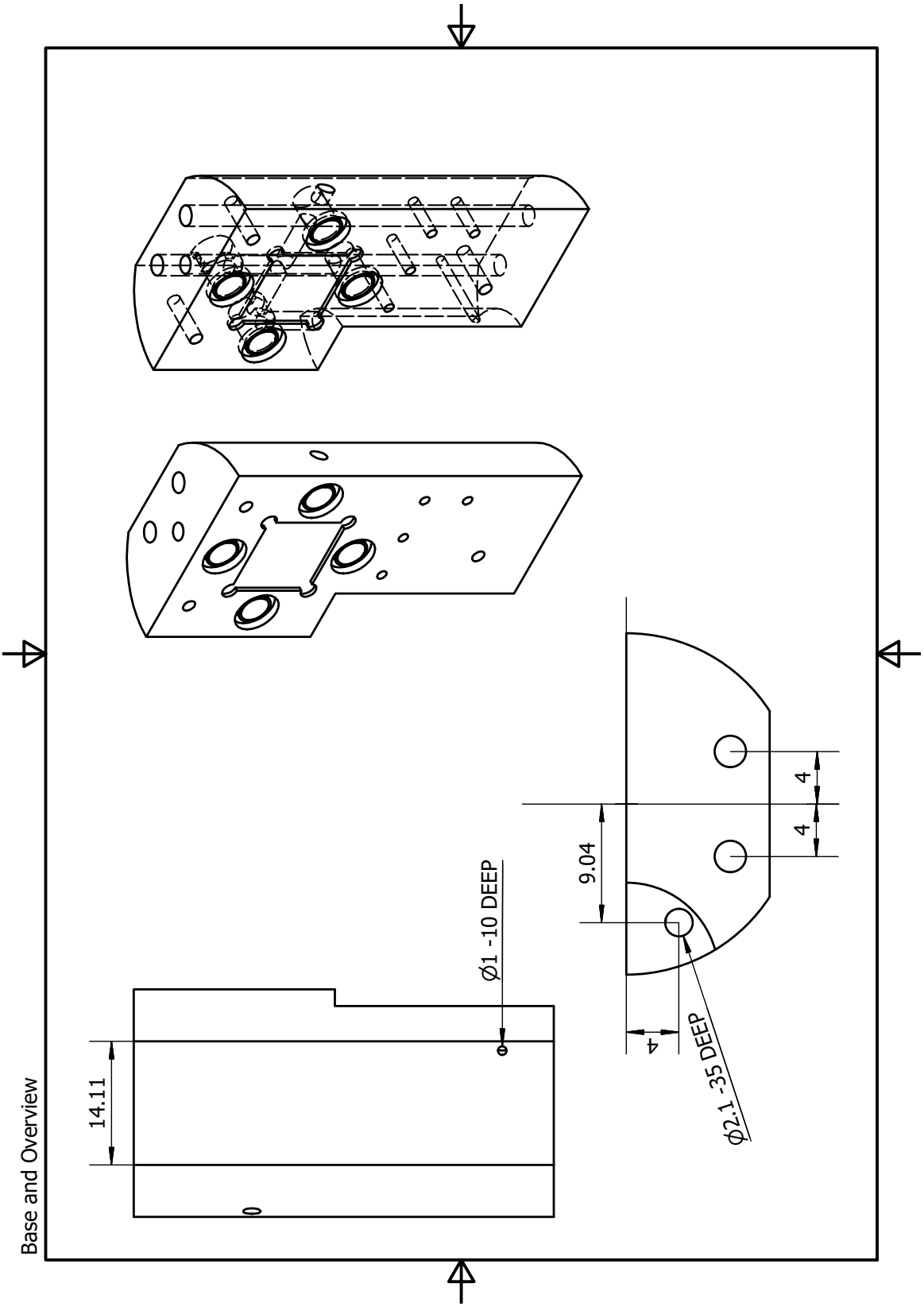
Base and Overview
14.11
Ø1 -10 DEEP
9.04
4
4
4
Ø2.1 -35 DEEP

Appendix B

Sinter Plug Drawing

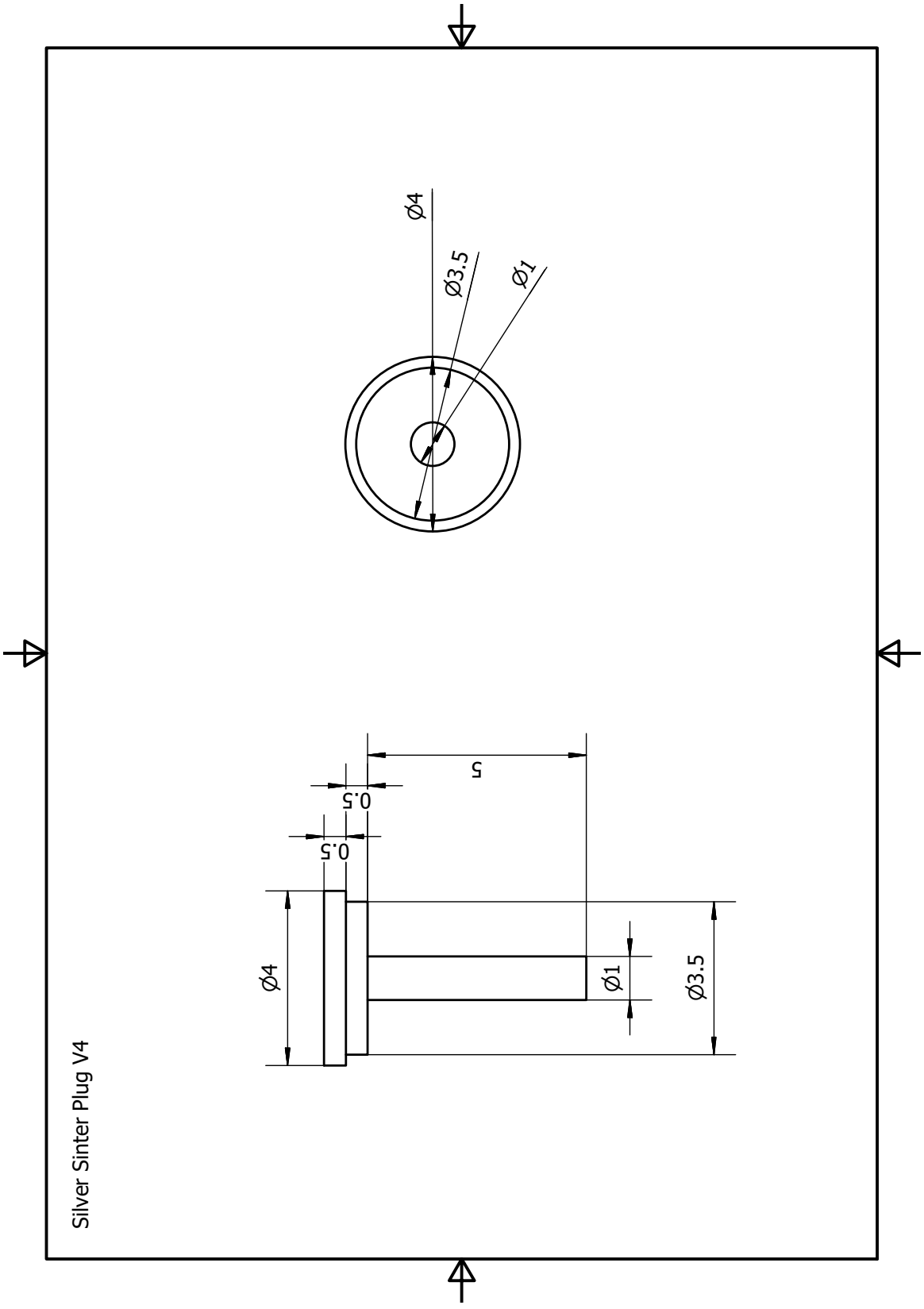
Ø4
Ø3.5
Ø1
5
0.5
0.5
Ø4
Ø1
Ø3.5
Silver Sinter Plug V4

Appendix C

Displacer Drawings

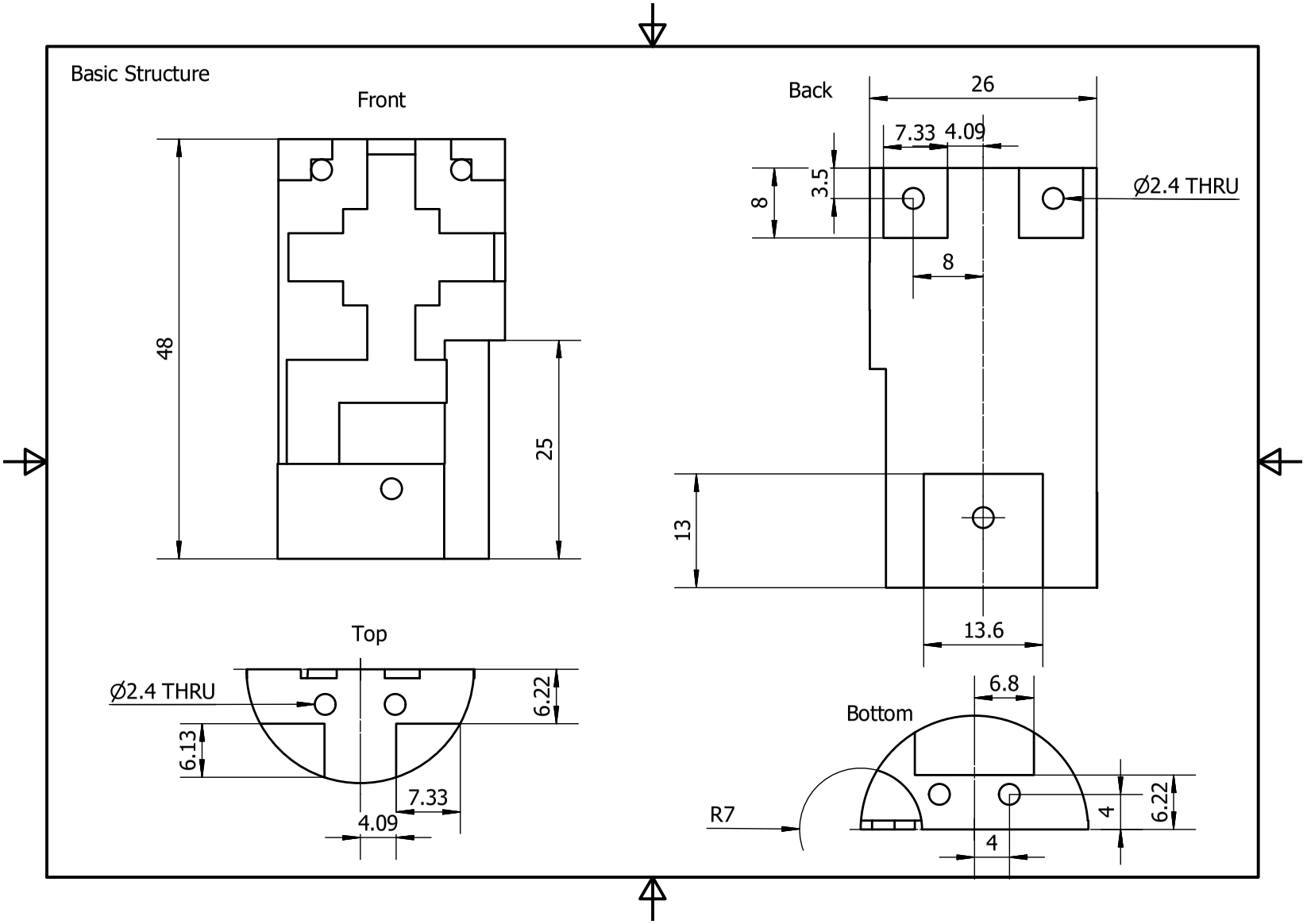
Basic Structure
Front
48
25
Back
26
7.33
4.09
8
3.5
Ø2.4 THRU
8
13
13.6
Top
Ø2.4 THRU
6.22
6.13
7.33
4.09
Bottom
6.8
R7
4
6.22
4

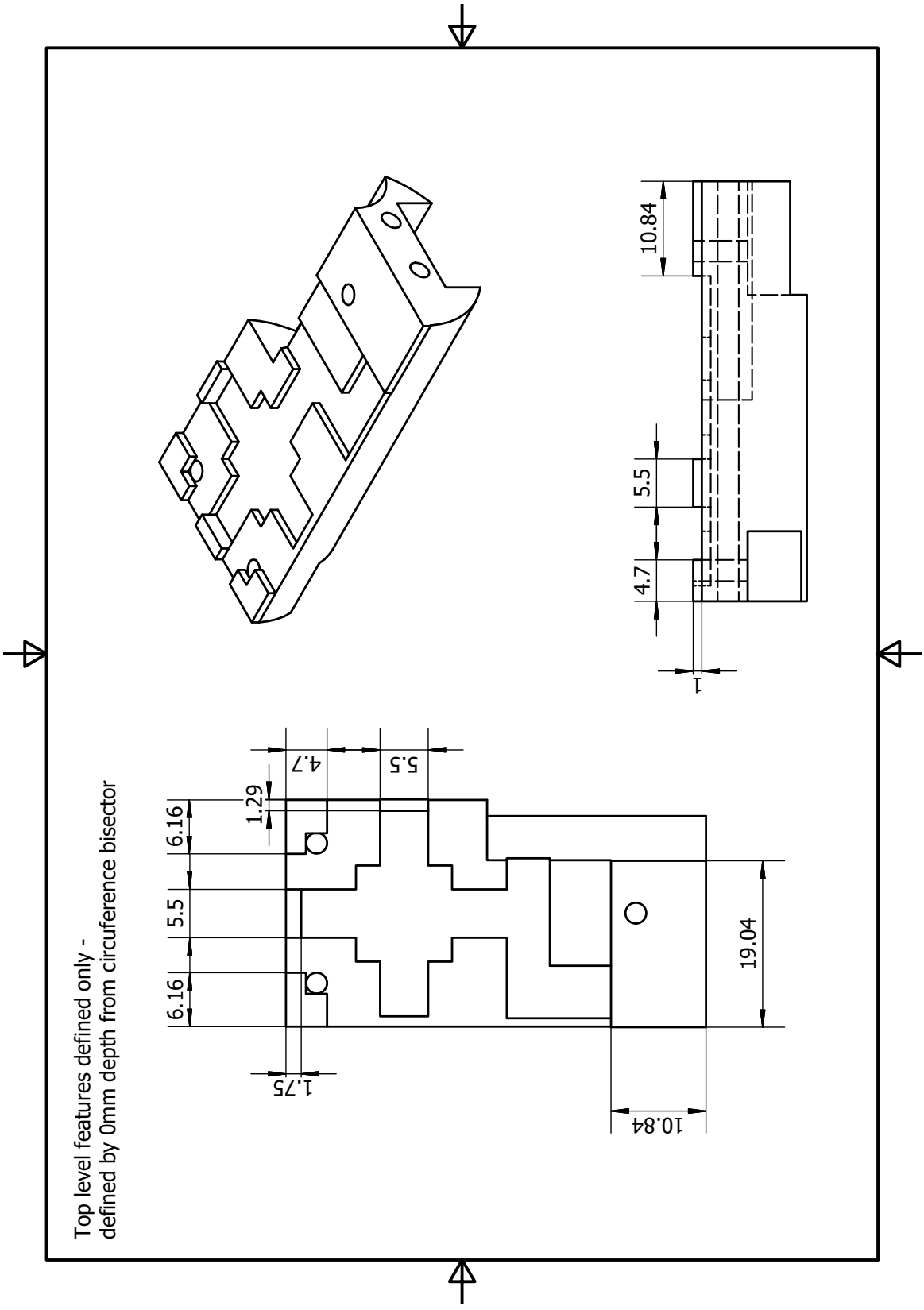
Top level features defined only -
defined by 0mm depth from circuference bisector
10.84
5.5
4.7
1
4.7
5.5
1.29
6.16
5.5
6.16
19.04
1.75
10.84

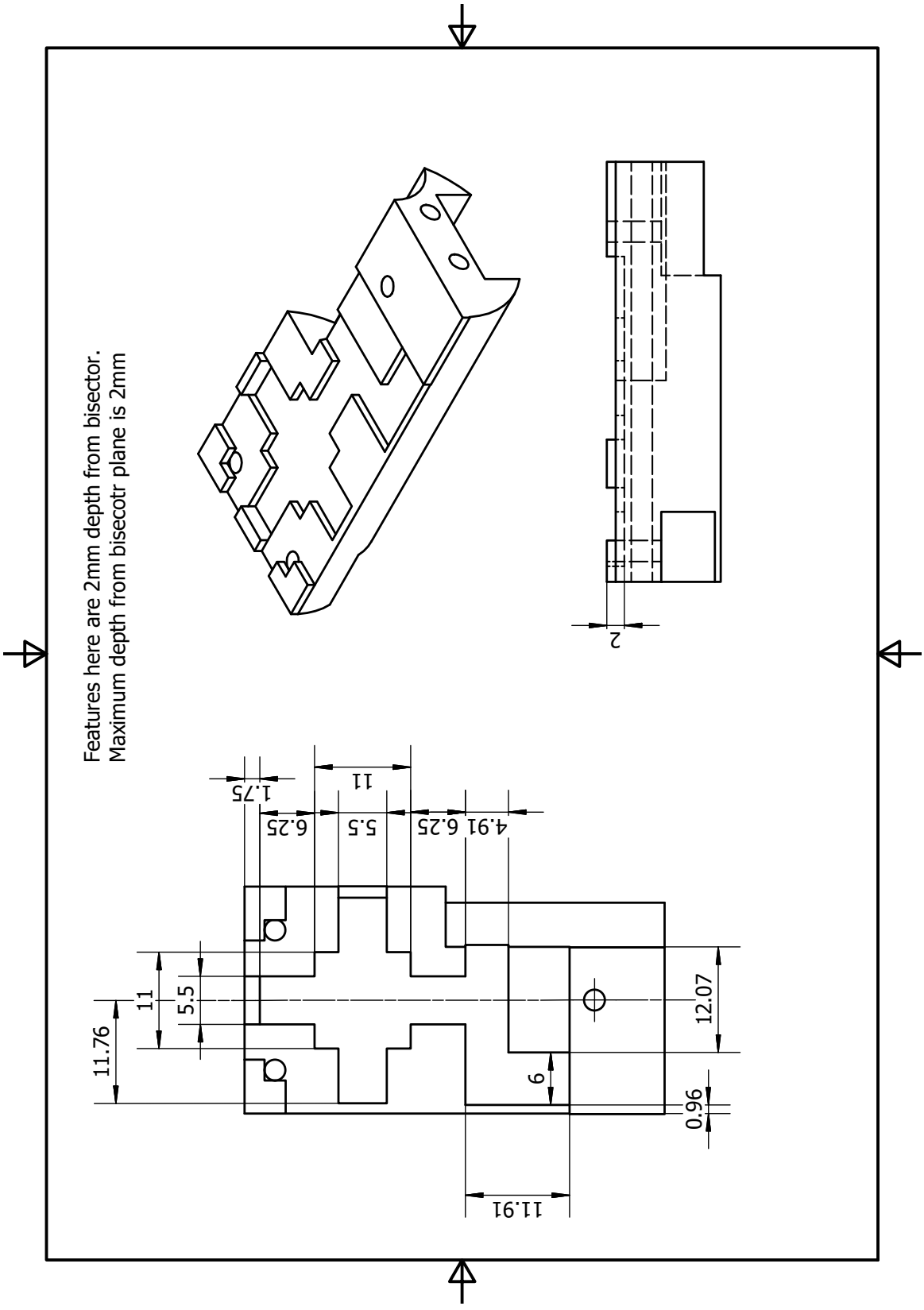
Features here are 2mm depth from bisector.
Maximum depth from bisecotr plane is 2mm
2
1.75
11
6.25
5.5
4.91
6.25
11.76
11
5.5
12.07
6
0.96
11.91

Appendix D

Cell Base Drawing

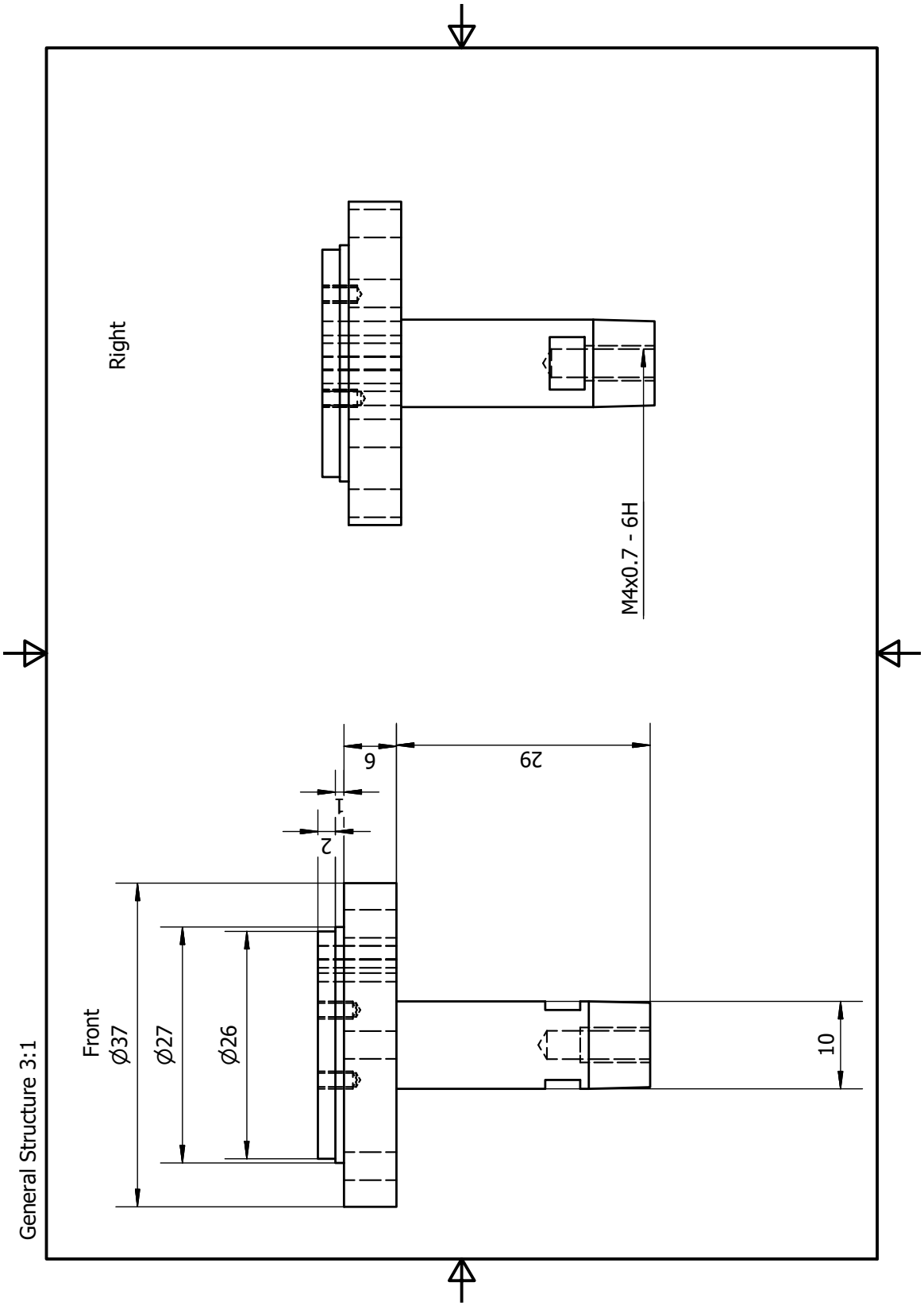
General Structure 3:1
Front
Ø37
Ø27
Ø26
2
1
6
29
10
Right
M4x0.7 - 6H

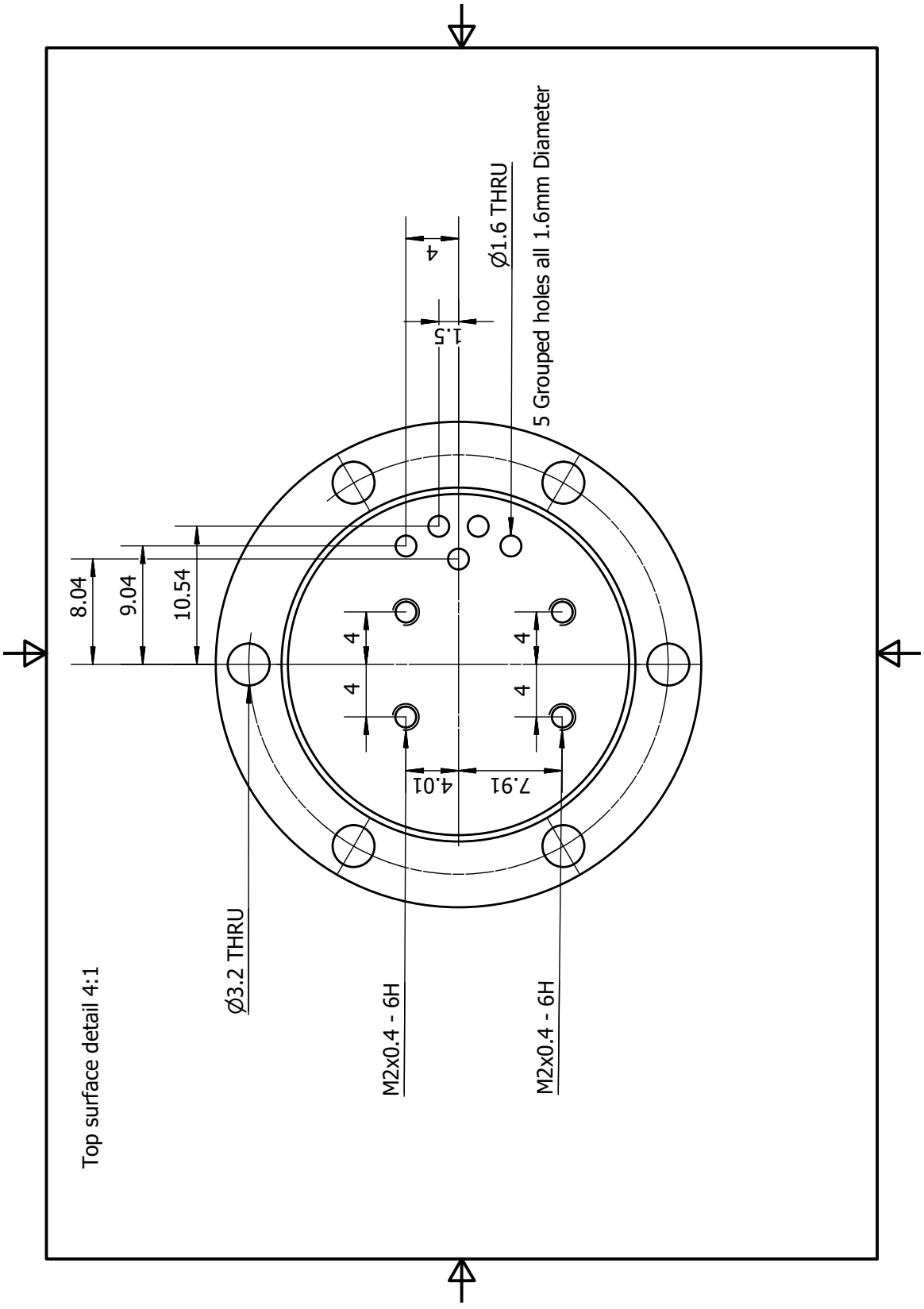
Top surface detail 4:1
Ø3.2 THRU
M2x0.4 - 6H
M2x0.4 - 6H
5 Grouped holes all 1.6mm Diameter
Ø1.6 THRU
8.04
9.04
10.54
4
4
4
4
4
1.5
4.01
7.91

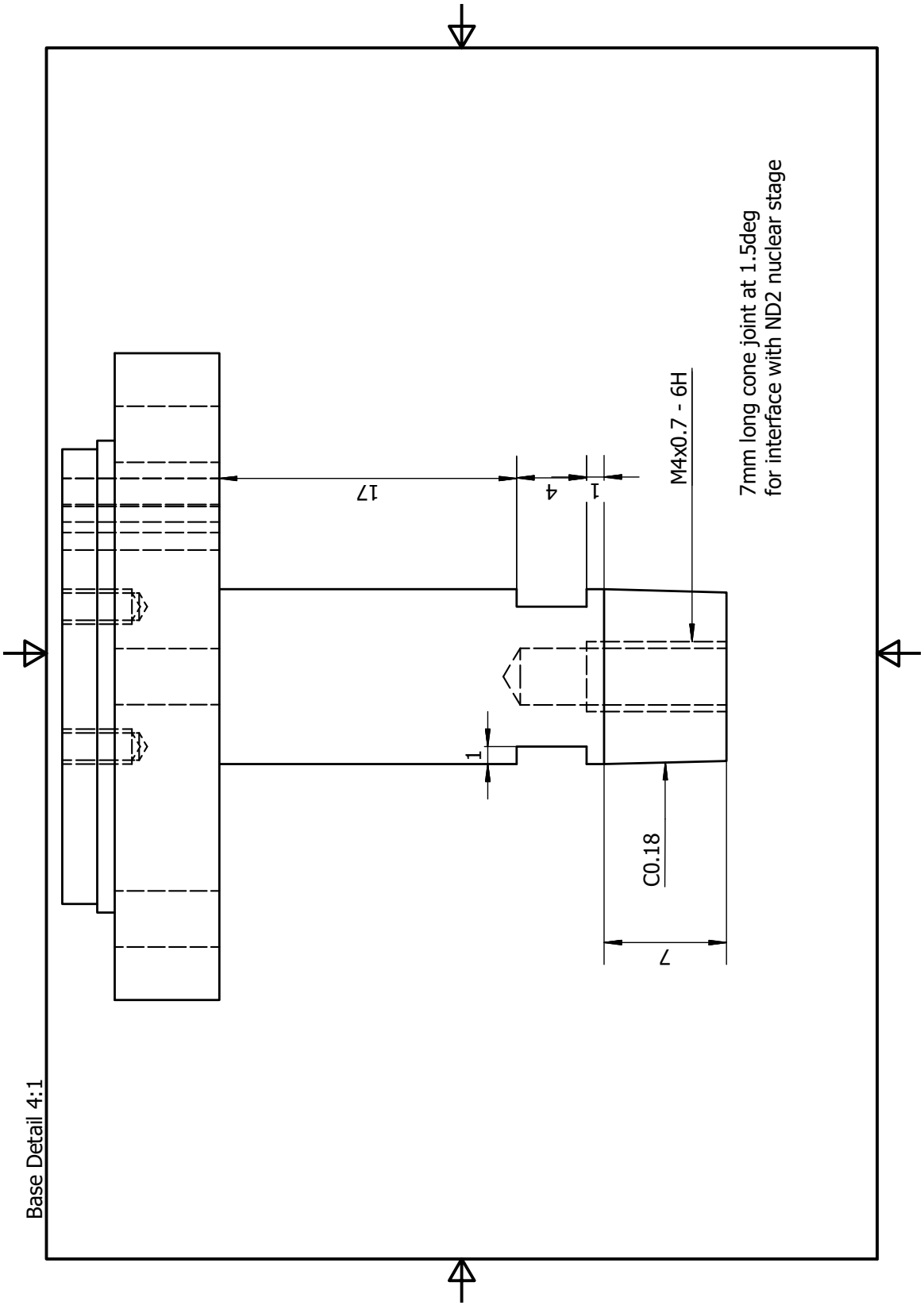
Base Detail 4:1
17
4
1
M4x0.7 - 6H
7mm long cone joint at 1.5deg
for interface with ND2 nuclear stage
1
C0.18
7

Appendix E

Cell Lid Drawing

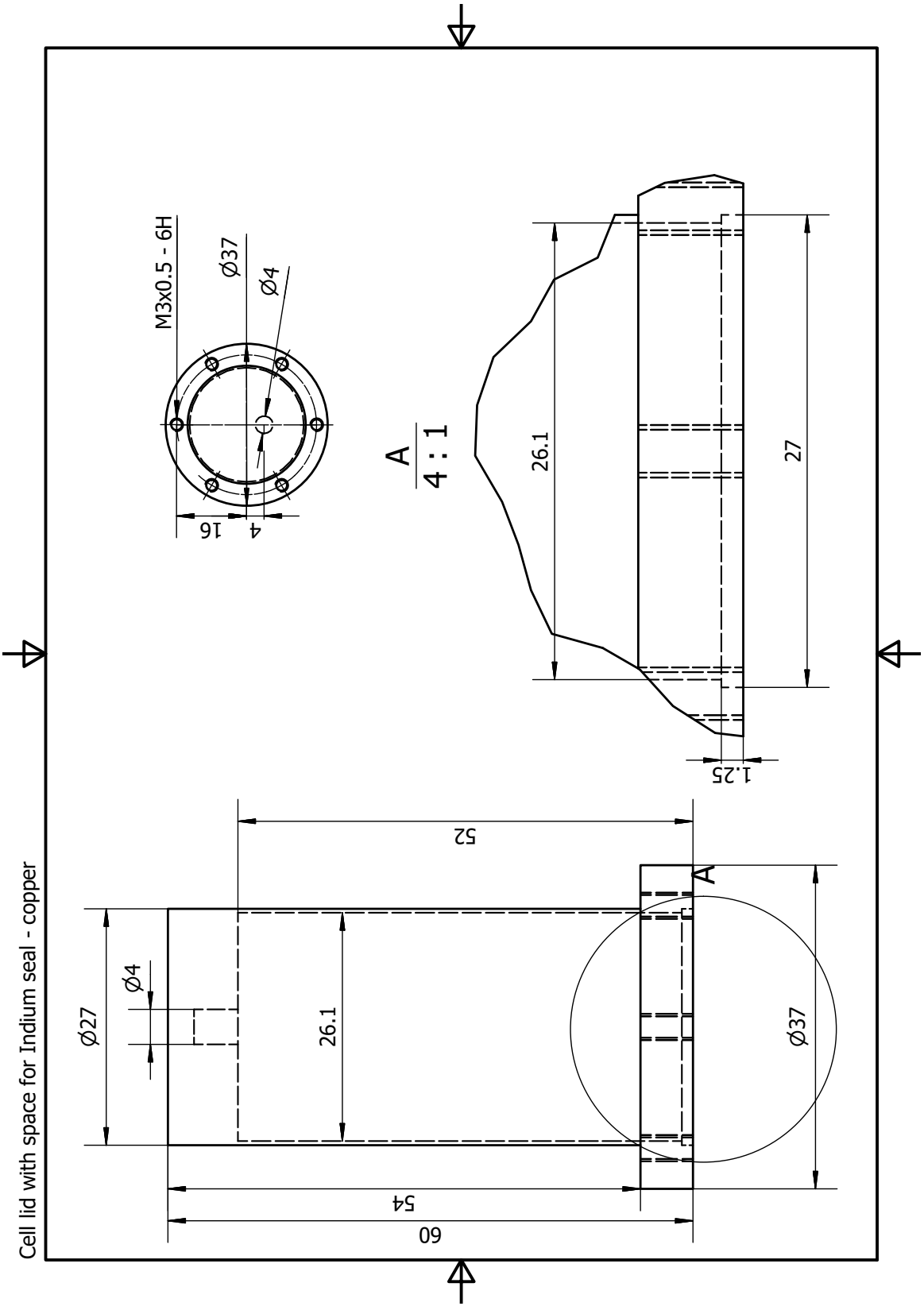
Cell lid with space for Indium seal - copper
M3x0.5 - 6H
Ø37
Ø4
16
4
A
4 : 1
26.1
27
1.25
52
A
Ø27
Ø4
26.1
Ø37
54
60

Appendix F

Heat Exchanger Drawings

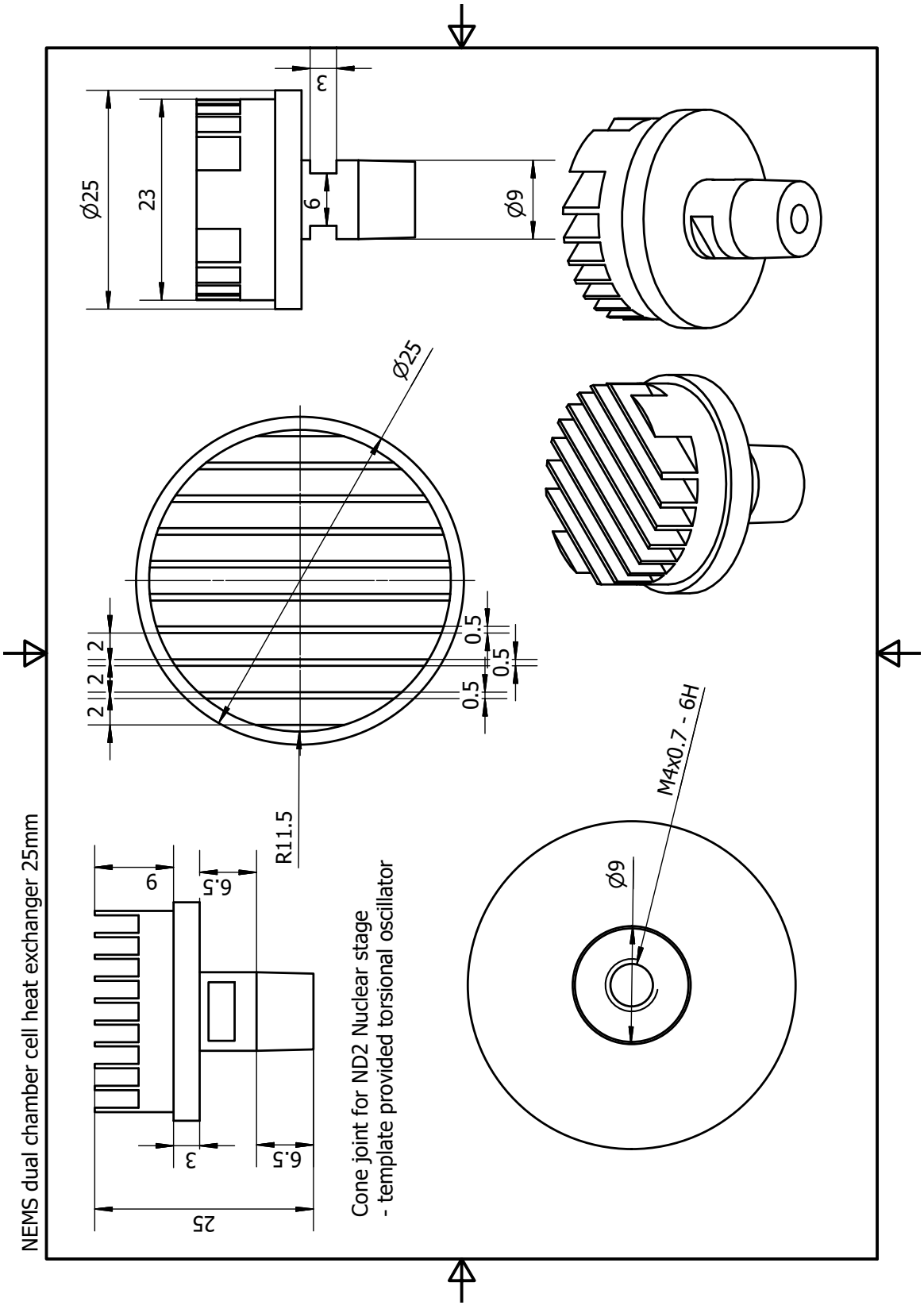
NEMS dual chamber cell heat exchanger 25mm
Cone joint for ND2 Nuclear stage
- template provided torsional oscillator
Ø25
23
9
3
Ø9
Ø25
2
2
2
0.5
0.5
0.5
R11.5
M4x0.7 - 6H
Ø9
9
6.5
3
6.5
25

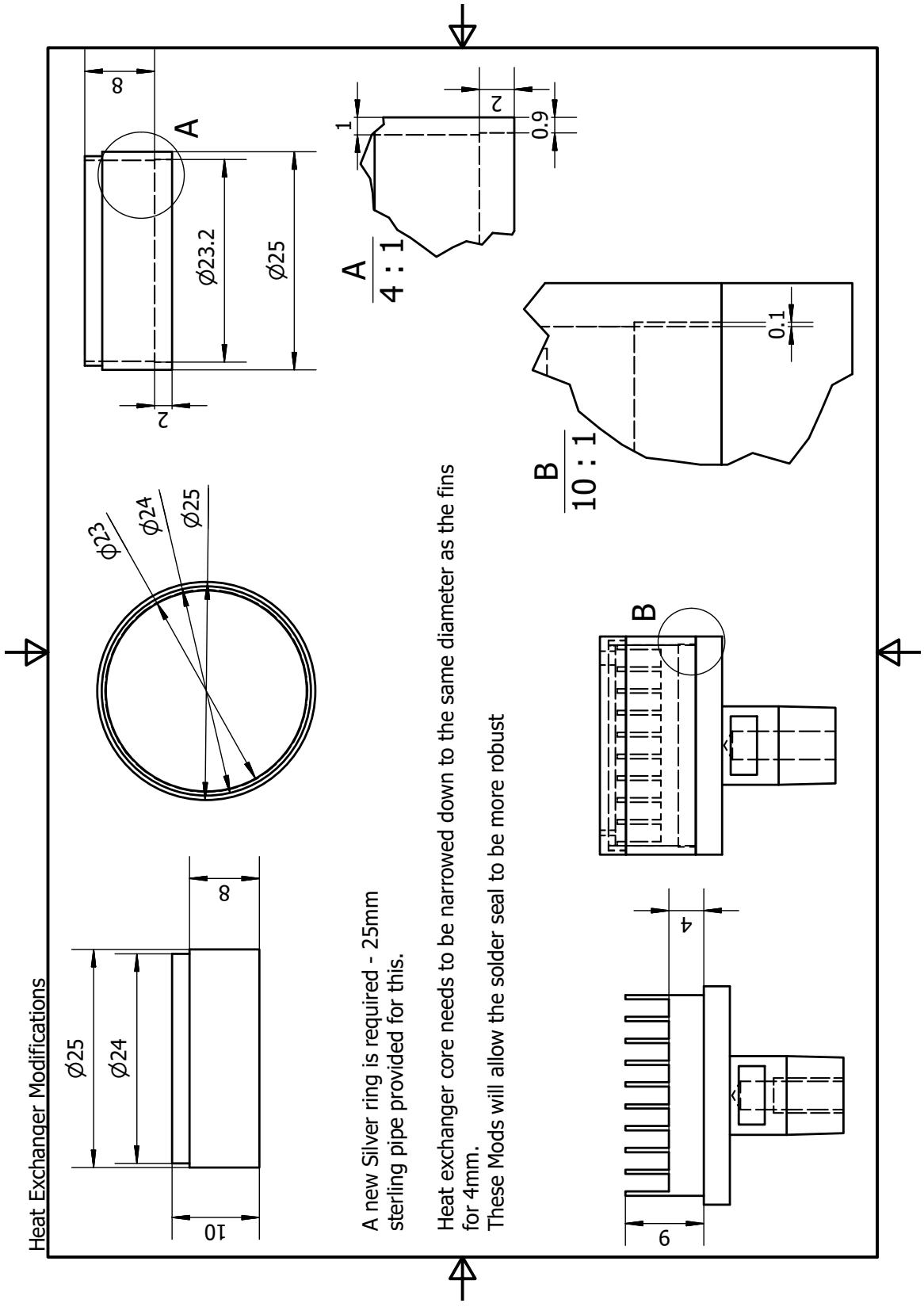
Heat Exchanger Modifications
A new Silver ring is required - 25mm sterling pipe provided for this.
Heat exchanger core needs to be narrowed down to the same diameter as the fins for 4mm.
These Mods will allow the solder seal to be more robust
A
4 : 1
B
10 : 1
Ø23.2
Ø25
Ø24
Ø23
8
2
10
9
4
0.1
0.9
1

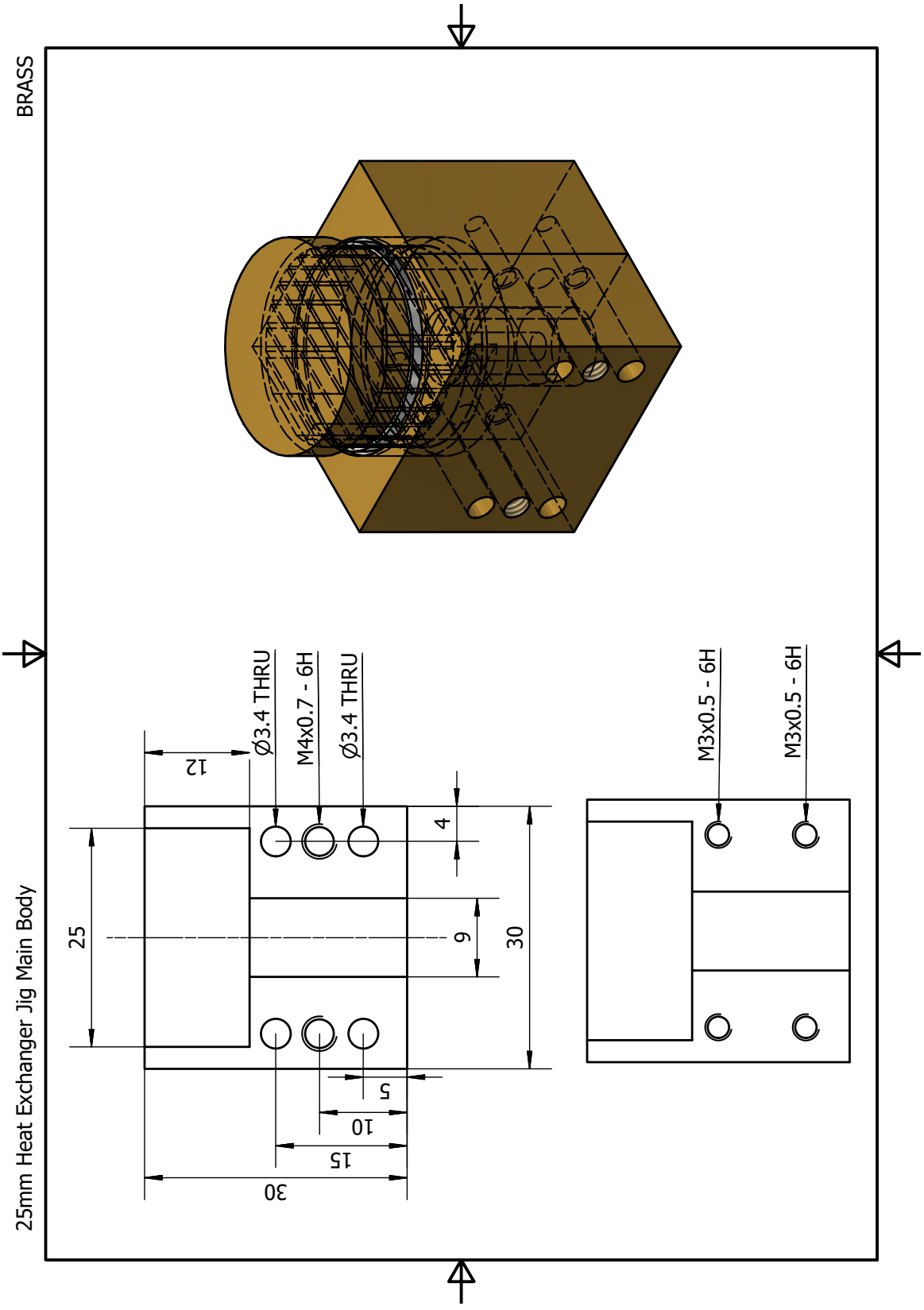
BRASS
25mm Heat Exchanger Jig Main Body
Ø3.4 THRU
M4x0.7 - 6H
Ø3.4 THRU
M3x0.5 - 6H
M3x0.5 - 6H
12
4
25
9
30
5
10
15
30

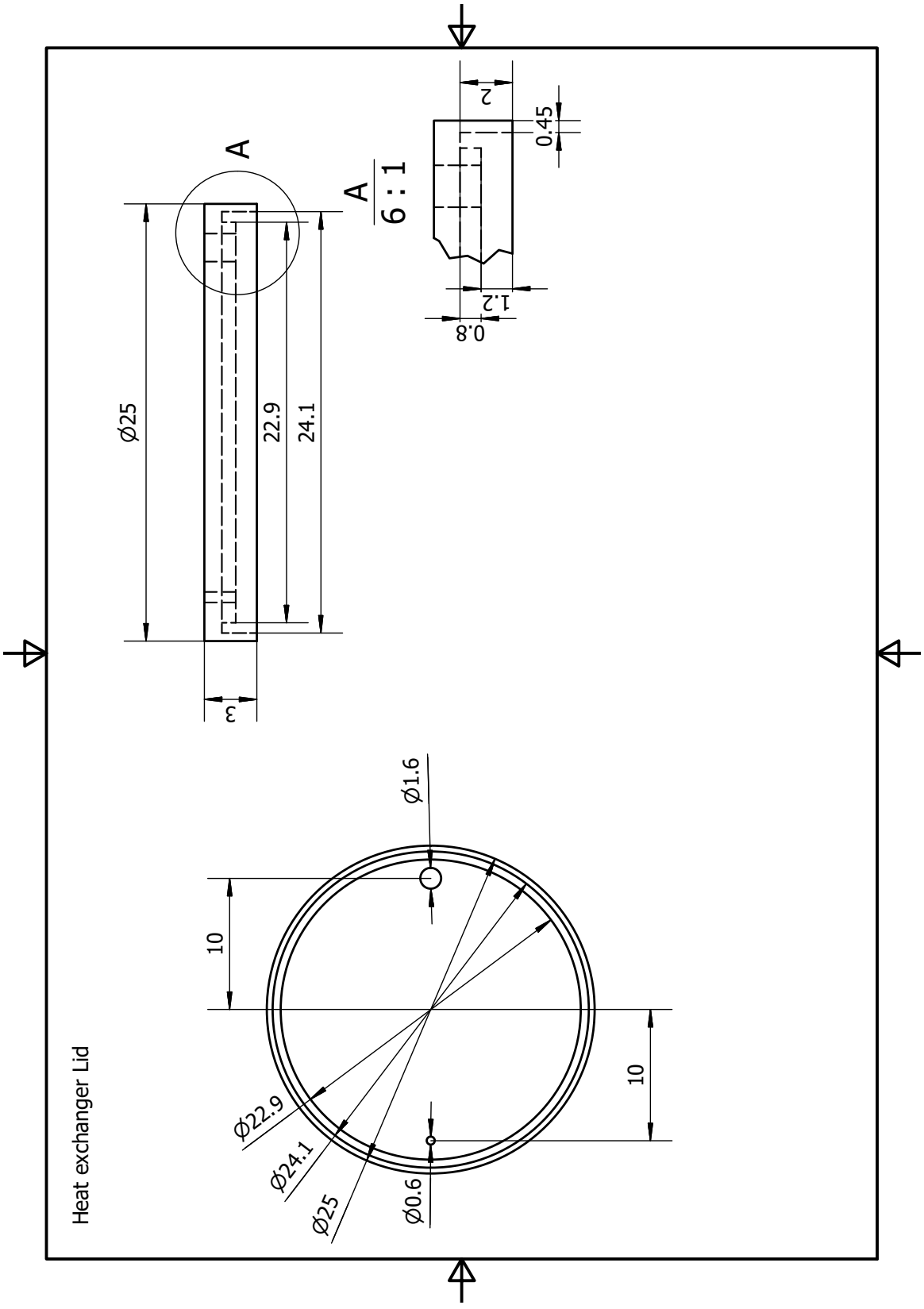
A
A
6 : 1
2
0.45
1.2
0.8
Ø25
22.9
24.1
3
Ø1.6
10
10
Ø22.9
Ø24.1
Ø25
Ø0.6
Heat exchanger Lid

Bibliography

[1] H. C. Nathanson, R. A. Wickstrom, *A resonant gate silicon surface transistor with high Q band pass properties*. Applied Physics Letters, vol. 7(4), 84-86 (1965).

[2] H. Nathanson, R. Wickstrom, *Microelectronic frequency selective apparatus with vibratory member and means responsive thereto* (1968).

[3] D. S. Eddy, D. R. Sparks, *Application of MEMS technology in automotive sensors and actuators*. Proceedings of the IEEE, vol. 86(8), 1747-1755 (1998), ISSN 0018-9219.

[4] C. D. Meinhart, H. Zhang, *The flow structure inside a microfabricated inkjet printhead*. Journal of Microelectromechanical Systems, vol. 9(1), 67-75 (2000), ISSN 10577157.

[5] E. Collin, J. Kofler, *et al.*, *Novel "Vibrating Wire Like" NEMS and MEMS Structures for Low Temperature Physics*. Journal of Low Temperature Physics, vol. 158(3), 678 (2009), ISSN 15737357.

[6] J. F. Annett, *Superconductivity, Superfluids, and Condensates (Oxford Master Series in Condensed Matter Physics)*. Oxford University Press, USA (2004), ISBN 0198507569.

[7] A. L. Fetter, S. Ullah, *Superfluid density and critical current of ^{3}He in confined geometries*. Journal of Low Temperature Physics, vol. 70(5), 515--535 (1988), ISSN 15737357.

[8] D. Drung, C. Assmann, *et al.*, *Highly Sensitive and Easy-to-Use SQUID Sensors*. Applied Superconductivity, IEEE Transactions on, vol. 17(2), 699--704 (2007).

[9] L. Hao, J. Gallop, *et al.*, *Focused Ion Beam NanoSQUIDs as Novel NEMS Resonator Readouts*. Applied Superconductivity, IEEE Transactions on, vol. 19(3), 693-696 (2009), ISSN 10518223.

[10] G. Batey, A. Casey, *et al.*, *A microkelvin cryogen-free experimental platform with integrated noise thermometry*. New Journal of Physics, vol. 15(11) (2013), ISSN 13672630.

[11] J. Moser, J. Güttinger, *et al.*, *Ultrasensitive force detection with a nanotube mechanical resonator*. Nature Nanotechnology, vol. 8(7), 1–4 (2013).

[12] A. Suhel, B. D. Hauer, *et al.*, *Dissipation mechanisms in thermomechanically driven silicon nitride nanostrings*. Applied Physics Letters, vol. 100(17), 173111 (2012).

[13] X. Rojas, J. P. Davis, *A Superfluid Nanomechanical Resonator for Quantum Nanofluidics*. arXiv.org (2014).

[14] S. Schmid, K. D. Jensen, *et al.*, *Damping mechanisms in high-¡span class="aps-inline-formula"¿¡math xmlns="http://www.w3.org/1998/Math/MathML" display="inline"¿¡mi¿Q¡/mi¿¡/math¿¡/span¿ micro and nanomechanical string resonators*. Physical Review B, vol. 84(16), 165,307 (2011).

[15] S. Y. Kim, H. S. Park, *The Importance of Edge Effects on the Intrinsic Loss Mechanisms of Graphene Nanoresonators*. Nano Letters, vol. 9(3), 969–974 (2009), pMID: 19239202.

[16] S. S. Verbridge, J. M. Parpia, *et al.*, *High quality factor resonance at room temperature with nanostrings under high tensile stress*. Journal of Applied Physics, vol. 99(12), 124,304–8 (2006).

[17] M. Poot, S. Etaki, *et al.*, *Tunable Backaction of a DC SQUID on an Integrated Micromechanical Resonator*. Phys. Rev. Lett., vol. 105, 207,203 (2010).

[18] W. J. Venstra, H. J. R. Westra, H. S. J. van der Zant, *Q-factor control of a microcantilever by mechanical sideband excitation*. Applied Physics Letters, vol. 99(15), 151,904–4 (2011).

[19] M. Defoort, K. J. Lulla, *et al.*, *Stressed Silicon Nitride Nanomechanical Resonators at Helium Temperatures*. Journal of Low Temperature Physics, vol. 171(56), 731--736 (2012).

[20] D. I. Bradley, R. George, *et al.*, *Operating Nanobeams in a Quantum Fluid*. Scientific Reports, vol. 7(1), 4876 (2017), ISSN 20452322.

[21] O. Maillet, X. Zhou, *et al.*, *Nonlinear frequency transduction of nanomechanical Brownian motion*. Phys. Rev. B, vol. 96, 165,434 (2017).

[22] D. Karabacak, T. Kouh, K. L. Ekinci, *Analysis of optical interferometric displacement detection in nanoelectromechanical systems*. Journal of Applied Physics, vol. 98(12), 124,309 (2005).

[23] S. S. Verbridge, D. F. Shapiro, *et al.*, *Macroscopic Tuning of Nanomechanics: Substrate Bending for Reversible Control of Frequency and Quality Factor of Nanostring Resonators*. Nano Letters, vol. 7(6), 1728-1735 (2007), pMID: 17497822.

[24] J. D. Teufel, J. W. Harlow, *et al.*, *Dynamical Backaction of Microwave Fields on a Nanomechanical Oscillator*. Physical Review Letters, vol. 101(19), 197,203–4 (2008).

[25] K. Usami, A. Naesby, *et al.*, *Optical cavity cooling of mechanical modes of a semiconductor nanomembrane*. Nature Physics, vol. 8, 168 (2012).

[26] A. Armour, *Hot electrons but cool vibrations*. Nature Physics, vol. 8, 110 (2012).

[27] S. Etaki, M. Poot, *et al.*, *Motion detection of a micromechanical resonator embedded in a d.c. SQUID*. Nature Physics, vol. 4(10), 785--788 (2008).

[28] A. Naik, O. Buu, *et al.*, *Cooling a nanomechanical resonator with quantum backaction*. Nature, vol. 443(7108), 193--196 (2006).

[29] M. Poot, H. S. van der Zant, *Mechanical systems in the quantum regime*. Physics Reports, vol. 511(5), 273 - 335 (2012), ISSN 03701573.

[30] S. Etaki, M. Poot, *et al.*, *DC SQUIDs as linear displacement detectors for embedded micromechanical resonators*. Comptes Rendus Physique, vol. 12(910), 817 - 825 (2011), ISSN 16310705.

[31] K. Ekinci, *Electromechanical Transducers at the Nanoscale: Actuation and Sensing of Motion in Nanoelectromechanical Systems (NEMS)*. Small, vol. 1(8-9), 786–797 (2005).

[32] S. Etaki, F. Konschelle, *et al.*, *Self-sustained oscillations of a torsional SQUID resonator induced by Lorentz-force back-action*. Nat Commun, vol. 4, 1803 (2013).

[33] M. Poot, S. Etaki, *et al.*, *Discrete time quadrature feedback cooling of a radio-frequency mechanical resonator*. Applied Physics Letters, vol. 99(1), 013113 (2011).

[34] L. Hao, D. C. Cox, *et al.*, *Coupled NanoSQUIDs and Nano-Electromechanical Systems (NEMS) Resonators*. IEEE Transactions on Applied Superconductivity, vol. 23(3), 1800,304–1800,304 (2013), ISSN 1051-8223.

[35] S. Bechstein, F. Ruede, *et al.*, *Design and Fabrication of Coupled NanoSQUIDs and NEMS*. Applied Superconductivity, IEEE Transactions on, vol. 25(3), 1-4 (2015), ISSN 10518223.

[36] O. Usenko, A. Vinante, *et al.*, *A superconducting quantum interference device based readout of a subattonewton force sensor operating at millikelvin temperatures*. Applied Physics Letters, vol. 98(13), 133105 (2011).

[37] G. Anetsberger, O. Arcizet, *et al.*, *Near-field cavity optomechanics with nanomechanical oscillators*. Nature Physics, vol. 5(12), 909–914 (2009).

[38] S. Pugnetti, Y. M. Blanter, R. Fazio, *SQUID Detection of Quantized Mechanical Motion*. ArXiv eprints (2009).

[39] D. Tilley, J. Tilley, *Superfluidity and Superconductivity*. Graduate Student Series in Physics, Taylor & Francis (1990), ISBN 9780750300339.

[40] F. Pobell, *Matter and Methods at Low Temperatures*. SpringerVerlag (1996), ISBN 9783540585725.

[41] J. D. Reppy, D. Depatie, *Persistent Currents in Superfluid Helium*. Phys. Rev. Lett., vol. 12, 187–189 (1964).

[42] A. C. Hollis-Hallett, *Experiments with oscillating disk systems in liquid helium II*. Proceedings of the Royal Society of London A: Mathematical, Physical and Engineering Sciences, vol. 210(1102), 404–426 (1952), ISSN 0080-4630.

[43] J. T. Tough, W. D. McCormick, J. G. Dash, *Viscosity of Liquid He II*. Phys. Rev., vol. 132, 2373–2378 (1963).

[44] L. D. Landau, I. M. Khalatnikov, *Theory of viscosity of Helium II. 1. Collisions of elementary excitations in Helium II*. Zhurnal Eksperimentalnoi i Teoreticheskoi Fiziki, vol. 19, 637 (1949).

[45] D. G. Henshaw, A. D. B. Woods, *Modes of Atomic Motions in Liquid Helium by Inelastic Scattering of Neutrons*. Phys. Rev., vol. 121, 1266–1274 (1961).

[46] A. A. Zadorozhko, . Y. Rudavskiĭ, *et al.*, *Viscosity and relaxation processes in the phonon-roton system of He II*. Low Temperature Physics, vol. 35(2), 100–104 (2009).

[47] D. O. Clubb, O. V. L. Buu, *et al.*, *Quartz Tuning Fork Viscometers for Helium Liquids*. Journal of Low Temperature Physics, vol. 136(1), 1–13 (2004), ISSN 1573-7357.

[48] E. Pentti, J. Rysti, *et al.*, *Studies on Helium Liquids by Vibrating Wires and Quartz Tuning Forks*. Journal of Low Temperature Physics, vol. 165(3), 132 (2011), ISSN 1573-7357.

[49] D. I. Bradley, M. J. Fear, *et al.*, *Transition to Turbulence for a Quartz Tuning Fork in Superfluid 4He*. Journal of Low Temperature Physics, vol. 156(3), 116–131 (2009), ISSN 1573-7357.

[50] M. J. Jackson, O. Kolosov, *et al.*, *Measurements of Vortex Line Density Generated by a Quartz Tuning Fork in Superfluid ^{4}He*. Journal of Low Temperature Physics, vol. 183(3), 208–214 (2016), ISSN 1573-7357.

[51] D. D. Osheroff, R. C. Richardson, D. M. Lee, *Evidence for a New Phase of Solid* He^3. Phys. Rev. Lett., vol. 28, 885–888 (1972).

[52] A. J. Leggett, *A theoretical description of the new phases of liquid* ^{3}He. Rev. Mod. Phys., vol. 47, 331–414 (1975).

[53] M. Bartkowiak, S. Fisher, *et al.*, *The Unique Superfluid 3He A-B Interface: Surface Tension and Contact Angle*. Journal of Low Temperature Physics, vol. 126, 533–538 (2002).

[54] V. Ambegaokar, P. G. deGennes, D. Rainer, *Landau-Ginsburg equations for an anisotropic superfluid*. Phys. Rev. A, vol. 9, 2676–2685 (1974).

[55] M. R. Freeman, R. C. Richardson, *Size effects in superfluid* ^{3}He *films*. Phys. Rev. B, vol. 41, 11,011–11,028 (1990).

[56] T. T. Heikkila, *The Physics of Nanoelectronics*. Oxford Master Series in Condensed Matter Physics, Oxford (2012).

[57] A. N. Cleland, *Foundations of Nanomechanics*. Springer (2002).

[58] B. Cowan, *Topics in Statistical Mechanics*. Imperial College Press Advance, Imperial College Press (2005), ISBN 9781860945649.

[59] F. Reif, *Fundamentals of Statistical and Thermal Physics*. McGraw Hill, Tokyo (1965).

[60] A. A. H. Pádua, J. M. N. A. Fareleira, *et al.*, *Electromechanical model for vibrating-wire instruments*. Review of Scientific Instruments, vol. 69(6), 2392–2399 (1998).

[61] D. R. Southworth, R. A. Barton, *et al.*, *Stress and Silicon Nitride: A Crack in the Universal Dissipation of Glasses*. Physical Review Letters, vol. 102(22), 231 (2009).

[62] A. Eichler, J. Chaste, *et al.*, *Parametric Amplification and Self-Oscillation in a Nanotube Mechanical Resonator*. Nano Letters, vol. 11(7), 2699–2703 (2011), pMID: 21615135.

[63] J. Clarke, A. I. B. (Eds.), *The SQUID Handbook*, vol. Vol. I Fundamentals and Technology of SQUIDs and SQUID Systems. WileyVCH (2004).

[64] D. Drung, *Improved dc SQUID readout electronics with low 1/f noise preamplifier*. Review of Scientific Instruments, vol. 68(11), 4066-4074 (1997).

[65] H. Weinstock, *SQUID Sensors: Fundamentals, Fabrication, and Applications*. NATO ASI series / E: NATO ASI series, Kluwer Academic Publishers (1996), ISBN 9780792343509.

[66] D. Drung, H. Koch, *An integrated DC SQUID magnetometer with variable additional positive feedback*. Superconductor Science and Technology, vol. 7(5), 242 (1994).

[67] D. Drung, J. Beyer, *et al.*, *Novel SQUID Current Sensors With High Linearity at High Frequencies*. Applied Superconductivity, IEEE Transactions on, vol. 19(3), 772--777 (2009).

[68] J. B. Johnson, *Thermal Agitation of Electricity in Conductors*. Phys. Rev., vol. 32, 97--109 (1928).

[69] H. Nyquist, *Thermal Agitation of Electric Charge in Conductors*. Phys. Rev., vol. 32, 110--113 (1928).

[70] A. Casey, F. Arnold, *et al.*, *Current Sensing Noise Thermometry: A Fast Practical Solution to Low Temperature Measurement*. Journal of Low Temperature Physics, vol. 175(5), 764–775 (2014), ISSN 1573-7357.

[71] R. A. Webb, R. P. Giffard, J. C. Wheatley, *Noise thermometry at ultralow temperatures*. Journal of Low Temperature Physics, vol. 13(3), 383–429 (1973), ISSN 1573-7357.

[72] B. D. Hauer, C. Doolin, *et al.*, *A general procedure for thermomechanical calibration of nano/micromechanical resonators*. Annals of Physics, vol. 339, 181--207 (2013).

[73] T. H. Stievater, W. S. Rabinovich, *et al.*, *Measurement of thermal-mechanical noise in microelectromechanical systems*. Applied Physics Letters, vol. 81(10), 1779–1781 (2002).

[74] K. L. Ekinci, Y. T. Yang, M. L. Roukes, *Ultimate limits to inertial mass sensing based upon nanoelectromechanical systems*. Journal of Applied Physics, vol. 95(5), 2682–2689 (2004).

[75] M. Wallquist, K. Hammerer, *et al.*, *Hybrid quantum devices and quantum engineering*. Physica Scripta, vol. 2009(T137), 014,001 (2009).

[76] A. Cleland, M. Roukes, *External control of dissipation in a nanometer scale radiofrequency mechanical resonator*. Sensors and Actuators (1998).

[77] R. De Alba, T. S. Abhilash, *et al.*, *Low-power photothermal self-oscillation of bimetallic nanowires*. arXiv.org, (7), 3995–4002 (2016).

[78] M. Poggio, C. L. Degen, *et al.*, *Feedback Cooling of a Cantilever's Fundamental Mode below 5 mK*. Physical Review Letters, vol. 99(1), 017,201–4 (2007).

[79] M. Zalalutdinov, K. L. Aubin, *et al.*, *Frequency entrainment for micromechanical oscillator*. Applied Physics Letters, vol. 83(16), 3281-3283 (2003).

[80] F. P. Milliken, J. R. Rozen, *et al.*, *50Ω characteristic impedance low-pass metal powder filters*. Review of Scientific Instruments, vol. 78(2), 024,701 (2007).

[81] J. Ekin, *Experimental Techniques for Low-Temperature Measurements: Cryostat Design, Material Properties and Superconductor Critical-Current Testing*. OUP Oxford (2006), ISBN 9780191524691.

[82] A. A. Abrikosov, I. M. Khalatnikov, *The theory of a fermi liquid (the properties of liquid 3 He at low temperatures)*. Reports on Progress in Physics, vol. 22(1), 329 (1959).

[83] O. Lounasmaa, *Experimental principles and methods below 1 K*. Academic Press (1974).

[84] G. L. Pollack, *Kapitza Resistance*. Rev. Mod. Phys., vol. 41, 48--81 (1969).

[85] R. Richardson, N. Bigelow, *et al.*, *Experimental Techniques in Condensed Matter at Low Temperatures*. AddisonWesley (1998), ISBN 0201360780.

[86] R. Bennett, *NMR Studies of Superfluid ^{3}He Confined to a Single 635 nm Slab*. Ph.D. thesis, Royal Holloway, University of London (2009).

[87] Y. Tsui, R. Mahmoud, *et al.*, *Superconducting and Mechanical Properties of Low-Temperature Solders for Joints*. IEEE Transactions on Applied Superconductivity, vol. 26(3), 1–4 (2016), ISSN 1051-8223.